CNWRA 95-010

EXPERIMENTAL INVESTIGATIONS OF FAILURE PROCESSES OF HIGH-LEVEL RADIOACTIVE WASTE CONTAINER MATERIALS

Prepared for

Nuclear Regulatory Commission
Contract NRC-02-93-005

Prepared by

Center for Nuclear Waste Regulatory Analyses
San Antonio, Texas

May 1995

CNWRA 95-010

EXPERIMENTAL INVESTIGATIONS OF FAILURE PROCESSES OF HIGH-LEVEL RADIOACTIVE WASTE CONTAINER MATERIALS

Prepared for

Nuclear Regulatory Commission
Contract NRC-02-93-005

Prepared by

N. Sridhar
G.A. Cragnolino
D.S. Dunn

Center for Nuclear Waste Regulatory Analyses
San Antonio, Texas

May 1995

PREVIOUS REPORTS IN SERIES

Number	Name	Date Issued
20-3704-042-005-900	Progress Report of Activities and Recommendations in the Integrated Waste Package Experimental Program	June 1990
CNWRA 90-01Q	Report on Research Activities for the Quarter January 1 through March 31, 1990	May 1990
CNWRA 90-02Q	Report on Research Activities for the Quarter April 1 through June 30, 1990	August 1990
CNWRA 90-03Q	Report on Research Activities for the Quarter July 1 through September 30, 1990	November 1990
CNWRA 90-01A NUREG/CR-5817	Report on Research Activities for Calendar Year 1990	February 1991 December 1991
CNWRA 91-004	A Review of Localized Corrosion of High-Level Nuclear Waste Container Materials—I	April 1991
CNWRA 91-01Q	Report on Research Activities for the Quarter January 1 through March 31, 1991	May 1991
CNWRA 91-008	Hydrogen Absorption and Embrittlement of Candidate Container Materials	June 1991
CNWRA 91-02Q	Report on Research Activities for the Quarter April 1 through June 30, 1991	August 1991
CNWRA 91-03Q	Report on Research Activities for the Quarter July 1 through September 30, 1991	November 1991
CNWRA 91-01A NUREG/CR-5817, Vol. 2	NRC High-Level Radioactive Waste Research at CNWRA, Calendar Year 1991	February 1992 May 1993
CNWRA 92-021	A Review of Stress Corrosion Cracking of High-Level Nuclear Waste Container Materials—I	August 1992
CNWRA 92-01S NUREG/CR-5817, Vol. 3, No. 1	NRC High-Level Radioactive Waste Research at CNWRA January–June 1992	September 1992 May 1993
CNWRA 92-02S NUREG/CR-5817, Vol. 3, No. 2	NRC High-Level Radioactive Waste Research at CNWRA July–December 1992	February 1993 July 1993

PREVIOUS REPORTS IN SERIES (cont'd)

Number	Name	Date Issued
CNWRA 93-003	Long-Term Stability of High-Level Nuclear Waste Container Materials: I—Thermal Stability of Alloy 825	February 1993
CNWRA 93-004	Experimental Investigations of Localized Corrosion of High-Level Waste Container Materials	February 1993
CNWRA 93-014	A Review of the Potential for Microbially Influenced Corrosion of High-Level Nuclear Waste Containers	June 1993
CNWRA 93-01S	NRC High-Level Radioactive Waste Research at CNWRA January–June 1993	August 1993
CNWRA 93-02S	NRC High-Level Radioactive Waste Research at CNWRA July–December 1993	February 1994
CNWRA 94-010	Review of Degradation Modes of Alternate Container Designs and Materials	April 1994
CNWRA 94-028	Environmental Effects on Stress Corrosion Cracking of Type 316L Stainless Steel and Alloy 825 as High-Level Nuclear Waste Container Materials	October 1994
CNWRA 94-01S	NRC High-Level Radioactive Waste Research at CNWRA January–June 1994	September 1994
CNWRA 94-02S	NRC High-Level Radioactive Waste Research at CNWRA July–December 1994	February 1995

ABSTRACT

This report presents the results of the past five years of research activities in the Integrated Waste Package Experiments (IWPE) Research Project, conducted at the Center for Nuclear Waste Regulatory Analyses (CNWRA) under the sponsorship of the Nuclear Regulatory Commission (NRC), Office of Nuclear Regulatory Research. Experimental research activities focused on localized corrosion, stress corrosion cracking, materials thermal stability, and hydrogen embrittlement of austenitic Fe-Cr-Ni-Mo alloys, selected as candidate materials for the construction of high-level radioactive waste (HLW) containers, are described. The applicability of a critical potential concept for long-term prediction of various corrosion modes is discussed. It is suggested that the repassivation potential for deep pits in aqueous environments containing chlorides can be used as a conservative parameter for predicting the long-term occurrence of pitting, crevice corrosion, and stress corrosion cracking on austenitic Ni-Fe-Cr-Mo alloys. The implication of this potential, as measured within a limited range of chloride concentration, is also discussed for predicting the occurrence of sensitization as a result of high-temperature thermal treatments. The possible presence of microbial activity in the partially saturated environment of the proposed HLW repository at Yucca Mountain is reviewed. The effect of microbial colonies on the evolution of the corrosion potential, which is considered to be an enabling parameter for defining the occurrence of localized corrosion modes above the repassivation potential, is examined. The effect of hydrogen absorption on the embrittlement susceptibility of austenitic alloys is summarized as well as a description of a measurement technique for hydrogen entry into metals. All the project objectives were essentially achieved. The mechanistic understanding and the experimental techniques developed during the course of this project will be used to address key technical uncertainties identified in the NRC license application review plan. Based on the results to date and the changes in the U.S. Department of Energy (DOE) waste package design, new areas of research were identified.

CONTENTS

Section Page

CONTENTS (cont'd)

CONTENTS (cont'd)

CONTENTS (cont'd)

Section Page

FIGURES

FIGURES (cont'd)

FIGURES (cont'd)

FIGURES (cont'd)

FIGURES (cont'd)

TABLES

ABBREVIATIONS

ACD	advanced conceptual design
ADC	analog-digital converter
AES	Auger electron spectroscopy
ASTM	American Society for Testing and Materials
ATP	adenosine triphosphate
BWR	boiling water reactor
CCP	cyclic potentiodynamic polarization
CDM	compliance determination methodology
CDS	compliance determination strategy
CNWRA	Center for Nuclear Waste Regulatory Analyses
DAC	digital-analog converter
DI	deionized
DOE	U.S. Department of Energy
EBS	Engineered Barrier System
EDS	energy dispersive spectroscopy
EIS	electrochemical impedance spectroscopy
EPR	electrochemical potentiokinetic reactivation
EPS	extracellular polymeric substances
ETS	electron transport system
GMAW	gas-metal arc welding
HAZ	heat-affected zone
HLW	high-level [radioactive] waste
ISE	ion selective electrode
IWPE	Integrated Waste Package Experiments
KTU	Key Technical Uncertainty
LARP	License Application Review Plan
LCI	localized corrosion index
LLNL	Lawrence Livermore National Laboratory
LVDT	linear voltage differential transducer
MA	mill annealed
MIC	microbially influenced corrosion
MPC	multipurpose canister
NRC	Nuclear Regulatory Commission
OSU	The Ohio State University
PFA	perfluoroalkoxy
PMMA	polymethyl methacrylate
PNL	Pacific Northwest Laboratory
PTFE	polytetrafluoroethylene
PWR	pressurized water reactor
RTD	resistance temperature detector
SA	solution annealed
SCC	stress corrosion cracking
SCE	saturated calomel electrode
SCP	Site Characterization Plan
SEM	scanning electron microscope

ABBREVIATIONS (cont'd)

SHE	standard hydrogen electrode
SRB	sulfate-reducing bacteria
SS	stainless steel
SSRT	slow strain rate test
STEM	scanning transmission electron microscopy
TEM	transmission electron microscopy
TTS	time-temperature-sensitization
WIPP	Waste Isolation Pilot Plant
WOL	wedge-opening loading

ACKNOWLEDGMENTS

The authors acknowledge the contributions of Yi-Ming Pan on scanning transmission electron microscopy studies and Peter Angell on microbially influenced corrosion. The support of various Southwest Research Institute staff members and summer students in carrying out the activities described in this report, specifically: W. Peters, B. Delgado, W. Machowski, H. Saldhana, R. Railsback, S. Lukezich, T. Page, D. Pile, J. Kucharczyk, J. Mehlem, S. Griffin, and T. Griffin is also acknowledged. The hydrogen transport research was conducted at The Ohio State University under Prof. Bryan Wilde, and the authors wish to acknowledge his contributions as well as those of S. Kesavan and C. Miller. The authors recognize the support provided by Prasad K. Nair throughout the project.

The authors gratefully acknowledge the technical reviews of Fred F. Lyle, Jr., and Hersh K. Manaktala and the programmatic review of Wesley C. Patrick. Appreciation is due to Bonnie L. Garcia and Esther Cantu for their assistance in the preparation of this report. The editorial assistance of C. Gray and J. Prior is acknowledged.

This report was prepared to document work performed by the Center for Nuclear Waste Regulatory Analyses (CNWRA) for the Nuclear Regulatory Commission (NRC) under Contract No. NRC-02-93-005. The activities reported here were performed on behalf of the NRC Office of Nuclear Regulatory Research (RES). The report is an independent product of the CNWRA and does not necessarily reflect the views or regulatory position of the NRC. Sources of data are referenced in each chapter. The respective sources of these data should be consulted for determining their levels of quality assurance.

EXECUTIVE SUMMARY

The NRC regulation 10 CFR 60.113 requires waste packages to provide substantially complete containment of radionuclides for a minimum period of 300 to 1,000 years. In satisfying this regulatory requirement, several key technical uncertainties (KTUs) have been identified that are relevant to the research reported here.

1. The uncertainty in prediction of the environment near and within the engineered barrier system (EBS)

   (i) Geochemical and thermohydrological effects such as evaporative concentration of chemical species

   (ii) Effects of container corrosion such as hydrolysis of metal cations

   (iii) Effects of man-made materials such as lubricants resulting in microbiological activity

2. The uncertainty in prediction of effects of environmental conditions on the waste package during the containment period

   (i) The extrapolation of short-term laboratory and prototype test results to predict long-term performance of waste packages and the EBS

   (ii) Thermomechanical effects on waste packages

3. The uncertainty in the prediction of effects of environmental conditions on the EBS during the post-containment period

   (i) The prediction of release path parameters such as size, shape, and distribution of penetrations of waste packages due to thermomechanical, environmental, or criticality effects.

To address these KTUs, the Integrated Waste Package Experiments (IWPE) Research Project, conducted at the Center for Nuclear Waste Regulatory Analyses (CNWRA) under the sponsorship of the Nuclear Regulatory Commission (NRC), Office of Nuclear Regulatory Research, is divided into five technical tasks and a sixth task of reporting: Task 1—Corrosion, Task 2—Stress corrosion cracking (SCC), Task 3—Materials stability, Task 4—Microbially influenced corrosion (MIC), Task 5—Other degradation modes, and Task 6—Reporting.

Throughout the program for siting, constructing and operating a repository at the proposed Yucca Mountain site, the U.S. Department of Energy (DOE) conceptual designs for the waste package were also evolving and, along with them, the alloys selected as candidate container materials. In order to accommodate these changes in designs and materials, the tasks within the IWPE project were aimed at identifying methodologies for long-term prediction pertaining to classes of materials, rather than detailed data generation on any single alloy. However, because of the difficulty inherent in maintaining any materials research activity completely generic, a focus alloy had to be chosen. This was alloy 825, since it has remained in the DOE list of candidate materials throughout design changes. This report concentrates on alloy 825 and other austenitic Ni-Fe-Cr-Mo alloys that have been in the DOE candidate container materials list. Although limited studies on copper-based alloys were performed, the results are not addressed here because they have been de-emphasized recently in the DOE program.

A historical perspective of the materials and designs in the DOE high-level nuclear waste disposal program is provided in Chapter 2. The current DOE advanced conceptual design (ACD) involves a multi-wall design with a corrosion allowance alloy (carbon or low-alloy steel) as the outer container material and a corrosion resistant alloy (alloy 825 or alloy C-22) as the inner container material. It is suggested that such a design may be beneficial for localized corrosion because the steel can act as a sacrificial anode once it is penetrated. However, other degradation modes such as hydrogen embrittlement have to be considered under such conditions.

The evolution of the environment contacting the waste package surface is reviewed in Chapter 2. The partially saturated nature of the proposed repository horizon at Yucca Mountain combined with significant variations in the proposed thermal loading strategy can result in a wide range of possible environmental conditions. While a dry zone around the waste packages is predicted by thermohydrological models, the presence of aqueous environments has been observed in some field heater tests. Hence, any attempt to predict the long-term performance of the waste packages must consider a wide variety of environmental conditions in testing and modeling.

Task 1: Localized Corrosion

For predicting the occurrence of localized corrosion modes, a simple approach based on critical and corrosion potentials of container materials is proposed. The applicability of the repassivation potential as the critical potential for the occurrence of localized corrosion modes is examined in detail. In Chapter 3, it is shown that the repassivation potential for deep pits is a conservative parameter in the sense that it attains a lower bound value independent of the depth of pitting after a depth of about 1 mm. The repassivation potential thus measured is also insensitive to surface features arising from processing, such as Cr depletion and surface roughness. It is also shown that the repassivation potential for deep pits is almost equal to the repassivation potential for crevice corrosion, although the depth of crevice corrosion needed to attain a lower bound value is lower than that of pitting. By measuring repassivation and initiation times at constant applied potentials, it is shown that the repassivation potential for deep pits, measured with the slow-scan rate test technique, can be used to predict the long-term occurrence of localized corrosion, as indicated by tests with a duration of 18 months or longer. Through measurements of crevice pH, chloride concentration, and potential, it is suggested that the fundamental mechanism of crevice corrosion initiation is pitting at isolated regions, which then propagate if the external driving force, as provided by an applied potential or a high redox potential of the environment, is sufficiently high. In this sense, crevice corrosion initiation is stochastic just as pit initiation is.

Task 2: Stress Corrosion Cracking

For austenitic alloys, such as type 316L stainless steel (SS) and alloy 825, in near-neutral chloride solutions, it has been suggested that SCC initiates within crevices and that the repassivation potential for localized corrosion is the critical potential above which SCC can occur. This concept is examined in detail because of the advantages in terms of simplicity that it will entail in the performance assessment of waste packages. It is shown in Chapter 4 that the repassivation potential for deep pits defines a lower bound below which SCC has not been observed on these materials. It is indicated that the slow strain rate test

(SSRT) may not be a conservative test, at least for type 316L SS, since SCC was observed in the constant deflection U-bend tests at lower chloride concentrations than those required to promote SCC in SSRTs. It is also shown that cracking in the U-bend tests almost always occurs just above the liquid-vapor interface, regardless of natural or applied potential conditions. Thiosulfate was found to be detrimental to localized corrosion resistance and SCC of both austenitic SSs and Ni-base alloys.

Task 3: Materials Stability

The sensitization kinetics of alloy 825 is examined in detail in Chapter 5, using both the standard boiling 65 percent nitric acid test, the standard sulfuric acid-ferric sulfate test, and various electrochemical tests including the electrochemical potentiokinetic reactivation (EPR) test and its variations. These results are then correlated to grain boundary Cr concentration profiles measured by scanning transmission electron microscopy (STEM). It is shown that standard electrochemical techniques, such as EPR, are not sufficiently sensitive for alloy 825, although they are very effective for austenitic SSs such as types 304L and 316. However, the repassivation potential measured using cyclic polarization tests in a 100 ppm chloride solution at 95 °C correlates very well with the boiling nitric acid tests and can be even more sensitive. The equivalent grain boundary Cr depletion width measured by STEM was correlated to both the nitric acid test results and the repassivation potential. It is expected that such correlations would enable long-term prediction of sensitization effects through the use of equilibrium and kinetic Cr depletion models.

Task 4: Microbially Influenced Corrosion

The possible occurrence of microbial activity and its influence on corrosion of candidate container materials is reviewed in Chapter 6. Based on a comprehensive literature review, it is suggested that microbial activity is possible in the proposed repository, even in the presence of thermal loading and radiation, provided that a water film can be stabilized on the container surfaces or in the porous media. The influence of microbial colonies on corrosion depends upon the candidate container material and other environmental conditions such as the redox potential, temperature, salt concentration, and nutrient availability, among others. One of the candidate materials currently proposed by the DOE as an additional overpack to be included for conditions giving rise to microbial activity, alloy 400, is shown to be highly susceptible to MIC. The effect of microbial activity on the corrosion potential is reviewed. While an increase in corrosion potential under microbial colonies forming a biofilm has been widely observed, the mechanism of such an effect is controversial and contradictory results have also been observed. Prediction of such an effect is critical to waste package performance evaluation because the corrosion potential is the enabling parameter for localized corrosion and SCC. Further studies on the mechanism of such an effect are suggested.

Task 5: Hydrogen Embrittlement

The results generated thus far, albeit very limited as reported in Chapter 7, indicate that the hydrogen embrittlement of candidate austenitic alloys decreases with an increase in temperature from 25 °C to 80 °C. However, any conclusions regarding repository performance from this limited study must be tempered with the knowledge that hydrogen embrittlement of austenitic SSs has been observed at higher temperatures provided sufficient hydrogen was present at crack tips. Hence, a quantitative understanding of the hydrogen concentration in the metal as a function of environmental conditions must be developed and coupled to a quantitative understanding of the relationship between concentration of hydrogen (either nominal or at the crack tip) in the metal and embrittlement at the temperatures of interest. It must be noted that the multiwall design with steel outer overpack can result in enhanced hydrogen generation on the inner alloy overpack.

In addition to a summary of the report, Chapter 8 includes a number of recommendations for further research on the degradation modes of container materials including consideration of fabrication-related issues, such as the effects on welds on localized corrosion, SCC, and MIC, taking into consideration the progress expected on the specific design of components in the ACD phase of the DOE program. Other specific recommendations include: (i) investigation of the effect of heat transfer and alternate wet and dry conditions on corrosion, (ii) evaluation of hydrogen embrittlement susceptibility of both carbon steel and the austenitic alloys, (iii) examination of thermal embrittlement of MPC and carbon steel due to long-term exposure to moderate temperatures, (iv) study of the ennoblement of corrosion potential by the type of microbial colonies anticipated in the proposed repository, as well as on the effect of microorganisms in the modification of the near-field environment, and (v) analyze the rate controlling processes in the dissolution of simulated spent fuel.

The project objectives have been essentially achieved, although the long-term tests, crack growth rate measurements using fracture mechanics specimens, and the investigation of microbial effects on rock and container materials are still continuing. The results of the project have already been used in waste package performance assessment codes. The experimental techniques and the mechanistic understanding developed in the project will be used to address KTUs identified in the NRC license application review plan.

1 INTRODUCTION

1.1 REGULATORY CONTEXT

This report is the culmination of five years of research activities in the Integrated Waste Package Experiments project, sponsored by the Nuclear Regulatory Commission (NRC) at the Center for Nuclear Waste Regulatory Analyses (CNWRA). To understand the scope of the NRC funded research, it is important to recognize that the NRC regulatory responsibilities are distinct from the responsibilities of the U.S. Department of Energy (DOE) in siting, constructing, and operating a repository for the permanent disposal of high-level nuclear waste (HLW). In fulfilling its responsibilities for assuring the radiological health and safety of the public, the NRC conducts confirmatory and exploratory research to:

- Develop the technical bases and licensing tools necessary to judge the adequacy of the DOE license application

- Ensure a sufficient independent understanding of the basic physical processes taking place at the proposed geologic repository site

- Maintain an independent, but limited, confirmatory research capability to be used in evaluating DOE prelicensing and license application submittals

Figure 1-1 depicts the basic relationship between the NRC research programs, modeling for auxiliary analyses and performance assessment, and licensing needs. Regulations applicable to the licensing of a HLW repository are expressed as regulatory requirements, each of which must be met before the NRC staff can recommend the issuance of a license. Compliance determination strategies (CDSs) and compliance determination methods (CDMs) are currently being developed and will be updated in the License Application Review Plan (LARP). Key technical uncertainties (KTUs) are defined based on the risk to compliance determination. Evaluation and reduction of those aspects of KTUs which are the primary responsibilities of the NRC are the objectives of the research program. The results of research are used in performance assessments and in development of methods for evaluating DOE compliance with the regulatory requirements.

The NRC regulation 10 CFR 60.113 requires waste packages to provide substantially complete containment of radionuclides for a minimum period of 300 to 1,000 yr. In satisfying this regulatory requirement, several KTUs have been identified:

1. The uncertainty in prediction of the environment near and within the engineered barrier system (EBS)

    (i) Geochemical and thermohydrological effects such as evaporative concentration of chemical species

    (ii) Effects of container corrosion such as hydrolysis of metal cations

    (iii) Effects of man-made materials such as lubricants resulting in microbiological activity

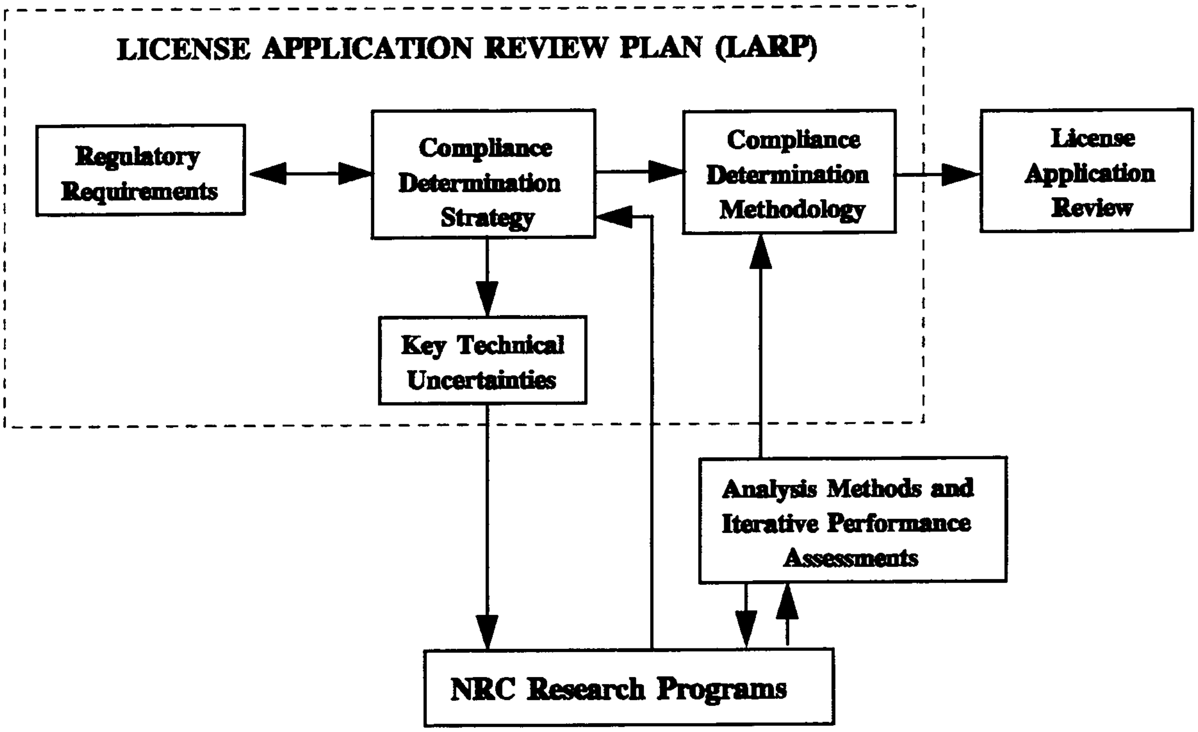

Figure 1-1. Relationship of NRC HLW Research Program to licensing needs

2. The uncertainty in prediction of effects of environmental conditions on the waste package during the containment period

    (i) The extrapolation of short-term laboratory and prototype test results to predict long-term performance of waste packages and the EBS

    (ii) Thermomechanical effects on waste packages

3. The uncertainty in the prediction of effects of environmental conditions on the EBS during the post-containment period

    (i) The prediction of release path parameters such as size, shape, and distribution of penetrations of waste packages due to thermomechanical, environmental, or criticality effects.

To address these KTUs, the Integrated Waste Package Experiments (IWPE) project is divided into five technical tasks dealing with the behavior of container materials and a sixth task of reporting. These tasks are: Task 1—Corrosion, Task 2—Stress corrosion cracking (SCC), Task 3—Materials stability, Task 4—Microbially influenced corrosion (MIC), Task 5—Other degradation modes, and Task 6—Reporting.

As will be mentioned later, the DOE container materials program has historically seen many changes in the choice of materials and is continuing to evolve. The tasks within the IWPE project were designed to focus, where possible, on generic issues that can be valid for a given class of materials, such as the austenitic alloys. This approach enables the techniques and the phenomenological understanding developed on a given alloy to be applied to a different alloy of the same class of materials without initiating new directions of research. It is realized, however, that the techniques developed on a given material can not be applied to a wide range of alloy classes and new research areas need to be identified depending upon the type of materials selected by the DOE for their final detailed design of the waste package. Task 5 in the IWPE project was designed for this purpose.

1.2 SCOPE OF THE REPORT

The progress of various tasks within the IWPE project has been documented in numerous topical reports (Cragnolino and Sridhar, 1991a; Sridhar et al., 1991; Cragnolino and Sridhar, 1992a; Cragnolino and Sridhar, 1993a; Sridhar et al., 1993a; Geesey, 1993; Sridhar et al., 1994a; and Cragnolino et al., 1994a) and semi-annual reports (Cragnolino and Sridhar, 1991b; 1992b; 1993b; Sridhar and Cragnolino, 1993a; Sridhar et al., 1993b, 1994b; Cragnolino et al., 1994b; and Dunn et al., 1995a). Several peer-reviewed papers were published on the basis of these reports (Cragnolino and Sridhar, 1991c; Sridhar and Cragnolino, 1993b,c; Sridhar and Dunn, 1994; Dunn et al., 1995b; Cragnolino et al., 1995).

The present report is a unification of all the information reported previously and provides a discussion of the various aspects of waste package performance in terms of the KTUs listed in the previous section. Chapter 2 details the history of the container materials program in the DOE, as it relates to the proposed repository site at Yucca Mountain, the materials selected for evaluation in the IWPE project, and their metallurgical characteristics. In addition, it provides a rationale for the environmental conditions employed in the IWPE project. In this project, the effort was concentrated on the interaction of materials and environments without attempting to study fabrication-related issues such as the effect of welding. It was considered that a more definitive selection of materials and designs should be done by the DOE before initiating an experimental study of issues related to fabrication. Chapter 3 describes the research conducted on localized corrosion of various Ni-Fe-Cr-Mo alloys. It does not include the investigation conducted on copper-based alloys terminated early in the project because of a lowering in priority of these alloys as candidate container materials. The results of the research conducted on copper-base alloys have been reported elsewhere (Sridhar et al., 1993a; Sridhar and Cragnolino, 1993c). Due to the formation of a passive, protective film on the alloys studied, their corrosion rate is expected to be low, and, hence, uniform corrosion was not investigated. Chapter 4 examines the SCC susceptibility of the austenitic alloys, the applicability of certain test techniques, and the use of the critical potential concept in predicting the occurrence of SCC. Chapter 5 focuses on the thermal stability and sensitization of one of the candidate container materials, alloy 825. Chapter 6 reviews the possibility of the presence of microbial colonies in the repository after waste emplacement and their influences on the near-field environment and container corrosion. Chapter 7 outlines the potential sources of hydrogen in the repository as well as the absorption and embrittlement problems associated with hydrogen. It also summarizes the experimental research conducted at The Ohio State University, as subcontract work, on the hydrogen embrittlement susceptibility of candidate container materials. Chapter 8 provides the conclusions from the project and specific recommendations for further research in the waste package area. The tabular data for the individual tasks are provided in the appendices.

2 MATERIALS AND ENVIRONMENTS

2.1 HISTORICAL BACKGROUND

In his Annotated History of Container Candidate Material Selection, McCright (1988) described the evolution of not only the list of candidate materials but also the conceptual and alternate designs of waste packages for disposal of spent fuel and reprocessed HLW. Although the conceptual designs are still evolving (U.S. Department of Energy, 1994), it is necessary to consider briefly the history of the waste package design in order to better understand the context within which the experimental investigations have been performed by the DOE and the CNWRA in the past few years.

In the years between 1981 and 1983, the main interest was in the saturated zone of the Yucca Mountain site for the repository horizon; hence, thick, self-shielded containers, made of carbon and low-alloy steels, were considered. Limited testing of type 304L SS, mainly to study the effect of gamma radiation, was initiated in December of 1982 at Pacific Northwest Laboratories (PNL).

By February 1983, the decision was made to study the unsaturated zone as the potential repository horizon. In October of 1983, a survey of 31 alloys as alternatives to type 304L SS was published (Russell et al., 1984). This list consisted of a wide variety of alloy classes including SSs, Ni-base alloys, Ti, Zr, and Cu-base alloys. The list was later shortened to 17 alloys (McCright, 1988), while retaining the same diversity of alloy classes. Out of this list, four Fe-Cr-Ni alloys that obtained the highest ranking in the combined consideration of cost, corrosion resistance, mechanical properties, and weldability were selected (types 304L, 316L, and 321 SSs, and alloy 825). In mid-1986, testing of type 321 SS was ended since this material did not offer a great advantage over type 316L SS. Some testing of carbon steel continued at PNL because it was still being considered as the only candidate for a borehole liner. Inclusion of copper alloys was requested early in 1984 at the urging of Congress, and investigations of three copper alloys began in October of 1984.

Initially, the pour canister, made of 304L type SS, was visualized as the only container for reprocessed HLW in the form of borosilicate glass, but a decision was made after late 1984 to use an overpack. The pour canister is subjected to thermal cycling during the glass pouring and resistance welding operations that may sensitize the material to intergranular corrosion. Because the pour canister was initially designed to be directly exposed to the groundwater environment, the effects of both high-temperature and low-temperature sensitization were examined in great detail. In June 1986, a project-wide stop-work order was issued to better identify quality assurance needs of various aspects of the work, and most of the experimental research was terminated by the end of 1986. The draft Site Characterization Plan (SCP) for the proposed Yucca Mountain site was completed in mid-1986 (U.S. Department of Energy, 1988). The three austenitic alloys (types 304L and 316L SS and alloy 825) and three copper-based materials (CDA-102, CDA-715, and CDA-613), were designated as the SCP design alloys (McCright, 1990).

The SCP design alloys have been the focus of investigation in the IWPE project along with a Ni-Cr-Mo alloy, C-22. The actual compositions of the heats of these alloys studied in the IWPE project are shown in Appendix A, Tables A-1 and A-2.

2.2 ADVANCED CONCEPTUAL DESIGN

Minimization of worker exposure to radiation during the overall waste handling process, consideration of longer-life containers, and the approaching deadlines for waste acceptance by the DOE have spurred alternate waste package conceptual designs (U.S. Department of Energy, 1994). In the initial stages of the advanced conceptual design (ACD) phase, seven alternate design concepts were considered:

- Metallic multibarrier in drift emplacement
- Metallic multibarrier shielded in drift emplacement
- Small metallic multibarrier in a borehole
- Nonmetallic/metallic multibarrier in drift
- Multipurpose canister (MPC) with a disposal overpack in drift
- Universal cask (multipurpose unit) in drift
- SCP design of single container in a borehole

The details of each of these designs are given elsewhere (U.S. Department of Energy, 1994). The need to accept waste from utilities 1998 has spurred DOE interest in implementation of the MPC concept throughout the waste management system (from power plants through transportation and monitored retrieval storage to final geologic disposal). The MPC has been conceived in terms of two reference designs: (i) a large MPC that has an estimated total weight of 125 metric tons and can contain up to 21 pressurized water reactor (PWR) fuel assemblies or 40 boiling water reactor (BWR) fuel assemblies, and (ii) a medium MPC that has an estimated total weight of 75 metric tons with a maximum capacity of 12 PWR or 24 BWR assemblies. Additionally, for reactor sites that are unable to handle the above weights, a small, 25-ton MPC, with capacity for 2 PWR or 4 BWR assemblies, has also been discussed. The current proposed design of the MPC consists of a type 316L SS canister 1.46 m (57.63 in.) in outer diameter (O.D.), 5 m (200.5 in.) long, and 3.5-cm (1.375-in.) wall thickness. While the details of the processing sequence by which the canister body will be manufactured are not available, one method of fabricating large-diameter vessels such as these is three-roll forming (ASM International, 1988).The combination of cylinder height and plate thickness involved in the MPC would require intermediate annealing operations (ASM International, 1988). The processing is usually completed by longitudinal welding and post-weld annealing. The ends of the canister consist of a thick steel shield plug, a SS cover plate, and a SS closure head. Automated welding has been chosen to be the closure method of choice for the canister ends (U.S. Department of Energy, 1994). However, details of the closure technique in terms of welding process, welding parameters, and filler metal composition have not been presented. The spent fuel assemblies will be contained in baskets made of type 316L SS sheet with a neutron absorber such as borated aluminum sandwiched between the basket walls. The MPC is proposed to be placed inside disposal overpacks (U.S. Department of Energy, 1994) as shown schematically in Figure 2-1, consisting of a thick carbon steel outer shell and a thinner austenitic alloy inner shell. The current slate of candidate materials for the outer overpack shell, inner overpack shell, MPC, and other components are shown in Table 2-1.

Some of the candidate materials in the ACD, shown in Table 2-1, such as type 316L SS and alloy 825, are included in the IWPE project. Additionally, alloy C-22 has been examined in the project in a preliminary fashion. The applicability of the methodologies developed in the IWPE project to other classes of candidate materials will be discussed in other chapters. Because the design of waste packages has changed in the last two years and along with it the fabrication processes, the IWPE project has not made any attempt to examine fabrication related issues such as weldments, except indirectly as in the case

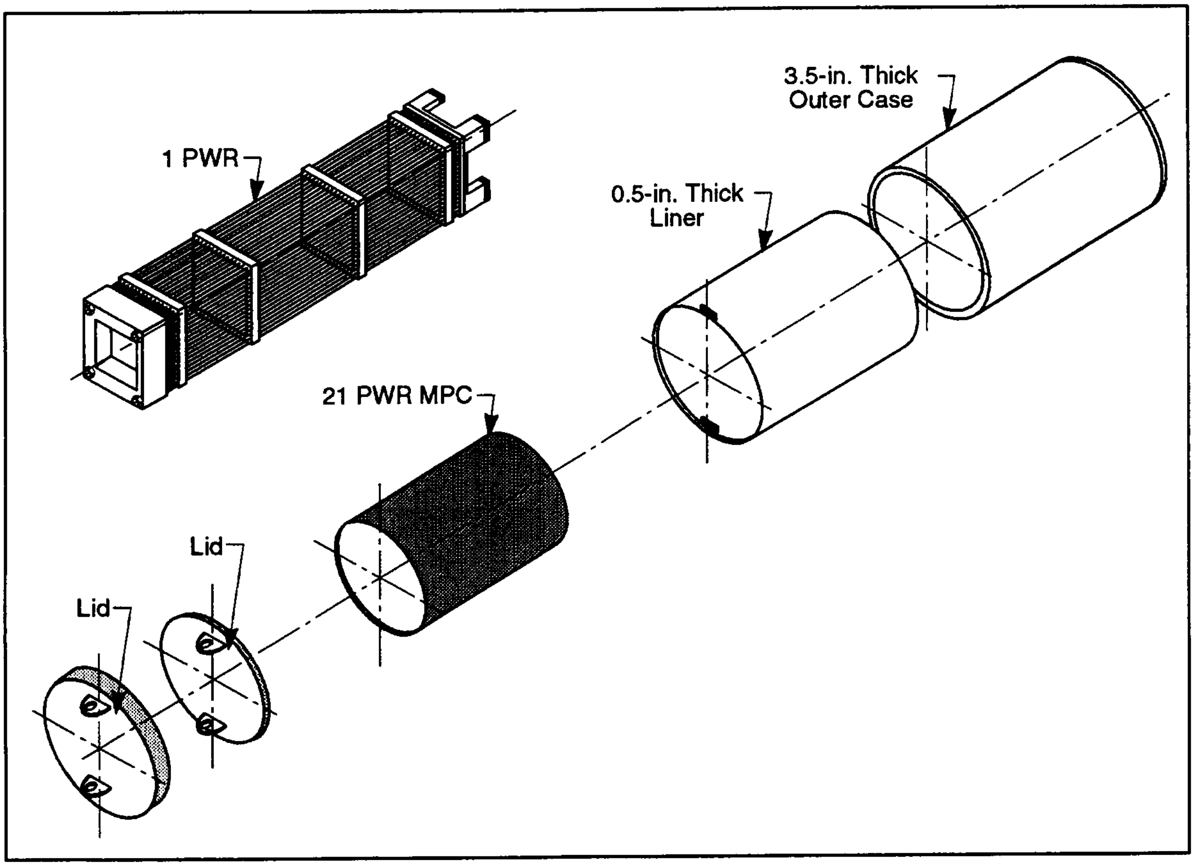

Figure 2-1. Schematic diagram of a proposed design for disposal overpacks and multipurpose canisters containing 21 pressurized water reactor fuel assemblies (U.S. Department of Energy, 1993)

of sensitization studies reported in Chapter 5. In the SCP design, based on thin containers, friction welding was listed as the most favorable welding process for closing the container after loading waste forms. However, in the ACD phase, involving much thicker containers, other welding methods such as Gas Metal Arc Welding (GMAW), have been suggested. The effects of fabrication, such as interdendritic segregation of alloying elements in the weld and residual stresses, will be part of the future scope of research.

2.3 ENVIRONMENTAL CONSIDERATIONS

It is well known that water extracted from the J-13 well (saturated zone) located in the vicinity of the Yucca Mountain site, has been used as the reference groundwater for experimental studies (Glassley, 1989), assuming that its composition is close to that of the vadose water in the unsaturated zone in the Topopah Spring tuff. However, the J-13 water has a range of composition for various species (Glassley, 1989) in which the prevailing ionic species are HCO_3^- and Na^+. Other anions, such as Cl^-, F^-, SO_4^{2-}, and NO_3^-, are present at lower concentrations. The silicon content of the water, in the form of

Table 2-1. Nominal chemical compositions of candidate alloys in the advanced conceptual design for the multipurpose canister with a disposal overpack (U.S. Department of Energy, 1994)

Waste Package Components	Alloy	Composition, Weight Percent							
		C, max.	Cr	Cu	Fe	Mo	Ni	Ti	Others
MPC	316L SS	0.03	17.0	—	Bal.	2.5	12.0	—	Mn: 2.0 max S: 0.03 max P: 0.045 max
Outer Disposal Overpack	A516 Steel[a] Gr 55	0.24	—	—	Bal.	—	—	—	Mn: 1.0 S: 0.024 max Si: 0.5
	A426 Steel Grade CP 15	0.15	—	0.5	Bal. (Si: 2.5)	0.44–0.65	—	—	Mn: 0.3–0.6 Si: 1.65 S: 0.045 P: 0.040
	A387 Steel[b] Grade 22	0.15	2.25	—	Bal.	1.0	—	—	Mn: 0.3–0.6 Si: 0.5 max S: 0.035 max P: 0.035 max
Inner Disposal Overpack	Alloy 825[a]	0.05	21.5	2.0	Bal.	3.0	42.0	1.0	—
	Alloy 825-High Mo	0.02	21.5	2.0	Bal.	6.0	42.0	1.0	—
	Alloy C-4	0.01	16.0	—	3.0 max	15.5	64.5	1.0	—
	Alloy C-22[b]	0.015	21.5	—	3.0	13.0	56.0	1.0	W: 3.0 V: 0.15 Mn: 1.0 Si: 0.1

[a] Primary material for testing

[b] Alternate material for testing

Table 2-1. Nominal chemical compositions of candidate alloys in the advanced conceptual design for the multipurpose canister with a disposal overpack (U.S. Department of Energy, 1994) (cont'd)

Waste Package Components	Alloy	Composition, Weight Percent							
		C, max.	Cr	Cu	Fe	Mo	Ni	Ti	Others
Inner Disposal Overpack	Ti-12	0.1	—	—	0.3 max	0.3	0.8	Bal.	H: 0.015 max O: 0.25 max N: 0.03 max
	Ti-16	0.1	—	—	0.3 max	—	—	Bal.	Pd: 0.05 H: 0.015 max O: 0.25 max N: 0.03 max
Additional Barrier (aggressive environments)	Alloy 400[a]	0.12	—	31.5	1.35	—	66.0	—	Mn: 2.0 S: 0.024 max Si: 0.5
	CDA-715[b]	0.02	—	Bal.	0.7	—	31.0	—	Mn: 1.0

[a] Primary material for testing [b] Alternate material for testing

silicic acid, is relatively high. Waters from other wells in the vicinity of Yucca Mountain have similar chemical compositions, but differences in pH and ion concentration ratios are considered to be significant (Kerrisk, 1987).

Of greater importance to all localized corrosion processes is the evolution of the chemical composition of the environment as a result of the emplacement of the waste packages in the repository. These changes in composition can occur by the following processes.

- **Rock-water interactions over long periods of time modified by the increase in temperature**: Modeling efforts in this area (Pabalan and Murphy, 1991) have shown that, as the temperature increases, the bicarbonate concentration will decrease due to CO_2 volatilization resulting in a concomitant increase in pH. In many of the SCC experiments conducted by the DOE, J-13 water conditioned by contact with crushed tuff at the test temperature has been used. It can be presumed, however, that the concentration of several species should be extremely dependent on the mineralogical composition of the rock and the temperature and also, unless equilibrium conditions were rapidly established, on the duration of the conditioning process and the mass to volume ratio of the rock and water. The evolution of J-13 water in contact with crushed tuff at 50 and 90 °C, under γ-irradiation, was evaluated experimentally by Westerman et al. (1987). The autoclaves were continuously purged with air and were open to the atmosphere via 9 m of outlet tubing. After each period of testing, the solution was replaced with fresh J-13 water. Fresh rock was replaced after each test period up to 10 months and not thereafter. Unfortunately, no systematic variations in the concentrations of any species were found. The pH at the end of each period was higher than the initial pH of the J-13 water reported (7.1–7.6), which is consistent with the model predictions (Pabalan and Murphy, 1991). The Cl^- and SO_4^{2-} concentrations were generally much higher than those found in the initial J-13 water used by the investigators. These results were corroborated by measurements of high conductivity at the end of each period. The authors reported that the measurements of high ionic concentrations were reproducible.

  A further confirmation of the increase in concentration of ionic species due to rock-water interactions has been presented by Abraham et al. (1986). When synthetic J-13 water was heated in the presence of crushed tuff to boiling temperatures (100 °C) under refluxing conditions, it was shown (Abraham et al., 1986) that the concentration of several anions and cations, such as SO_4^{2-}, NO_3^-, Cl^-, Na^+, K^+, and Ca^{2+}, increases significantly with time. Detailed solution analyses were carried out after various time periods of testing. Interestingly, reaction of boiling distilled water with tuff produced an initial increase in Cl^- to about 160 ppm which, upon further treatment with new distilled water, decreased to a steady value of about 20 ppm, more than three times the 6 ppm concentration reported nominally for J-13 water.

  In contrast to the above experiments, a review of rock-water interaction experiments performed at Lawrence Livermore National Laboratories (LLNL) (Knauss et al., 1985; Oversby, 1985; Glassley, 1989) indicated no significant changes from the initial J-13 values for chloride, fluoride, nitrate, and sulfate. These experiments were conducted in essentially closed systems. In the results reported by Oversby (1985), the pH increased to about 9 after 70 days at 150 °C, whereas, a slight decrease in the dissolved bicarbonate content was observed. This was attributed to the gradual exsolution of CO_2 from the solution through the pores in the polytetrafluoroethylene (PTFE) liner. Knauss et al. (1985) used an impermeable gold bag, and, hence, did not observe any increase in pH during the course of their experiments. A slight decrease in the pH (measured at 25 °C) was noted and attributed to the precipitation of Ca and Mg carbonates which have retrograde solubility. The most significant compositional change was the dissolution of Si from the tuff.

- **Changes due to occluded regions such as crevices**: It has been well established that the concentration of anionic species such as chloride can increase greatly in creviced regions, while pH can decrease due to hydrolysis of cationic species such as Fe^{2+}, Cr^{3+}, and Ni^{2+} (Turnbull, 1983; Alavi and Cottis, 1987; Luo et al., 1992; Sridhar and Dunn, 1994). Additionally, highly reducing conditions may be created in occluded regions due to the rapid depletion of oxygen and slow rediffusion from the bulk. The radiolysis reactions in acidic reducing solutions within crevices may be significantly different from those in the bulk oxidizing solutions (Spinks and Woods, 1990).

- **Changes due to repeated or episodic evaporation and re-wetting of container**: This process has been modeled recently by Walton (1993), who predicted that a saturated salt solution layer can form on the container surface leading to a stabilization of aqueous conditions well above the boiling point of pure water. Capillary forces can also stabilize water within pores and cracks. Experimental measurements of Beavers et al. (1992) have shown increases in anionic concentrations linearly proportional to the number of boil-down and refill cycles. However the relationship of these procedures to actual conditions in the repository is not clear. Westerman et al. (1987) performed boil-down tests in autoclaves at 200 °C and 1,000 psig maintaining for 7 days a liquid phase and for 1 day dry conditions. The dry period was achieved by reducing the pressure. The reported concentrations of chloride and sulfate after 15 and 50 boil-down cycles were higher than the initial values, but not high enough as calculated from the number of boil-down cycles if complete evaporation is assumed.

- **Changes due to radiolysis**: The γ dose rate from spent fuel containers in the SCP design is expected to be as high as 0.1 Mrad/hr and, typically, about 0.01 Mrad/hr (Reed and van Konynenburg, 1991). The dose rate from glass waste assuming the SCP design is expected to be somewhat less, about 0.005 Mrad/hr (van Konynenburg, 1986). Some of the early field evidences of the effects of radiolysis on corrosion and SCC were observed in the Spent Fuel Test—Climax Program (Patrick, 1986). Corrosion of the carbon steel liners exposed to spent-fuel containers and cracking of Ni-Fe extensometer connecting rods were noted. In the latter case, laboratory simulation of SCC of Ni-Fe specimens in groundwater environments was achieved only upon addition of an oxidizing chloride salt, $CuCl_2$. In addition to galvanic effects due to coupling with copper components, it is probable that radiolysis of the groundwater environment increased the concentration of oxidizing species, thus raising the corrosion potential high enough to cause corrosion and cracking.

Experimental investigations of chemical and electrochemical effects of γ-radiation have been reported by van Konynenburg (1986), Glass et al. (1986), Kim and Oriani (1987a,b), and Reed and van Konynenburg (1991). van Konynenburg (1986) interpreted the experimental results related to reaction of various types of glasses with water and water reacted with tuff. The major species present as a result of γ-radiation of water in contact with air were nitrite and nitrate. The ratio of nitrite to nitrate was dictated by the presence of catalytic surfaces such as tuff and ionic species such as bicarbonate in the water. In the absence of tuff rock and ionic species in water, the nitrite/nitrate ratio was close to 1. This is presumably due to the oxidation of nitrite to nitrate by the hydrogen peroxide that is formed in the water as a result of radiolysis. In the presence of catalysts that promote decomposition of hydrogen peroxide, the nitrite concentration increased. While the hydrogen peroxide concentration was not reported, van Konynenburg (1986) speculated that it would have been quite low. Reed and van Konynenburg (1990, 1991) reported that, in a moist-air system (at relative humidities of 15 percent at 90 °C), nitrites and nitrates were the main species as a result of radiolysis. Under these conditions copper specimens formed hydrated cupric nitrates. In the 100 percent relative humidity environment, only Cu_2O and CuO were found on copper specimens. Irradiation experiments by Yunker (1990) on various copper alloys under 100 percent relative humidity conditions at 95 °C have resulted in the formation of mainly CuO. Yunker reported estimated concentrations of NO_2^- in the gas phase of moist air mixtures exposed to irradiation but did not report any observation of nitrate corrosion products on copper specimens. Colloidal Fe(III) compounds, thought to be from the reaction of SS vessels with the moist environment, have also been reported in these investigations (van Konynenburg, 1986). In situations where the aqueous phase is predominant (Glass et al., 1986) or where the aqueous phase is in contact with an inert gas such as argon (Kim and Oriani, 1987b), the formation of H_2O_2 and O_2 in the solution is more likely, although only indirect evidence for this has been provided. Unfortunately, the effect of radiolysis on environments within occluded regions such as crevices and cracks has not been studied systematically. However, designs currently considered in the ACD phase of the DOE program include a thick double-shell waste package in which almost complete shielding of γ-radiation is anticipated at the outer surface.

- **Changes due to repository construction**: The presence of engine fluids and large amounts of grouting may cause formation of organic acids in the former case and alkaline conditions in the latter. Microbial colonies can either be introduced or promoted due to the presence of nutrients from repository construction (Geesey, 1993). The potential for microbial activity at the proposed Yucca Mountain site is discussed briefly in Section 6.2.

- **Seismic activity**: Ground motion due to seismic activity can affect the position of the water table by changing the permeability and the fracture network of the rock. Also, seismic activity after closure of the repository can result in intrusion of water from perched condensate zone above the repository to the drifts in which waste packages will be emplaced.

- **Volcanic activity**: The consequences of volcanic activity would depend on the distance from the eruption. However, in addition to the high temperatures and deformation rates usually associated with volcanic activity, generation of gaseous sulfur compounds is expected. This can influence both gaseous and aqueous corrosion processes.

The foregoing discussion indicates that considerable uncertainty exists concerning the environment adjacent to the waste packages. Therefore, in discussing the performance of alternate waste package concepts and materials, a range of environmental conditions must be considered. A more complete discussion of plausible changes in the environment close to the waste packages over time can be found in a previous report (Sridhar et al., 1993a).

3 LOCALIZED CORROSION

3.1 BACKGROUND

Localized corrosion as related to the performance of HLW container materials has been reviewed by many (Beavers and Thompson, 1990a; Farmer et al., 1988a,b; Cragnolino and Sridhar, 1991a). The review of Cragnolino and Sridhar (1991a) included not only the conclusions of previous reviews by others, but also examined the advantages and limitations of different test techniques available to predict and characterize localized corrosion over extended periods of time. The salient conclusions from this review were:

- Conducting studies in groundwater of a specific composition, such as J-13 well water, is of limited value and a range of anionic and cationic concentrations have to be explored. On the other hand, the extensive test matrix used by Thompson et al. (1992) to overcome that problem has many limitations in terms of the choice of factors examined and choice of measured variables. A low correlation coefficient observed in their studies (i.e., r^2=0.143 for alloy 825) attests to these problems with the experimental matrix.

- Very little work had been conducted prior to this review with respect to the crevice corrosion of HLW container materials. No crevice corrosion was observed on type 304L SS and alloy 825 by Beavers et al. (1992) in long-term tests (8,065 hr) in an aerated, simulated J-13 water (6 ppm chloride) subjected to weekly drying periods. It must be noted that the corrosion potential was monitored in these tests for both alloys and ranged in the long term from $-250\ \mathrm{mV_{SCE}}$ to $-100\ \mathrm{mV_{SCE}}$. In another series of long-term tests (3,000 hr) in an aerated 1,000 ppm Cl^- solution (pH 10), pitting was observed in creviced areas of type 304L SS but not on alloy 825. However, the crevice geometry was not controlled and the corrosion potential was not measured.

- Rather extensive investigation of the applicability of E_{rp} for the long-term prediction of localized corrosion has been carried out in Japan with respect to a variety of austenitic alloys, carbon steels, and titanium alloys (Tsujikawa and Hisamatsu, 1984; Fukuda and Akashi, 1992; Nakayama and Akashi, 1991; Okayama et al., 1987a). These investigations have demonstrated the independence of the repassivation potential with respect to the extent of crevice corrosion and the applicability of this potential in predicting the occurrence of crevice corrosion over the long term (several months). However, they have not related the repassivation potential for pitting and crevice corrosion and have suggested (Tsujikawa and Hisamatsu, 1984) that the repassivation potential for pitting may not be a constant with respect to pit depth and, hence, may not be a conservative predictive parameter.

One of the main recommendations arising from the previous review of localized corrosion (Cragnolino and Sridhar, 1991a) was that the concept of repassivation potential should be fully explored to determine its usefulness as a bounding parameter for performance assessment of waste package materials under aqueous corrosion conditions. From this point of view, three types of studies were undertaken in Task 1 of the IWPE project: (i) cyclic potentiodynamic polarization (CPP) tests to determine the effect of environmental factors on localized corrosion, (ii) stepwise decreasing potential and potentiostatic tests to determine the adequacy of repassivation potential for long-term prediction of pitting and crevice corrosion (E_{rp} and E_{rcrev}), and (iii) mechanistic studies to determine the relationship of chemistry changes in crevices to initiation and repassivation and to determine the electrochemical behavior of alloys in simulated pit/crevice solutions.

In a previous report (Sridhar et al., 1993a), the effect of environmental factors on the localized corrosion of austenitic Ni-Fe-Cr-Mo alloys and copper-based alloys (CDA-102 and CDA-715) was described. Since the copper-based alloys were de-emphasized in the DOE program, no further experiments were conducted on these alloys. Therefore, studies on these alloys are not reported in this chapter. Instead, the chapter focuses on the austenitic alloys. The information presented in the previous report (Sridhar et al., 1993a) is summarized and updated in this chapter.

3.2 EXPERIMENTAL APPROACH

3.2.1 Specimens

The dimensions of various specimens used in this investigation are given in Figure 3-1. All the specimens of the alloys tested were machined from 12.5-mm-thick plate. The microstructures and chemistries of these plates have been described elsewhere (Sridhar et al., 1993a). Cylindrical specimens (Figure 3-1a) measuring 6.3 mm in diameter with a 600-grit finish were used in CPP tests and repassivation time tests. Additional CPP tests were carried out using rectangular specimens (Figure 3-1b), measuring 63.5×12.7×3.1 to 6.3 mm, prepared by cold rolling the material from 21 to 61 percent, as determined by the final thickness. These specimens were finished to either a 600-grit or a 36-grit finish. Potentiostatic tests were conducted with cubic specimens (Figure 3-1c), having a total surface area of 15 cm^2 including both polished and Cr-depleted, mill-finished surfaces described in a previous publication (Dunn et al., 1995b). Specimens having a controlled crevice (Figure 3-1d) were used in stepwise decreasing potential repassivation tests.

3.2.2 Cyclic Potentiodynamic Polarization Tests

The CPP technique was used to study the localized corrosion behavior of these alloys. The test procedure is similar to that given in the ASTM Standard G 61-86 (American Society for Testing and Materials, 1994e). The test apparatus consisted of a 5-port glass cell fitted with a water-cooled Allihn-type condenser and a water trap to minimize air intrusion. Cylindrical specimens 6.3 mm (0.25 in.) in diameter and 19.0 to 48.6 mm (0.75 to 1.9 in.) in length were used. These specimens were polished wet to a 600-grit finish with SiC paper. In most experiments, the specimens were fully immersed in the solution. In some experiments, they were partially immersed in the solution to avoid crevice corrosion in the gasket area where electrical connection is made to the specimens. Crevice corrosion was important in the low chloride solutions or at low temperatures which are marginal conditions for causing pitting. A long salt bridge-Luggin probe with a porous silica (vycor) tip was used so that the tip was in the test solution and the other end was at room temperature. In experiments with dilute solutions such as the J-13 water, the electronic noise was high if a salt bridge with low chloride concentration (e.g., same concentration as the test solution) was used. This problem became especially acute for the EG&G Model 273 potentiostat which has a differential input. To avoid this problem, a more concentrated salt bridge solution, typically 0.5 M to saturated NaCl, was used. The liquid junction potential for the 0.5 M NaCl salt bridge solution was 4.8 mV and was lower for the more concentrated solutions. The saturated calomel electrode (SCE) was used as the reference electrode in all the experiments. All potentials are referred to the SCE scale at ambient temperature (~22 °C), without correction for the thermal diffusion potential along the nonisothermal salt bridge. Platinum was used as a counter electrode in most of the experiments. In some

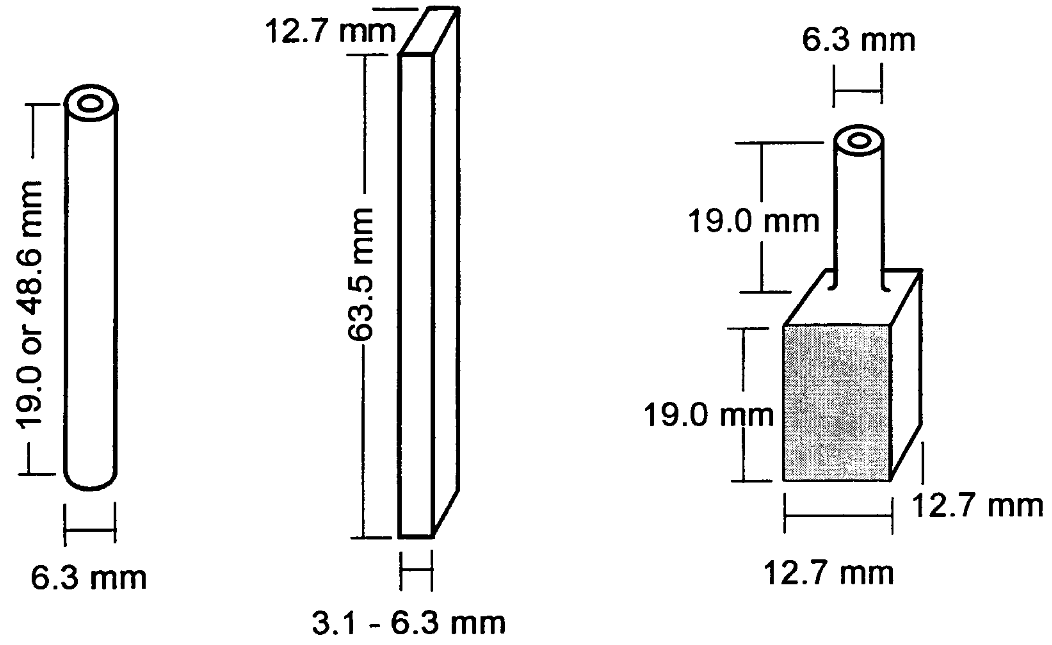

A. Cylindrical Specimen

B. Cold Rolled Specimen

C. Long term test specimen with polished and mill-finished surfaces

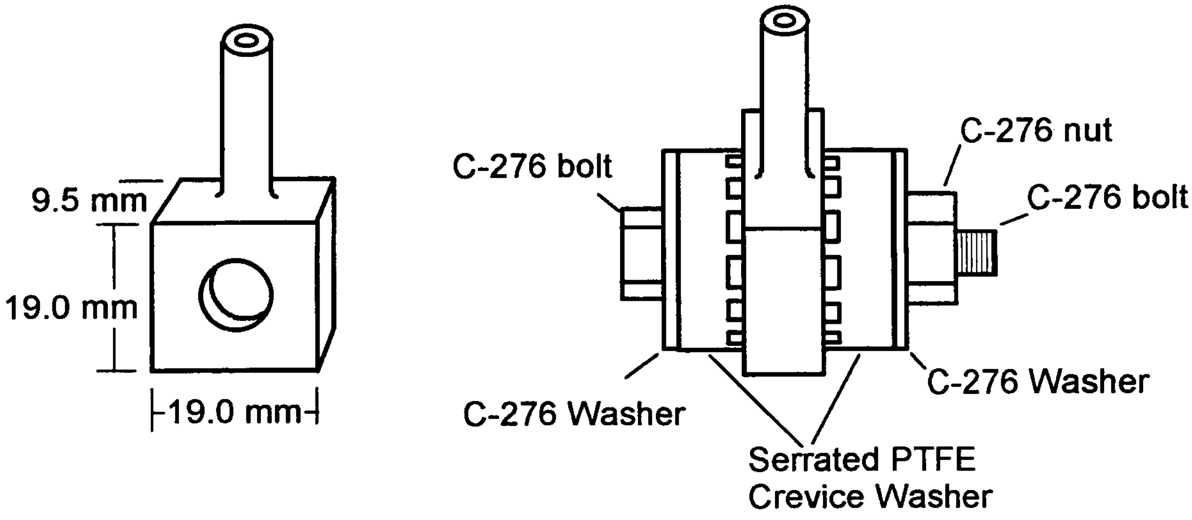

D. Crevice specimen

Side view of Crevice specimen with PTFE Crevice washers attached with C-276 bolt

Figure 3-1. Dimensions of specimens for localized corrosion studies

cases, a graphite rod was used. The solutions were continuously deaerated with high-purity argon or nitrogen. The corrosion potentials of the specimens and the Pt electrode were measured independently using a Keithley Model 614 electrometer. Polarization was performed using EG&G Models Versastat, 273, and 173/276 potentiostats. Post-test visual examination of the specimens was performed under a 70x stereoscope, and in selected cases, in the scanning electron microscope (SEM) fitted with an energy dispersive spectroscopic analyzer (EDS).

Three types of solutions were used to study the effects of environmental factors:

- Simulated J-13 environments which contained various anionic species (Cl^-, NO_3^-, F^-, SO_4^{2-}, and CO_3^{2-}) and a mixture of cationic species including Na^+, K^+, Ca^{2+}, and Mg^{2+}. Silica was not added to these solutions because of its slow rate of dissolution and low solubility. These solutions will be referred to as SJ-13 water with appropriate modifiers related to the specific changes made (e.g., SJ-13 water + 300 ppm Cl^- refers to a simulated J-13 water whose total chloride concentration is 300 ppm).

- Factorial study environments which contained various anionic species, but where the cationic species were Na^+ and H^+. The pH of these solutions was maintained at a relatively constant level by the addition of bicarbonate. These solutions will be referred to by their ionic concentrations (e.g., 1,000 ppm Cl^- solution)

- Simulated crevice/pit solutions which contained various anionic concentrations and in which pH was altered by the addition of HCl. Again, Na^+ was the only other cationic species. These solutions will be referred to by their ionic concentrations.

The preparation and analyses of these solutions are described in Appendix B.

Additional experiments were conducted on alloy 825 received in the form of a 12.5-mm plate with mill-finished surfaces. Specimens having dimensions of 12.5×12.7×17.8 mm were cut from the plate. Care was taken to preserve the mill-finished surfaces. All other surfaces were polished to either a 60- or 600-grit finish using silicon carbide (SiC) paper. Prior to testing, the specimens were cleaned ultrasonically in detergent, rinsed in deionized (DI) water, ultrasonically cleaned in acetone, and dried. Solutions consisted of 1,000 ppm Cl^-, 85 ppm HCO_3^-, 20 ppm SO_4^{2-}, 10 ppm NO_3^-, and 2 ppm F^-, all as Na salts. All tests were performed at 95±2 °C. Solutions were deaerated with high-purity argon for the CPP tests or nitrogen for the potentiostatic tests. Following the completion of the experiments, the specimens were rinsed in DI water and ultrasonically cleaned in a mixture of 4 mL 2-Butyne-1,4-diol (35 percent aqueous solution)+3 mL concentrated HCl+50 mL H_2O to remove the attached corrosion products (Tromans and Frederik, 1984). Tests on control samples indicated that this cleaning procedure does not result in measurable corrosion of the alloy. The specimens were then reweighed and examined using a 70x stereoscope. Compositional analysis of the specimen surfaces was performed with a scanning electron microscope using energy dispersive spectroscopy (SEM-EDS). The surface roughness of the mill-finished and polished surfaces was measured with a surface profilometer using a stylus with a 5-µm radius.

3.2.3 Repassivation Potential Tests

The tests were conducted in a 1-L reaction kettle (approximately 900 mL of solution), shown schematically in Figure 3-2, fitted with a fritted gas bubbler, platinum counter electrode, temperature

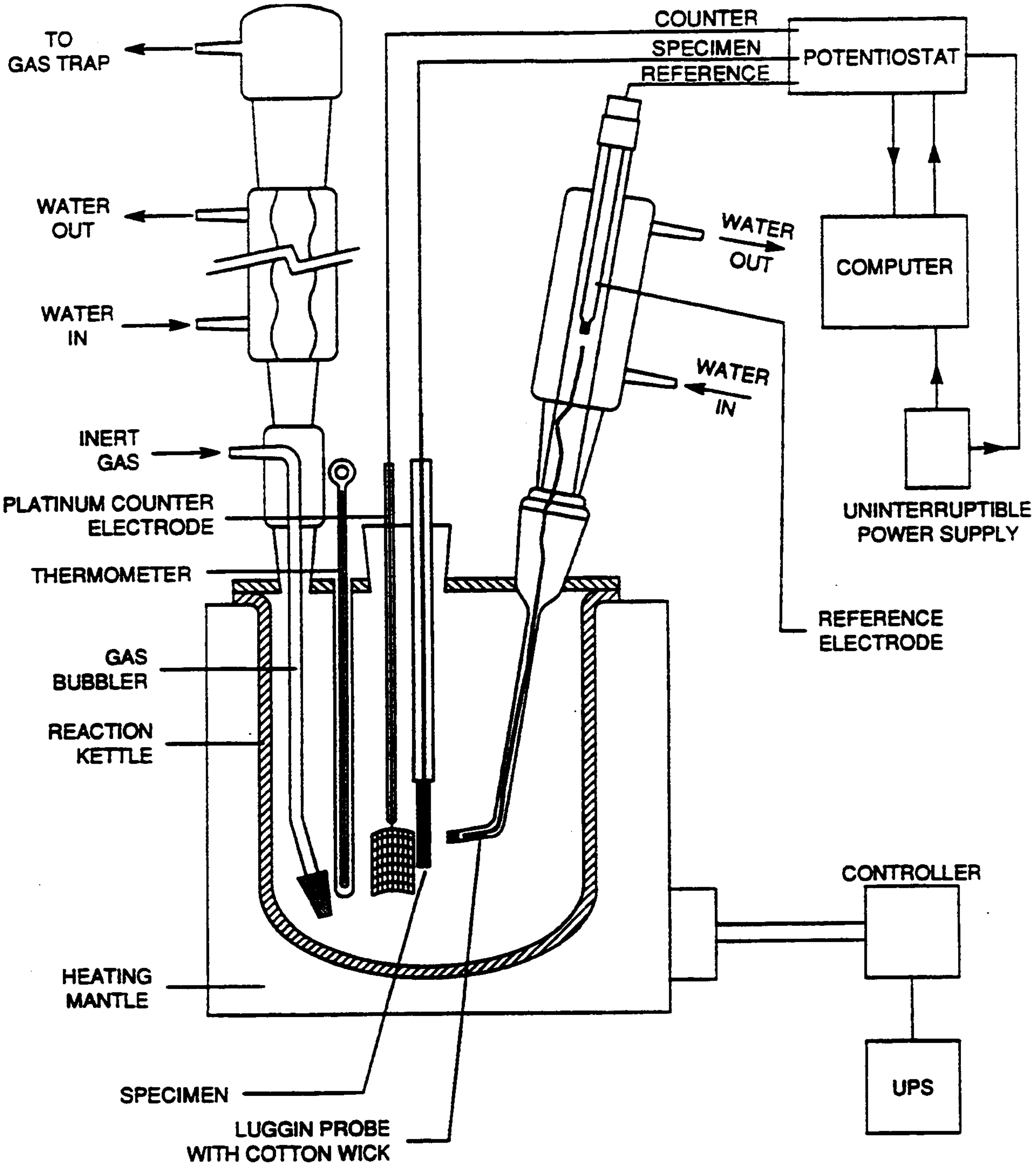

Figure 3-2. Schematic diagram of the cell and electrochemical testing system for the repassivation experiments

probe, and a Luggin probe with a short salt bridge for the reference electrode. Nitrogen was bubbled for 1 hr prior to the start and throughout the tests, the exit end going through a water trap to prevent back-diffusion of oxygen. A water-cooled condenser ensured that evaporative concentration of the solution did not take place. The Luggin probe had a porous silica tip to prevent drainage of the salt bridge solution. The salt bridge, which was filled with the test solution, was fitted with a water-cooled condenser. This ensured that the reference electrode tip was always at room temperature, which resulted in a reproducible thermal liquid junction potential and prevented the deterioration of the reference electrode at high temperatures. The SCE was used as the reference electrode in all the tests. A problem that was frequently encountered in the initial tests was the formation of air bubbles in the salt bridge. The discontinuity or poor electrical contact between the reference electrode and the test solution resulted in the generation of large noise signals in the measured current. A cotton wick, presoaked in the test solution, was introduced into the salt bridge (Figure 3-2) providing a continuous electrolyte path even in the presence of bubbles. The test vessel was sealed and heated to the desired temperature before introduction of the specimen.

An Electrosynthesis Model 440 multi-channel potentiostat was used to control the potential. This was connected to a Strawberry Tree ACPC-16-16, 16-bit, 16-channel, analog-digital converter (ADC) and a ACAO 12-8, 12-bit, 8-channel, digital-analog converter (DAC) in a 386 computer. The resulting potential and currents were stored on a disk for later analyses. The resolution of the ADC was adjusted to 17 ms per channel so that line noise was filtered out. The sampling rate was set at 10 Hz. The resolution of the ADC varies as a function of the selected voltage range. The software is capable of choosing the range automatically depending on the input value. Since the current is measured in terms of volts across a 10Ω resistor, the maximum resolution of current is approximately 1.25×10^{-7} A. The potential and current measurements were checked independently using a Keithley Model 614 electrometer and a Keithley Model 485 picoammeter. The data acquisition and control were performed using Workbench® software. This is an icon-based programming environment capable of acquiring signals, performing arithmetic and logical operations on the signals, and controlling external instrumentation based on the results of the calculations.

Stepwise decreasing potential repassivation tests were conducted on cylindrical specimens (Figure 3-1a) and crevice specimens (Figure 3-1d), the latter with two PTFE crevice washers bolted to the surface. The C-276 bolt and nut were torqued to 0.28 N · m (20 in. · oz) prior to specimen exposure. The bolt was insulated to prevent contact with the specimen. After pitting was initiated at 600 $\mathrm{mV_{SCE}}$, or crevice corrosion at 550 $\mathrm{mV_{SCE}}$, the applied potential was decreased to 400 $\mathrm{mV_{SCE}}$ to allow the localized corrosion to propagate. When sufficient growth was obtained, as measured by the amount of charge passed, the potential was decreased in 10 mV steps every 2 s until the current density remained below 50 $\mu\mathrm{A/cm^2}$. This potential was then taken as the repassivation potential. After testing, the crevice specimens were cleaned of corrosion products and the depth of attack perpendicular to the crevice surface was determined using an optical microscope with a calibrated fine focus adjustment. For pitting corrosion, the penetration depths were determined by cross sectioning the specimens.

Crevice devices made of PTFE and alumina (to simulate rock-metal crevices) were tried. However, the alumina crevice washers suffered cracking upon exposure to the solution and because of its rigidity did not form as tight a crevice as PTFE. Therefore, the alumina crevice washers were not used subsequently.

3.2.4 Long-Term Potentiostatic Tests

The validity of using E_{rp} from short-term tests as a parameter for determining long-term performance was tested by potentiostatically polarizing specimens for extended periods (up to 18 months) at potentials above and below the E_{rp}. Potentiostatic polarization tests were conducted in an ASTM G 31-72-type (American Society for Testing and Materials, 1994f) reaction kettle with approximately 1,500 mL of solution. The cell was equipped with a platinum counter electrode and a SCE reference electrode maintained at room temperature. The SCE was connected to the cell through a salt-bridge with a porous silica tip and a water-cooled Luggin probe ensuring reproducible liquid junction potentials and preventing deterioration of the reference electrode. Specimens were connected to a computer controlled multichannel potentiostat. A constant potential was applied for test intervals of 28 days, between which the specimens were examined for weight loss and visible signs of corrosion while the test solution was changed. No further exposures were conducted on specimens after localized corrosion was observed.

3.2.5 Repassivation Time Tests

Repassivation time tests for pitting corrosion were conducted with a setup similar to the potentiostatic polarization tests with the exception that the solutions were deaerated with high-purity nitrogen. Pits were initiated at 600 mV_{SCE} on cylindrical specimens with the specimen-PTFE gasket interface above the solution level. Pits were then grown at 400 mV_{SCE}. During pit growth, the charge density was continuously monitored. Since it was desired to compare the repassivation time of pits of approximately equal depth, the applied potential of the specimen was decreased to allow repassivation after either attaining low charge densities (<55 coulombs/cm^2) for shallow pit depths, or high charge densities (>70 coulombs/cm^2) for deep pits, allowing a comparison of repassivation times with pit depth. The repassivation time was measured as the time required for the current density to decrease below 50 µA/cm^2 after the potential of the specimen was decreased rapidly from 400 mV_{SCE} to the desired potential. An example of this technique, shown as a plot of the specimen potential and current density versus time, is presented in Figure 3-3.

3.2.6 Crevice Chemistry Studies

For alloy 825, both a 12.5-mm-thick plate and 3-mm-thick sheet were used, the latter to examine surface Cr depletion effects. The surface chemical composition was analyzed using a SEM, EDS, and Auger electron spectroscopy (AES). These results have been reported elsewhere (Dunn et al., 1995b). The surface of mill-finished alloy 825 had a significantly lower Cr concentration than that in the bulk. The specimens were 6.3 cm×1.3 cm×3 mm in dimension in the initial tests. Later, disc-shaped specimens, 3 cm in diameter, were used for radial symmetry of the crevice geometry. All specimens, except the mill-finished specimens, were wet ground on all surfaces. For the mill-finished specimens, only the top surface was left in the mill-finished condition. Wires of the same alloy as the specimen were spot welded for electrical connection. Spot welding conditions were adjusted such that local heating was minimized and post-test examination indicated that, in most cases, crevice corrosion did not occur in this area.

The crevice assembly was constructed by sandwiching the specimen between blocks of polymethyl methacrylate (PMMA) as shown in Figure 3-4. Care was taken in this design to avoid creating reservoirs for solution inside the crevice which tended to reduce the sensitivity of detection of chemistry changes. Grooves were provided on the bottom crevice assembly so that no crevice corrosion occurred on the bottom surface. Crevice tightness was controlled by clamping the top and bottom crevice blocks

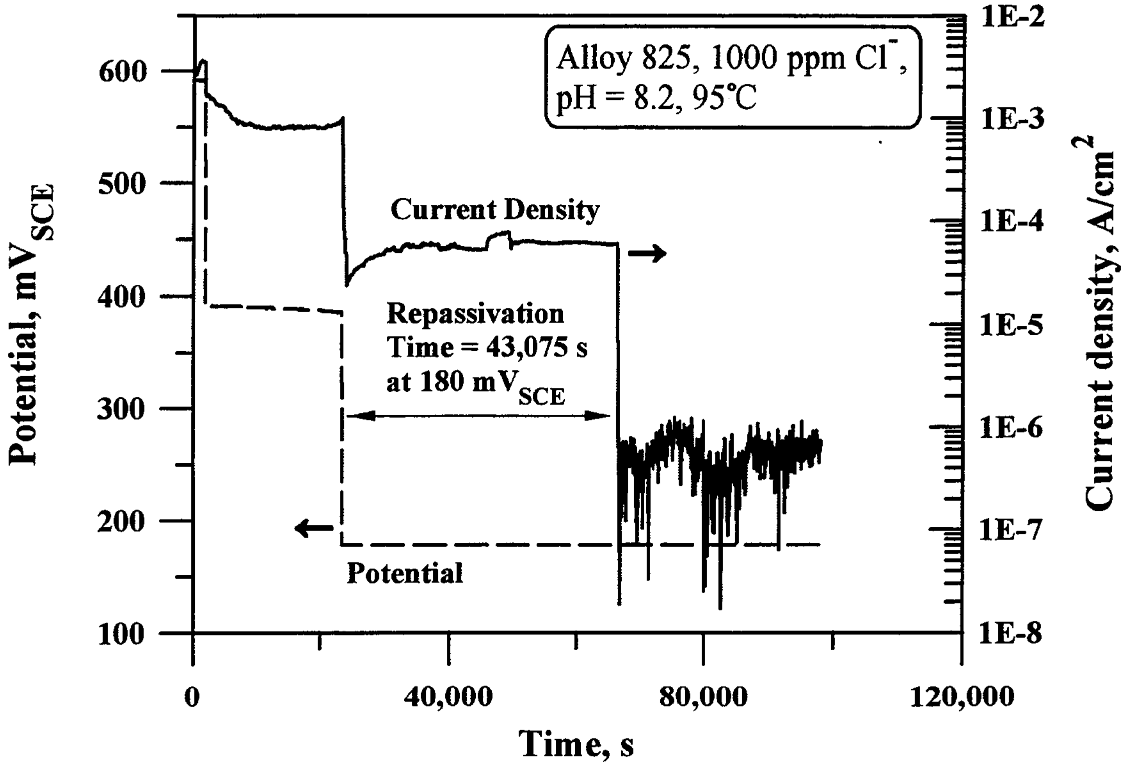

Figure 3-3. Illustration of repassivation time technique. An example of one of the experimental runs is shown.

on the specimen using alloy C-276 bolts under a controlled torque of 0.14 N · m (20 in. · oz). For the rectangular crevice assembly, ports in the top crevice assembly for the microelectrodes were located at distances of 12.5 mm and 37.5 mm from the mouth of the crevice. These locations will be referred to as "mouth" and "tip," respectively. For the radial crevice assembly, the ports for the mouth and tip were located at radial distances of 2 mm and 8 mm from the outer circumference of the crevice, respectively, the total crevice device radius being 10 mm. The whole crevice assembly was placed in a glass vessel fitted with a PMMA top which had ports for the various electrodes and gas purging. The solution level was adjusted to be below the entry ports in the crevice assembly. The glass vessel also had a side compartment connected through a frit containing the counter electrode (Pt foil). This arrangement minimized the change in pH in the bulk solution due to cathodic processes on the counter electrode. The cell was placed in a Faraday cage to minimize noise by the high impedance electrodes.

A flexible glass electrode (Microelectrodes Inc. Model MI506) was used along with a double-junction reference electrode (Model MI403) for pH measurements. A silver chloride (Ag/AgCl) electrode (Microelectrodes Inc. Model MI200) was used along with a double-junction reference electrode for chloride measurements as an ion selective electrode (ISE). A separate double-junction (Ag/AgCl, 3 M KCl) reference electrode was used for potential measurements. The outer barrel of the double-junction reference electrode was filled with the test solution thus ensuring that the chloride leakage from the reference compartment did not affect the results significantly. For bulk solution measurements, a single-junction reference electrode (Microelectrodes Inc., Model MI402) was used along with glass and chloride electrodes. The pH and chloride electrodes were connected to pH/Selective ion meters with output were

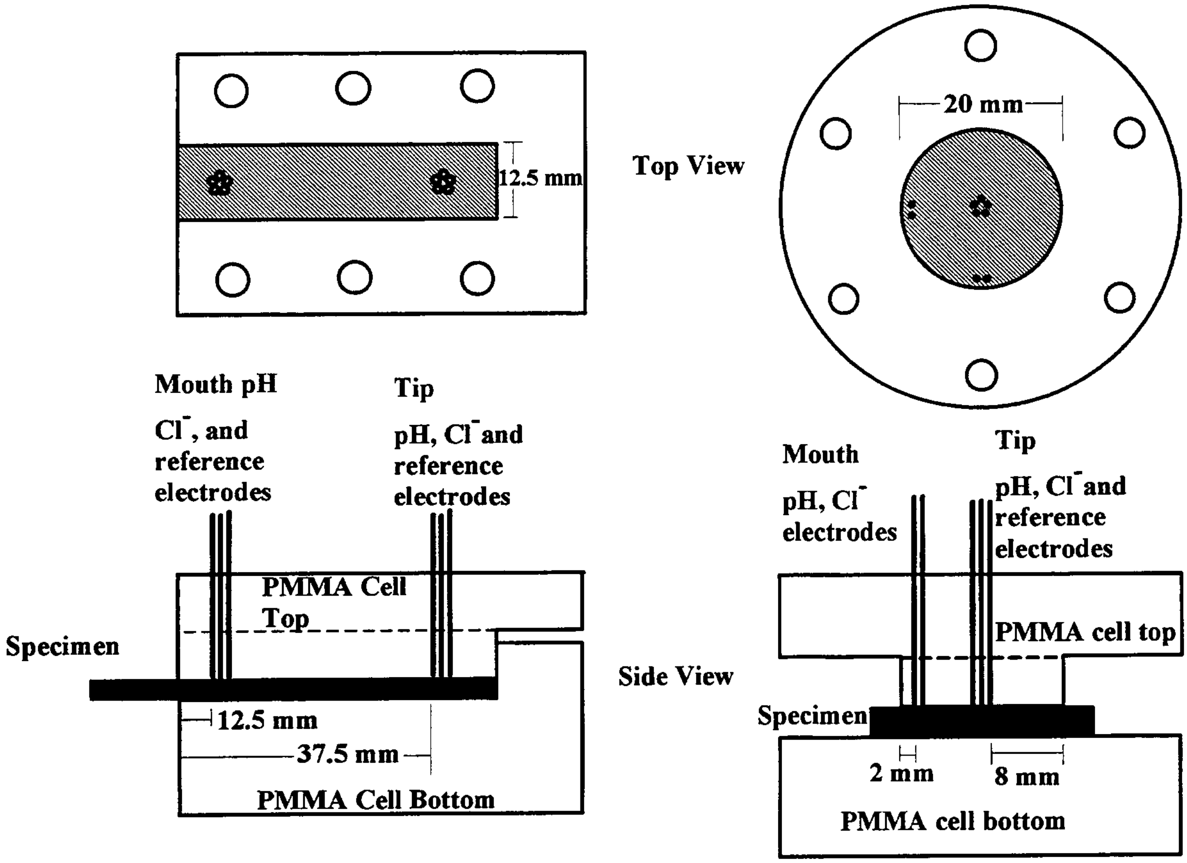

Figure 3-4. The geometries of the rectangular and radial crevice devices indicating the location of the microelectrodes

connected to chart recorders or data acquisition cards. The pH and chloride electrodes were calibrated using standard solutions before and after the experiments to verify their performance. The microelectrodes were about 1 mm in diameter and required about a 1 mm depth of immersion. In the initial design of the cell, the ports were filled with PTFE tape to reduce the volume of electrolyte collected in these spots. In later designs, holes for tight fitting of the electrodes were drilled into the top block of the crevice cell.

The reference electrodes for potential measurements, as well as the working and counter electrodes, were connected through a 6-channel potentiostat (Electrosynthesis Model 440) to a 16-bit/16-channel data acquisition system (Strawberry Tree Inc.). All the tests were carried out with the unstirred solution exposed to ambient air. All potentials in these studies are referred to the standard hydrogen electrode (SHE). The reported current density refers to an equivalent uniform current density, including both creviced and exposed areas. Post-test observation did not indicate any localized corrosion in the open area and, therefore, any increase in current can be attributed to crevice corrosion. Post-test examination also indicated that the crevice corroded area often was significantly lower than the overall specimen area. Hence, the effective current density in most cases can be an order of magnitude larger. The solutions in these tests, in similarity to the crevice tests, were not deaerated, and, hence, some level of oxygenation was present due to exposure to ambient air. The specimens were immersed completely such that the specimen to specimen holder crevice was exposed to the solution. Prior to the crevice chemistry tests, CPP tests at a scan rate of 0.17 mV/s were conducted on cylindrical specimens to identify breakdown and repassivation potentials. The potentials applied in the crevice chemistry tests were between these measured breakdown and repassivation potentials.

3.3 RESULTS

3.3.1 Effects of Environmental Factors

3.3.1.1 Factorial Experiments

A properly designed factorial experiment can reveal the effects of several variables and their interactions with a relatively modest expenditure of experimental effort. It is well known that several environmental factors, including aggressive anion concentration and temperature, can affect the localized corrosion behavior of a given alloy (Szklarska-Smialowska, 1986). However, a review of the literature (Cragnolino and Sridhar, 1991a) indicated that few systematic studies of the localized corrosion behavior of SSs and Ni-base alloys existed for environments containing low concentrations of various anions such as those found in J-13 water. Beavers et al. (1990) were the first to use a fractional factorial matrix to study the effects of groundwater composition on localized corrosion behavior of candidate container materials. However, as mentioned earlier, their design of the test matrix and the choice of measured parameters for analysis posed several disadvantages:

- Choice of a fractional factorial matrix did not enable them to investigate interactions between various environmental parameters

- The assumption that the chosen factors were independent is not true for factors such as pH and bicarbonate concentration

- The solubility of some species such as SiO_2 is very low and time-dependent. Hence, analysis of results in terms of the effect of Si is questionable

- The results were analyzed in terms of purely electrochemical parameters, although the authors acknowledged the lack of correlation between actual observation of localized corrosion and electrochemical parameters in some alloys

The above-mentioned limitations of the approach of Beavers et al. (1990) and Thompson et al. (1992) resulted in a low correlation coefficient. For example, the R^2 value for the analysis of pitting potential ranged from 0.143 (for alloy 825) to 0.555 (for CDA-715). Hence, a further refinement of the factorial approach was attempted at the CNWRA. The approach was to use a full factorial design enabling an examination of interactions between all factors, limit the number of factors studied to those that have been found to be the most important in the literature, limit the study to the effect of anionic species by using Na^+ as the only cation, and use more realistic measures of localized corrosion as discussed below.

The details of the factorial design have been elaborated elsewhere (Cragnolino and Sridhar, 1991c) and will not be repeated here. More elaborate treatments of the subject of statistical experimental design can be found in Box et al. (1978) and Mason et al. (1989). For the factorial experiments performed over limited ranges of Cl^-, SO_4^{2-}, NO_3^-, and F^- concentrations and temperature, the relationship of localized corrosion to environmental factors has been derived using a localized corrosion index (LCI) (Cragnolino and Sridhar, 1991c). This LCI was devised specifically for alloys 825 and C-22, since the electrochemical behavior did not always correlate with visual observation of localized corrosion. This was especially true in low chloride environments where the alloy exhibited passivity up to potentials beyond the oxygen evolution regime. For types 304L and 316L SSs, there was a much better correlation between localized corrosion and electrochemical parameters. However, for consistency and for purposes of comparison, the LCI was modified to account for the effect of lower pitting potential, and the modified LCI was used for all alloys (Cragnolino and Sridhar, 1993b).

Since the original LCI is no longer used, the modified LCI will be referred to in this report as the LCI, defined as

$$LCI = \frac{(E_p - E_{rp}) \cdot 100}{E_p} \cdot \textit{Visual Rating} \tag{3-1}$$

where E_p is the pit initiation potential, E_{rp} is the repassivation potential, and ***Visual Rating*** is obtained by a combination of stereoscopic observation of pits at 70× and SEM-EDS analysis of corrosion products surrounding the pits (Cragnolino and Sridhar, 1991c). Five broad classifications were created, and a rating number was assigned to each of these classifications. Details of the SEM examination were reported previously (Cragnolino and Sridhar, 1991c). While these ratings have a certain element of subjectivity, it should be noted that a rating based only on the number of pits per unit area is insufficient to characterize the behavior, especially of alloy 825, since both the depth of pits and type of corrosion products associated with the pits varied. The most severe cases (Rating=4) had not only deep pits but also crevice corrosion. There were no thick corrosion products deposited on the pits. Specimens of Rating=3 also exhibited deep pits of a similar kind but did not show extensive crevice corrosion. The pits were found to have considerable undermining beneath the surface. SEM-EDX examination indicated that the corrosion products associated with these pits were rich in Cr and Mo. In some specimens, the pits were quite numerous but shallow and covered with a brown deposit. No crevice corrosion was observed in these specimens, which were given a rating of 2. SEM-EDX examination of these pits indicated that they were associated with corrosion products rich in Fe and low in Cr and Mo. Finally, in one specimen, the pits were found to be flat depressions surrounded by a brown corrosion product rich in Fe. This specimen was given a rating of 1 to distinguish it from the shallow but narrow pits of Rating 2. A rating of zero was assigned to specimens with no pitting or crevice corrosion as observed at 70×.

The results of the factorial experiments are tabulated in Appendix C (Tables C-1 through C-4). The results of the analysis of the full-factorial experiments using LCI as the measure of localized corrosion for type 316L SS and alloy 825 are shown in Eqs. (3-2) and (3-3), respectively. The analysis considers the independent variables to be scaled on a −1 to +1 range, as shown in Eq. (3-4) where A is the actual value (in ppm or degrees C) of a given factor and X_A is the scaled value of the same factor. The factor effect is the contribution of any factor to LCI at its highest level (+1). The coefficients in Eqs. (3-2) and (3-3) are the factor effects divided by 2. The standard error and 95-percent confidence interval were calculated for each of the factor effects (Appendix C, Tables C-3 and C-4), and only those factors whose factor effects were greater than the 95-percent confidence interval (C.I.) are included in Eqs. (3-2) and (3-3).

$$(LCI)_{316L} = 364.12 + 320.2(X_{Cl}) \tag{3-2}$$

$$\begin{aligned}(LCI)_{825} = {} & 95.5 + 84.5(X_{Cl}) - 84.5(X_{NO_3}) - 87.0(X_{Cl} \cdot X_{NO_3}) \\ & - 10.2(X_F) + 9.4(X_T \cdot X_F) - 8.1(X_T \cdot X_{NO_3}) \\ & - 7.0(X_{Cl} \cdot X_T \cdot X_{NO_3})\end{aligned} \tag{3-3}$$

$$X_A = \frac{2(A - A_{avg})}{(A_{max} - A_{min})} \tag{3-4}$$

Equation (3-2) indicates that, for type 316L SS, the only factor of importance is chloride, which promotes localized corrosion (positive coefficient). Nitrate and chloride-nitrate interaction have marginal impact on the LCI of type 316L SS, whereas all the other factors have no significant effect. Temperature was not examined as a factor for this alloy. In contrast, for alloy 825, Eq. (3-3) indicates that chloride, fluoride, and nitrate are all significant. The positive coefficient of chloride in Eq. (3-3) means that it promotes localized corrosion, whereas the negative coefficients of nitrate and fluoride indicate that they inhibit localized corrosion. The interactions of Cl-NO_3, T-F, T-NO_3, and Cl-T-NO_3 are also significant. The average value of LCI for type 316L SS is higher than that of alloy 825, indicating that the latter is more resistant to localized corrosion. This is understandable because the Cr and Mo contents of alloy 825 are significantly higher than those of type 316L SS. In contrast to the results of Thompson et al. (1992), the empirical Eqs. (3-2) and (3-3) exhibit adjusted R^2 values of 0.991 and 0.977, respectively, confirming that the choice of measured parameters and independent factors is crucial in factorial designs.

There are, however, several limitations to the factorial experiments:

- The Eqs. (3-2) and (3-3) are valid only within the ranges of the factors studied. Thus, while nitrate did not have any effect on the LCI of type 316L SS in the 10–1,000 ppm range, it can inhibit localized corrosion at higher concentrations. Similarly, the lack of a temperature effect for alloy 825 in the factorial experiments is valid only within the 6–1,000 ppm chloride concentration range. Temperature was found to decrease E_p and E_{rp} of alloy 825 in the 10,000 ppm Cl^- solution (Cragnolino and Sridhar, 1991b).

- The linear relationship assumed is a reasonable approximation only within the range of concentrations studied. It is well known that E_p decreases with the logarithm of chloride concentration (Szklarska-Smialowska, 1986).

- The parameter, LCI, while useful for the factorial analysis of the localized corrosion of alloy 825, is of limited value in long-term prediction.

The ranges of concentrations of various anionic species assumed in the factorial experiments stemmed from prior studies by Abraham et al. (1986) on evaporative concentration of simulated J-13 water. However, even higher concentrations of some species may be possible, as discussed in Chapter 2. Hence, further experiments, using the CPP technique, were conducted to determine the effects of chloride, sulfate, nitrate, and pH.

3.3.1.2 Effect of Chloride Concentration and pH on Localized Corrosion Parameters

The effect of chloride concentration on the E_p and E_{rp} of alloy 825 and type 316L SS at 95 °C is shown in Figures 3-5 and 3-6, respectively. These potentials were measured using CPP tests at a scan rate of 0.167 mV/sec. In addition, the effect of thiosulfate is also indicated in these figures as these are pertinent to later discussions on SCC. At low chloride concentrations, significant scatter in the E_{rp} of alloy 825 is noted as indicated by the bars because only a few of the multiple specimens tested underwent localized corrosion. At 100 ppm chloride concentration, crevice corrosion is the dominant corrosion mode. At higher chloride concentrations, both pitting and crevice corrosion occurred. The data for chloride concentrations equal or lower than 1,000 ppm are provided in Table C-5 (Appendix C) and for higher concentrations in Table C-6. As shown in Figure 3-5, the pH does not a have a significant effect on the critical potentials of alloy 825 (Figure 3-5). This is in accord with data reviewed for SSs by Szklarska-Smialowska (1986) and can be explained by the observation that the pH of the solution inside the pit/crevice is quite acidic despite near-neutral pH values in the bulk solutions. The changes in pH inside a crevice will be discussed later in this chapter. It can also be seen that at high chloride concentrations, the E_{rp} of alloy 825 is not very different from that of type 316L SS. This suggests that if a layer of saturated saline solutions forms on the container due to evaporation, alloy 825 may not be significantly more resistant than type 316L SS to localized corrosion. Thiosulfate reduces the E_{rp} for both alloys, as shown in Figures 3-5 and 3-6. In these figures, the range of values attained by E_{corr} under various oxidizing conditions is also shown.

The eventual performance of these materials, from the point of view of localized corrosion, will not only depend upon the critical potential but will be dictated by the corrosion potentials. The open-circuit potentials of alloy 825 and Pt in various chloride solutions and in the presence of a variety of redox conditions are shown in Table 3-1. The open-circuit potentials of both alloy 825 and Pt in aerated solution

Table 3-1. Effect of aeration and H_2O_2 addition on open-circuit potentials (mV_{SCE}) of alloy 825 and Pt in simulated J-13 solutions at 95 °C

Condition	Alloy 825		Platinum	
	6 ppm Cl	1,000 ppm Cl	6 ppm Cl	1,000 ppm Cl
Deaerated, Argon	−545	-525	−478	−448
Argon + 0.5 mM H_2O_2	118	108	73	59
Aerated	−298	−280	170	140
Aerated + 0.5 mM H_2O_2	132	106	79	53

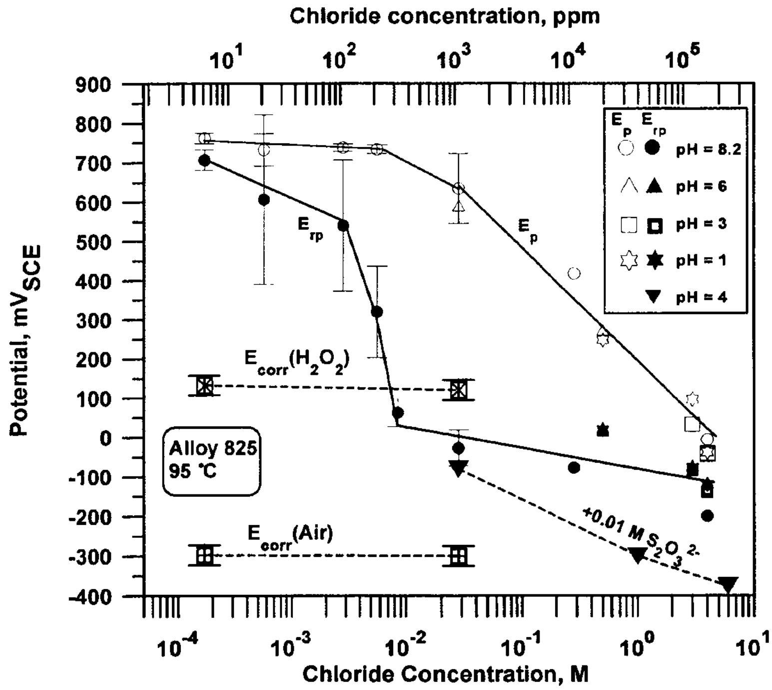

Figure 3-5. Effect of chloride, thiosulfate, and pH on E_p and E_{rp} for alloy 825 at 95 °C. Cyclic potentiodynamic polarization curves at a scan rate of 0.167 mV/sec from E_{corr} in deaerated solutions. Ranges of E_{corr} values under two oxidizing conditions are indicated by bars.

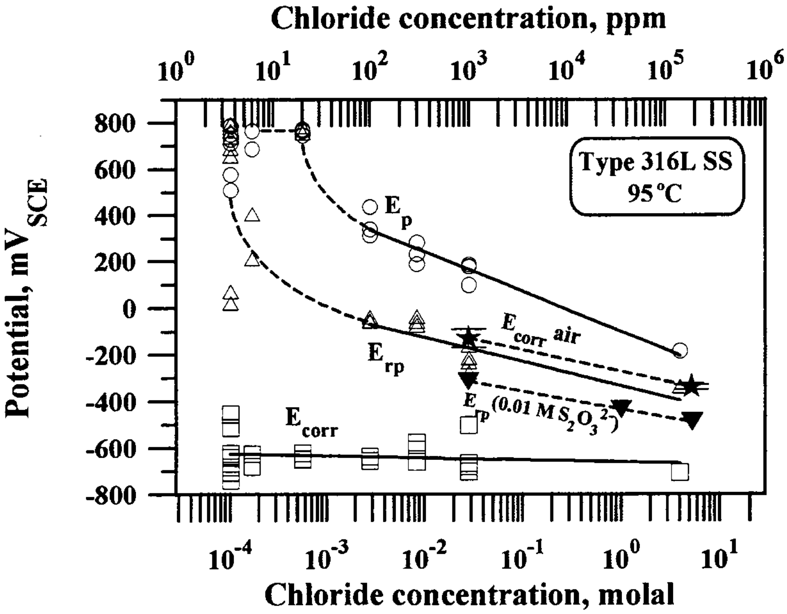

Figure 3-6. Effect of chloride concentration and thiosulfate addition on E_p and E_{rp} for type 316L stainless steel at 95 °C. Cyclic potentiodynamic polarization curves at a scan rate of 0.167 mV/sec from E_{corr} in deaerated solutions. Range of E_{corr} values in aerated solutions is indicated by bars.

containing 1,000 ppm chloride attained steady values of −280 mV and 140 mV, respectively. Although the value observed for Pt is well below the equilibrium value for the oxygen reduction reaction, the potential measured on alloy 825 indicates that this reaction is even more irreversible on this alloy surface. These open-circuit measurements are governed not only by charge-transfer conditions at the metal/solution interface but also by transport limiting processes in solution. Hence, the measurements deviate considerably from the thermodynamically expected values. In the case of deaerated environments, the potentials of both alloy 825 and Pt increased with the addition of peroxide, although the increase was more pronounced for alloy 825 than for Pt (Table 3-1). The value of the potential for alloy 825 and Pt in the 0.5 mM H_2O_2 solution is almost independent of the presence of dissolved oxygen, indicating that the reduction of H_2O_2 is the controlling cathodic reduction reaction on both metals.

3.3.1.3 Effect of Nitrate and Nitrite

The inhibiting effect of nitrate for alloy 825 and type 316L SS is compared in Figure 3-7 (see also Tables C-7 and C-8 in Appendix C). A lower concentration of nitrate is required to inhibit localized corrosion of alloy 825 completely. This can be rationalized by the higher Cr content of the alloy in comparison to type 316L SS. It can also be seen from Table C-7 that nitrite has a similar inhibiting capacity to nitrate for alloy 825. A series of experiments was conducted on alloy 825 where the 1,000 ppm nitrate addition was made to a 1,000 ppm Cl^- solution at a potential below the E_p observed in other tests and after significant localized corrosion had already occurred (when the scan was almost reversed). Inhibition was observed when the nitrate addition was made before E_p was attained, but not after significant localized corrosion occurred. Both nitrate and nitrite are anticipated under conditions of radiolysis of air plus steam mixtures (Van Konynenburg, 1986), although the concentrations that may be attained are uncertain. Furthermore, since radiolysis plays an important role in the early time period when the environment is anticipated to be dry and the proposed double-wall container may lessen the impact of radiolysis, the effects of nitrate and nitrite may not be significant for performance prediction.

3.3.1.4 Effect of Sulfate

While sulfate at concentrations above 10,000 ppm inhibits localized corrosion of alloy 825 more efficiently than for type 316L SS (Figure 3-8), it is not as effective an inhibitor as nitrate (see Tables C-7 and C-8). It is interesting to note that sulfate elevates the pit initiation potential, especially for type 316L SS, but does not affect the repassivation potential significantly. The effect of sulfate on pit initiation potential of type 316L SS is consistent with the literature on a variety of SSs (Rosenfeld and Danilov, 1967; Leckie and Uhlig, 1966; Bogaerts and van Haute, 1985). From the present data and the literature, it appears that the anticipated concentrations of sulfate and sulfate to chloride ratio in the repository environment are not sufficient to affect localized corrosion of these alloys significantly.

3.3.1.5 Effect of Other Ionic Species

The effects of bicarbonate, silica, and Mg^{2+} were reported previously (Sridhar et al., 1993a) and will not be repeated here because these effects are not considered to be significant. The results of CPP for these ionic species are shown in Appendix C, Tables C-7 and C-8, for alloy 825 and type 316L SS, respectively.

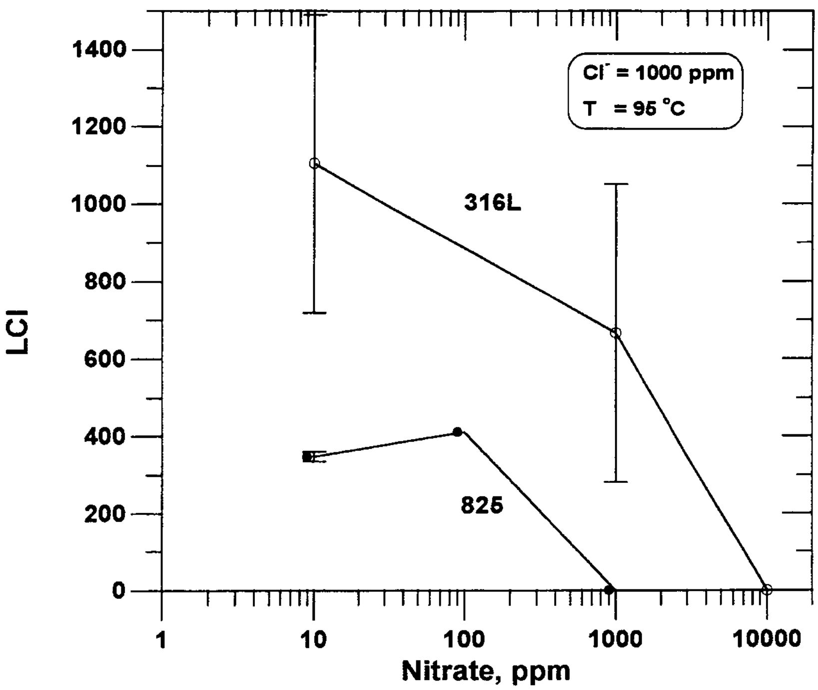

Figure 3-7. Effect of nitrate on localized corrosion of type 316L stainless steel and alloy 825 in a 1,000 ppm Cl⁻ solution at 95 °C

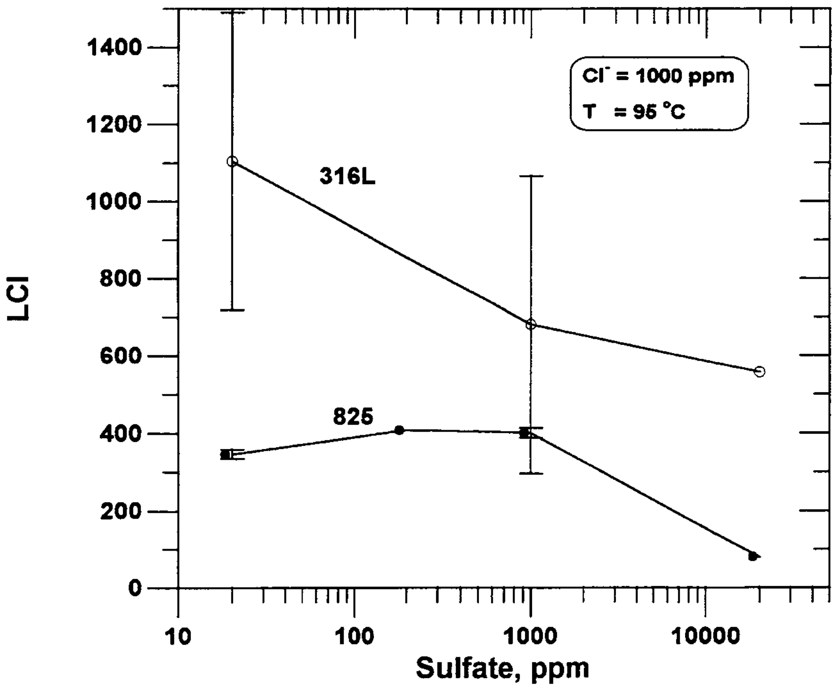

Figure 3-8. Effect of sulfate on localized corrosion of type 316L stainless steel and alloy 825 in a 1,000 ppm Cl⁻ solution at 95 °C

3.3.2 Repassivation Potential Experiments

The effect of pit/crevice corrosion growth on the repassivation potential for alloy 825 in the solution containing 1,000 ppm Cl^- at 95 °C is shown in Figure 3-9. Similar results have been shown for type 316L SS (Sridhar and Cragnolino, 1993b). Both the E_{rp} and the E_{rcrev} initially decreased with the amount of charge passed, and remained virtually constant and almost identical at high charge densities. The differences in the values of the E_{rp} and the E_{rcrev} obtained for high charge densities are believed to be insignificant since the potential was decreased in 10 mV increments. The E_{rcrev}, however, decreases faster than the E_{rp} at low charge densities. The E_{rp} and the E_{rcrev} values shown in Figure 3-9 are as much as 250 mV lower than the repassivation potentials measured in CPP tests. This decrease is a result of the faster scan rate used in the stepwise decreasing potential repassivation tests. A decrease in the E_{rp} with increasing backward scan rate has previously been reported for alloy 825 (Sridhar and Cragnolino, 1993b).

The specific charge density, defined as the amount of charge passed divided by the area of the corroded regions of the specimens, was also calculated for each specimen. For creviced specimens, the area of crevice corrosion was taken as the total area of the crevice region provided by the serrated PTFE washer. For pitted specimens, the area of the corroded region was assumed to be twice the pit area fraction multiplied by the total specimen area. The pit area fraction was determined by SEM image analyses of pitted surfaces. The maximum depth of pitting and crevice corrosion as a function of the specific charge density was determined to be:

$$\textbf{Maximum Depth (mm)} = \mathbf{0.04(Q)^{0.46}} \tag{3-5}$$

where Q is the specific charge density in coulombs/cm^2. The repassivation potential for pitting corrosion as a function of maximum penetration depth calculated from the above relationship is shown in Figure 3-10. The similarities between Figure 3-9 and Figure 3-10, are readily apparent for the case of pitting corrosion. The E_{rcrev} as a function of penetration depth measured for each specimen is also shown in Figure 3-10. While there is significant scatter in the value of E_{rcrev} at low penetration depths, the E_{rcrev} is generally lower than the E_{rp} at shallow penetration depths. It may appear that the lower bound values of repassivation potential were measured at very large charge densities, especially for pitting. However, as shown later from potentiostatic tests, the deep pit results are not overly conservative for long-term prediction of the initiation of stable pits/crevices. These results are compared to literature results in Section 3.4.2.

3.3.2.1 Repassivation Kinetics and Long-Term Tests

Previously reported results (Sridhar and Cragnolino, 1993b) indicated that the E_{rp} was a function of backward scanning rate. For a given charge density (pit depth), higher backward scan rate resulted in lower values of E_{rp}. It must be emphasized that this observation, which at first may appear to contradict the commonly held notion that a higher scan rates results in higher E_{rp}, was made with predefined pit growth. Thus, the effect of scan rate on the extent of pit growth was eliminated. In order to study the effect of scan rate further, the repassivation kinetics were examined as mentioned before.

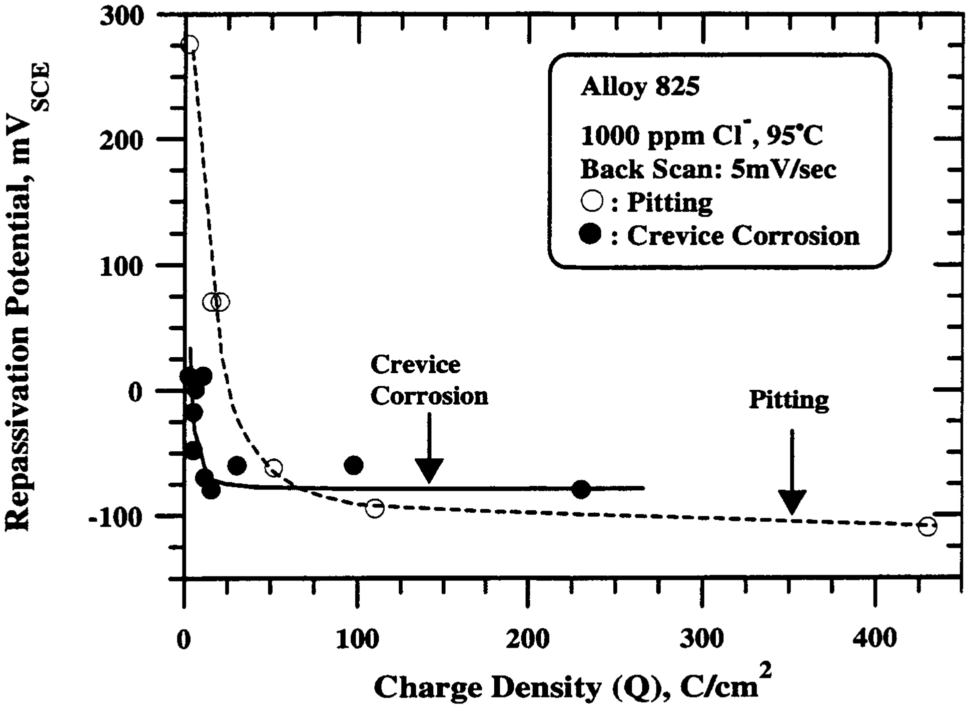

Figure 3-9. Effect of charge density on the repassivation potential for pitting and crevice corrosion

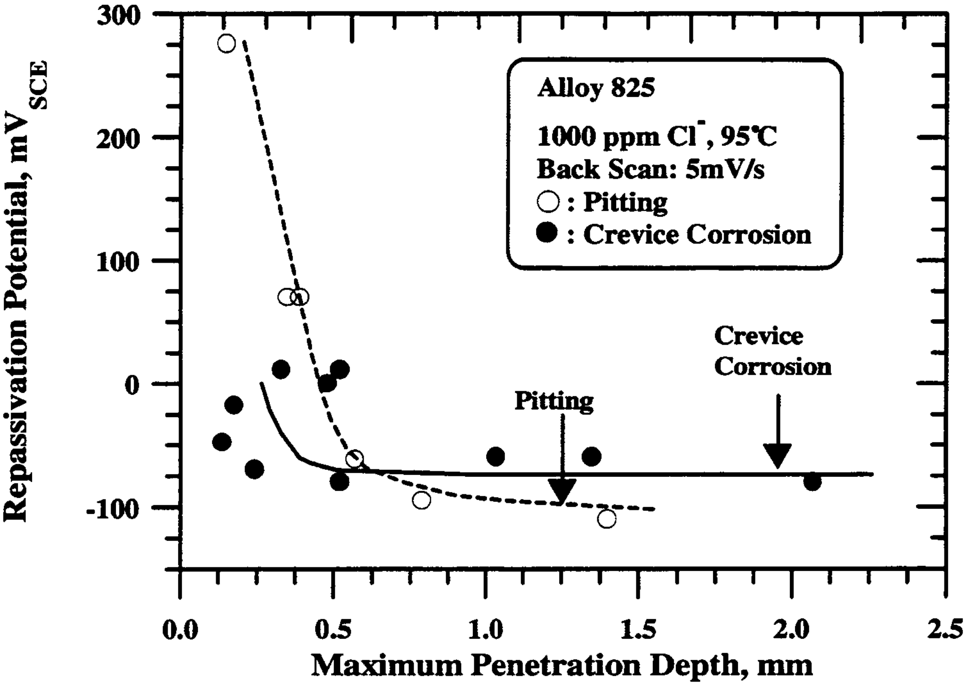

Figure 3-10. Effect of maximum penetration depth on the repassivation potential for pitting and crevice corrosion

The repassivation time and the localized corrosion initiation time are plotted in Figure 3-11 as functions of applied potential. The repassivation time for pits was observed to be dependent on both the depth of the pit and the applied potential. For pits less than 0.6 mm deep, shown as the dark circles in this figure, the repassivation time increased rapidly above an applied potential of 170 mV_{SCE}. At lower potentials the repassivation time was observed to be less than 500 s and was relatively independent of potential. For pits deeper than 0.8 mm, represented by the open circles, the repassivation time increased above applied potentials of 20 mV_{SCE}. The horizontal arrows attached to the open circles in Figure 3-11 indicate that the experiments were terminated before repassivation occurred. Below 20 mV_{SCE}, the repassivation time was in the range of 500–2,000 s and was relatively independent of potential. If repassivation is assumed to be related to the outward diffusion of Cl^-, then the repassivation time, t_r, in the potential independent region should be (Strehblow, 1984):

$$t_r = \frac{r^2}{2D} \tag{3-6}$$

where r is the pit radius and D is the diffusivity of chloride ion. Assuming hemispherical pits, the repassivation time for pits 0.6 mm deep should be 360 s, if r is the pit depth and D is 5×10^{-6} cm^2/s. The difference between the calculated and measured values may be related to a diffusion boundary layer at the mouth of the pit increasing the effective pit radius (Strehblow, 1984).

The results of long-term potentiostatic tests have shown that localized corrosion did not occur at 0 mV_{SCE} (a potential 100 mV lower than the E_{rp} measured in CPP tests) over a cumulative test time of 18 months. The plot of current density versus time for this test, presented as Figure 3-12, shows that occasional brief current spikes occurred immediately after the start of each new test period. The current density then rapidly decreased to a value of less than 1 $\mu A/cm^2$ for the remainder of the test segment. The weight of the sample during 18 months of testing did not change and there was no visible indication of localized corrosion. In contrast, crevice corrosion at the specimen-PTFE gasket interface was observed on the specimen held at 100 mV above the E_{rp} after 6 months of testing. The onset of crevice corrosion was indicated by a prolonged average current density greater than 10^{-5} A/cm^2, as shown in Figure 3-13. However, the actual current density of the corroding region was in the range of 10^{-3} A/cm^2 because the crevice corrosion only occurred on an area of less than 0.3 cm^2, and the current density displayed in Figure 3-13 was calculated using the total specimen surface area of 15 cm^2. The total charge accumulated in the last test segment was 105 coulombs and the maximum depth of crevice corrosion was measured to be 700 μm. This compares well to the calculated penetration depth of 590 μm using Eq. (3-5) and an area of 0.3 cm^2. Significant weight loss was also observed at the conclusion of the last 28-day testing period, as shown in Figure 3-13.

The initiation time for localized corrosion was very short at high potentials (Figure 3-11). A significant increase in the initiation time was observed at lower potentials. No pitting corrosion was observed at potentials of 500 mV_{SCE} or less even after testing for more than 2×10^5 s or 2.3 d. In contrast, crevice corrosion was observed at potentials as low as 200 mV_{SCE} when test times were increased to 10^7 s or 115 days. Taken together, the results plotted here indicate that the difference between the initiation potentials for pitting and crevice corrosion (E_p and E_{rcrev}) and the repassivation potentials (E_{rp} and E_{rcrev}) decreased as time increased. Similar results were reported by Thompson and Syrett (1992) who postulated that there is a unique potential, E_u, defined as the point where initiation potential for localized corrosion is identical to the repassivation potential. At potentials above the E_u, the material is prone to pitting or

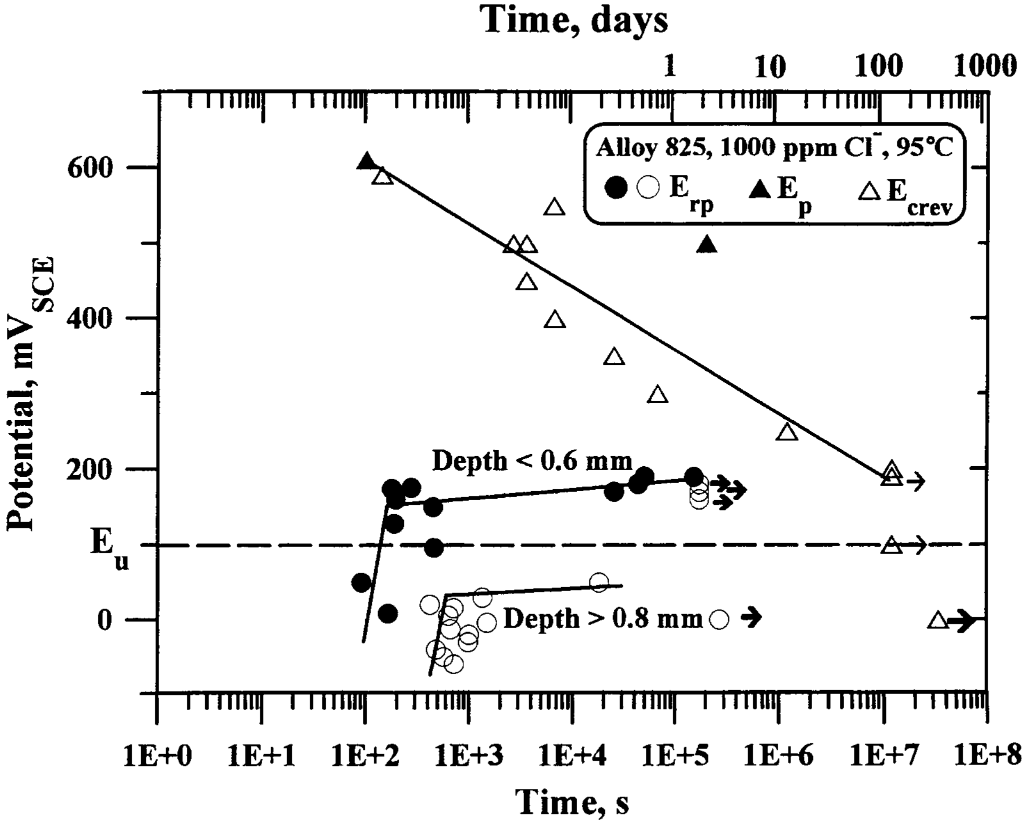

Figure 3-11. Effect of applied potential on the initiation and repassivation of localized corrosion. E_u: unique potential.

crevice corrosion. Below the E_u, the material is immune from localized attack. However, the present results differ in the method used to arrive at the "unique potential" from that of Thompson and Syrett (1992). They plotted the repassivation potential (protection potential) as a function of the time for pit growth (controlled by scan rate) and the initiation potential as a function of exposure time at any potential. In the present paper, both initiation and repassivation potentials are plotted as functions of exposure time. As pointed out later, this can lead to differences in the interpretation of the unique potential.

3.3.2.2 Effects of Surface Finish and Cold Work

The CPP scan of polished alloy 825 specimen showed that the E_p was 690 mV_{SCE} and E_{rp} was 160 mV_{SCE}. A significant hysteresis indicative of pitting corrosion was observed. Post-test examination with a 70x stereoscope confirmed the presence of pits. In contrast, the CPP scan for the mill-finished specimen had a E_p of 20 mV_{SCE} and a E_{rp} of −250 mV_{SCE}, significantly more active than the polished, bulk composition specimen. However, very little hysteresis was observed for the mill-finished specimen, and the post-test examination did not reveal any pits. Multiple CPP scans were conducted successively on a single specimen having a mill-finish surface, with fresh solution being used for each scan. Once again, very low E_p and E_{rp} values were obtained in the first and second scans of Cr-depleted surfaces, but only uniform corrosion was observed. Subsequent scans, however, exhibited large hysteresis, indicating

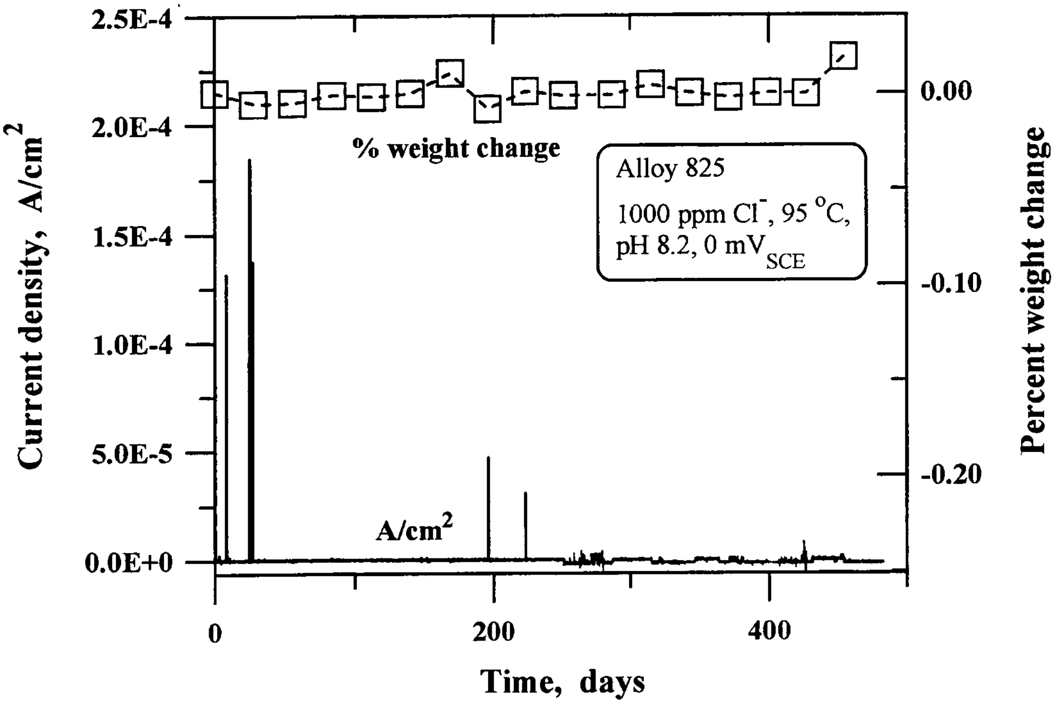

Figure 3-12. Current density and percent weight change during potentiostatic testing at 0 mV$_{SCE}$ in 1,000 ppm Cl$^-$, pH 8.2, at 95 °C (28-day test intervals)

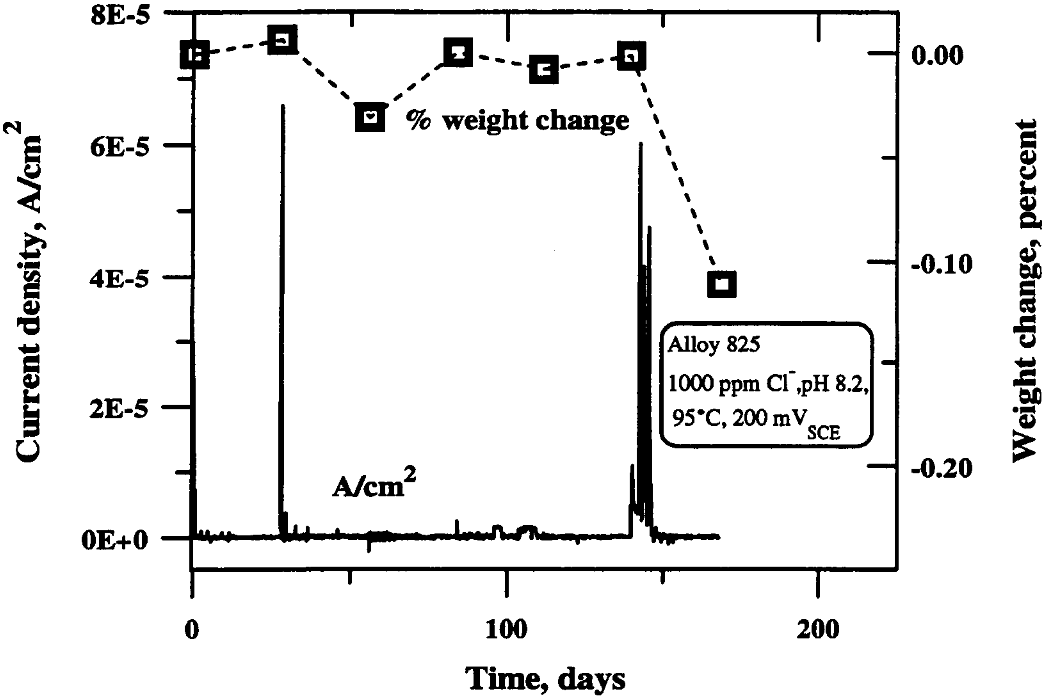

Figure 3-13. Current density and percent weight change during potentiostatic testing at 200 mV$_{SCE}$ in 1,000 ppm Cl$^-$, pH 8.2, at 95 °C (28-day test intervals)

the occurrence of localized corrosion. Examination of the specimens using a 70× stereoscope revealed that the mill-finished surface pitted after 3 or 4 scans. On the other hand, the adjacent surfaces, which attained the bulk composition through polishing to either a 60- or 600-grit finish did not show any evidence of pitting.

For the mill-finished surfaces, the E_{rp} was found to increase with cumulative charge density, or total amount of charge passed per unit area, contrary to previous results obtained for polished specimens. Analyses of the mill-finished specimens using SEM-EDS revealed that the Cr content at the surface increases with the amount of charge passed. Figure 3-14 plots the results of the CPP tests in terms of E_p and E_{rp} as a function of the Cr content measured on nonpitted regions at the conclusion of successive scans. This figure was generated using the results of both mill-finished surfaces having less than the bulk concentration of Cr and polished specimens having 22 percent Cr. The observed variation of E_p and E_{rp} for the polished surfaces in three tests was approximately 50 mV. Larger variations, observed with the mill-finished specimens are, most likely, the result of fluctuations in the surface composition and surface roughness of the Cr-depleted layer. However, it is evident from this plot that E_p and E_{rp} are strongly dependent on the concentration of Cr at the surface. Below a surface Cr concentration of 17 percent, uniform corrosion predominated. Localized corrosion occurred at surface Cr concentrations higher than 17 percent. Pitting of the Cr-depleted surfaces was initiated at potentials as low as 220 mV_{SCE}. In addition, the E_{rp} of these surfaces, following the initiation of pitting, was found to be much more active than that of the bulk material.

The results of potentiostatic tests on mill-finished specimens of alloy 825 are shown in Figures 3-15 and 3-16. Pits were initiated on specimens polished to a 600-grit finish at a potential of 600 mV_{SCE}. Below this potential, the alloy corrodes at a very low rate corresponding to the passive current density. This is shown in Figure 3-15 for the 600-grit specimen held at 500 mV_{SCE}. The absolute value of current density is plotted because at low current densities observed on this specimen there are brief bursts of cathodic current. In contrast, the mill-finished surface with a lower Cr content exhibits a very high corrosion rate at 450 mV_{SCE}. Post-test examination of the specimen revealed the presence of deep pits on the mill-finished surfaces. Adjacent surfaces polished to a 600-grit finish showed no indication of pitting. Figure 3-16 shows the results of additional potentiostatic tests on mill-finished specimens. These results indicate that pitting of the Cr-depleted surface is easily possible at potentials greater than 300 mV_{SCE}. Pits only occurred on the mill-finished surfaces, and no preferential attack at the solution/vapor interface was observed. At 275 mV_{SCE}, the specimen initially exhibited a high current density which then decreased to a value corresponding to the passive current density. Post-test examination of this specimen did not reveal any indication of pitting. The near-surface Cr concentrations measured by SEM-EDS for unpitted specimens, potentiostatically polarized at potentials of 200 to 275 mV_{SCE}, showed that the concentration of Cr tends to increase from 15.6 to 16.5 percent with applied potential. Analysis of the specimen held at 300 mV_{SCE} in a region where pits were not present indicated the Cr concentration was 17 percent. Specimens polarized at higher potentials had a Cr of concentration of 15 percent at the surface, indicating the degree of uniform corrosion was low and that localized attack was quickly initiated leaving some areas of the original surface free from corrosion (Dunn et al., 1995b).

Since the mill-finished surfaces were also rougher, potentiostatic tests were carried out on specimens having the same surface roughness as the mill-finished specimens (about 36-grit) but without the Cr-depleted surface layer. These experiments indicated that at 500 mV_{SCE}, pits were initiated, but a longer initiation time, compared to the mill-finished surfaces, was observed (Dunn et al., 1995b). The

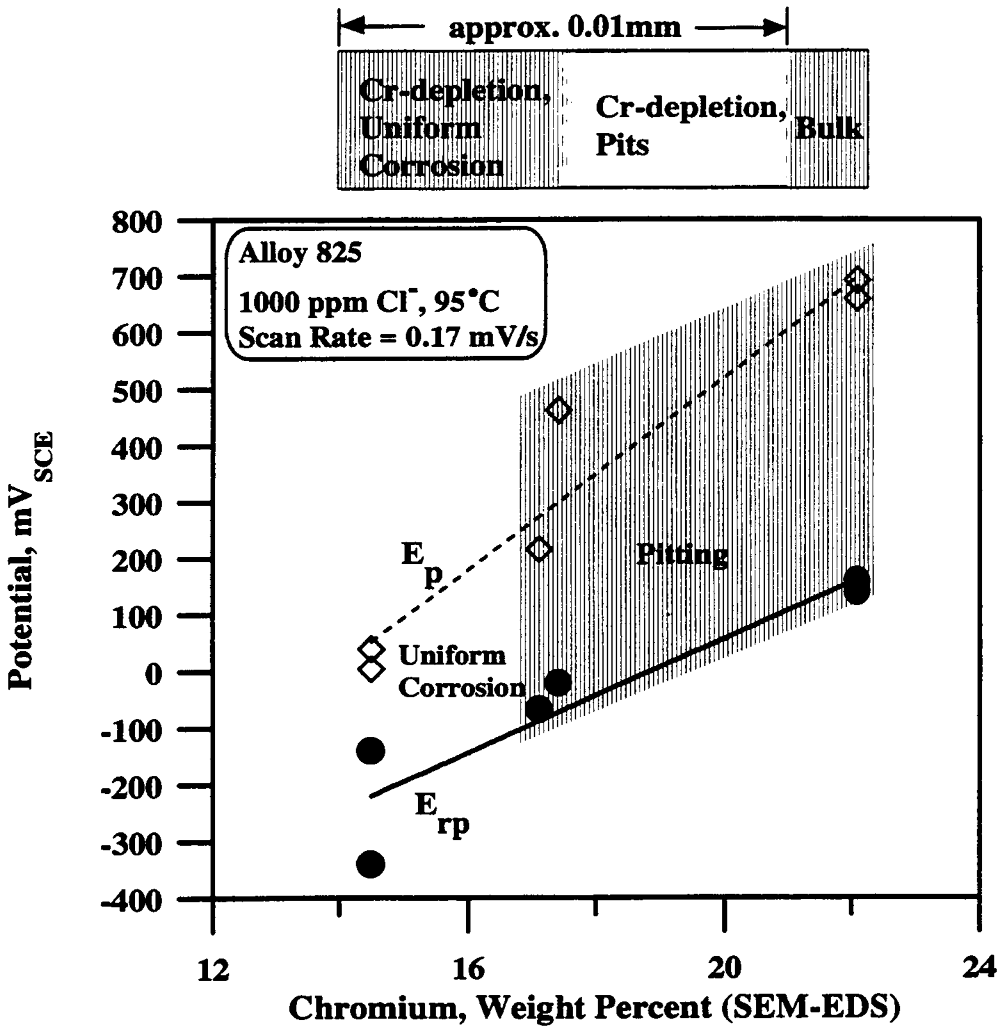

Figure 3-14. Breakdown and repassivation potential versus surface chromium concentration after cyclic potentiodynamic polarization tests

specimen held at 300 mV$_{SCE}$ exhibited a passive current density throughout the duration of the test, and no pits were observed during subsequent examination.

The effect of surface finish and cold work on the E_p and the E_{rp}, obtained by CPP tests, can be seen in Figure 3-17. The E_p is nearly independent of the amount of cold work. The variation in the E_p observed for the 600-grit finish specimens was typical of the variation observed for identically prepared specimens of alloy 825 that were tested in this solution. Increasing the surface roughness decreased the E_p by more than 100 mV. In contrast, the E_{rp} was found to be practically independent of the surface finish and the degree of cold work.

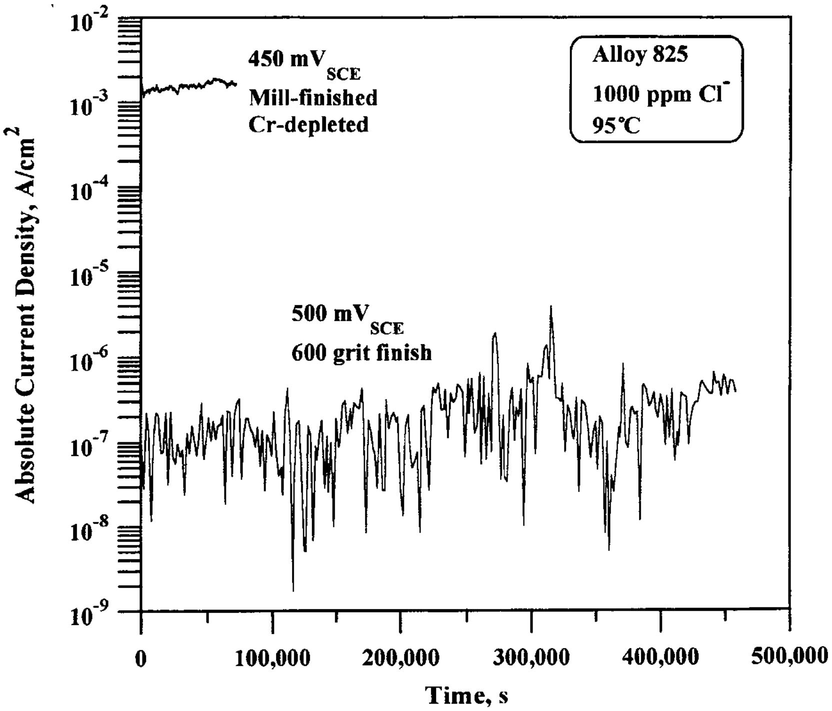

Figure 3-15. Potentiostatic test results on Cr-depleted, mill-finished, and polished (600-grit) alloy 825

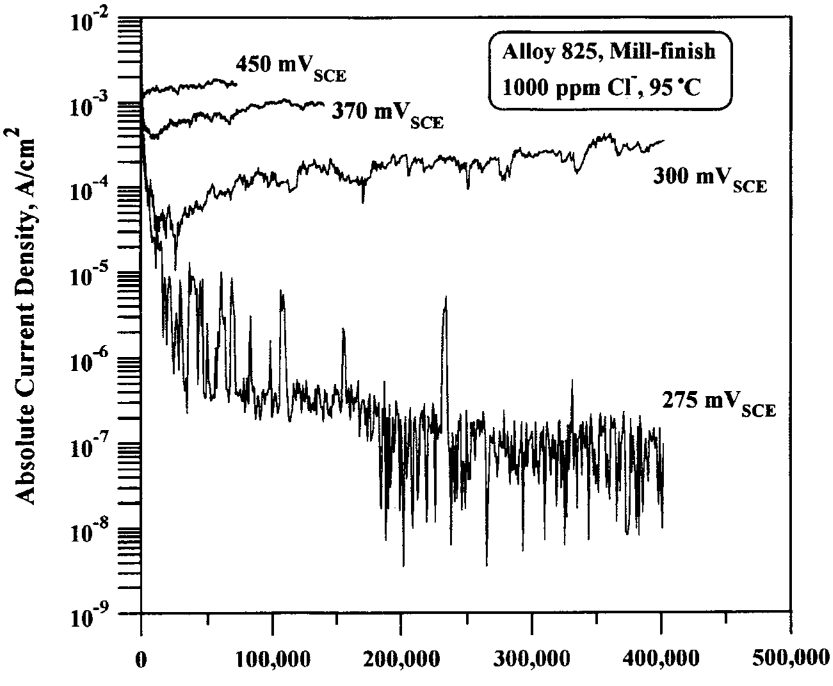

Figure 3-16. Results of potentiostatic tests at various applied potentials on mill-finished alloy 825

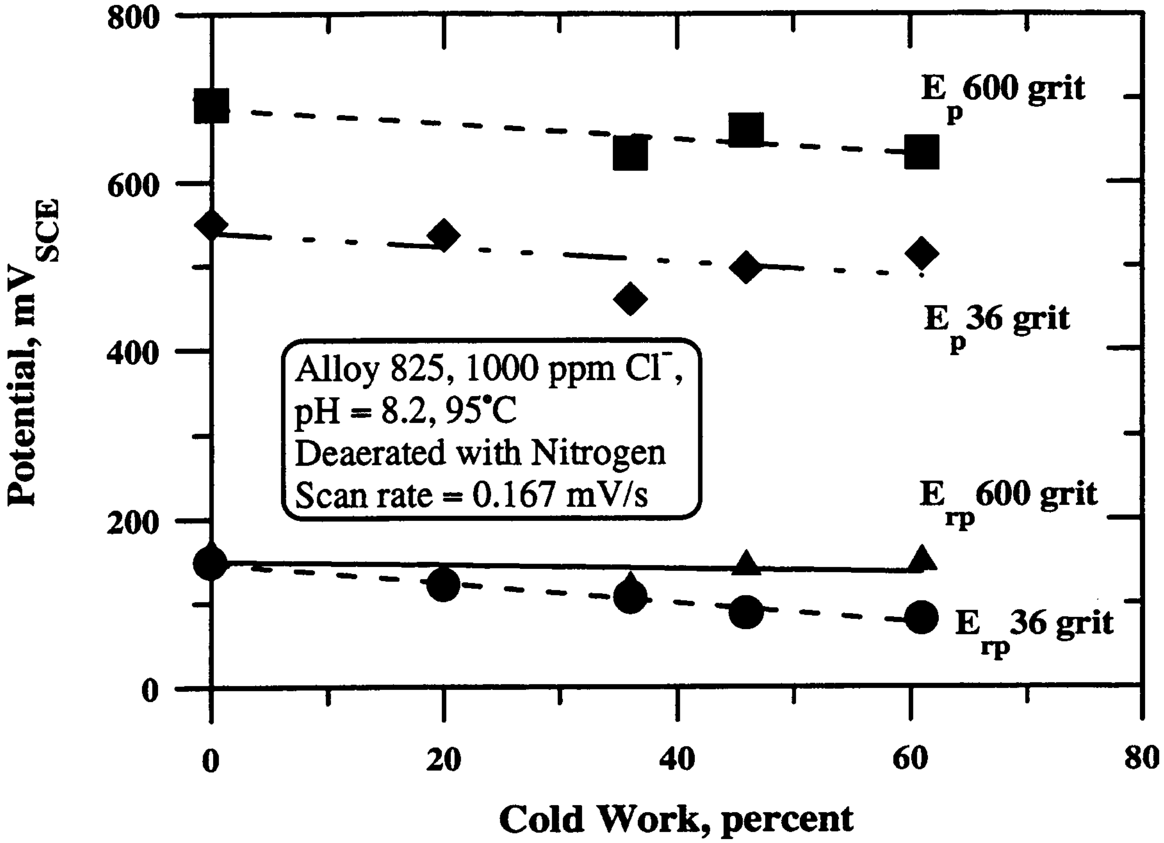

Figure 3-17. Effect of cold work and surface finish on the initiation and repassivation potentials for pitting corrosion of alloy 825

3.3.2.3 Effect of Alloying Elements—Behavior of Alloy C-22

The beneficial effects of Mo and W on the localized corrosion resistance of Ni-Fe-Cr alloys are well known (Szklarska-Smialowska, 1986). Hence, alloy C-22 is expected to be superior to alloy 825 in localized corrosion resistance. However, certain anomalies were observed for alloy C-22 in CPP tests. The results of the CPP tests for this alloy are detailed in Appendix Table C-9. Even in chloride solutions of low concentrations, alloy C-22 exhibits considerable hysteresis in the polarization curves. For example, as shown in Table C-9, in the nonchloride and the 6 ppm Cl$^-$ solutions, a difference of about 150 mV between the "breakdown" and "repassivation" potentials was observed. In these cases, the specimen was covered by a gold-colored film and dark spots appeared when the applied potential was raised to very high values (beyond 800 mV$_{SCE}$). These spots appeared to be shallow pits under the microscope, but were not always reproducible. When the chloride concentration was increased to 1,000 ppm, the spots appeared at high potentials, but faded eventually. These spots are generally not attacked regions, but islands of unattacked areas surrounded by areas of very light attack. At 10,000 ppm chloride, no pitting was observed and the specimen was covered by a uniform gold-colored film. Note that even in this solution significant hysteresis in the polarization curves was observed (Table C-11). These observations are similar to those reported by Lukezich (1989). He reported that the current in the 1,000 ppm Cl$^-$ solution did not increase or decrease when the potential was held constant above the breakdown potential. Decreasing the pH to 4 eliminated the hysteresis in the polarization curve (Lukezich, 1989); this was attributed to the increase in the equilibrium potential for the oxidation of Cr^{3+} to Cr^{6+} such that the oxygen reduction reaction became the predominant transpassive reaction. In the 1,000 ppm Cl^- solution, Lukezich (1989) observed pitting on alloy 825 and type 316L SS, which is consistent with the findings reported here.

When 0.01 M $S_2O_3^{2-}$ was added to the 1,000 ppm Cl^- solution, deep pits were observed on alloy C-22 in the CPP tests. However, the $\boldsymbol{E_{rp}}$ was quite high in these tests (689 mV_{SCE}). At higher chloride concentrations, addition of 0.01 M $S_2O_3^{2-}$ resulted in only very small pits that were difficult to see with a naked eye. The overall observation in the studies conducted on alloy C-22, albeit preliminary in nature, is that the CPP technique is not suitable for investigating the localized corrosion parameters of this alloy. Further studies are necessary, if this alloy becomes a major candidate in the waste package design.

3.3.3 Crevice Chemistry Experiments

3.3.3.1 Crevice Gap Measurements

Crevice gap is one of the more difficult parameters to characterize in a given service application as well as to control in an experiment. If the crevice is made tight in order to initiate crevice corrosion more easily, then the crevice gap is dependent on the surface finishes of the mating surfaces as well as on their hardness as the asperities in their surfaces are compressed together. If the crevice gap is increased, the surface asperities play a relatively minor role in defining the crevice gap. However, crevice initiation becomes difficult and corrosion may not initiate within an experimentally convenient time scale. In practice, many engineering components exhibit rather tight crevices. In the present case, the crevice was made tight by clamping two PMMA blocks on the specimen, but a reasonably low torque was used to minimize plastic flow of the PMMA surfaces. Profilometer traces of the PMMA surface before and after clamping did not reveal any significant difference. The surface profiles of the mating surfaces are discussed in greater detail elsewhere (Sridhar and Dunn, 1994). The crevice gap between the PMMA and 600-grit specimen surfaces was approximately 4 μm. In contrast, a 60-grit surface exhibited much deeper grooves and the gap between the PMMA surface and a 60-grit surface was about 17 μm. It must be emphasized that the above mentioned crevice gap values were the maximum values assuming that no grooves narrower in width than the stylus were present. Actually, the crevice gap assumes a range of values from extremely low values between peaks of the mating surface asperities to large values between peaks and valleys of mating asperities.

The surface roughness measurements can be represented by the mean of all peak to valley heights, R_zDIN, measured over a given length of traverse of the stylus or by the maximum of the various peak to valley heights, R_{max}DIN. These measurements are listed in Table 3-2 for various surfaces before and after corrosion tests. The values for standard blocks reflect those for triangular grooves (R_zDIN=4×R_a). It can be seen that the surface roughness becomes larger after crevice corrosion tests for the 600-grit surface. Visual observation of the corroded surface also indicated mostly uniform corrosion with some shallow pits. For the 60-grit surface, crevice corrosion did not produce a significant change in surface roughness. The roughness measurements on alloy 825 with various surface finishes indicated that beyond 400-grit, the peak to valley height did not decrease significantly. There were also considerable differences between surface roughness of the mill-finished surfaces. It is possible that the rougher surface of the 12.5 mm plate reflects the effects of grit blasting after annealing and before descaling.

Table 3-2. Surface roughness measurements on specimens before and after tests

Specimen Description	Uncorroded Area		Crevice Corroded Area	
	R_zDIN µm	R_{max}DIN µm	R_zDIN µm	R_{max}DIN µm
Type 304L, 60-Grit Finish, Transverse scan	8.3	12.7	10.4	13.2
Type 304L, 600-Grit Finish, Transverse Scan	1.1	1.4	5.4,8.1,6.0	14.8,21, 11.1
Alloy 825, 600-Grit Finish, Transverse Scan	1.6,1.6	2.0,2.1	15.8*	35.6*
Alloy 825, 36 Grit, Transverse Scan	41.5	46.7	—	—
Alloy 825, 60 Grit, Transverse Scan	9.3	10.9	—	—
Alloy 825, 120 Grit, Transverse Scan	4.9	6.8	—	—
Alloy 825, 320 Grit, Transverse Scan	1.8	2.3	—	—
Alloy 825, 400 Grit, Transverse Scan	1.8	2.4	—	—
Alloy 825 Mill Finish, 3 mm Sheet	10.7	13.0	15.0	16.3
Alloy 825 Mill Finish, 12.5 mm Plate	34.9	48.9	—	—
Plexiglas, Crevice Block	4.0	4.4	—	—
0.35 micron R_a Reference Block	1.4	1.4	—	—
6.07 micron R_a Reference Block	24.3	24.5	—	—

R_a = Average peak height from centerline
R_zDIN = Average peak-valley height
R_{max}DIN = Maximum peak-valley height
* = Includes corroded and uncorroded areas

3.3.3.2 Crevice Chemistry in Type 304L Stainless Steel

Based on the CPP tests, the applied potentials for the crevice chemistry experiments were chosen to be below the breakdown potential (about 0.5 V_{SHE}), but above the repassivation potential, (about 0.2 V_{SHE}) in 1,000 ppm Cl^- solution at room temperature. In the first series of crevice chemistry experiments, the applied external potential was increased in steps. The results of this trial are shown in Figure 3-18. There was an initial increase in crevice pH, probably attributable to oxygen reduction inside the crevice. This was followed by a decrease in pH from 8.5 to a constant pH value of about 7. The potential drop in the crevice attained a relatively constant value of about 50 mV. The crevice current density was about 10^{-7} A/cm^2 which is just above the resolution limit of the data acquisition system. When the external potential was raised to 0.4 V_{SHE}, there was an immediate increase in current density which underwent a series of repassivation steps before increasing to a stable high value. A marked change in pH and chloride concentration occurred after a certain time interval following the current increase (Figure 3-18). Simultaneously with the change in pH, there was a decrease in potential at the tip (deepest part of the crevice) and the mouth, the latter being intermediate between the tip and the external potentials. Surprisingly, while the potential and chloride electrodes indicated a difference between the tip and mouth, the pH electrodes did not. Immediately following a decrease in external potential the crevice repassivated (low current density). The potential difference between the tip and the external reference electrodes decreased again to 50 mV. However, there was no immediate change in pH and chloride concentration. The corrosion inside the crevice was uniform when observed at 70x.

In two subsequent series of tests on 600-grit polished specimens, the potential was raised to 0.3 V_{SHE} after 1 hr at the open-circuit potential and maintained at that value throughout most of the test. As shown in Figure 3-19, after an initial increase, the current decreased to a low value, followed by two more irregular cycles of increase and decrease in current density. There was a small lag in the decrease in pH at the tip of the crevice, but the tip pH eventually decreased to about 4. The tip potential decreased along with the pH, while the chloride increased. This was quite reproducible. As before, the fall and rise in pH follows with a slight lag the rise and fall of current density. It can also be seen that, once a stable crevice corrosion growth is established at 0.4 V_{SHE}, the pH does not rise as fast upon reduction in current density. Post-test examination indicated that the corrosion was greater at the tip and was essentially uniform.

The results from a test on a 60-grit finish specimen are compared to those from a 600-grit polished specimen in Figure 3-20. A salient feature of these results is that a much longer time period was needed for initiating crevice corrosion. This is also revealed in the much longer time for the decrease in pH and potential inside the crevice for the 60-grit specimen. Secondly, the final pH in the crevice was not as low as that for the 600-grit polished specimen. A slightly smaller potential drop was also observed. These observations are consistent with predictions of crevice chemistry change models and can be explained by the greater volume of solution in the crevice of the 60-grit finish specimen. Post-test examination indicated that the corrosion occurred midway between the tip and mouth electrodes and was essentially uniform. One deep pit was noted in the crevice corroded area. As in the case of the 600-grit finish specimen, there was a time lag between the current increase and the pH decrease for the 60-grit specimen.

3.3.3.3 Crevice Chemistry in Alloy 825

The CPP curves for alloy 825 in 0.028 M (1,000 ppm) and 0.5 M (17,750 ppm) Cl^- solutions (containing other anionic species as reported in a previous section) indicated that, at room temperature,

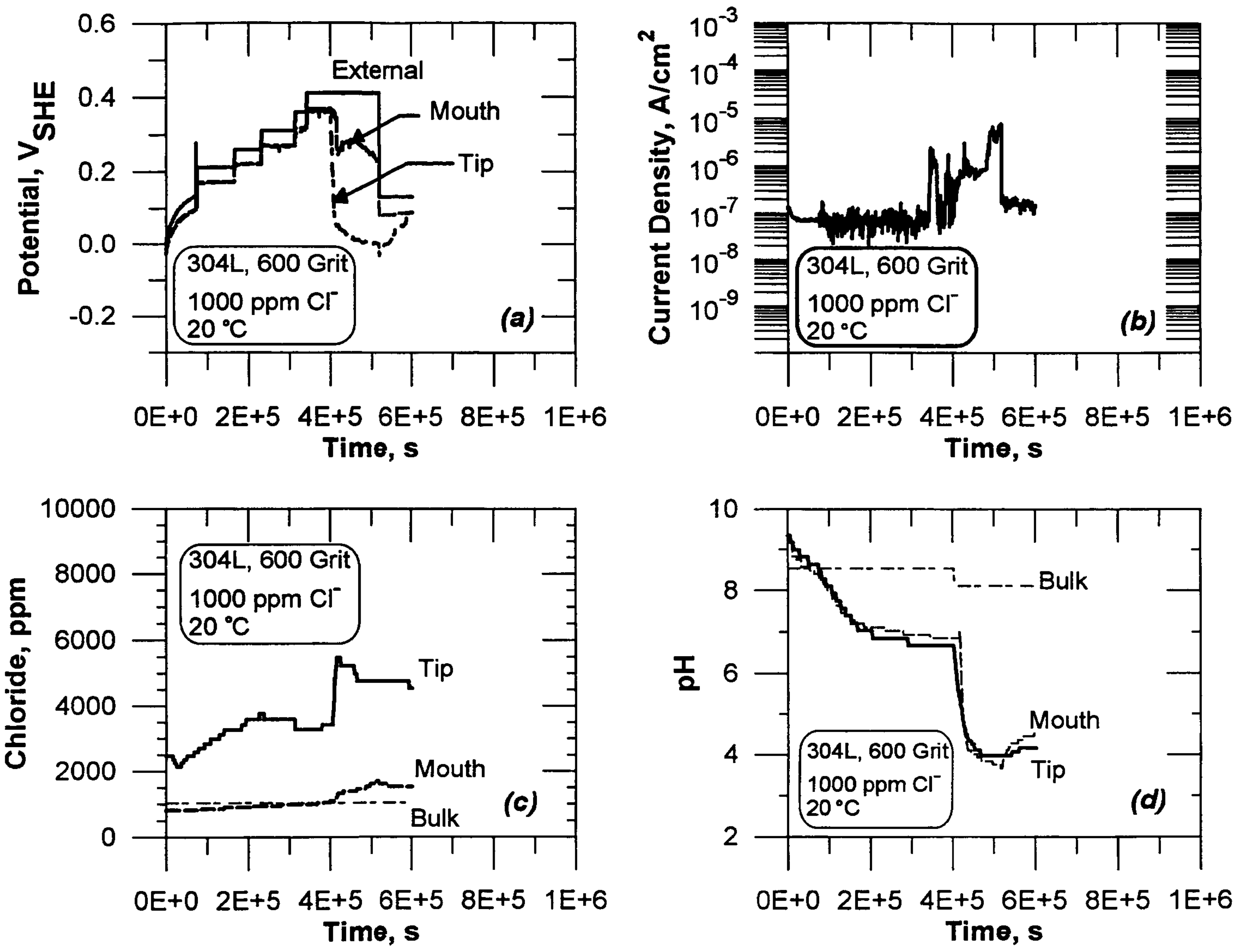

Figure 3-18. Changes in the current density, potential, pH, and Cl⁻ concentration inside a type 304L stainless steel (600-grit)-polymethyl methacrylate crevice in a 1,000 ppm Cl⁻ solution at room temperature

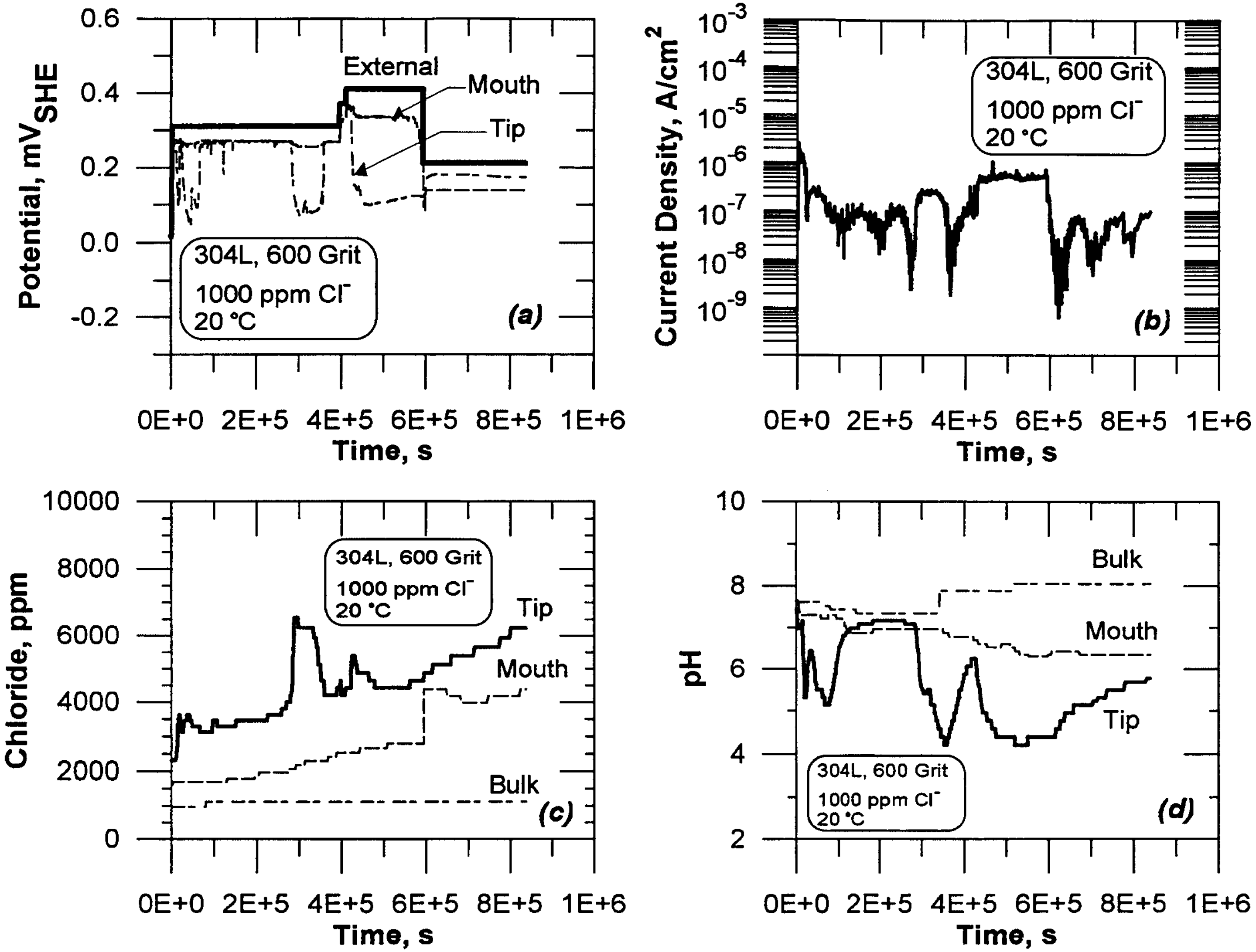

Figure 3-19. Same conditions as in previous figure, potential was held at 0.3 V$_{SHE}$ for a longer time

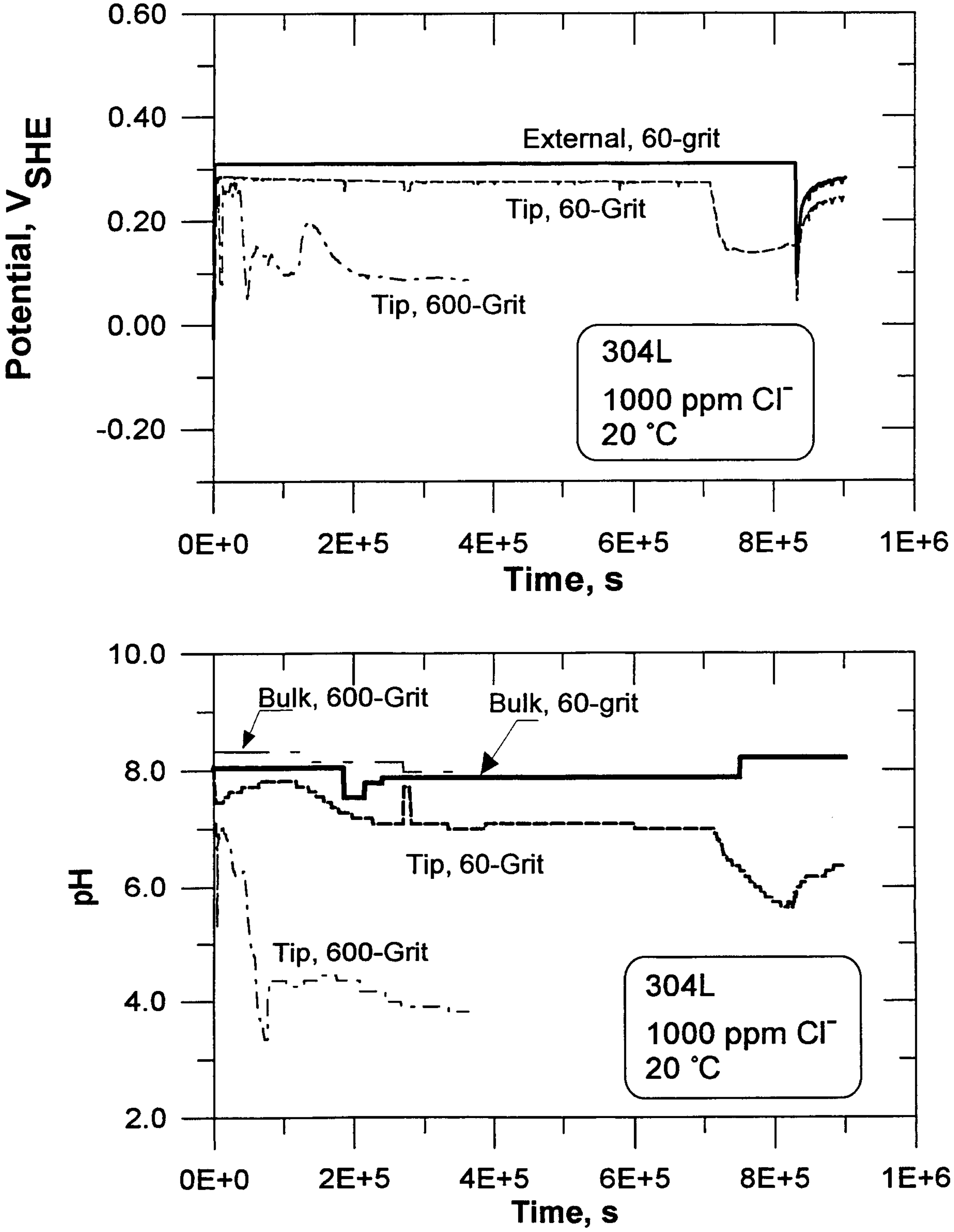

Figure 3-20. Changes in the potential and pH inside a type 304L stainless steel (600-grit)-polymethyl methacrylate crevice for two different surface roughness (crevice gap)

the breakdown potentials were quite high, 1.2 and 1.1 V_{SHE}, respectively. The repassivation potentials were 0.32 and 0.25 V_{SHE} respectively in the two solutions. Based on these experiments, applied potentials of 0.7 to 0.5 V_{SHE} were chosen so that pitting was not initiated on the open surface of the specimen.

The chemistry and potential changes in the crevice of a 600-grit polished alloy 825 specimen in 0.5 M Cl^- solution are shown in Figure 3-21. At an applied potential of 0.5 V_{SHE}, the crevice current density increased quite rapidly to high values. As in the case of type 304L SS, the pH and the potential decreased subsequent to an increase in the current density. The pH value at the tip was found to be higher than that at the mouth contrary to that observed in type 304L SS. The minimum pH values in the crevice were lower than those observed for type 304L SSs. The free-chloride in the crevice decreased below the bulk value. Post-test calibration did not reveal any changes in the electrodes.

The changes in the crevice conditions for an alloy 825-plexiglass crevice exposed to 1,000 ppm Cl^- solution are shown in Figure 3-22. Here, a high anodic potential was applied to induce crevice corrosion, although the potential was less than the pit initiation potential. Interestingly, the chloride concentration at the tip increased just as in the case of type 304L SS. The pH also decreased as in the previous experiment for alloy 825. The crevice repassivated spontaneously after about 5×10^5 (i.e., without any reduction of externally applied potential) as shown in Figure 3-22. While the crevice tip and the mouth potentials reverted back to the external potential values upon repassivation, the pH and the chloride concentrations did not return to the bulk values, with the exception of the chloride concentration at the mouth of the crevice. The corrosion potential increased to high values after the applied potential was switched off.

The effect of a mill-finished surface on crevice corrosion is shown in Figure 3-23. The changes in pH and potential of the mill-finished specimen were essentially the same as those in the 600-grit finished specimen. However, the decrease in pH and potential occurred more rapidly. The surface roughness of the mill-finished alloy 825 specimen was coarser than a 600-grit finished surface (Table 3-2), so the accelerated change in potential and pH was more significant than it appears from Figure 3-23. Post-test SEM-EDS analysis of the crevice corroded area indicated a Cr content of 21 percent. In contrast, the Cr content of the mill-finished surface was 18 percent. This indicates that the crevice corrosion depth exceeded the Cr-depleted layer thickness. For the mill-finished specimen, no change in chloride concentration in the crevice with respect to the bulk concentration was observed for the 0.5 M Cl^- solution.

The crevice corroded areas were examined under a stereoscope and SEM. The crevice corroded areas were generally smaller in extent for type 304L SS than for alloy 825. However, this observation does not indicate their relative corrosion resistance since they were tested under different conditions to produce active crevice corrosion. Inside the crevice-corroded areas, the surfaces were largely uniformly corroded. However, isolated, shallow pits were also seen in some of the crevice specimens. In most cases, crevice corrosion was not observed on the bottom surface of the specimens. No localized corrosion was observed on the open portion of the specimens.

3.3.3.4 Control Tests

In order to verify that the electrodes were responding only to changes in chemistry and that the lag time was not related to the response time of the electrodes, control tests were conducted. In these tests, a crevice was formed between PMMA and alloy 825 surfaces in a 1,000 ppm Cl^- solution at the open-circuit potential thus avoiding initiation of crevice corrosion. The potential monitored inside the crevice

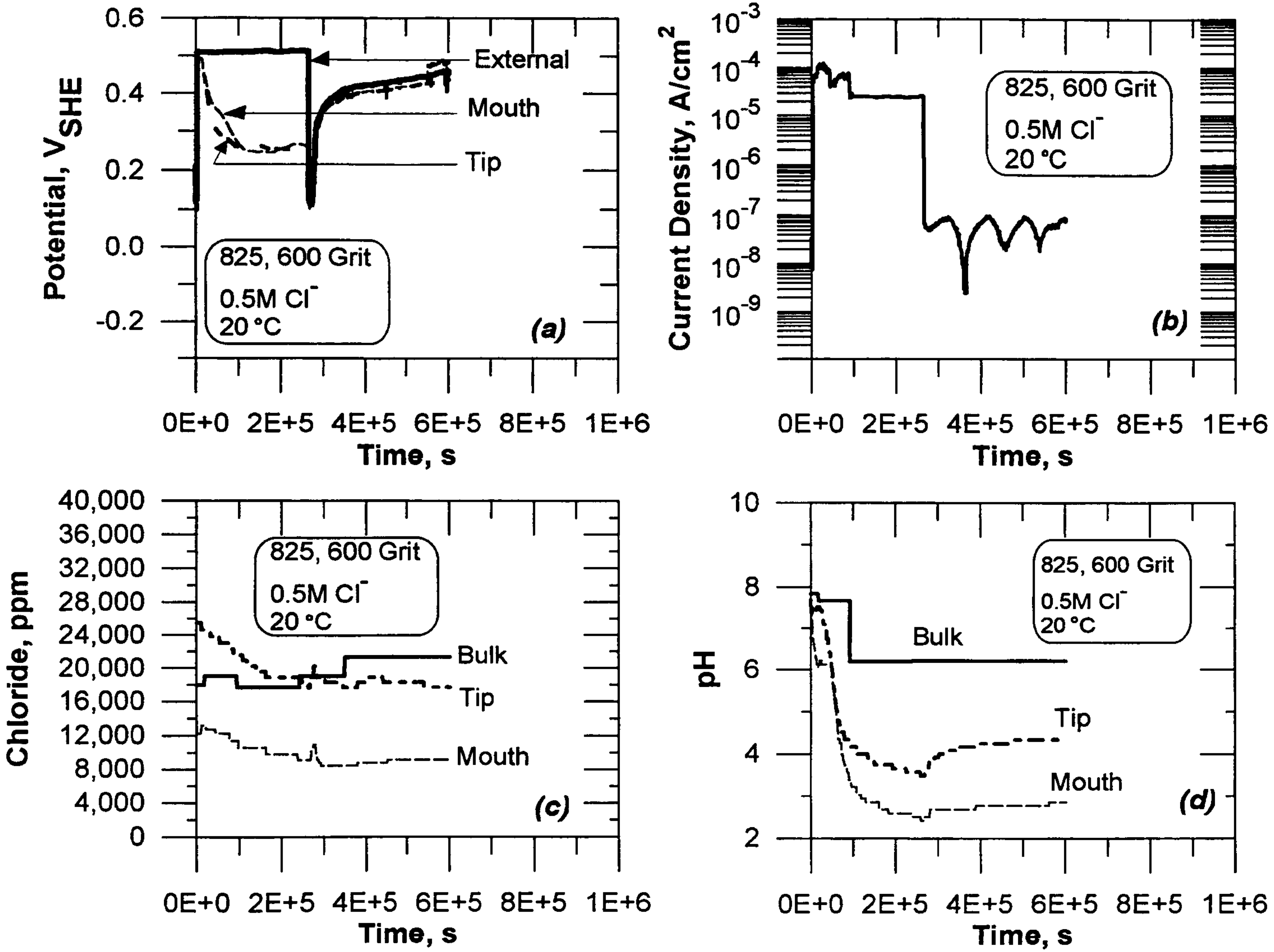

Figure 3-21. Changes in the current density, potential, pH, and Cl$^-$ concentration inside an alloy 825 specimen (600-grit)-polymethyl methacrylate crevice in a 0.5 M Cl$^-$ solution at room temperature

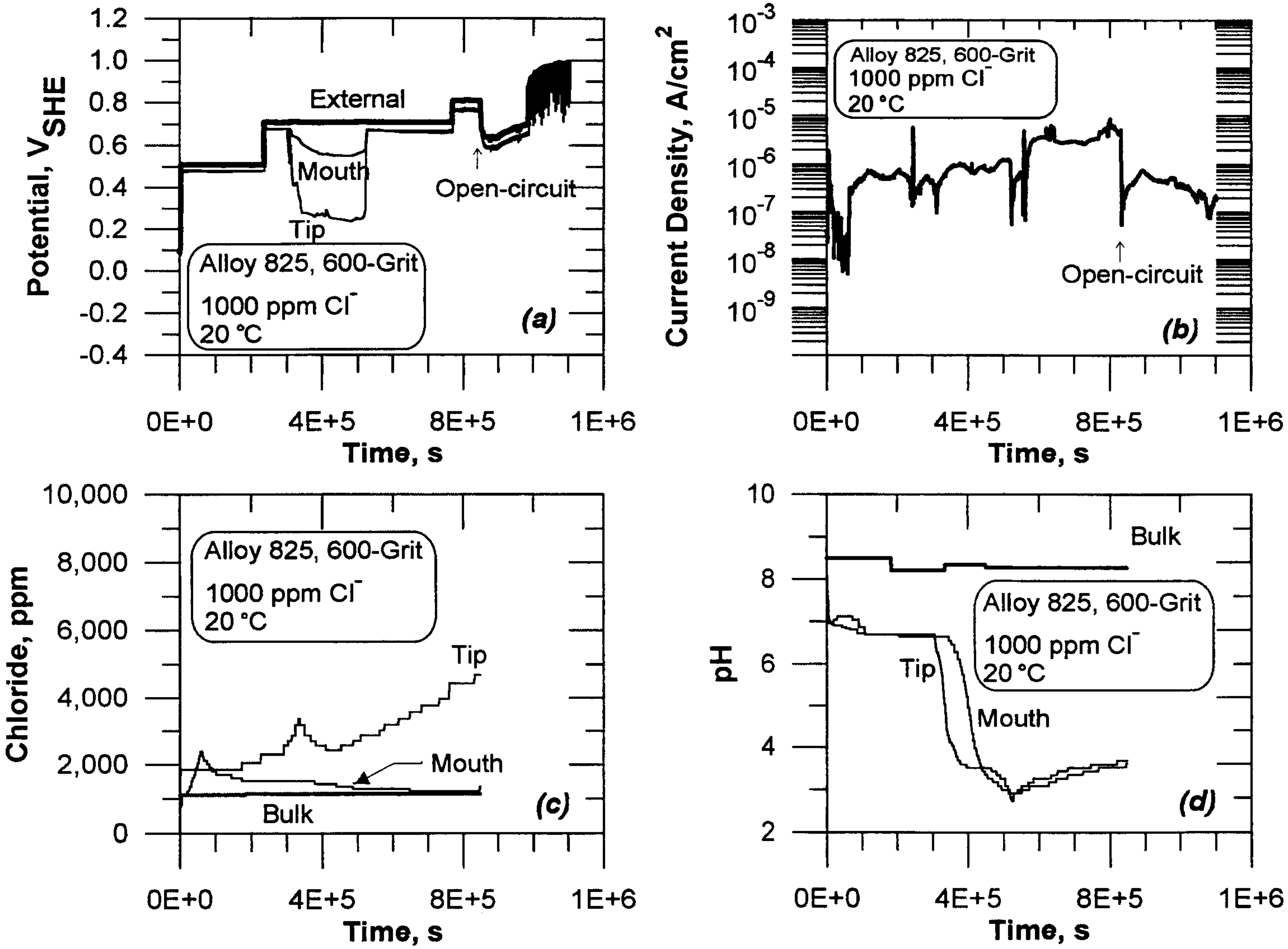

Figure 3-22. Changes in the current density, potential, pH, and Cl$^-$ concentration inside an alloy 825 specimen (600-grit)-polymethyl methacrylate crevice in a 1,000 ppm Cl$^-$ solution at room temperature

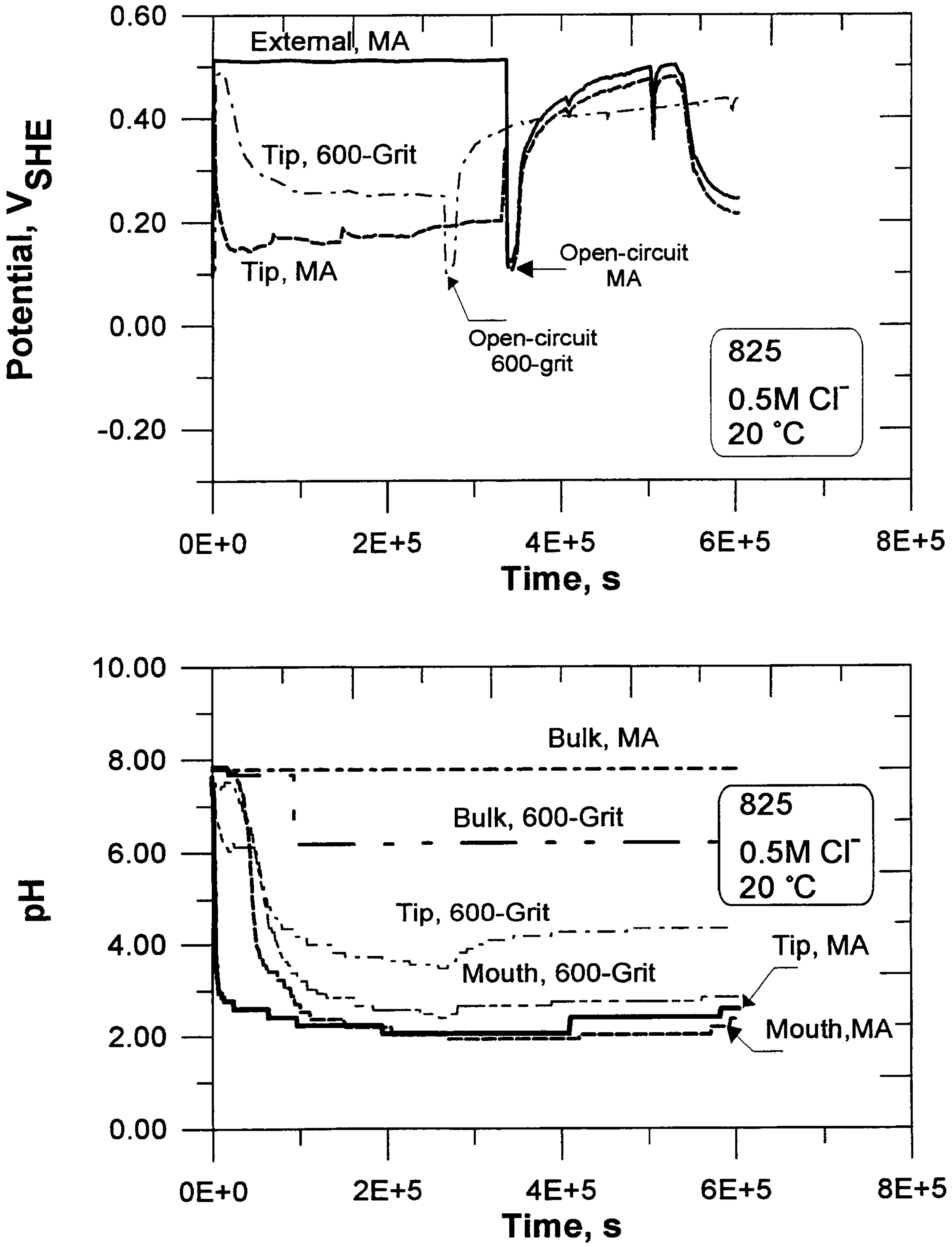

Figure 3-23. Effect of surface Cr depletion on the changes in crevice chemistry of alloy 825 in a 0.5 M Cl^- solution at room temperature. Constant external potential of 0.5 V_{SHE}.

did not indicate any active shift confirming that no crevice corrosion was initiated. Changes in bulk pH were made by the addition of HNO_3, while maintaining the bulk chloride concentration constant. The bulk pH and crevice pH were monitored. In another experiment, the bulk pH was held constant and the bulk chloride concentration increased by the addition of NaCl. When the bulk pH was changed from 8 to 2, the bulk pH electrode responded almost instantaneously to the addition of the acid, while the pH electrodes at the tip and mouth of the crevice indicated a decrease in pH to 2 after about 25,000 s. This is indicative of the transport of H^+ ions from the bulk into the crevice as shown in Figure 3-24. Surprisingly, both the mouth and tip electrodes indicated that the change in pH from 8 to 4 at these locations occurred at approximately the same rate, with further decrease occurring more slowly at the mouth electrode. The chloride electrode did not show any significant change when the pH was changed. When the bulk chloride concentration was changed, the bulk chloride electrode responded rapidly, while the tip and mouth electrodes showed a steady increase approaching steady state after about 500,000 s. The rate of increase of chloride in the crevice was much slower than that of the decrease of pH, due to the lower diffusion coefficient of Cl^- ions. The rate of increase in chloride concentration at the tip was faster than that at the mouth electrode.

3.3.3.5 Radial Crevice Experiments

Only a limited number of tests were conducted with the radial cell. Since the control tests of the rectangular crevice cell indicated that the crevice was not unidimensional, time dependent chemistry changes could not be measured as functions of crevice depth with this cell geometry. Control tests with the radial cell are shown in Figure 3-25. Here, the pH of the solution was acidified by the addition of HNO_3 and the pH at two locations inside the crevice was monitored with time. It is apparent that the change in bulk pH was detected by an electrode placed just outside the crevice shortly after the pH of the bulk solution was lowered. After a period of approximately 900 s, the pH at the mouth of the crevice started to decrease. A measured decrease in pH at the tip was not observed until 3,600 s after the bulk solution pH was altered. These results indicate that unlike the rectangular crevice, diffusion occurred from the mouth, or the very edge of the crevice, to the tip, which is located in the interior part of the crevice.

Results of crevice chemistry tests with type 304L SS in a 1,000 ppm Cl^- solution are shown in Figure 3-26. At the start of this test, the specimen is at open circuit and both the external potential and the tip potential gradually increase with time. The pH at the tip and the mouth decrease from approximately 8.0 at the start of the test to 6.0 while the specimen is at open circuit. Likewise, the chloride concentration was measured to vary between 1,000 and 5,000 ppm. After 150,000 s, a potential of 0.34 V_{SHE} was applied to the specimen. The current increased to 2×10^{-6} A/cm^2. However, no significant decrease in pH or increase in chloride was observed while the specimen was held at this potential. The difference between the external potential and the tip potential was only a few millivolts suggesting that crevice corrosion had not initiated. When the external potential was increased to 0.38 V_{SHE}, the current increased to a value of 1×10^{-5} A/cm^2 and, after a few hours, rapidly increased to $>4\times10^{-5}$ A/cm^2. A simultaneous decrease in the tip potential was observed when crevice corrosion was initiated. After a short delay, a rapid decrease in pH inside the crevice was observed. The decrease in pH was more rapid at the mouth than at the tip and the minimum pH was measured to be approximately 1.0. While no significant increase in the chloride concentration was observed at the mouth, the chloride concentration at the tip reached a maximum of over 20,000 ppm. Upon decreasing the potential, the current density decreased to below 1×10^{-5} A/cm^2, and a slight increase in the tip potential were observed. The pH inside the crevice increased to 3.0, and the chloride concentration at the tip decreased to approximately 10,000 ppm. Further decreases in the external applied potential resulted in only small chemistry changes inside the occluded region. No further increase in the tip potential, which remained

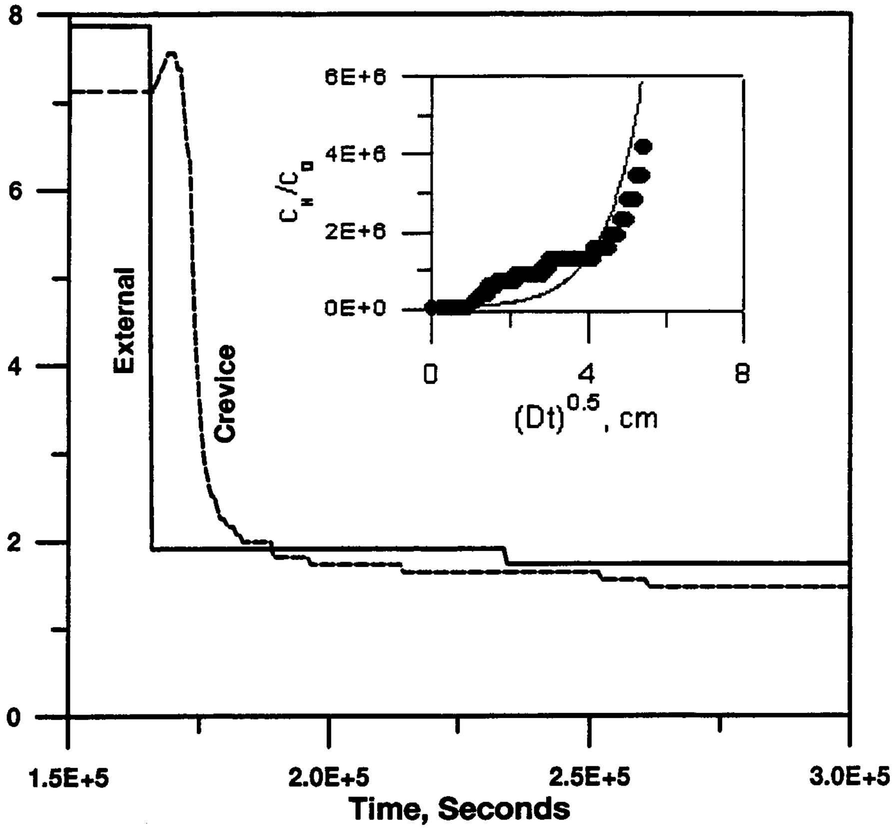

Figure 3-24. Changes in crevice pH as a result of external pH changes in a control experiment where no localized corrosion occurred. Alloy 825-polymethyl methacrylate crevice in 1,000 ppm Cl^- solution at the open-circuit potential. Inset shows the expanded plot of the increase in H^+ concentration upon the addition of HNO_3.

150 mV less than the external potential, was observed. At approximately 300,000 s into the test, the Cl^- ISE failed and subsequently, gave erroneous measurements. The failure of this electrode is not surprising since the AgCl layer on this ISE can be dissolved in acidic concentrated chloride solutions. In addition, the pH electrode at the tip location also failed because of the accumulation of corrosion products on the porous pH glass. A post-test check of all other electrodes verified their consistent performance throughout the duration of the test.

Type 316L SS was also tested using the radial crevice cell. The results of these tests were similar to those shown for type 304L with the radial crevice cell. When the external applied potential was increased sufficiently to initiate crevice corrosion, a rapid current increase and potential drop inside the crevice were observed. The minimum pH and maximum chloride concentrations during active crevice corrosion were similar to the measurements reported for type 304L. However, at the completion of some tests performed with type 316L, when the specimen potential was switched to open circuit, the E_{corr} increased in a similar manner reported for alloy 825.

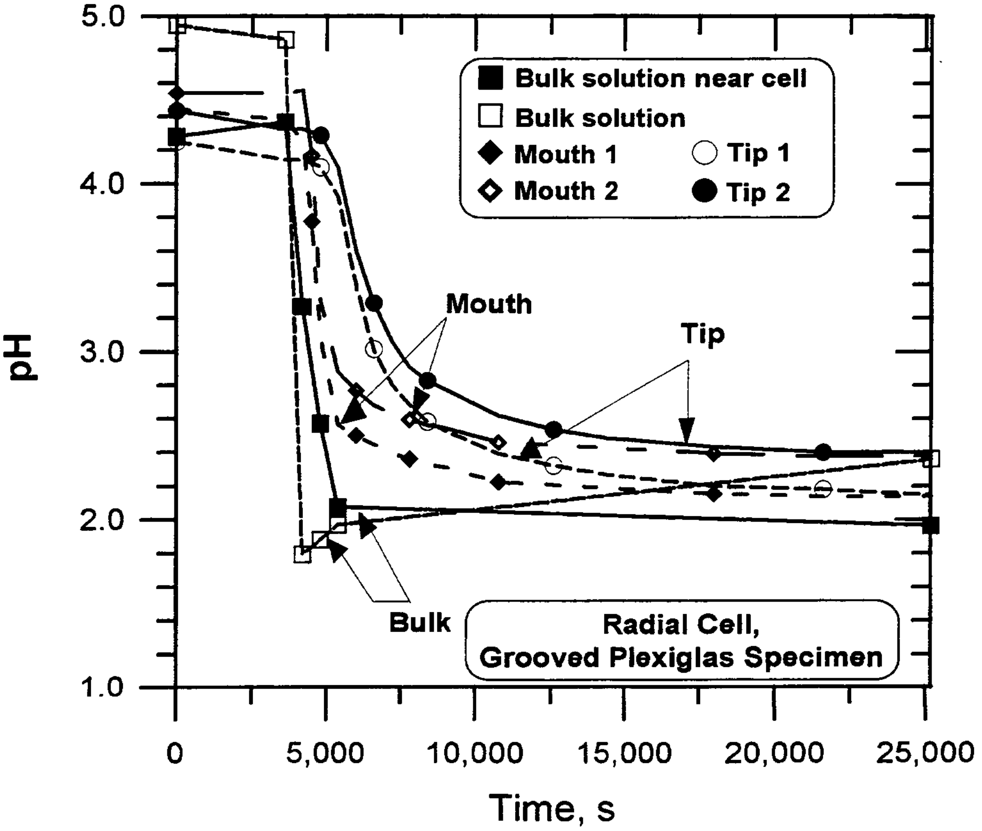

Figure 3-25. Changes in pH in a radially symmetrical crevice made of polymethyl methacrylate after adding nitric acid to a 1,000 ppm Cl^- solution

In both the rectangular and radial crevice experiments, metal-polymer crevices were examined. However, the phenomenology is not expected to differ in other crevice material combinations, such as metal–metal crevices.

3.3.3.6 Electrochemical Behavior in Simulated Pit Solutions

It is currently well established and confirmed by the results presented in previous sections, that solutions inside active pits or crevices of a variety of alloys are more acidic and high in anionic concentration than the bulk solution (Turnbull, 1983). There have also been many investigations of the electrochemical response of various alloys in simulated crevice/pit solutions (Crolet et al., 1976; Oldfield and Sutton, 1978b; Rosenfeld et al., 1978; Okayama et al., 1987b; Tsujikawa et al., 1987; Batista et al., 1988; Lott and Alkire, 1989a; Hakkarainen, 1990). However, most of these investigators have examined the electrochemical response using potentiodynamic, galvanostatic, and potentiostatic techniques, but not CPP tests. Using cyclic polarization tests, the repassivation behavior in simulated crevice solutions can be obtained. Additionally, the lack of a hysteresis loop is a good indicator of true depassivation.

For the tests in simulated crevice solutions, chloride concentrations ranging from 0.5 to 4 M were considered based on the predictions of various crevice corrosion models (e.g., Walton and Kalandros, 1992) and experimental measurements (e.g., Luo et al., 1992). The effect of sulfate was studied by varying

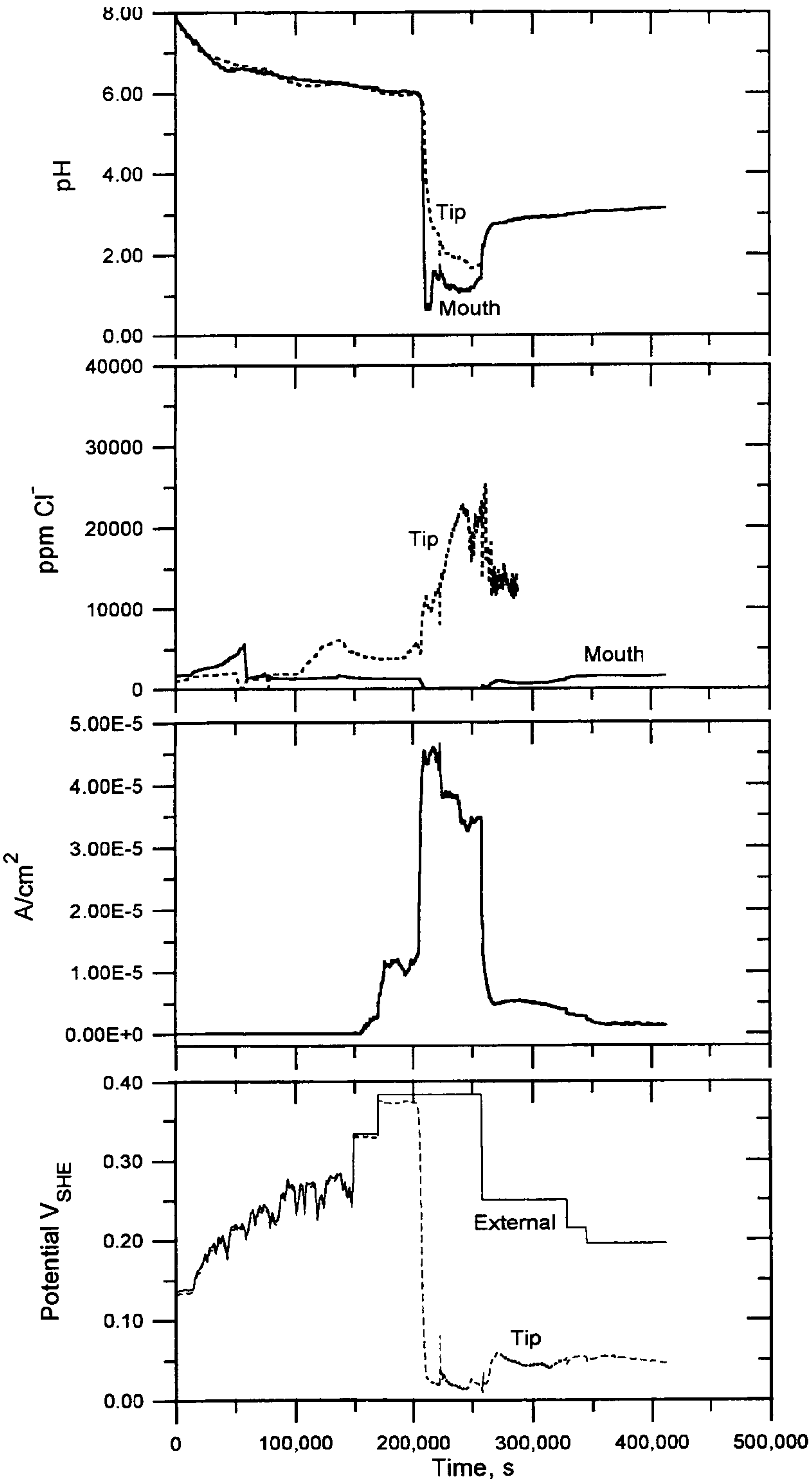

Figure 3-26. Changes in pH, chloride concentration, potential, and current density inside a radially symmetrical crevice cell of type 304L stainless steel in 1,000 ppm Cl$^-$ solution at room temperature

the sulfate and chloride concentrations such that the total ionic strength was approximately the same. All salts were added as sodium salts, although this does not simulate the pit solution completely (Hakkarainen, 1990). The near-neutral solutions contained bicarbonate to an initial concentration of 85 ppm. The pH of the solutions was adjusted by using HCl and, hence, the resultant concentration of chloride was higher depending on the pH. For the 4 M Cl^- solution with a pH of 0, the resulting concentration of Cl^- was 4.2 M. However, for the 0.5 M Cl^- solution, the addition of HCl to make the pH 0 resulted in a final Cl^- concentration of approximately 1.1 M. For future studies on the effect of pH at the low chloride concentrations, it should be convenient to use alternate techniques, such as the ion-exchange method used by Okayama et al. (1987b).

The results of these tests are shown in Tables C-6, C-10, and C-11 (Appendix C). Two examples of series of CPP curves for alloy 825 and type 304L SS are shown in Figures 3-27 and 3-28, respectively. There was no crevice corrosion observed on any of these specimens because they were partially immersed maintaining the metal–gasket crevice above the solution. As can be seen from Tables C-6 and C-10, the specimens exhibited passivity in solutions with pH below a certain value. In this regime of pH, ranging typically from 8 to 1, depending on the chloride concentration, the specimens pitted at potentials above a critical potential and the CPP curves exhibited significant hysteresis. Below a certain pH, which depended upon the alloy composition and to a lesser extent of the temperature, the alloys exhibited essentially an active behavior (Figures 3-27d and 3-28d). The pH at which a completely active behavior was observed is termed the depassivation pH, pH_D. Since the experiments were conducted at relatively large intervals of pH, no attempt is made to measure the pH_D exactly. The approximate range of pH_D values is summarized in Table 3-3.

Table 3-3. Depassivation pH of three alloys measured by cyclic potentiodynamic polarization technique in various simulated crevice solutions at two temperatures

Alloy	Temperature (°C)	pH_D		
		4 M Chloride	0.5 M Chloride	3 M Chloride + 0.25 M Sulfate
Alloy 825	30	$-0.4<pH<0.0$	—	—
	95	$0.1<pH<1.0$	$0.1<pH<1.0$	$0.0<pH<1.1$
Type 316L Stainless Steel	30	—	—	—
	95	$pH<1.1$	—	—
Type 304L Stainless Steel	30	$0.0<pH<1.1$	$0.1<pH<1.1$	—
	95	$1.3<pH<3.0$	$0.1<pH<1.1$	—

It must be emphasized that the pH values reported in Table 3-3 contain at least two sources of error: (i) they do not consider the liquid junction potentials arising between the reference electrode solution and the test solution that can be significant for concentrated solutions (Marcus, 1989), and (ii) they do not consider changes to the activity coefficient of chloride in highly concentrated solutions (Knauss et al., 1990). A third possible source of error, that of the pH measured with a glass electrode in highly acidic solutions, being higher than the actual pH, is not significant over the range of pH used in these

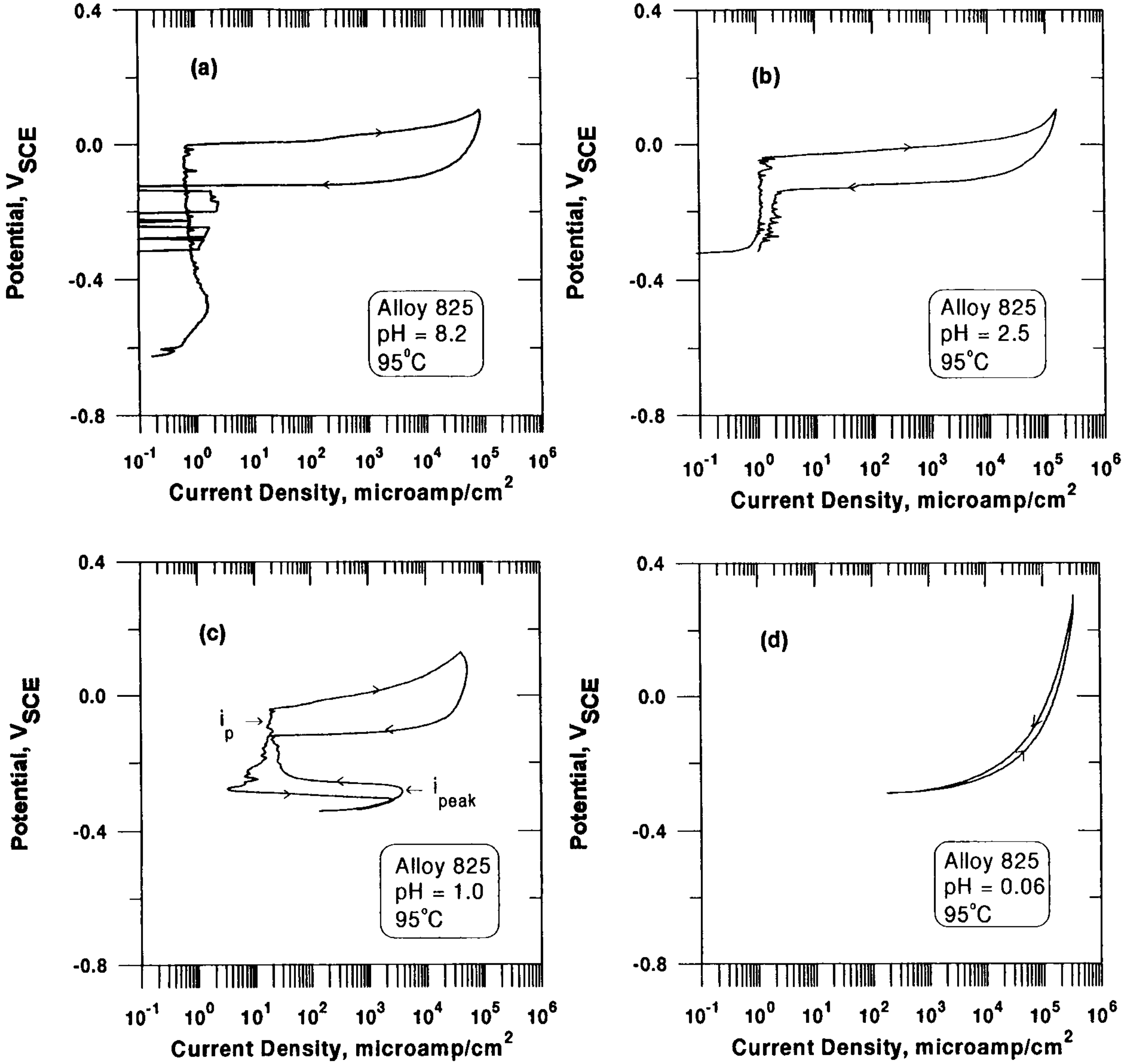

Figure 3-27. Cyclic potentiodynamic polarization curves of alloy 825 in simulated crevice solutions of various pH values. The solutions were deaerated, and the scan rate was 0.167 mV/s.

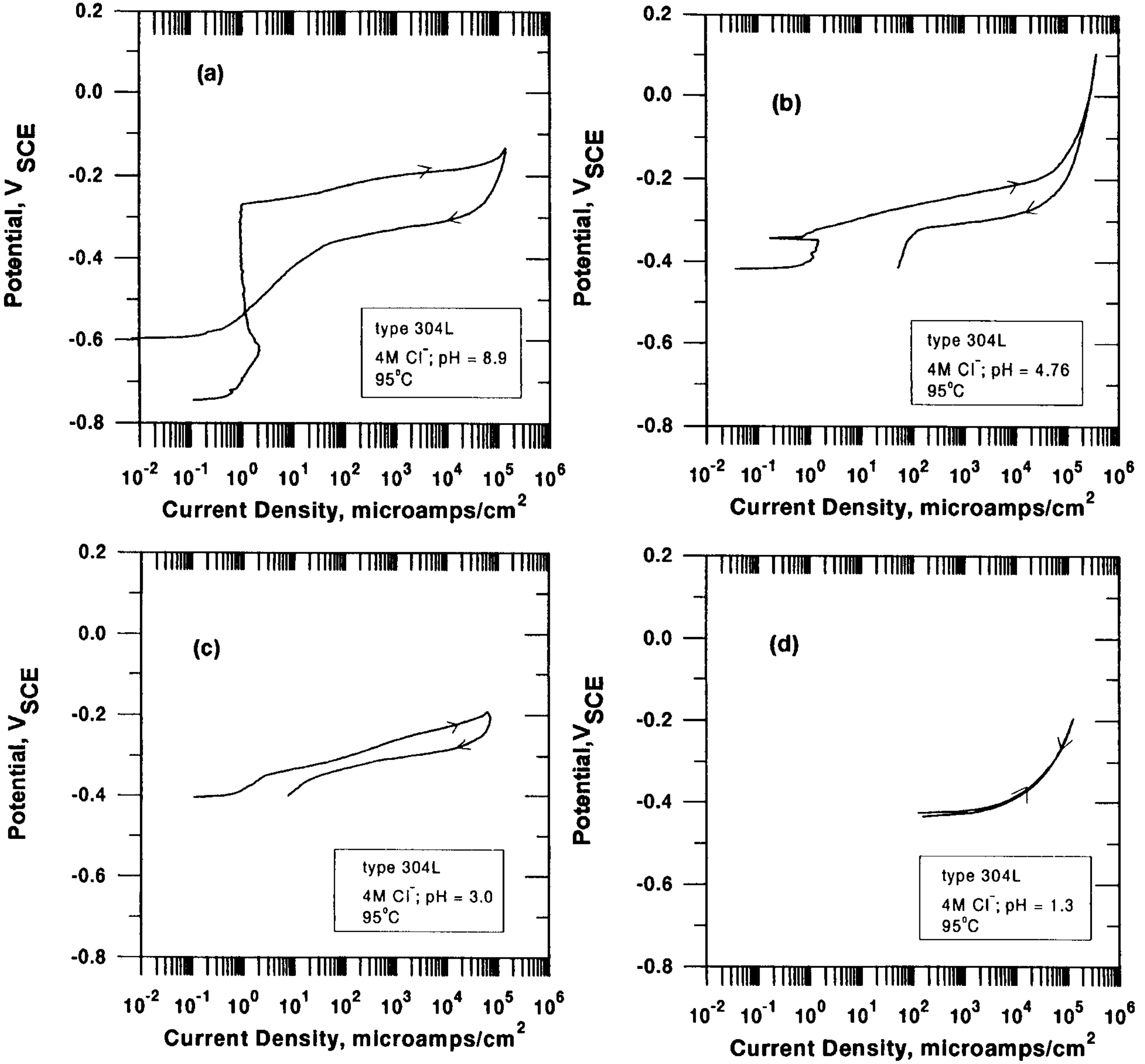

Figure 3-28. Cyclic potentiodynamic polarization curves for type 304L stainless steel in simulated crevice solutions of various pH values. The solutions were deaerated, and the scan rate was 0.167 mV/s.

experiments (Bates, 1964). The pH_D has been assumed by many investigators to be relatively independent of chloride concentration and temperature (e.g., Okayama et al., 1987b). As shown in Table 3-3, the pH_D of alloy 825 is not dependent on the chloride and sulfate concentrations within the scatter in the data. However, pH_D decreases with decreasing temperature. For type 304L SS, the pH_D is dependent both on temperature and chloride concentration. The pH_D values for types 304L and 316L SS in 4 M Cl^-, shown in Table 3-3, are similar to the values reported by Okayama et al. (1987b) and slightly lower than those reported by Oldfield and Sutton (1978b). The results differ from those in the literature in the effect of temperature and chloride concentration on pH_D, possibly because of differences in test technique. For example, Okayama et al. (1987b) used open-circuit conditions to determine the pH at which the corrosion potential fell sharply to active values. It must be assumed, from their data, that the deaeration of the solution was insufficient, since rather high corrosion potentials were observed at pH values above pH_D while low corrosion potentials were observed at pH values below pH_D. From Figure 3-28c, it can be seen that the high peak current density prior to complete depassivation may lead to a lowering of corrosion potential or an unstable corrosion potential, depending on the redox condition of the test.

Conducting a cyclic polarization test, while more time consuming, is a more reliable technique for determining depassivation. Oldfield and Sutton (1978b) conducted potentiodynamic tests (monotonic instead of cyclic) to determine depassivation pH. Below a pH of about 3, an anodic peak in the polarization curve prior to passivation was observed. By assuming a criterion of critical anodic peak for depassivation of 10 $\mu A/cm^2$, they calculated the depassivation pH of type 316 SS to be 1.65. The criterion of a critical anodic peak current density for determining depassivation pH suggests that alloy 825 depassivated between pH values of 2.5 and 1, as shown in Figures 3-28b and 3-28c. However, the cyclic polarization tests show that pitting is still observed at pH 1 and completely active corrosion is not observed until the pH drops to about zero. Hence, it is not surprising that the depassivation pH arrived at by Oldfield and Sutton (1978b) for type 316 SS is slightly higher than that reported in Table 3-3. Additionally, type 304L SS does not exhibit an active peak at any pH value at 95 °C, as shown in Figures 3-28a through 3-28c. In contrast, the hystereses in the cyclic polarization curves are more clear indicators of depassivation. As shown in Table C-10, more pronounced active-passive peaks are observed for type 304L SS in lower chloride concentrations or lower temperatures. Similar behavior is also seen for type 316L SS (Table C-11).

3.4 DISCUSSION

3.4.1 Effect of Environmental Factors

The factorial experiments showed the importance of chloride and nitrate concentrations to localized corrosion of austenitic alloys. While sulfate tended to increase the short-term E_p, it did not have a significant effect on the E_{rp}. Nitrate is present only in small concentrations in the groundwater, but may increase in concentration either due to evaporation or due to radiolysis. However, radiolytic generation of nitrate or nitrite is of significance only for humid air and not for aqueous conditions (Reed and Konynenburg, 1990). Nitrate appears to be a better inhibitor for alloy 825 (lower concentrations are required for the same chloride concentration) than for type 316L SS, possibly because of the former's higher Cr concentration. The mechanism of nitrate and sulfate inhibition has been considered by many. Competitive adsorption was originally proposed by Leckie and Uhlig (1966) and modified by others (Rosenfeld and Danilov, 1967; Brookes and Graham, 1989). Alternatively, Galvele (1981) suggested that nitrate inhibits pitting by reduction to nitrogen consuming H^+ ions. This is consistent with the observation (Table C-6) that nitrate has an inhibiting action only when it is added before significant pitting growth occurred. Once significant pit growth has occurred, the microchemistry inside the pit (pH, Cl^- concentration) is already established and the nitrate is not expected to migrate to the inside of the growing pit.

The reduction in E_{rp} with increasing chloride concentration must be combined with the changes in E_{corr} in order to determine the chloride concentration above which localized corrosion may be expected for a given alloy. Values of E_{corr} are shown in Figure 3-5 for alloy 825 under two redox conditions to indicate the relation to E_{rp}. It must be noted that the E_{corr} values shown in this figure were measured on freshly polished specimens for two chloride concentrations, but at approximately the same pH. This figure suggests that, because the E_{corr} of alloy 825 under deaerated and aerated conditions is below the E_{rp} for chloride concentrations up to 4 M (close to the saturation value of NaCl at 95 °C), no localized corrosion ought to be expected under these conditions. On the other hand the presence of 0.5 mM H_2O_2 increases the E_{corr} such that localized corrosion may be expected at as low as 300 ppm (~0.008 M) chloride concentration at 95 °C. The E_{corr} for aerated conditions reported in Table 3-1 and Figure 3-5 is significantly lower than those reported for similar conditions for type 304L SS and Ti by others (Nakayama et al., 1993; Kosaki and Komada, 1991). These authors found the E_{corr} values for type 304L SS, Ti-1, and Ti-12 in aerated solutions were similar and were related to pH by:

$$E_{corr}(mV_{SHE}) = 733 - 59\ pH \tag{3-7}$$

They did not find a significant temperature dependence for the E_{corr}. For a pH=9 solution, this would result in a E_{corr} of 200 mV_{SHE} or −42 mV_{SCE}, which is about 240 mV higher than those values reported in Table 3-1. While these authors did not report the electrode surface preparation completely, such a discrepancy may arise from changes in the surface condition of the electrode. This is illustrated in Figure 3-29. It can be seen that, for the polished surface, E_{corr} increased by about 200 mV due to thermal aging of the passive film. The increase in E_{corr} was even more pronounced (about 400 mV) for the deaerated environment, although the reason for such an increase is not clear at this time. For the mill-finished surface, the effect of passive film aging was not significant. In the H_2O_2 containing solutions, the mill-finished surfaces exhibited uniform corrosion, possibly providing a reason for the lower E_{corr} of the mill-finished specimens compared to the polished specimens. The above discussion underscores the need for further study of the kinetics of cathodic reactions, such as oxygen and H_2O_2 reduction, on austenitic alloy surfaces under conditions relevant to the repository. As will be pointed out in a subsequent chapter, the presence of certain microbial colonies can further increase the E_{corr}.

3.4.2 Dependance of E_{rp} and E_{rcrev} on the Extent of Corrosion

Pourbaix et al. (1963) were the first to show the existence of a critical potential, named protection potential, below which even active pits ceased to grow. However, later investigations by Wilde and Williams (1971), Wilde (1974), and Rosenfeld et al. (1978) suggested that the protection potential decreased with the extent of pit growth and, hence, the interest in using this parameter for long-term prediction waned. Starr et al. (1976) classified the protection potential as either deactivation potential or repassivation potential, depending upon the mechanism of protection. If upon cessation of pitting, the potential is increased slightly and active pit growth ensues, then the potential is defined as deactivation potential. On the other hand, if the protection is maintained even upon significant increase of potential,

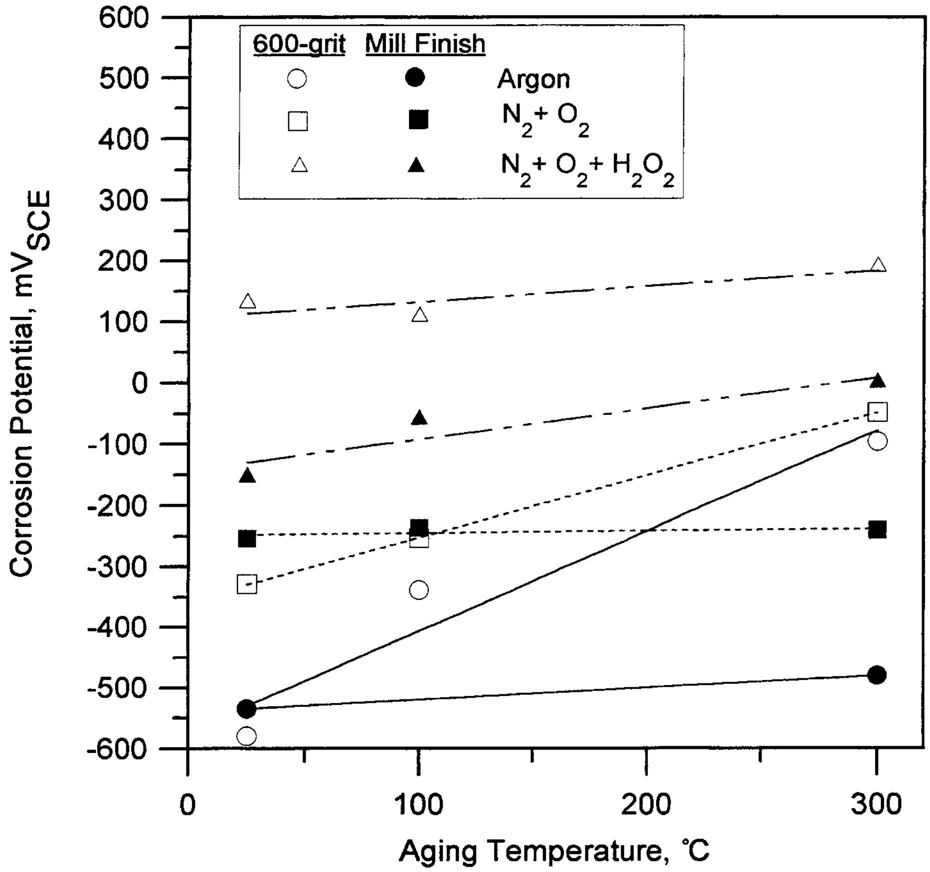

Figure 3-29. Effect of prior thermal oxidation in a dry atmosphere for 30 days on the E_{corr} of alloy 825 in a 1,000 ppm Cl^- solution at 95 °C

the protection potential was defined as repassivation potential. While such a distinction is perhaps useful for marginally passive alloys, for the type of austenitic materials considered in this report the term repassivation potential, E_{rp} for pitting and E_{rcrev} for crevice, is used throughout. This is consistent with the definition of Starr et al. (1976) because it has been observed repeatedly that, once a specimen is repassivated at a low potential, then reinitiation of localized corrosion does not occur unless the potential is raised by a few hundred millivolts.

Tsujikawa and Hisamatsu (1984) reported that while the E_{rp} for pits decreased with the extent of pit growth, the E_{rcrev} for crevice attained a stable lower-bound value. In a survey of literature, it was found that such is the case for pitting also, provided the pit growth occurs beyond a certain depth and that the effect of scan rate and pit growth time are not confounded. This is illustrated in Figure 3-30 as a plot of repassivation potential versus charge density for pitting, for a wide variety of alloy-environment combinations. From this perspective, the conclusion reached by Wilde (1974) was clearly based on insufficient pit growth. It must be noted that these experiments all involved multiple pit initiation. However, Newman and Franz (1984) measured the E_{rp} on samples with single pits. They found that the E_{rp} was relatively independent of pit depth ranging from 25 to 125 µm, corresponding to calculated charge densities of approximately 25 to 125 C/cm^2.

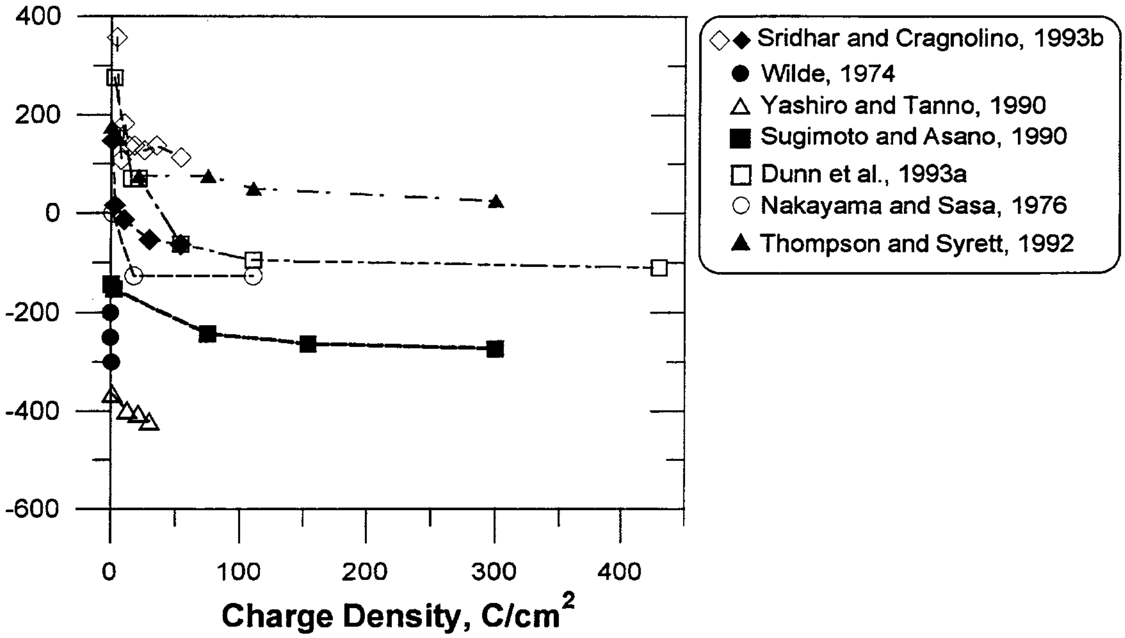

Figure 3-30. A compendium of repassivation potential versus charge density data from the literature for various Ni-Fe-Cr-Mo alloys in Cl^- solutions. Some of the charge densities were calculated from the data provided in the original references.

It can also be seen from Figure 3-9 that the E_{rcrev} attains a stable value at lower charge densities than E_{rp}, which is consistent with the observations of Tsujikawa and Hisamatsu (1984). It is apparent from the results plotted in Figure 3-10 that the E_{rp} is dependent on the penetration depth for shallow pits. For crevice corrosion, the E_{rcrev} also depends on depth. However, the depth in the case of the crevice corrosion includes the lateral depth of the occluded region (distance from the mouth of the serrated washer to approximately the center of the crevice areas along the plane of the crevice) and the depth of the pits within the occluded region perpendicular to the plane of the crevice. The depth shown in Figure 3-10 for crevices is only the depth of pit perpendicular to the plane of crevice. For shallow penetrations, the E_{rcrev} depends on the lateral depth of the crevice or the length of the occluded region, since the total depth is dominated by the lateral depth of the crevice. The width of the teeth on the serrated PTFE crevice washers is 1.4 mm. The lateral depth of an active crevice initiated at the center of this dimension would be 0.7 mm. The observed scatter in the E_{rcrev} at low penetration depths may be caused by a distribution of crevice corrosion initiation sites under the serrated PTFE washer. If crevice corrosion was initiated close to the edge of the PTFE teeth, the lateral depth of the occluded region would be considerably less and the E_{rcrev} would be expected to be more noble. With the progression of crevice corrosion, the depth of crevice attack increases, and the E_{rcrev} becomes increasingly dependent on the penetration depth of pits perpendicular to the plane of crevice. For penetration depths greater than 0.6 mm, the values of the

E_{rp} and the E_{rcrev} remain constant and are almost the same. In the case of pitting corrosion, the E_{rp} rapidly decreases as the depth of penetration increases up to depths of 0.6 mm. For very shallow pits, the E_{rp} approaches 300 mV_{SCE} even with a fast scan rate of 5 mV/s. Such behavior was not observed for crevice corrosion. Even for very low charge densities, corresponding to shallow penetration depths, the E_{rcrev} was always less than 20 mV_{SCE} for alloy 825 in a 1,000 ppm Cl^- solution at 95 °C. The observed differences may be a result of the occluded cell geometry and the test technique. The fast scan rate used here would, most likely, allow time for significant chemistry changes in only very shallow pits. However, the geometry of crevices is significantly different from pits. Because the occluded region is already in place prior to the onset of localized corrosion, large penetration depths are not necessary to have a deep crevice.

3.4.3 Repassivation Potential Measurements on High-Nickel Alloys

As indicated in Table C-9, and discussed previously, the CPP measurements on alloy C-22 were not consistent with the visual evidence of localized corrosion. Hence, this technique cannot be used reliably as an accelerated test technique for this class of alloys. A similar conclusion was reached by Lukezich (1989) for other alloys in the high-nickel alloy class. Wilde and Wilde (1993) investigated alloy C-22 but did not measure the repassivation potential. Okayama et al. (1987a) reported the E_{rp} of a wide variety of high-nickel alloys, including alloys C-276 and C-4 in 3 weight-percent (~0.5 M) NaCl at 80 °C. The value of E_{rcrev} measured for alloy C-276 (–20 mV_{SCE}) is similar to that reported here for E_{rp} of alloy 825 in 1 M Cl^- solution at 95 °C. It is surprisingly low, indicating that this alloy would suffer localized corrosion in mildly oxidizing environments containing chloride. This is not consistent with the generally superior localized corrosion resistance exhibited by alloy C-276 in the field and results of salt brine tests reported by Smialos et al. (1990), Schwartzkopf et al. (1992), and Sorensen and Molecke (1992). Secondly, the E_{rcrev} value reported by Okayama et al. (1987a) for alloy C-4 was higher than that for alloy C-276, which again is inconsistent with the field experience of these two alloys. Okayama et al. (1987a) stated that crevice corrosion could not initiate in these alloys immersed in 3.5 percent NaCl solution by merely increasing the potential. They had to first initiate localized corrosion in concentrated HCl (presumably the highest concentration attainable of about 35 percent), prior to measuring the repassivation potential in the NaCl solution. If this class of alloys becomes the focus of future waste package design, further studies on the technique for measuring the repassivation potential need to be evaluated.

3.4.4 Stochastic Aspects of Pitting Corrosion Considering Repassivation Versus Initiation

It is clear from Figure 3-11 that the initiation of stable pits on smooth surfaces or stable crevice corrosion occurs above the repassivation potential for both deep pits (greater than 0.8 mm deep) and crevice corrosion. This introduces an apparent anomaly because pit initiation is viewed as stabilization of microscopic pit nuclei which, prior to stabilization, are constantly being nucleated and repassivated. A rationalization of Figure 3-11 on the basis of the stochastic models of pitting corrosion initiation requires that the processes leading to stabilization of pit nuclei at long time intervals and repassivation of deep pits must be similar. The similarity of crevice corrosion with pitting will be discussed in the next section.

The stochastic aspects of pit initiation have been examined by a number of authors. However, most of these attempts have focused on relating the stochastic parameters to potentiodynamically generated pit initiation potential. The following discussion is based on the stochastic model proposed by Williams et al. (1985a, b). In this model, pitting is divided into three stages: (i) processes leading to breakdown of passivity, including those involving the initiation and repassivation of unstable pits; (ii) growth of these unstable pits to a critical size, also referred to in terms of time as critical life of unstable pits; and (iii) growth of stable pits. The model considers that: (i) unstable pits nucleate at a rate of λ ($s^{-1} \cdot cm^{-2}$); (ii) some die out or repassivate with a probability of μ (s^{-1}); and (iii) unstable pits which survive beyond a critical time, τ_c (s), continue to grow according to deterministic rate. Thus, the rate of birth of stable pits is given by:

$$\Lambda(s^{-1}) = a\lambda \exp(-\mu\tau_c) \tag{3-8}$$

where a is the specimen area in cm^2, and the other terms have been defined previously. The probability that no stable pit will be formed in time t, $P(0)$, is then given by:

$$\ln[P(0)] = -\lambda a(t-\tau_c)\exp(-\mu\tau_c) \tag{3-10}$$

A somewhat similar treatment is given for stable pitting by Shibata and Takamiya (1986), although they only consider the rate of generation and repassivation of stable pits. Based on experiments on multiple specimens, Williams et al. (1985b) found that λ was only slightly dependent upon potential, μ was relatively independent of external potential, and τ_c increased with decreasing potential. This is similar to the findings of Shibata and Takamiya (1986). Williams et al. hypothesize that pit nucleation occurs because of gradients in pH and chloride concentration established over the size scale of the specimen surface roughness. The stability of such a gradient in solution chemistry depends upon the local current density, which in turn depends upon the external potential. Another factor that affects the stability of this local chemistry gradient is the depth of pit nuclei, which in turn may be related to surface roughness. If the depth of pit nuclei is low, any chemical gradient created by local current fluctuation may be dissipated by mixing with the bulk solution. However, if the depth of the pit nuclei exceeds a critical depth, the chemical gradient may be sustained beyond a time period, τ_c, required for stabilization of the pit. The τ_c then may be expected to decrease with an increase in the external potential (increase in local current density) or with an increase in surface roughness (greater depth of pit nuclei). Under potentiodynamic conditions, the decreased τ_c leads to a decrease in the breakdown potential. Such an effect of increased surface roughness on E_p is seen in Figure 3-17. Unfortunately, such a microscopic model leads only to a qualitative understanding of parameters in the stochastic treatment of pit initiation. Since in the measurement of E_{rp} the chemical gradients are first maintained artificially by propagating a stable pit, the similarity of E_{rp} to long-term pit initiation can be understood qualitatively.

3.4.5 Stochastic Aspects of Crevice Corrosion Considering Repassivation Versus Initiation

While crevice corrosion is generally recognized to be similar in many respects to pitting, it has been modeled quite differently. The two general types of crevice corrosion models are displayed schematically in Figure 3-31. The chemistry change models tend to predict that depassivation occurs at the deepest point in the crevice, where a critical solution composition is reached first. On the other hand, the potential change models would predict that the initiation of crevice corrosion would occur at some

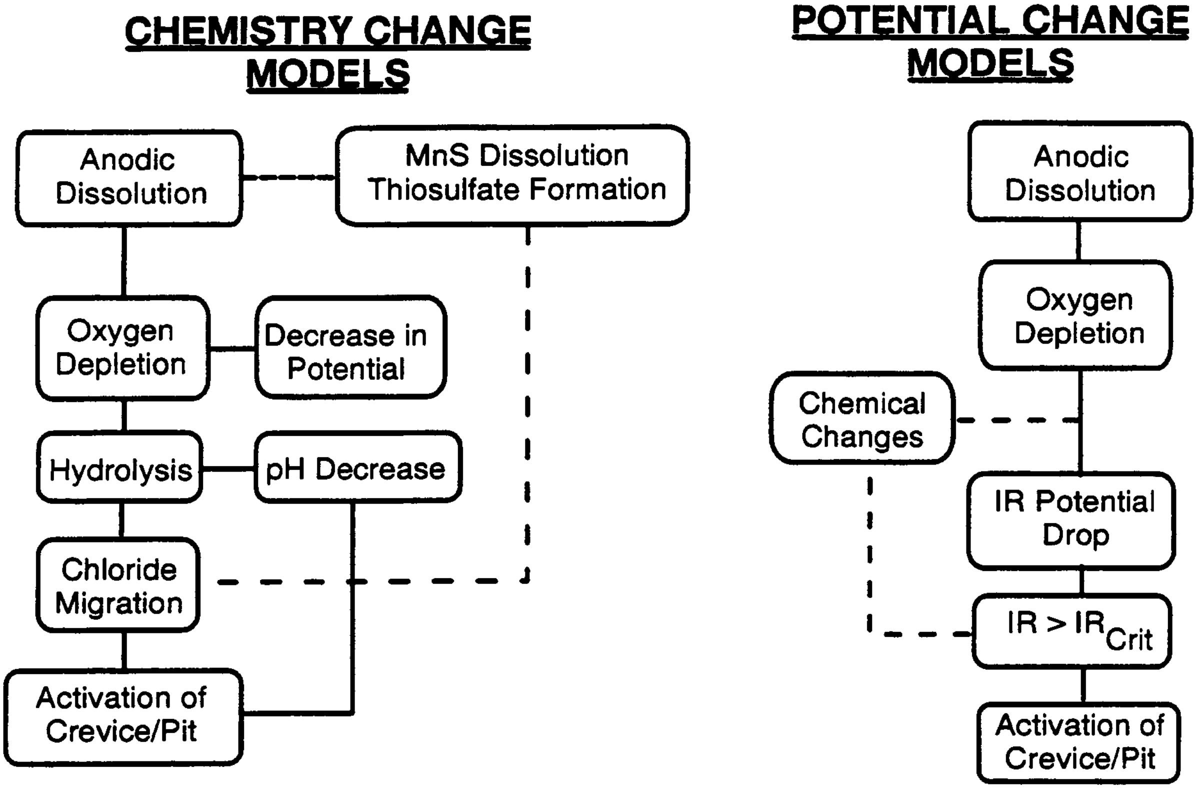

Figure 3-31. Schematic illustration of the approaches used in the literature to model crevice corrosion initiation

intermediate depth where the active-passive peak will be located. Both these predictions are deterministic in nature. They predict that the change in pH (chemistry change models) or potential (potential change models) ought to precede macroscopic initiation of crevice corrosion. However, as shown in Figures 3-18 and 3-19 for type 304L SS and Figures 3-21 and 3-22 for alloy 825, the decrease in pH and potential inside the crevice always followed the increase in current (indicating crevice initiation). Previous investigations of crevice or pit chemistry (Suzuki et al., 1973; Alavi and Cottis, 1987; Luo et al., 1992; Sugimoto and Asano, 1990, Cavanaugh et al., 1983) did not monitor both the current and chemistry changes simultaneously from pre-initiation to repassivation stages. Other findings of this work agree with literature rather well. For example, it is well known that crevice gap, as influenced by surface finish of the mating surfaces, controls the crevice initiation time. This is indeed observed in Figure 3-20 where the rougher surface shows a much longer initiation time and a higher crevice pH. A mill-finished surface of alloy 825 has a lower surface Cr concentration (Dunn et al., 1995b) and, hence, would be expected to dissolve at a faster rate. This would result in a faster drop in pH due to hydrolysis of cations released from dissolution. Indeed, this is observed in Figure 3-23. The tip and mouth pH change at about the same rate in Figure 3-18, and the pH decreases faster for the mouth than for the tip in Figure 3-21. This is contrary to what would be expected from crevice corrosion models (Oldfield and Sutton, 1978a; Watson and Postlethwaite, 1990; Sridhar et al., 1994c; Walton and Kalandros, 1992) where the transport of H^+ ions occurs from the inside to the bulk. Two reasons may be offered for this observation. First, in the rectangular crevice geometry it is difficult to avoid ionic transport from the sides. (Indeed in control experiments, where the pH in the bulk was lowered by nitric acid addition and pH inside was monitored, the pH of the mouth decreased at the same rate as that at the tip. Second, the nucleation of crevice corrosion can occur at a number of favorable locations on a microscopic scale.

The measured crevice chemistry, in terms of maximum Cl^- concentration and minimum pH, using the radial cell geometry did not greatly differ from the measurements made with the rectangular cell. The main differences observed using these two cell geometries was with respect to the timing of the chemistry changes when crevice corrosion initiated. The model for crevice corrosion initiation proposed by Oldfield and Sutton (1978a) predicts that chemical changes that occur inside the crevice preceed the initiation of crevice corrosion. However, the results observed in this study with both cell geometries indicate that the initiation of crevice corrosion under potentiostatic conditions occurs as a result of the local breakdown of the passive film in a manner similar to pitting corrosion. Chemical changes were always observed to be preceded by an increase in current density and a potential drop inside the crevice.

For the rectangular cell, a large, variable lag time was observed between the current increase and the subsequent potential drop inside the crevice and the associated chemistry changes. This lag time could not be completely explained in terms of crevice gap or distance between the initiation site and the location of the pH and Cl^- ISE electrodes (Sridhar and Dunn, 1994). For the radial cell, no lag time between the current increase and the potential drop inside the crevice was observed and measured chemistry changes lagged behind the increase in current by approximately 6,000 s. These results again suggest that under potentiostatic conditions the initiation of crevice corrosion occurs as a result of the breakdown of the passive film. The large lag time between the current increase and the potential decrease inside the crevice observed in the rectangular cell is most likely a result of the cell geometry. Current increases could be measured virtually instantaneously (within the time resolution of the data collection frequency). However, the potential drop is dependent on the relation between the location of the initiation site and the reference electrode. The active corrosion front initiated at a considerable distance from the reference electrode would have to extend toward the reference electrode location in order for a potential drop to be measured. The geometry of the rectangular cell was such that the most occluded part of the crevice was a considerable distance from the electrodes. In contrast, the radial cell geometry had electrodes located very close to the tip of the crevice. As a result, when crevice corrosion was initiated the current increase coincided with a measured potential drop inside the crevice. The lag time between the initiation of crevice corrosion and the measured chemistry changes was not as large with the radial cell. This again can be attributed to the improved electrode locations of the radial cell. However, even if the initiation of crevice corrosion under potentiostatic conditions does not occur as a result of chemistry changes inside the crevice prior to crevice activation, acidification and Cl^- migration into the occluded region would be expected to occur after crevice corrosion was initiated. It is evident that the minimum volume required to measure chemistry changes with these relatively large electrodes is still a limitation and the probable cause of the measured lag time between initiation and chemistry changes.

Results of crevice chemistry measurements with type 316L SS were similar to the results obtained with type 304L SS. The initiation of crevice corrosion was marked by an increase in current and a simultaneous potential drop inside the crevice. Chemistry changes were again observed to lag slightly behind the activation of the crevice. For type 316L, the initiation of crevice corrosion occurred at slightly higher potentials compared to type 304L. In addition, the open-circuit potential of type 316L specimens following repassivation of crevice corrosion was observed to increase to very high potentials in a manner similar to that observed for alloy 825 (Sridhar and Dunn 1994). Such behavior was not observed for type 304L. Since both type 316L SS and alloy 825 contain Mo, this observation for type 316L could be explained by the reduction of molybdate species during repassivation. The fact that this behavior was only observed when the external applied potential of type 316L exceeded 0.3 V_{SHE}, a potential which is required for the oxidation of Mo to Mo(IV) (Cavanaugh et al., 1983; Wanklyn 1981) and not observed for type 304L under similar conditions, further supports this mechanism.

While the crevice initiation models are deterministic, the results presented here, as well as in the recent literature, suggest that crevice corrosion initiation is a stochastic process because the initiation in a crevice proceeds by pitting. This has been illustrated vividly by Shinohara et al. (1990, 1993), using the Moiré fringe technique. In this technique, the crevice is formed between the specimen and an optically flat glass plate. The surface of the glass plate away from the contact area with the specimen was coated with chromia to form a grating. The light reflected from a filtered source formed a Moiré fringe pattern. The spacing between bands in this patterns is a function of depth perpendicular to the light path and, hence, depth of corrosion at any point. Such a distribution of pits within a rectangular crevice area is illustrated in Figure 3-32 (Shinohara et al., 1990). It is clear from this figure that nucleation of crevice corrosion occurs as discrete sites, then propagates laterally, but is quite uneven after extended time periods. The pH, chloride, and potential measurements shown in Figures 3-18 and 3-19 provide additional support to these observations. The increase in current density clearly preceded any decrease in pH or potential. Since the latter two parameters are dependent upon a certain volume of solution with a changing chemistry, whereas the current density measurements are quite sensitive to small nucleation events, it appears that the crevice corrosion initiation process must occur at certain favorable locations and then propagate laterally. For example, crevice corrosion initiation may occur at contact points between surface asperities. Indeed, in radially symmetrical crevices, the drop in pH did not occur systematically either near the mouth or near the tip of the crevice, again supporting the stochastic aspects of crevice corrosion initiation.

A further support to the stochastic aspects of crevice corrosion initiation was provided by Fujimoto et al. (1994). In this case, the authors affixed a pair of multiple-teeth washers on a specimen and mounted reference electrodes in various teeth. When crevice corrosion initiated under any tooth, the potential dropped. Although this type of measurement is not amenable to a strictly stochastic treatment because the initiation of crevice corrosion under one tooth can influence initiation under neighboring teeth, the data are plotted as crevice corrosion generation rate, λ (s^{-1}), versus potential (Figure 3-33). The interesting feature of this figure is that the extrapolation of potential to values of the order of repassivation potential reported by Okayama et al. (1987a) of about –200 mV_{SCE} leads to a crevice corrosion generation rate of the order of 10^{-12} s^{-1} (i.e., more than 30,000 years are needed to initiate the attack in the crevice).

3.4.6 Mechanistic Considerations of Repassivation Process

Several mechanisms of the repassivation process have been proposed in the literature (Wilde, 1974; Okada, 1984; Gaudet et al., 1986; Steinsmo and Isaacs, 1993). Repassivation of deep pits and crevices has been proposed to occur (Wilde, 1974) by decreasing the external potential of the specimen such that the potential inside the deepest portion of the pit is below the E_{corr} of the metal in the occluded cell solution. For shallow pits without a salt film, the ohmic drop in the pit will depend on the pit solution resistance and the depth of the penetration. The high E_{rp} values measured for shallow pits may be the result of a very small ohmic drop and the occurrence of significant chemistry changes inside the pits. For deep pits, the ohmic drop may be controlled by the presence of a precipitated salt film. Similarly, the ohmic drop inside a crevice will depend on the depth of the crevice and the presence of a salt film. Large ohmic drops have been experimentally measured very shortly after the onset of crevice corrosion (Sridhar and Dunn, 1994). However, the repassivation kinetics by this mechanism are expected to be extremely rapid since no transport of ionic species is involved. An alternate mechanism is related to the stability of

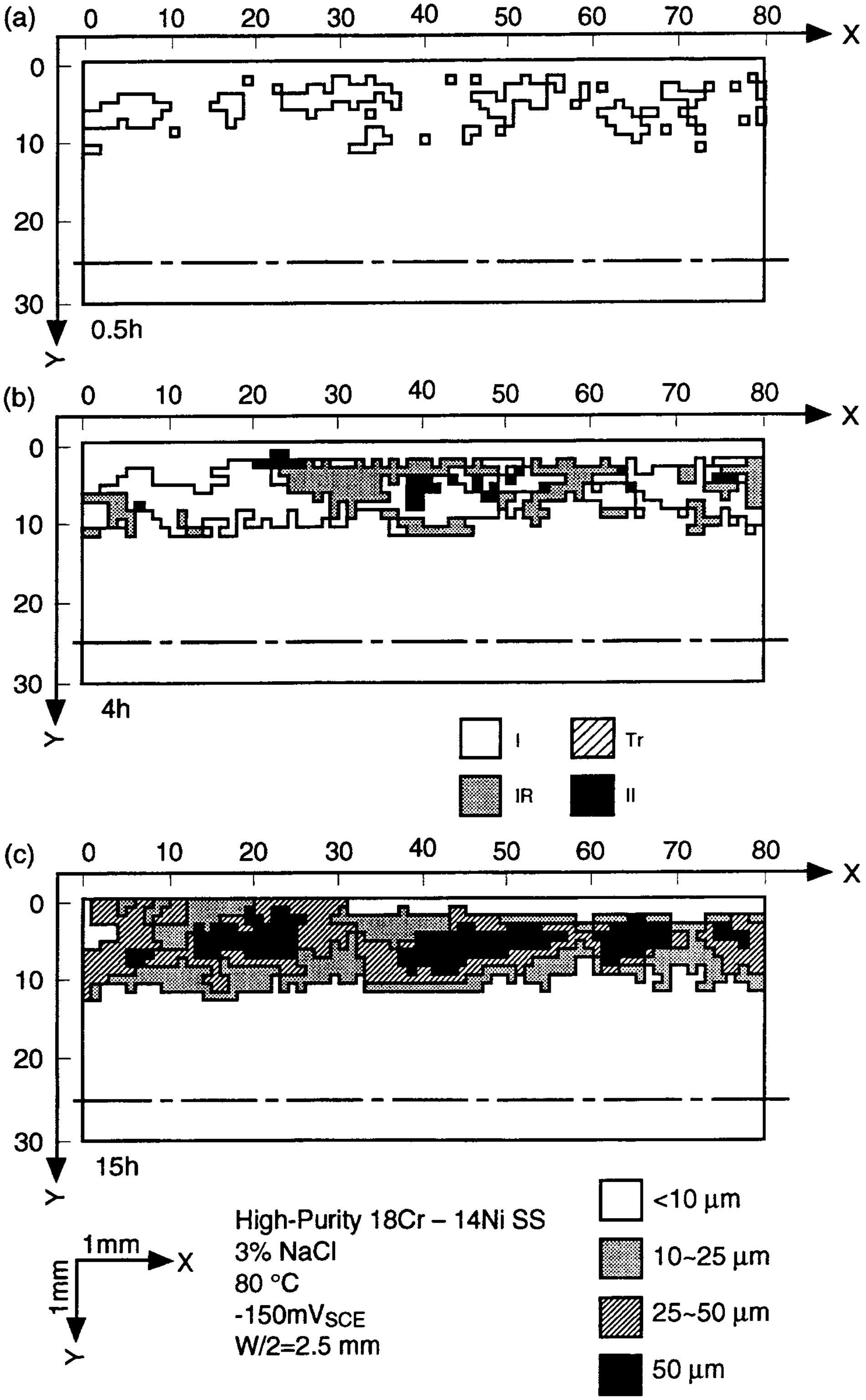

Figure 3-32. Depth measurement contours using Moiré fringe technique in the crevice between a stainless steel specimen and an optically flat glass (Shinohara et al., 1990)

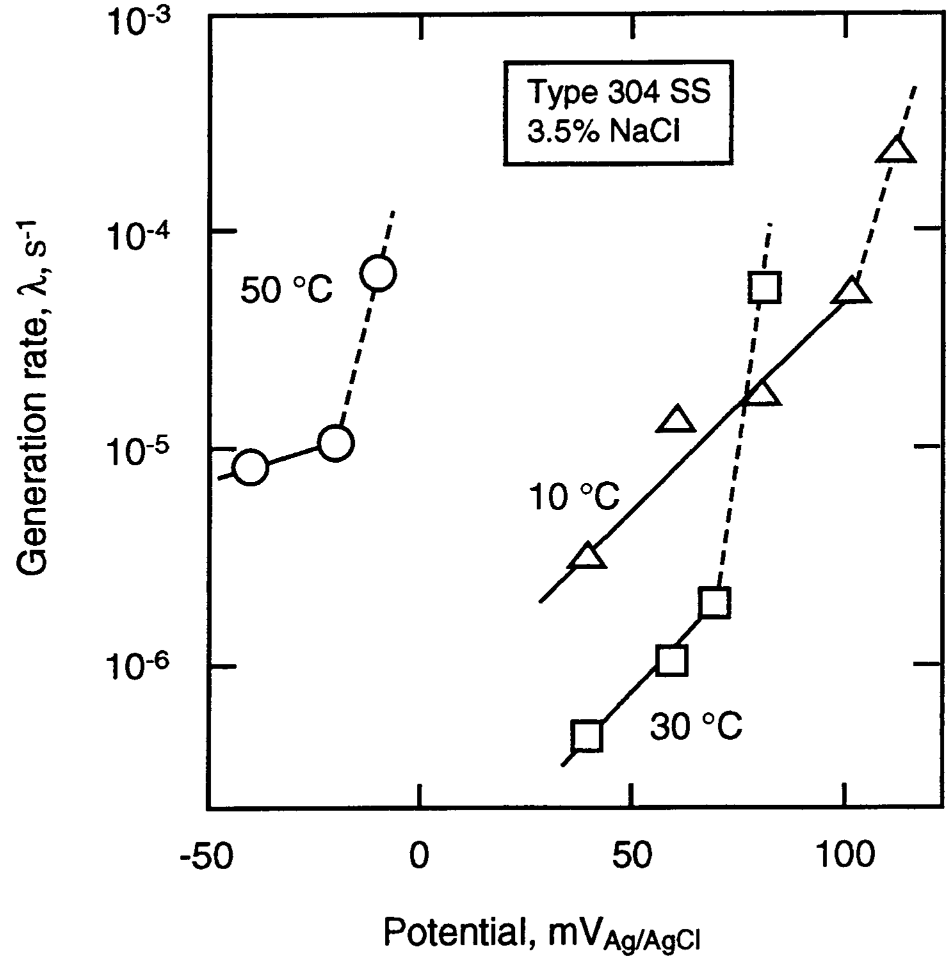

Figure 3-33. Crevice corrosion generation rate as a function of applied potential for type 304 stainless steel-teflon crevice immersed in 3.5 weight percent NaCl solution (Fujimoto et al., 1994)

chloride salt film as a function of potential. As suggested by Okada (1984), the repassivation process occurs by the nucleation and growth of an oxide in a chloride salt film. While he considered transport processes in the solution, his criterion for repassivation involved competitive surface reaction rates of oxide formation and chloride formation at the pit bottom. The attractive feature of this theory is that it relates repassivation potential to pit initiation potential through the competitive rates of formation of salt and oxide films.

A variation of the above theory has been suggested by Gaudet et al. (1986) and Steinsmo and Isaacs (1993) involving changes in chloride concentration inside the pit. Repassivation, according to these theories, occurs when the concentration of metal chloride complexes inside the pit bottom falls below a critical percentage of the saturation value. The critical percentage of saturation was suggested to depend on the alloy composition, but was relatively independent of external potential (Steinsmo and Isaacs, 1993). However, the rate at which the chloride concentration decreased to the critical value inside the pit depended upon the external potential. These authors showed that as the external potential decreased, the time for the chloride concentration at the pit bottom to reach the critical saturation value decreased until a low enough potential was reached, at which the rate of decrease of chloride concentration was predicted to be independent of external potential. This is consistent with data reported in Figure 3-11. It must be emphasized, however, that the chloride concentration values reported by Gaudet et al. (1986) and Steinsmo and Isaacs (1993) are calculated values from current measurements of lead-in-pencil type electrodes and not directly measured. Independent, *in situ* analyses of chloride concentration inside pits are needed to further advance the understanding of repassivation processes.

3.5 LABORATORY DATA VERSUS FIELD EXPERIENCE

While the applicability of E_{rp} to long-term localized corrosion prediction was discussed in previous sections, comparison of short-term laboratory data to field experience with these alloys has not been attempted. The main hindrance for this is the lack of E_{corr} data in many field tests or in-service components. A limited attempt is made here to compare the performance of alloys in those field tests where some information was available or the E_{corr} can be estimated. The following issues are addressed with respect to alternate austenitic materials (the high-nickel base alloys) for the disposal overpacks: (i) the types of available laboratory data on localized corrosion, (ii) the applicability of E_{rp} concept and test technique to these types of alloys, and (iii) the comparison of laboratory test data to field experience.

Bernhardsson and Mellström (1983) reported failure due to pitting of alloy 825 compressor coolers on a gas lift platform. The environment was chlorinated seawater at 42 °C and failure took place after 4 months (minimum penetration rate was estimated to be about 5 mm/yr). The E_{rp} for alloy 825 in 0.5 M chloride (the approximate concentration of chloride in seawater is 0.55 M) at 20 °C is 60 mV_{SCE} (Sridhar and Dunn, 1994). Since the E_{rp} is expected to decrease with an increase in temperature and the E_{corr} in chlorinated seawater has been measured to be around 200 mV_{SCE} (Shaw et al., 1993), this in-service failure is consistent with the use of E_{rp} as a determining factor for localized corrosion. In stagnant, aerated 3 percent NaCl solution at 60 °C, Bernhardsson and Mellström (1983) found that type 316L SS underwent crevice corrosion after 2 months while alloy 825 did not. Although these are still relatively short-term tests, the results are consistent with even shorter-term E_{rp} values. For example, Okayama et al. (1987a) reported a value of −360 mV_{SCE} for E_{rp} of type 316 SS and −100 mV for alloy 825 in 3 percent NaCl at 80 °C. These values are expected to be slightly higher at a lower temperature. The E_{corr} of these alloys in aerated chloride solution at 95 °C has been reported to be about −280 mV_{SCE} and is anticipated to increase slightly with a decrease in temperature due to higher solubility of oxygen. Again, from these values of E_{corr} and E_{rp}, the observed crevice corrosion of type 316L SS and absence of crevice corrosion in alloy 825 in aerated NaCl is not surprising.

Protection against corrosion in highly oxidizing pulp and paper bleach plant washer fluids using controlled potential has been reported (Laliberté and Garner, 1981). In this case, the material is typically a type 317L SS (Fe-19Cr-12Ni-3.5Mo) and the E_{corr} in chlorine waters is in the range of 100–500 mV_{SCE} depending upon residual chlorine. This is far higher than the potential at which crevice corrosion was observed in potentiostatic tests (considered to be roughly equal to the E_{rp}). For type 317L SS in this environment (typically 1,000–5,000 ppm Cl^- and pH 2) the E_{rp} was measured to be about −30 mV_{SCE}. In these cases, cathodic protection by maintaining the potential at −500 mV_{SCE} has resulted in successful performance of the washer drums for over 10 yr.

In filtered, natural seawater (mean temperature 25.2 °C), Kain (1993) observed crevice corrosion on type 316L SS after 60 days, but no crevice corrosion on alloy 59 (61Ni-22Cr-15Mo). Slight crevice corrosion was observed on alloy C-276 (Ni-16Cr-5Fe-16Mo-4W). He measured a E_{corr} in the range of 200–300 mV_{SCE}. In natural seawater, microbially enhanced cathodic reduction of oxygen is believed to be responsible for the high E_{corr} values. Again, the observed crevice corrosion of type 316L SS is consistent with the measured E_{rp} at this temperature of 0 mV_{SCE} (Asphahani, 1980). A large number of Fe-Ni-Cr-Mo alloys were tested in natural, filtered seawater at 30 °C for 30 days by Hack (1982). The specimens were fitted with crevice washers of PTFE. In this limited duration test, alloys C-276 and 625 (Ni-22Cr-5Fe-9Mo-4Nb) suffered no localized corrosion, while type 316 SS and alloy 825 suffered significant crevice corrosion. The E_{rp} for alloy 825 in 0.5 M Cl^- is −60 mV_{SCE} (Sridhar and Dunn, 1994), which is lower than the E_{corr} values reported for these alloys in natural seawater. An evaluation of all the published data on the E_{rp} values of alloy 825 and type 316/316L SS indicates that if the chloride concentration becomes higher than approximately 0.5 M, alloy 825 may not be significantly better than type 316L SS in localized corrosion resistance (Sridhar et al., 1993c).

Postlethwaite et al. (1988) have conducted both cyclic polarization and natural immersion tests on alloys C-276 and 625 in various chloride solutions. They report on the visual observation of localized corrosion on the specimens after these tests as a function of chloride concentration and test temperature. The authors did not report E_{rp} or E_{corr} values. No localized corrosion was observed on alloy C-276 for up to 260 days at temperatures up to 120 °C in continuously aerated 1–20 weight-percent NaCl solutions. The temperature at which localized corrosion was observed increased with lower chloride concentrations. Okayama et al. (1987a) report a E_{rp} for alloy C-276 in 3 percent NaCl at 80 °C of −20 mV_{SCE} while the E_{corr} under aerated conditions is expected to be about −280 mV_{SCE}. Hence, the lack of observation of localized corrosion by Postlethwaite et al. (1988) in 3 percent NaCl at temperatures up to 140 °C is consistent with the available data.

Laboratory studies of the effect of alloying elements on the E_{rp} in a 3 percent NaCl solution at 80 °C have been reported by Okayama et al. (1987a). This remains one of the most extensive and systematic studies of the E_{rp} as a function of alloying elements. However, some of the conclusions of this report contradict previously reported data and may point to the effect of test technique. For example, the E_{rp} reported by these authors for alloy 625 is slightly lower than that for alloy 825, although most localized corrosion data published to date based on both laboratory and field experience would suggest the opposite (e.g., Hack, 1982). Okayama et al. (1987a) also report that they could not initiate localized corrosion on alloy C-276 in 3 percent NaCl at 80 °C and, hence, used concentrated HCl to initiate localized corrosion prior to measuring E_{rp} in 3 percent NaCl. Use of a similar procedure on alloy C-4 (in which they were able to initiate pits in NaCl solution) did not seem to alter the E_{rp}.

However, the E_{rp} values that Okayama et al. (1987a) report for these alloys (−20 mV_{SCE} for alloy C-276 and 0 mV_{SCE} for alloy C-4) are surprisingly low, suggesting that these alloys would readily suffer localized corrosion in this environment if moderately oxidizing conditions are present. However, 1-yr tests in NaCl brine under γ-irradiation (Smialos et al., 1990) did not indicate susceptibility to localized corrosion for alloy C-4. Hence, the test technique for measuring E_{rp}, and the application of this potential to predict the performance of highly alloyed materials such as alloy C-4, need further evaluation.

Long-term exposure studies on alloy C-4 and other austenitic SS have also been performed in salt repositories for time periods of up to 5 yr (Smialos et al., 1990; Schwartzkopf et al., 1992; Sorensen and Molecke, 1992). Unfortunately, in none of these tests were the E_{corr} values measured, nor were independent measurements of E_{rp} carried out. Hence, it is difficult to incorporate these findings in the current long-term predictive scheme. Nevertheless, the findings of these investigations can be important in considering the effect of environments arising from evaporative concentration of groundwater, as modeled by Walton (1993).

In laboratory tests of alloy C-4 specimens immersed in Q-brine ($MgCl_2$+NaCl, [Cl^-]= 8.4 molal, pH=4.9) at 90 °C and with a specimen surface/volume ratio of 1 cm^2/5 mL for 1 yr, Smialos et al. (1990) found pitting and crevice corrosion at γ dose rate of 10 Gy/hr (1,000 rad/hr) and higher. The rate of pit growth was found to increase from 20 µm/yr at 10 Gy/hr to 1 mm/yr at 1,000 Gy/hr. No localized corrosion was observed in the unirradiated solution (saturated oxygen concentration was 3.7 ppm at 25 °C). Since the E_{corr} in the irradiated solution is expected to be much higher than in the unirradiated and aerated solutions, the observation of localized corrosion is in qualitative agreement with the findings of Postlethwaite et al. (1988) on alloy C-276. In another series of tests in the Asse salt mine (Smialos et al., 1990), specimens of alloy C-4 were placed on the borehole wall and heated to a maximum temperature of 210 °C while subjected to γ-radiation from a Co-60 source. No localized corrosion was observed in tests lasting 700 days. The lower corrosion rate can be attributed to the high temperature (above the boiling point) and the small volume of the migrating brine. In a later test, Schwartzkopf et al. (1992) reported that cast steel explosively clad with alloy C-4 and exposed to Q-brine in *in situ* heater tests in the Asse salt mine showed extensive but shallow pits on alloy C-4 after 18 months. The maximum depth of pits was about 15 µm.

Sorensen and Molecke (1992) reported results of coupon tests conducted over a 5-yr period in WIPP brine at 90 °C. They did not measure E_{corr} of the specimens, but found localized corrosion and SCC on type 304L SS, localized corrosion on type 316L SS, and no corrosion on alloy 625.

4 STRESS CORROSION CRACKING

4.1 BACKGROUND

The literature on SCC of candidate materials for HLW containers has been previously reviewed, among others, by Beavers and Thompson. (1990), Farmer et al. (1988b), Gdowski (1991), Maiya (1989), Cragnolino and Sridhar (1992a) and Sridhar et al. (1994a). These reviews cover the full range of alloys included in the SCP as well as those considered in the new ACD. In the review of Cragnolino and Sridhar (1992a), in addition to a critical analysis of the conclusions presented in previous reviews, the advantages and limitations of different test methods available to characterize SCC and to determine suitable bounding parameters for long-term life prediction were examined. The more important conclusions of this review were as follows:

- The use of several test methods was recommended for evaluating the SCC resistance of the candidate container materials over a wide range of environmental conditions, instead of relying on a single technique. The advantages of the slow strain rate test (SSRT) technique were noted as an appropriate screening tool for determining environmental conditions, including electrode potential ranges, in which a given material can be susceptible to SCC. However, taking into consideration contradictory results reported for austenitic SSs in hot chloride solutions using this technique (Beavers and Koch, 1992), the concurrent application of constant-deflection tests, using U-bend specimens for simplicity, was emphasized.

- Although not directly applicable to the anticipated repository conditions, extensive information on the SCC susceptibility of types 304L and 316L SS in chloride-containing environments was available in the reviews quoted above. However, phenomenological information and long-term data were found to be extremely limited in the case of alloy 825. Even though a very extended program was conducted at Argonne National Laboratory, using initially SSRTs (Maiya et al., 1990) and later fracture mechanics techniques (Park et al., 1991; 1992; 1994), the applicability of the data is limited because the testing was confined to simulated J-13 well water purged with synthetic air as a single environment and all the tests were conducted only under open-circuit conditions. Beavers and Durr (1992) did not observe the occurrence of SCC in long-term (13,400 hr) boildown tests using U-bend specimens in simulated J-13 well water purged with air. However, the final chloride concentration reached only 750 mg/L with a pH close to 11.0. The corrosion potential of unstressed specimens tested simultaneously ranged from -250 to $-100\ \mathrm{mV_{SCE}}$, but the precipitation of calcium carbonate as a compact deposit on the stressed specimens may have minimized the access of the solution to the specimen surface. No SCC was observed in additional tests in which the chloride concentration was increased up to 100,000 ppm

- Whereas the occurrence of SCC of austenitic SS (specifically for type 304 SS) in hot, concentrated, acidic chloride solutions above a critical potential was well established during the late 1960s, no SCC has been observed in laboratory experiments in dilute, neutral solutions between 60 and 100 °C until recently, despite the many failures that have been reported in service. It was noted, however, that in a series of papers (Tsujikawa et al., 1985; Tamaki et al., 1990), Tsujikawa and coworkers have shown that SCC can occur in more dilute solutions in the presence of a crevice. Under such conditions, SCC only occurs at potentials above E_{rp} for crevice corrosion.

Indeed, one of the main recommendations of the review of Cragnolino and Sridhar, (1992a) was that the concept of a critical potential for SCC as related to the E_{rcrev} should be carefully investigated for performance assessment of waste package materials because it can provide a unified bounding parameter not only for localized corrosion but also for SCC.

The activities in Task 2 of the IWPE Project were then oriented towards the application of the SSRT and the constant-deflection test techniques for evaluating the SCC resistance of some selected materials. Since the consideration of type 304L SS as a candidate material for the HLW container is questionable in terms of its relatively poor resistance to SCC and localized corrosion in chloride-containing solution, the experimental work was conducted using 316L SS and alloy 825. Some preliminary tests were conducted on copper alloys. Since these alloys were de-emphasized in the DOE program, no further experiments were performed. In the previous review (Cragnolino and Sridhar, 1992a), it was also recommended that a limited number of tests be conducted using a fracture mechanics approach, once the environmental and potential conditions were better defined, to evaluate the possibility of crack arrest by displacement of the potential below the critical potential for SCC, as well as the determination of K_{Iscc} and crack growth rates. This part of the program is currently under way and, consequently, will be reported at a later date.

4.2 EXPERIMENTAL

The chemical compositions of the heats of type 316L SS and alloy 825 used in this study are given in Table A-1 in Appendix A. The heats of both materials obtained in the form of hot-rolled and annealed plates, 12.7 mm (0.5 in.) thick, were used for SSRTs. Detailed characterization of these two heats was reported previously (Sridhar et al., 1993a). No grain boundary precipitation was observed, but MnS inclusions were detected in type 316L SS and cuboidal particles of Ti (C,N) were observed in alloy 825. Round specimens were machined with the tensile axis perpendicular to the rolling direction from bars cut from the plates, after the bars were centerless ground to a diameter of 6.35 mm (0.245 in.). Two types of specimens were used. One of them was a round, smooth tensile specimen with a waisted section having a gage length of 12.7 mm (0.5 in.) and a diameter of 3.175 mm (0.125 in.). The other type was a round, notched specimen, in which a circumferential notch, with a depth of 1.588 mm (0.0625 in.), an included angle of 60°, and a radius of 51 μm (2 mils), was machined. The notched specimen was used to facilitate crack initiation. In some tests, an O-ring was placed in the notch position to create an artificial crevice. Except when noted, tests were conducted with the alloys in the as-received condition, without any heat treatment after machining. The specimens were wet-ground longitudinally along the gage length with 600-grit SiC paper, and washed with acetone and deionized water just before the tests.

The heats of type 316L SS and alloy 825 used for constant-deflection tests were obtained in the form of cold-rolled and mill-annealed (MA) sheets, 3.175 mm (0.125 in.) thick (Table A-1). U-bend specimens were machined from these sheets and stressed, without any heat treatment, to a radius of bend curvature of 6.35 mm (0.25 in.), using an appropriate device according to American Society for Testing and Materials (ASTM) Practice G 30-90 (American Society for Testing and Materials, 1994a). Bolts and nuts made of alloy C-276, electrically isolated from the specimens by zirconia spacers, were used for the single-stage stressing operation. The resulting tensile stress was perpendicular to the rolling direction (transverse specimens), and the total strain on the outer fiber of the bend was estimated to be about 25.0 percent, using the expression given in ASTM Practice G 30-90. In order to compare the behavior in constant-deflection tests of the two heats of type 316L SS, U-bend specimens were prepared from the plate after reducing its thickness from 12.7 mm (0.5 in.) to 3.175 mm (0.125 in.). After bending, the specimens were cleaned in 10 percent HNO_3 at room temperature for 1 hr to remove any accidental surface contamination with steel particles produced during the bending operations. The specimens were then rinsed in deionized water.

4.2.1 Slow Strain Rate Tests

The SSRTs were conducted according to an international standard (International Organization for Standardization, 1989) using machines in which the pull rods holding the specimens were electrically isolated from the frame. Solutions (approximately 350 mL in volume) were contained in electrochemical cells made of glass and PTFE. The temperature was maintained at the desired value by using external heating tapes, a platinum resistance temperature detector (RTD), and a temperature controller. The cells were fitted with a gas bubbler and a water-cooled condenser connected to a water trap to prevent evaporation of water and back-diffusion of air. A platinum electrode and a SCE were used as counter and reference electrodes, respectively. A Luggin capillary with a porous silica tip connected the cell, through a salt bridge containing a cotton wick, to the SCE, which was located in a separate reservoir at room temperature. Accordingly, all the potentials are referred to the SCE scale at ambient temperature (22 °C), without correction for the thermal diffusion potential along the nonisothermal salt bridge.

Most of the tests were conducted under potentiostatic conditions. Potentials were controlled using an Electrosynthesis Model 440 multichannel potentiostat, connected through a Strawberry Tree ACPC-16-16, 16-bit, 16-channel ADC and an ACAO 12-8, 12-bit, 8-channel DAC to an Austin 386 computer. In addition to the potential and the current, measured as a potential drop through a 10-ohm resistor, voltage signals from load cells and linear voltage differential transducers (LVDT) were also fed into the ADC through appropriate signal conditioners. The load cells and the LVDT were used to measure the load on the specimen and its extension, respectively, during the course of the test. The data acquisition was performed using the Workbench® software. This software is an icon-based program through which external instruments are controlled, signals are acquired, and algebraic and logical operations can be performed in order to obtain the required data in the appropriate units. The data were then stored on a magnetic disk for further analysis. In addition, the potential and the current were checked independently by using a Keithley Model 614 electrometer and a Keithley Model 485 picoammeter, respectively. The load cells and the LVDTs, in conjunction with their corresponding signal conditioners, were calibrated using a proving ring and a micrometer, respectively, as standards.

In the initial set of SSRTs, the solutions contained 85 ppm HCO_3^-, 10 ppm NO_3^- and 2 ppm F^-, with the addition of 1,000 or 10,000 ppm Cl^- and 20, 1,000, or 10,000 ppm SO_4^{2-}. All these double anions were added as Na^+ salts. The solutions were prepared with reagent grade chemicals and double DI water. Solution compositions were selected on the basis of the localized corrosion studies reported in Section 3.3.1.2, in which E_p, E_{rp}, and E_{corr} values for type 316L SS and alloy 825 were determined. All these tests were conducted at 95 °C under potentiostatic conditions, and the solutions were purged either with N_2 gas to remove the dissolved oxygen, or with CO_2 to attain a pH close to 5.0, simultaneously removing oxygen. A single test was conducted under open-circuit conditions. In this case, synthetic air ($79\%N_2$—$21\%O_2$) was bubbled into the solution. In some tests, the pH of the solutions was initially adjusted to pH 4.0 by the addition of HCl.

A second set of tests was conducted in the same solutions as above with the addition of 0.001 or 0.01 mol/L of $Na_2S_2O_3$. These tests were performed at 95 °C, and the solutions were purged with CO_2. A third set of SSRTs was performed in concentrated chloride solutions, prepared with salts of different cations (Mg^{2+}, Li^+, and Na^+) but without the presence of additional anions. The solutions in this set of tests were fully deaerated with nitrogen. Additional tests were conducted in concentrated NaCl solutions with the addition of thiosulfate to compare the behavior of alloy 825 with that of type 316L SS. In these tests, the solutions were purged with CO_2 and the temperature was 95 °C. Several tests were performed using a specially designed crevice-forming device, made of perfluoroalkoxy (PFA) tubing and a PTFE holder, mounted in the gage length of the smooth tensile specimens. These tests were conducted either under potentiostatic or galvanostatic control in 1 M NaCl solution, acidified to pH 4.0, to determine if cracks can be initiated under occluded cell conditions leading to active crevice corrosion.

An extension rate of 1.27×10^{-5} mm/s (5.0×10^{-7} in./s), which represents an initial strain rate of 1.0×10^{-6} s^{-1} for the smooth tensile specimens, was used in the first series of SSRTs. For the notched specimens, this nominal extension rate may represent a strain rate at the notch tip at least two orders of magnitude greater than that for the smooth specimens. The extension rate was reduced to 4.6×10^{-6} mm/s (1.8×10^{-7} in./s) and to 2.8×10^{-6} mm/s (1.1×10^{-7} in./s) in several tests to increase the sensitivity of the slow strain rate technique.

After a specimen was mounted inside the cell, the solution was purged with the selected gas and then heated to the desired temperature. The specimen was allowed to attain a steady-state corrosion potential before the selected potential was applied. In tests conducted under galvanostatic conditions, a constant current was applied, and the corrosion potential was monitored during the course of the test. An initial load of approximately 133 N (30 lb) was applied to the specimen, and straining was started as soon as a steady current or potential was obtained. After failure, the fracture and side surfaces of all specimens tested were examined with a stereoscope. Selected specimens were further examined in the SEM. Such examination was conducted after corrosion products deposited in the fracture and side surfaces were ultrasonically removed using a solution of 3 mL of concentrated HCl in 50 mL of double-deionized water, inhibited with 4 mL of 2-butyne-1,4 diol (35-percent aqueous solution).

4.2.2 Constant-Deflection Tests

Constant-deflection tests were conducted simultaneously in four 1-L glass cells using the experimental setup described previously (Sridhar and Cragnolino, 1993b; Sridhar et al., 1993a). Two U-bend specimens were tested simultaneously in each cell. Except when noted, the specimens were partially immersed in the solutions such that the legs of the U-bend were in the vapor space while the apex of the bend was completely submerged in the liquid. In addition to the single U-bend specimens, several tests were conducted using double U-bend specimens to create a crevice environment at the apex of the inner U-bend where the tensile stresses reached the highest value. One of the specimens was exposed to the solution at a controlled anodic potential, whereas the second one was maintained under open-circuit conditions. The multichannel potentiostat and the remaining electronic instrumentation for controlling the potential and for data acquisition were similar to that described above for the SSRTs.

The constant-deflection tests were performed in most of the solutions used for SSRTs. Solutions containing 1,000 ppm chloride with and without the addition of $Na_2S_2O_3$ were used in some tests. Concentrated chloride solutions prepared with either $MgCl_2$, LiCl or NaCl reagents were used to compare the effect of the cations on the SCC behavior of both type 316L SS and alloy 825. These solutions were prepared using double-deionized water with the pH adjusted to 4.0. In some tests, $Na_2S_2O_3$ was added to concentrated chloride solutions to compare the results with those from the SSRTs. The constant- deflection tests were conducted in successive periods of 21 to 28 d. At the end of each period, the specimens were optically examined at a magnification of about 70x after being cleaned using an ultrasonic cleaner. If no signs of SCC or severe localized corrosion were detected, the same specimens were exposed, using freshly prepared solutions, to identical environments for an additional time interval. In all these tests, the temperature of the solutions was maintained at 95 °C. Selected specimens were examined in the SEM, and then cross-sectioned and mounted for metallographic observation of cracks.

4.3 RESULTS

4.3.1 Type 316L Stainless Steel

4.3.1.1 Slow Strain Rate Tests

As noted previously, one of the main objectives of these tests was to demonstrate a possible relationship between the repassivation potential for pitting/crevice corrosion and a critical potential for SCC that defines the lower limit of the susceptibility range. To select the appropriate potentials for SSRT of type 316L SS, E_p, E_{rp}, and E_{corr} obtained at 95 °C on unstressed specimens, using CPP tests at a scan rate of 0.167 mV/s (Sridhar et al., 1993a), were obtained as a function of chloride concentration, as shown in Figure 3-6. Following an abrupt decrease at low chloride concentrations, both E_p and E_{rp} decrease linearly with the logarithm of chloride concentration at concentrations above 100 ppm. These two potentials define a potential range that contracts from approximately 400 mV at 100 ppm Cl^- to 200 mV at 10^5 ppm Cl^- as shown in Figure 4-1, in which the data points are not included. This potential range is that within which SCC could be expected (Cragnolino and Sridhar, 1992a), because pitting corrosion should predominate at higher potentials, whereas at lower potentials any tendency to crack initiation would be overcome by the repassivation of the locally damaged passive film. Using this basis, SSRTs and U-bend tests were conducted at potentials located between E_p and E_{rp} in a variety of chloride-containing solutions. Complete details of all SSRTs are provided in tabular form in the Appendix D. Slow strain rate control tests conducted in glycerine, an inert environment, at 95 and 120 °C, resulted in a completely ductile failure with 60.4 and 54.4 percent elongation, respectively. The data are shown in Table D-1.

The results of SSRTs conducted on type 316L SS in NaCl solutions with chloride concentrations ranging from 1,000 to 35,450 ppm (0.028 to 1 molar Cl^-) at 95 °C are summarized in Figure 4-1. Additional details are provided in Tables D-2 and D-3. It is seen that no SCC was observed in any test using either 1,000 or 10,000 ppm Cl^-, even at relatively high potentials within the potential range defined by E_p and E_{rp}. The elongation to failure was found to be 55.6 percent on average for all the smooth tensile specimens exhibiting ductile failure with a standard deviation of approximately 10 percent, indicating a high degree of ductility but a relatively large dispersion in the elongation values. In a single case, a specimen failed as a result of severe pitting corrosion, exhibiting an elongation of only 20.2 percent. In other tests, predominantly ductile failure accompanied by pitting corrosion was observed leading to a reduced elongation to failure as compared to the cases in which purely ductile failure occurred. It can be concluded from these results that in prolonged tests, pitting is initiated at potentials lower than E_p measured in CPP tests but the pits do not seem to act as initiation sites for cracks under these experimental conditions. All these tests were conducted potentiostatically, with the exception of one test carried out under open-circuit conditions in which synthetic air (79 vol% N_2—21 vol% O_2) was bubbled into the solution. The corrosion potential decreased during the test from 0 to −200 mV_{SCE}, but only ductile failure was observed.

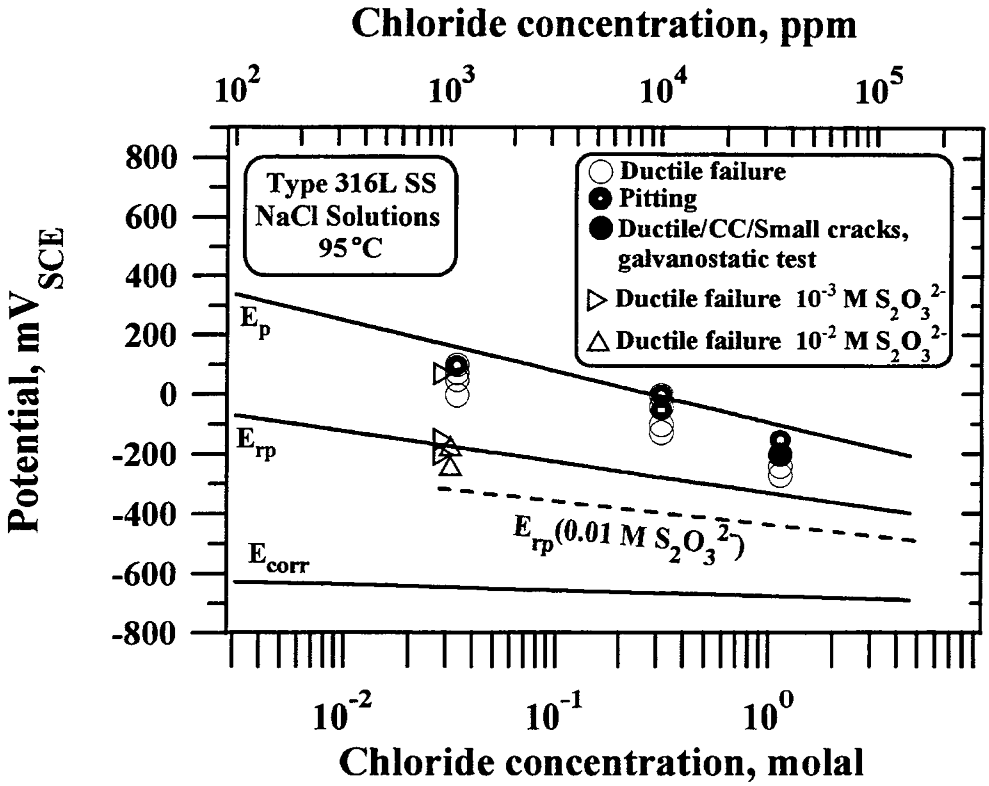

Figure 4-1. Results of slow strain rate tests of type 316L stainless steel in dilute chloride solutions at 95 °C with and without the addition of thiosulfate, in relation to pitting (E_p) and repassivation (E_{rp}) potentials

No SCC was observed, even in some specific tests conducted in 1,000 ppm Cl^- in which a piece of PTFE tape was wrapped around the gage section of tensile specimens in order to promote crevice conditions that may lead to crack initiation. Using the tensile specimen with the improved crevice device, some small cracks were observed in a 1 M NaCl solution adjusted to pH 4 at a strain rate of $2.2\times10^{-7}s^{-1}$. The potential of this specimen, tested galvanostatically using a current of 10 µA, varied between −160 and −250 mV_{SCE}. Although small cracks were apparent, crevice corrosion and ductile failure were the dominant features. Small cracks were also observed in two additional specimens tested galvanostatically using currents of 3 and 50 µA, in which the failures were ductile but accompanied by extensive crevice corrosion. The results of these tests are summarized in Table D-3 (Appendix D) and are also indicated in Figure 4-1.

The use of notched specimens did not lead to the initiation of cracks, although an O-ring was used to create crevice conditions. It was expected that a notch would facilitate crack initiation by localized intensification of the stress, avoiding the simultaneous initiation at several cracks. However, it appears that the extension rate at the root of the notch was too high, and ductile failure occurred before any crack could be initiated. It should be noted that the failure times for tests conducted with notched specimens were shorter than those for tensile specimens, by a factor of about four, which significantly decreases the exposure time. It appears that the extension rate should be reduced, at least by an order of magnitude, to promote crack initiation in a notched specimen.

Slow strain rate tests were conducted in solutions containing 1,000 ppm chloride with the addition of thiosulfate, based on the suggestion of Lott and Alkire (1989) that thiosulfate can be generated by the dissolution of MnS inclusions present in certain austenitic SSs, such as type 304 SS and 316. In addition, thiosulfate is an anionic species of interest because it can be formed as a byproduct of the metabolism of sulfate-reducing bacteria (Geesey, 1993). In conjunction with chloride, thiosulfate promotes passivity breakdown in these alloys. It is known that transgranular cracking of quench-annealed austenitic SSs in chloride solutions initiates from localized corrosion trenches or slots where breakdown of the passive films occurs (Silcock and Swann, 1979). Concentrations of thiosulfate equal to 0.001 and 0.01 mol/L were chosen because Newman et al. (1982) reported the most significant decrease in the pitting potential of type 304 SS in chloride-containing solutions by the addition of thiosulfate within that range of concentrations. Potentials were selected to avoid widely distributed pitting corrosion and then adjusted during the course of the test to avoid significant increases in current associated with pit initiation.

No SCC was observed in the presence of 0.001 or 0.01 M of $Na_2S_2O_3$ even at an applied potential 280 mV above the open-circuit potential. The results of these tests are summarized in Table D-4 (Appendix D) and shown in Figure 4-1 for comparison to those conducted in the absence of thiosulfate. SCC did not occur in tests conducted in solutions containing 0.01 mol/L $Na_2S_2O_3$ even though the extension rate was decreased more than four times, which implies that the severity of the tests was increased with respect to that conducted at the low-thiosulfate concentration. The use of a notched specimen did not lead to crack initiation, even though an O-ring was used to create crevice conditions and a very low extension rate was applied. No SCC occurred after 950 hr of straining, and the test was, therefore, interrupted.

A final test of this series with the addition of thiosulfate was conducted using a solution-annealed (SA) specimen of type 316L SS to evaluate if the SA material was more susceptible to SCC than that in the MA condition. An elongation to failure of 69.4 percent was obtained in this test, indicating that pure ductile failure occurred as confirmed by stereoscopic examination. The elongation to failure was similar to that obtained for MA materials in the absence of localized corrosion.

Four tests was conducted under constant elongation conditions using smooth tensile specimens at the open-circuit and anodic-applied potentials (Table D-5 in Appendix D). Two of these tests were conducted in a solution containing 1,000 ppm Cl^- with the addition of 0.01 M $Na_2S_2O_3$. The pH was adjusted to 4.0 by the addition of HCl, and the solution was purged with synthetic air to attain a higher open-circuit potential. Both specimens were loaded initially up to 105 percent of the nominal yield point. After 476 hr of testing without any signs of crack initiation and growth as indicated by the lack of load relaxation, the load was increased to 130 percent of the yield point. No load relaxation was observed during the subsequent 456-hr period, and both tests were then terminated. Localized corrosion was observed, but no cracks were detected on the specimen surfaces. Two tests were performed on smooth specimens having a crevice device placed on the gauge length in a solution containing 1 M NaCl, with and without the addition of 0.01 M $Na_2S_2O_3$. These tests were conducted galvanostatically with a current of 1–3 μA. Crevice corrosion was observed on the specimen tested in the solution containing thiosulfate. Nevertheless, in agreement with the results of comparable SSRTs conducted in 1 M NaCl, no SCC was observed as indicated by the lack of load relaxation and the microscopic examination of specimen surfaces.

Figure 4-2 summarizes the results of the set of tests conducted in various concentrated chloride solutions of different cations using smooth tensile specimens. These solutions were selected to increase the concentration of chloride ions beyond that obtained with NaCl as an electrolyte and to be able to

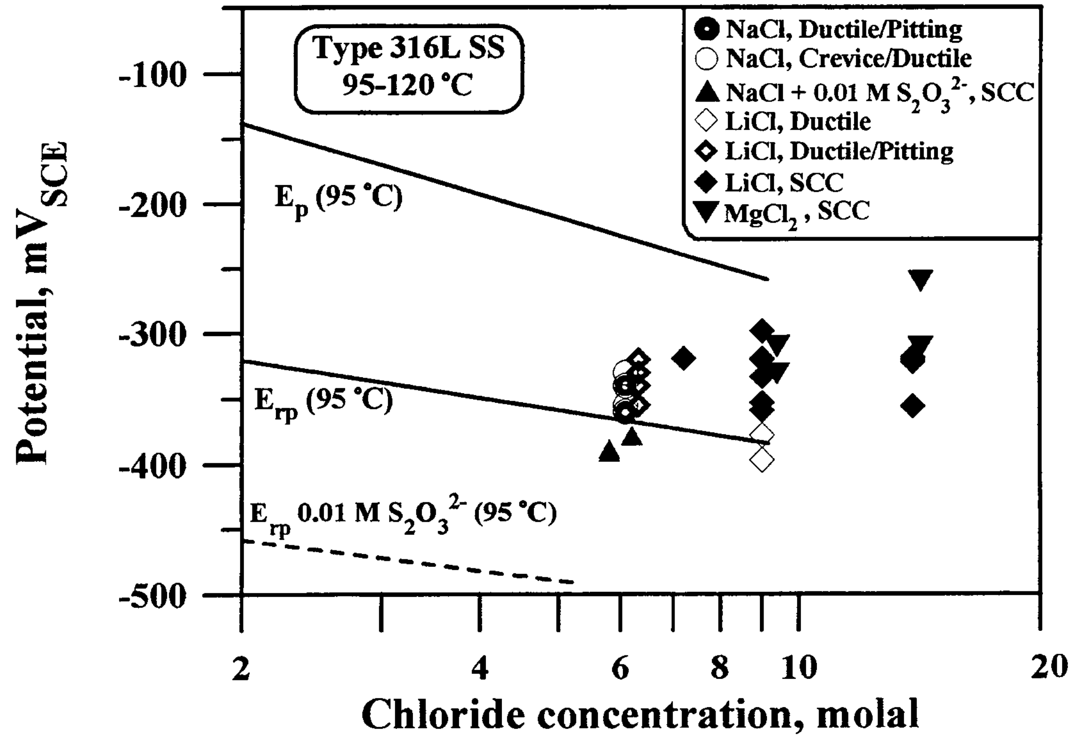

Figure 4-2. Results of slow strain rate tests of type 316L stainless steel in concentrated chloride solutions ($MgCl_2$, LiCl, and NaCl) in terms of potential and chloride concentration at temperatures ranging from 95 to 120 °C. Failure modes after testing are indicated.

conduct tests under atmospheric pressure at temperatures higher than 100 °C. E_p and E_{rp} as a function of chloride concentration are plotted in Figure 4-2 using data obtained in CPP tests. The initial tests of this set were conducted at 120 °C in 40 percent $MgCl_2$ solution (14.0 molal Cl^-) at the corrosion potential (approximately −300 mV_{SCE}) and at a slightly anodic potential (−280 mV_{SCE}). SCC was observed under both conditions, in which elongation values of 7.4 and 4.6 percent were obtained, respectively. Similar results were obtained at a lower temperature (110 °C) in a less concentrated solution (30 percent $MgCl_2$) in which the chloride concentration was 9.1 molal. In this case again, a decrease in the elongation to failure from 49.4 to 15.2 percent was observed by increasing the potential to slightly anodic values with respect to the open-circuit potential.

Extensive secondary cracking was observed on the side surfaces of these specimens (Figure 4-3), with the exception of the specimen tested at the open-circuit potential in the less concentrated solution in which very few incipient cracks were detected. Fractographic examination revealed that, besides the "cleavage-like" features (Figure 4-4) typical of the transgranular cracking of austenitic SSs in boiling $MgCl_2$ solutions (Scully, 1971), intergranular cracking occurred over a large proportion of the fracture surface (Figure 4-5). An overall view of the fracture surface seems to indicate that cracking initiated transgranularly but propagated mostly in an intergranular fashion through the specimen (Figure 4-6). The proportion of intergranular cracking diminished with the decrease in the severity of the environment, in terms of chloride concentration and temperature, and also with the decrease in potential.

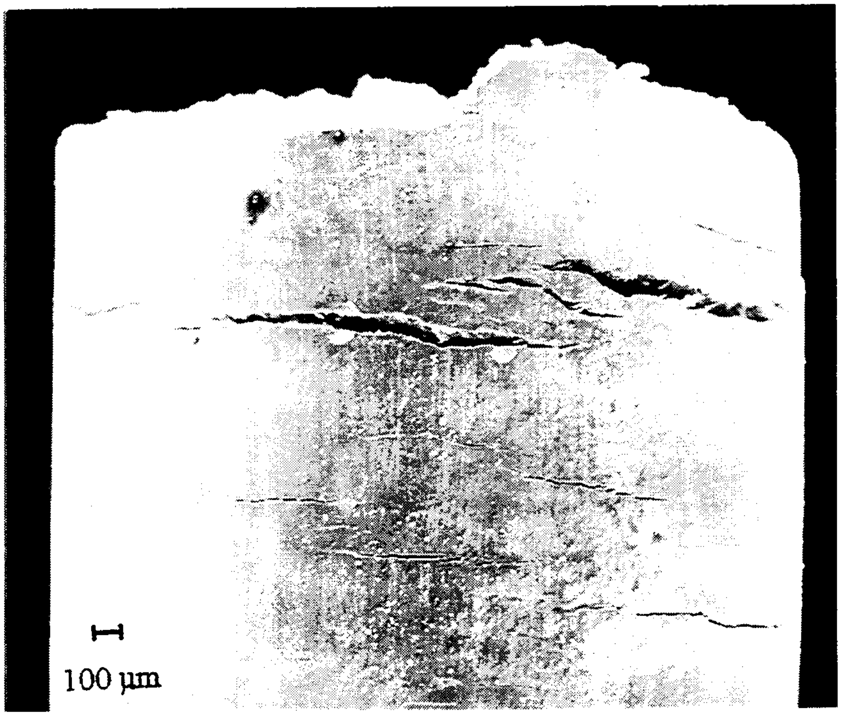

Figure 4-3. Side surface of the type 316L stainless steel specimen tested under open-circuit conditions in 40 percent $MgCl_2$ solution at 120 °C showing the presence of many secondary cracks

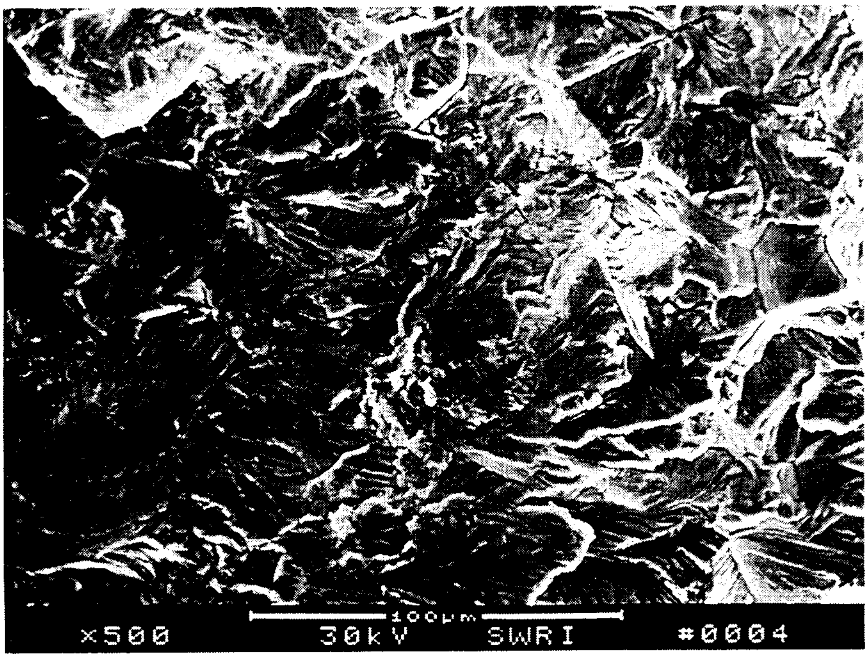

Figure 4-4. Fractograph showing the transgranular stress corrosion cracking area of the type 316L stainless steel specimen tested under open-circuit conditions in 40 percent $MgCl_2$ solution at 120 °C

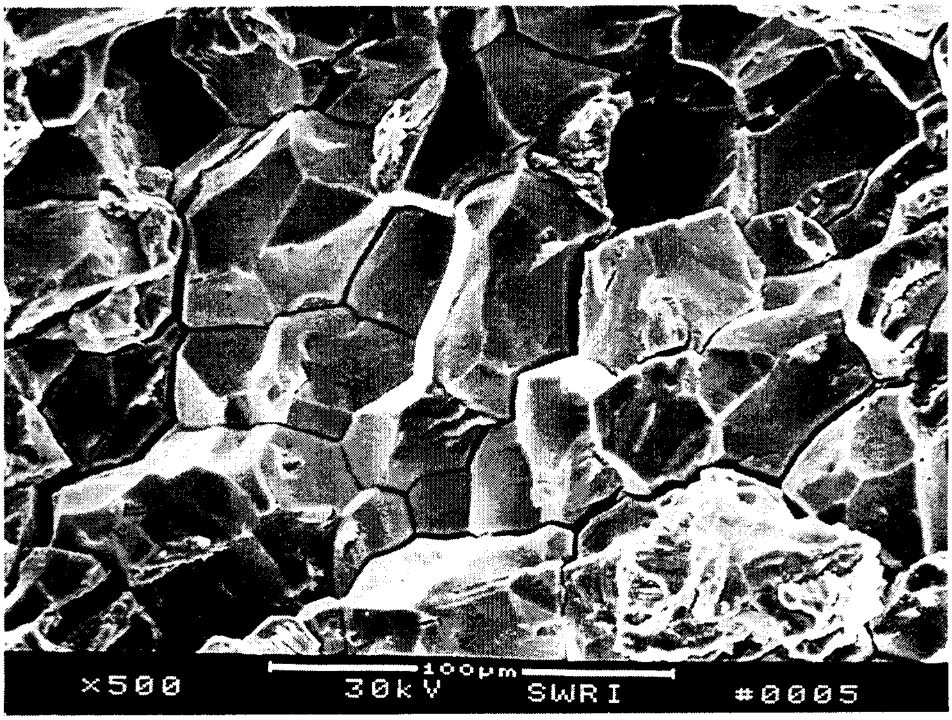

Figure 4-5. Fractograph showing the intergranular stress corrosion cracking area of the type 316L stainless steel specimen tested under open-circuit conditions in 40 percent $MgCl_2$ solution at 120 °C

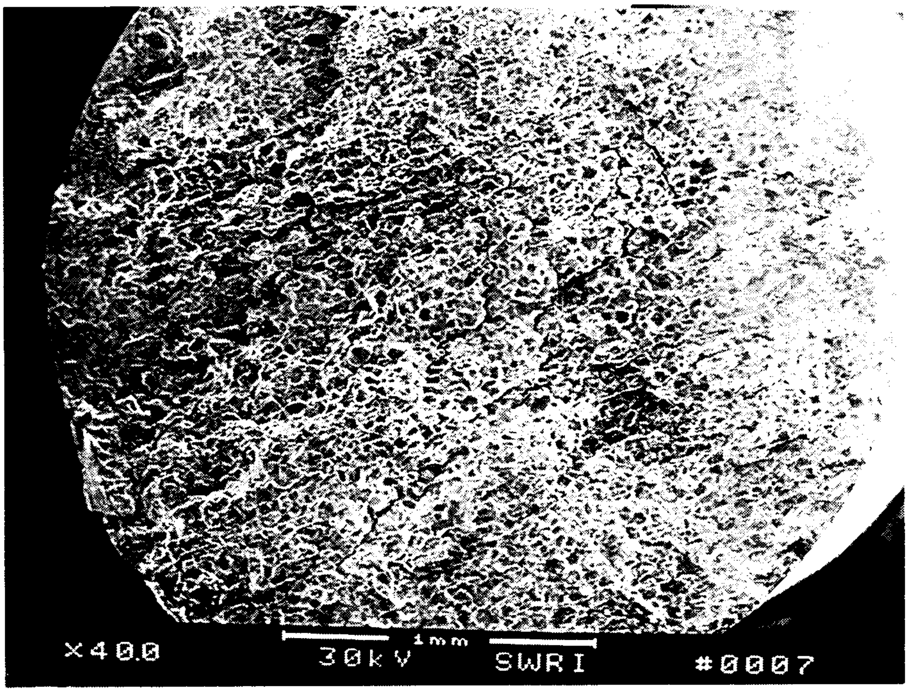

Figure 4-6. Overall fracture surface of type 316L stainless steel specimen tested under open-circuit conditions in 40 percent $MgCl_2$ solution at 120 °C

SCC was also observed in tests conducted at temperatures ranging from 120 to 95 °C in concentrated LiCl (≥ 7.2 molal) solutions acidified by the addition of HCl. The pattern was similar to that found in $MgCl_2$ solutions at equivalent chloride concentrations and temperatures. SCC occurred under open-circuit conditions, but cracking susceptibility increased significantly with anodic polarization. These observations were confirmed by fractographic examination. Extensive areas of intergranular and transgranular SCC were observed in these fractographs (Figures 4-7 and 4-8). It appears, however, that the proportion of intergranularly cracked areas was smaller than observed under equivalent conditions in $MgCl_2$ solutions. The susceptibility to SCC, as evaluated from the elongation to failure values and the appearance of the fracture surfaces, decreased with decreasing chloride concentration and temperature.

Several tests were conducted at 95 °C in concentrated NaCl and LiCl solutions (6.2 molal Cl^-) in which the pH was adjusted to 2.5±0.02 by the addition of HCl. This chloride concentration was chosen because it is close to the solubility of NaCl at 95 °C, which is equal to 6.7 molal (Linke, 1965). Since SCC was not observed in these tests, additional tests were conducted in which the strain rate was decreased to $2.2 \times 10^{-7}\ s^{-1}$ to increase the sensitivity of the technique. No SCC was observed in this series of tests in which open-circuit and anodic conditions were tested under both potentiostatic and galvanostatic control. Indeed, galvanostatic tests were used in an attempt to avoid the occurrence of pitting corrosion by limiting the applied current to values typical of the passive range. This galvanostatic control was reflected in corrosion potentials during straining ranging from −350 to −380 mV_{SCE}, which are just below E_p. Nevertheless, pitting corrosion still accompanied the ductile failure. No signs of cracks were observed on the side surfaces of these specimens. As noted before, details of these tests are presented in Table D-6 in Appendix D.

Several stress-versus-elongation curves obtained in some of the tests conducted in concentrated LiCl solutions are plotted for comparison in Figure 4-9. The different curves represent the range of behavior from severe SCC to ductile failure with minor pitting corrosion. The significant decrease in ductility promoted by the application of an anodic overpotential of only 30 mV with respect to the corrosion potential is clearly seen in the curves for the 9.1 molal LiCl solution at 110 °C. The slow relaxation of the load, caused by the propagation of cracks, is particularly noticeable in this test. On the other hand, a very high elongation to failure, close to 55 percent, accompanied by a sudden drop in the load characterizes the predominantly ductile behavior in the 6.2 molal LiCl solution at 95 °C.

The results of the tests conducted in concentrated LiCl solutions are presented as a function of chloride concentration in Figure 4-10 to illustrate the important effect of this variable on the elongation to failure ratio, defined as the elongation to failure in the solution to that in an inert environment at the same temperature. A significant decrease in the elongation to failure ratio at chloride concentrations greater than 6.2 molal, which levels off at higher concentrations, is shown in Figure 4-10. The effect of temperature on the elongation to failure ratio at two chloride concentrations is shown in Figure 4-11. The effect of potential on the results of the SSRTs conducted in 9.1 molal LiCl solutions at 95 °C is shown in Figure 4-12. An increase in the applied potential promoted cracking which is evident from the decrease in the elongation to failure ratio at potentials above the repassivation potential for localized corrosion.

Smooth tensile specimens of type 316L SS were also tested in concentrated NaCl solutions containing 0.01 M $Na_2S_2O_3$ with the pH adjusted to 4.0 by the addition of HCl. SCC of MA type 316L SS was observed at the open-circuit potential, which was found to be −390 mV_{SCE}, a value approximately 40 mV lower than that in the absence of thiosulfate, and also at low-anodic potentials (−420 to −390 mV_{SCE}). The elongation to failure in these two tests, 12.2 and 18.0 percent, was very low, indicating

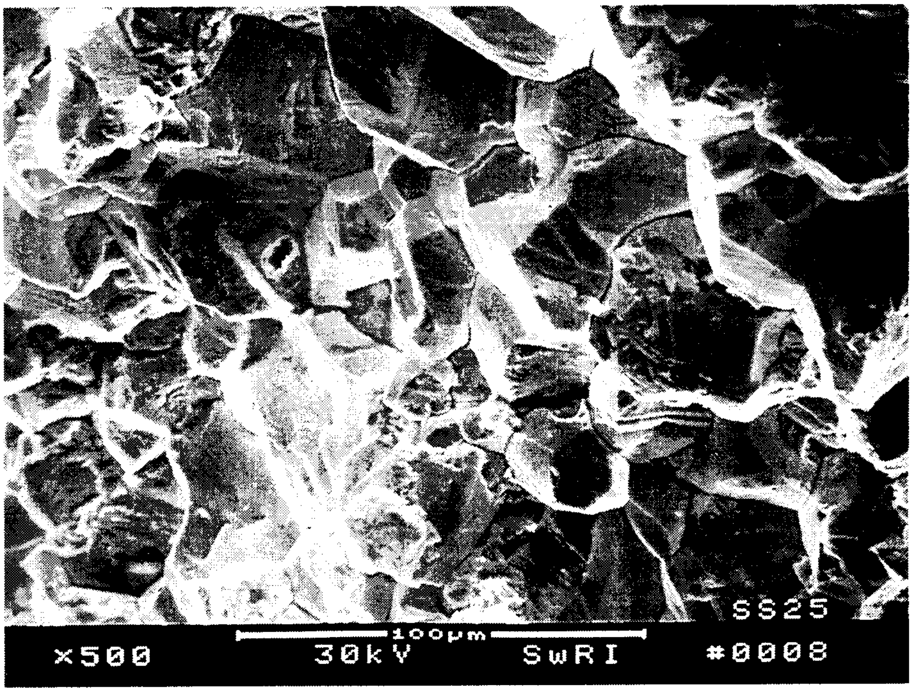

Figure 4-7. Fractograph showing the intergranular stress corrosion cracking area of the type 316L stainless steel specimen tested under an anodic potential in 13.9 molal LiCl solution at 120 °C

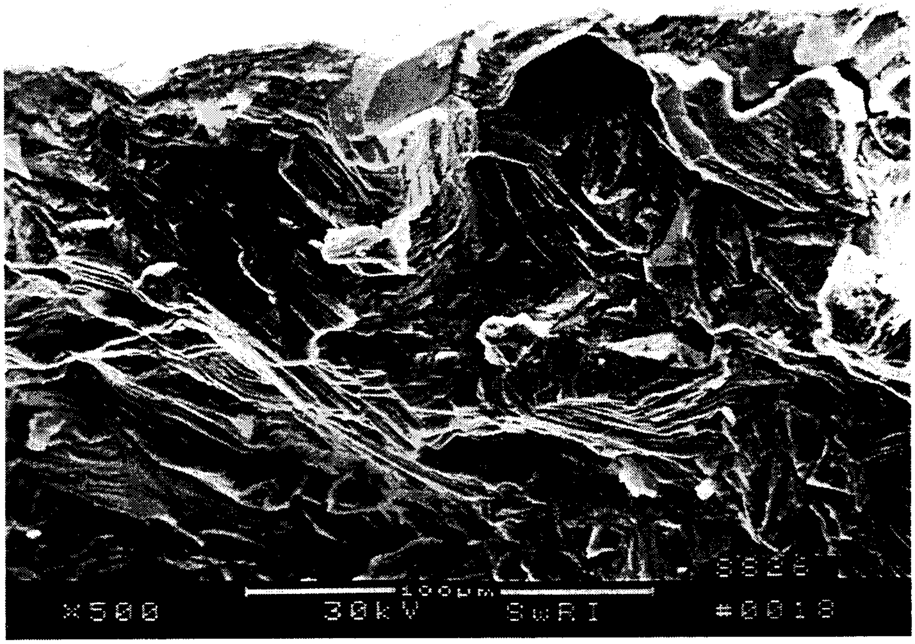

Figure 4-8. Fractograph showing the transgranular stress corrosion cracking area at the edge of the fracture surface in the type 316L stainless steel specimen tested under open-circuit conditions in 13.9 molal LiCl solution at 120 °C

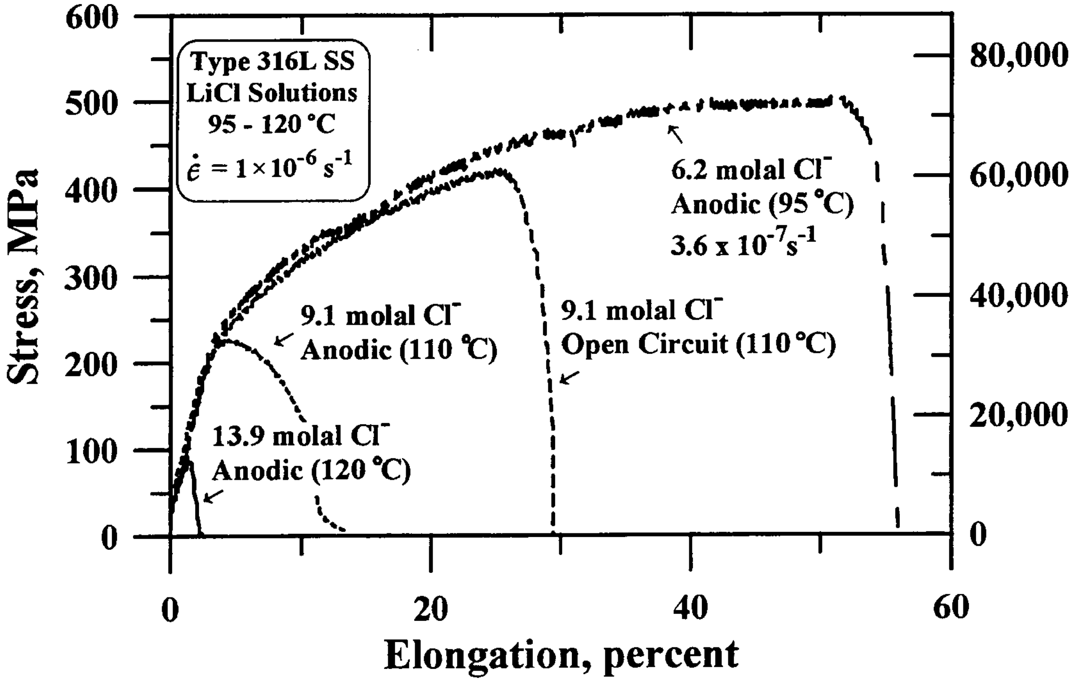

Figure 4-9. Stress versus elongation curves obtained in slow strain rate tests of type 316L stainless steel in concentrated LiCl solutions at temperatures ranging from 95 to 120 °C

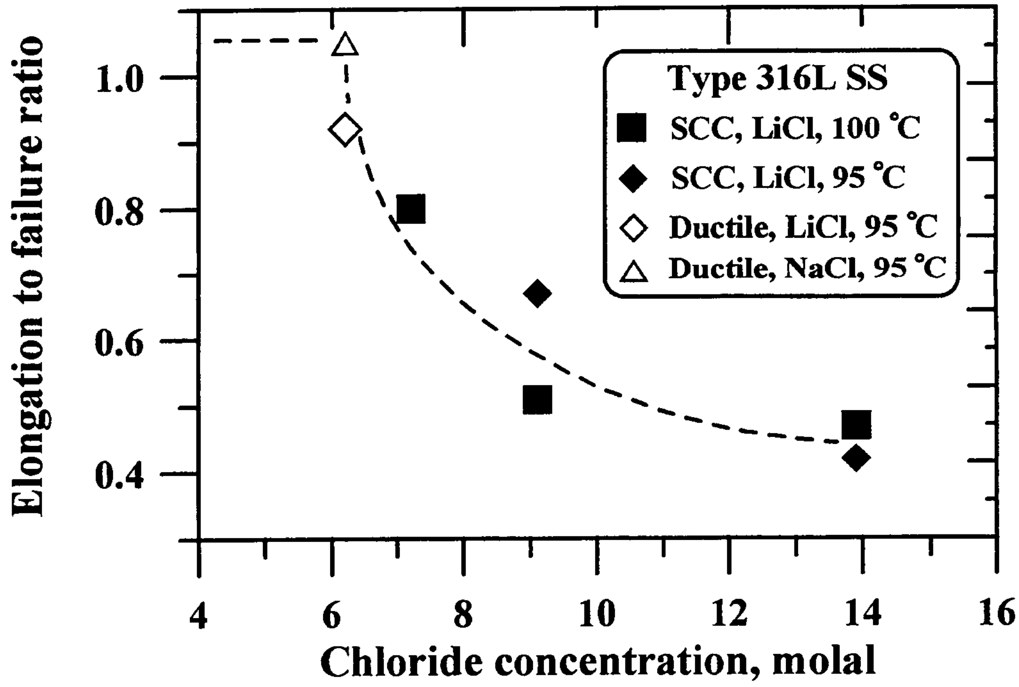

Figure 4-10. Elongation to failure ratio as a function of chloride concentration for slow strain rate tests of type 316L stainless steel in LiCl solutions at 95 and 100 °C under open-circuit conditions

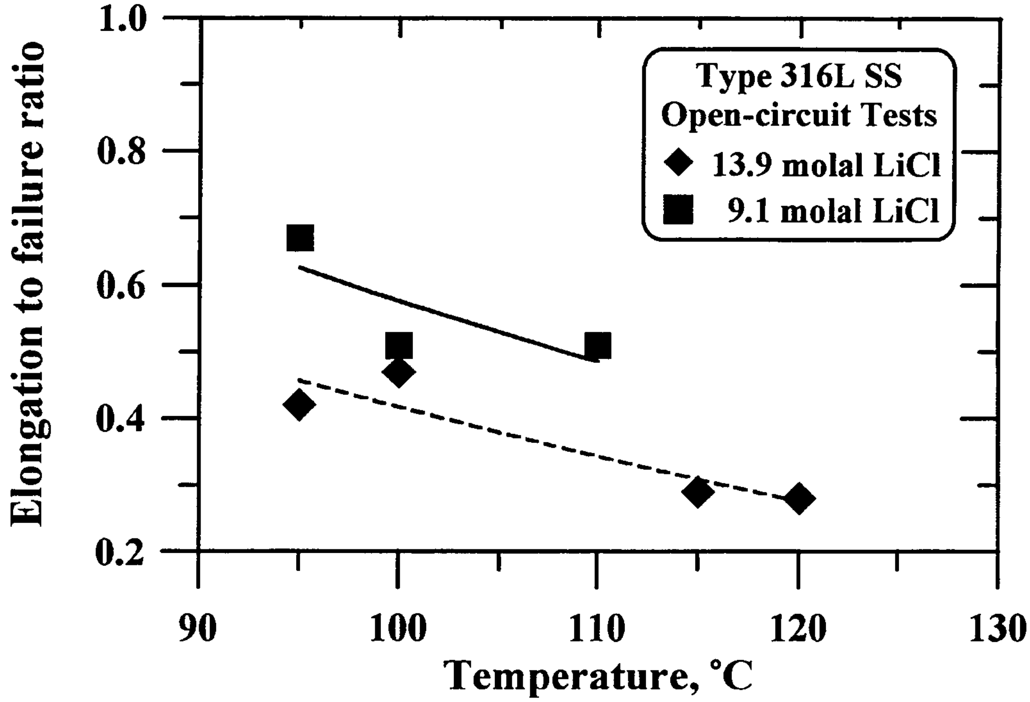

Figure 4-11. Elongation to failure ratio as a function of temperature for slow strain rate tests of type 316L stainless steel in 9.1 and 13.9 molal LiCl solutions under open-circuit conditions

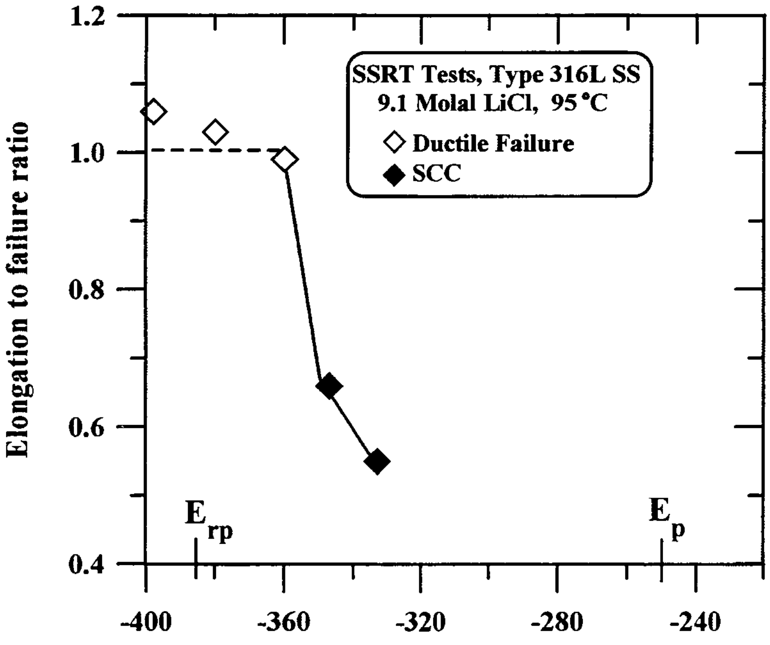

Figure 4-12. Results of slow strain rate tests of type 316L SS in 9.1 molal LiCl solution at 95 °C showing the effect of potential. E_{rp} and E_p were measured in CPP tests at 0.167 mV/s scan rate.

a significant susceptibility to SCC in this environment. To avoid the occurrence of pitting corrosion, the potential in the test conducted potentiostatically was maintained during most of the test time below the open-circuit potential, which may explain the increased elongation to failure obtained in this test with respect to that under open-circuit conditions. Figures 4-13 and 4-14 show the typical appearance of the fracture surfaces observed in these tests in which the coexistence of intergranular and transgranular cracking can be clearly noted. For comparison, a SA specimen of type 316L SS was tested at the open-circuit potential in the same solution. The elongation to failure, 11.4 percent, was similar to that for the MA specimen. Details are provided in Table D-7.

4.3.1.2 Constant-Deflection Tests

U-bend specimens of type 316L SS were tested in either an upright orientation with the apex of the bend immersed in solution or an inverted orientation where the legs of the U-bend were immersed and the apex of the bend was continuously above the solution level. A schematic of the specimen orientations is shown in Figure 4-15. The results of upright U-bend tests of 316L SS are shown in Figure 4-16. (Additional details are shown in Table D-8.) For specimens tested in 1,000 ppm Cl^-, the incidence of SCC was greater on specimens tested under applied anodic potentials as compared to those tested under both open-circuit conditions. As previously reported, the cracks were found above the vapor/solution interface on the legs of the specimens despite the fact that the legs are the less stressed part of the U-bend specimens (Cragnolino et al., 1994a, 1995). Cracks were detected in as short as 22 days on some specimens to as long as 77 days for others. Pitting, which occurred predominantly at the vapor/solution interface, occurred on all specimens tested.

Cracking was found to be more severe in the presence of thiosulfate, even though the addition of this species decreased the corrosion potential by approximately 100 mV in solutions purged with the N_2/O_2 gas mixture simulating air. As in the case of plain chloride solutions, cracks were always found above the vapor/solution interface. Cracks on all specimens were detected in time intervals varying between 12 to 49 days of testing.

In concentrated chloride solutions, SCC was observed in all the U-bend specimens with the exception of one specimen tested in 6.2 molal NaCl solution at the open-circuit potential, in which pitting corrosion instead of SCC was observed in the bend area. LiCl solutions appear to be marginally more aggressive in terms of promoting SCC, because SCC was observed in all the tests conducted in solution containing at least a chloride concentration equal to 5.8 molal, regardless of the application of an anodic overpotential. In the case of NaCl solutions, no SCC was detected under open-circuit conditions at 6.2 molal, but this test lasted only 288 hr. On the other hand, the addition of thiosulfate or the application of an anodic overpotential promoted cracking in the same time interval. In this concentrated chloride solution, the addition of thiosulfate did not have any significant effect on the corrosion potentials, which were about -350 ± 20 mV_{SCE} in most of these tests. Severe SCC was observed on the specimen tested under open-circuit conditions in 9.1 molal LiCl (E_{corr}=350 mV_{SCE}) after 28 days of testing. In contrast, no SCC was noted on the portions of a companion specimen exposed to the solution at a cathodic potential of -400 mV_{SCE}. However, small cracks were detected above the vapor/solution interface, even in the less stressed part of the specimen. Additional details of these tests are included in Table D-9.

Inverted U-bend tests were conducted with specimens oriented such that the apex of the bend was continuously above the solution level. The results of these tests, as summarized in Table D-10 and shown in Figure 4-17, indicate that SCC was observed after 28 days in a 1,000 ppm Cl^- solution with

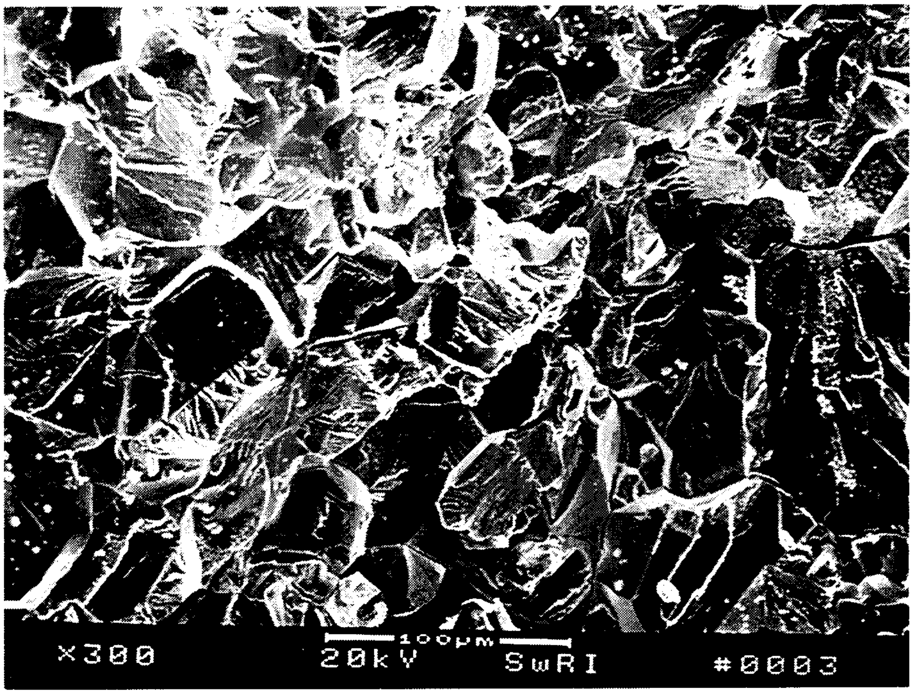

Figure 4-13. Fractograph showing a predominantly transgranular cracked area in the fracture surface of the type 316L stainless steel specimen tested under open-circuit conditions in 5.8 molal NaCl solution with the addition of 0.01 M $Na_2S_2O_3$ at 95 °C

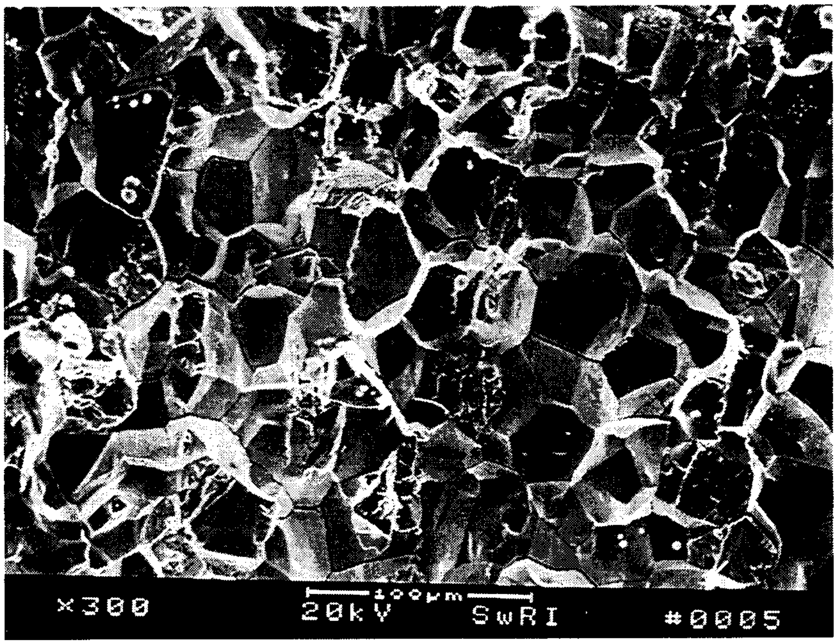

Figure 4-14. Fractograph showing the intergranular cracked area in the fracture surface of the type 316L stainless steel specimen tested under open-circuit conditions in 5.8 molal NaCl solution with the addition of 0.01 M $Na_2S_2O_3$ at 95 °C

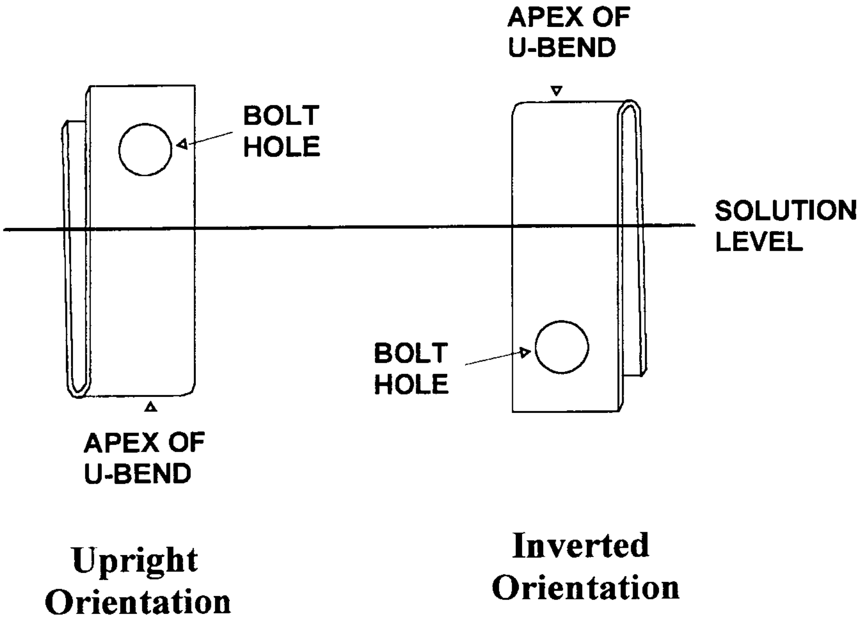

Figure 4-15. Schematic drawing showing the orientation of the U-bend specimens for constant deflection tests

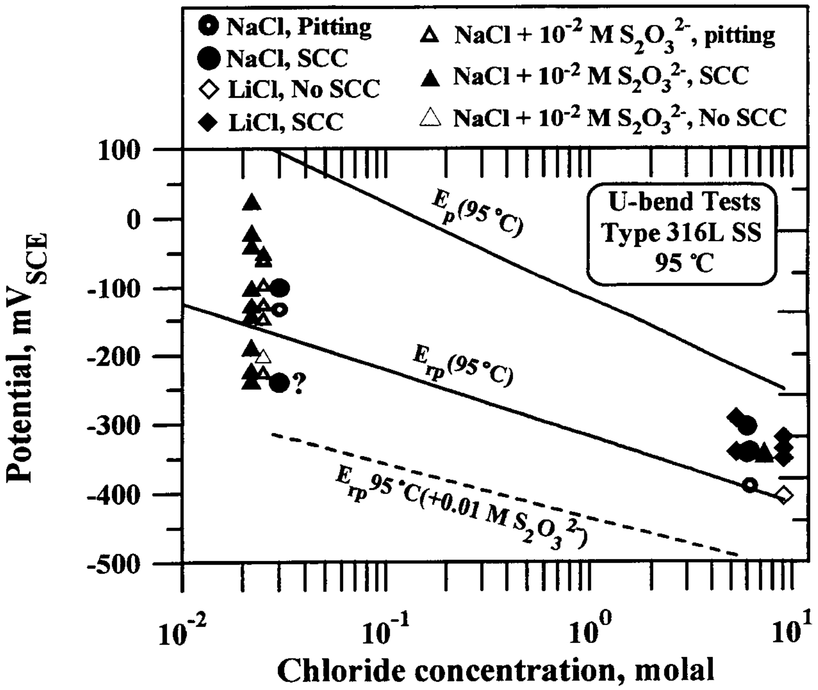

Figure 4-16. Results of constant-deflection tests using U-bend specimens of type 316L stainless steel in chloride solutions, with and without the addition of thiosulfate, in terms of potential and chloride concentration at 95 °C

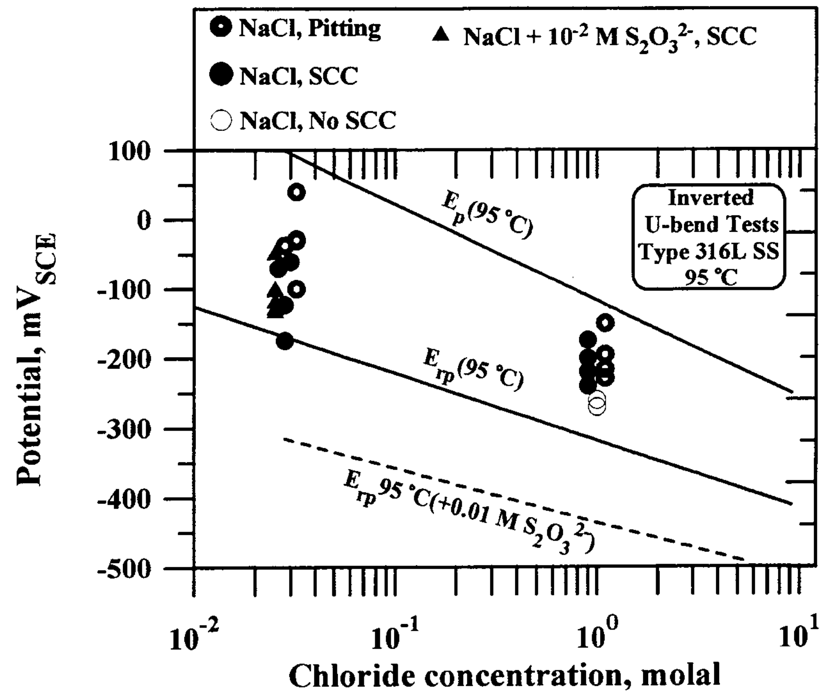

Figure 4-17. Results of constant-deflection tests using inverted U-bend specimens of type 316L stainless steel in chloride solutions, with and without the addition of thiosulfate, in terms of potential and chloride concentration at 95 °C

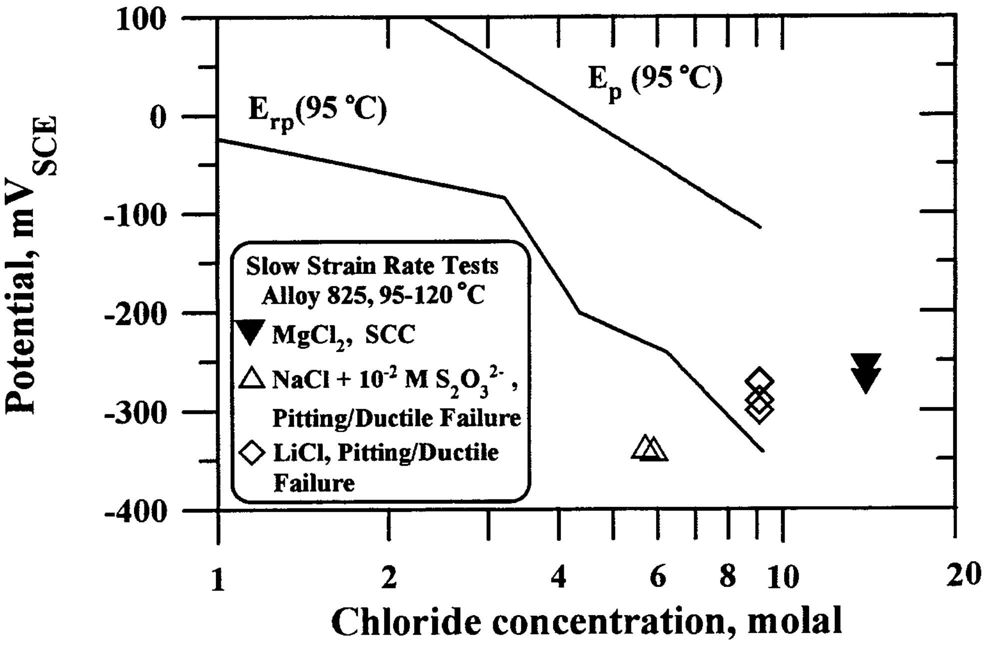

Figure 4-18. Results of slow strain rate tests of alloy 825 in concentrated chloride solutions ($MgCl_2$, LiCl, and NaCl), with and without the addition of thiosulfate, in terms of potential and chloride concentration at temperatures ranging from 95 to 120 °C

0.01 M thiosulfate for both heats of 316L SS. The cracks were located on the apex of the U-bend above the solution vapor interface. Cracking at the apex was also observed on specimens of the two heats of type 316L SS in a 1,000 ppm Cl^- solution without the addition of thiosulfate. Pitting was also observed on these specimens and pitting corrosion was the dominate localized corrosion mode on other specimens tested under similar conditions. In 1 M Cl^- solution without the addition of thiosulfate extensive pitting corrosion was observed after 28 days. SCC was observed above the vapor/solution interface on specimens of both heats of material. However, no SCC was detected for the specimen of heat P80746 (1/2-in. plate) under open-circuit conditions. Double U-bend specimens tested in 1 M Cl^-, which were essentially free from all localized attack after 28 days of testing at both open-circuit and at anodic-applied potentials, were observed to have cracks after a total test time of 56 days. Additional information on these tests is provided in Tables D-10 and D-11.

In summary, failure by SCC of type 316 SS was not observed in SSRTs at chloride concentrations lower than 7.2 molal in the absence of thiosulfate. In the presence of 0.01 M thiosulfate, SCC was observed in solutions containing 5.8 molal Cl^- but not in 0.028 molal Cl^- (1,000 ppm). In U-bend tests, SCC of both heats of 316L was observed in chloride concentrations as low as 1,000 ppm above the vapor/solution interface. At high chloride concentrations, SCC was observed on the immersed portions of the specimens. No noticeable difference in SCC susceptibility was observed in U-bend tests by comparing the two heats of type 316L SS under investigation.

4.3.2 Alloy 825

4.3.2.1 Slow Strain Rate Tests

The results of SSRTs of alloy 825 in concentrated chloride solutions are presented in Table D-12 and Figure 4-18. As in the case of type 316L SS, E_p and E_{rp} measured on unstressed specimens of alloy 825 using a scan rate of 0.167 mV/s (Sridhar et al., 1993a), are plotted as a function of chloride concentration to indicate the location of the open-circuit or applied potentials used in the SSRTs. The E_p line is a regression fit line, whereas the E_{rp} curve is drawn through the lowest value of this parameter measured at each chloride concentration. It should be noted that above 4 molal Cl^-, E_{rp} deviates significantly from the linear dependence on the logarithm of chloride concentration observed in more dilute chloride solutions. SCC was observed, both at an anodic potential as well as at the E_{corr} only in 40 percent $MgCl_2$ solution (14.0 molal Cl^-) at 120 °C. The elongation to failure was 44 percent at the E_{corr} (approximately -270 mV_{SCE}) and decreased to 36 percent at a slightly anodic potential (-260 mV_{SCE}) whereas the elongation to failure corresponding to a purely ductile fracture was approximately 53 percent.

No SCC was observed in solutions containing 9.1 molal LiCl at 110 °C or 5.8 molal NaCl with the addition of 0.01 M $Na_2S_2O_3$ at 95 °C under either open-circuit and anodic-applied potentials. In these tests, ductile failure promoted by coalescence of microvoids and signs of pitting corrosion were detected on the fracture surface. Failure by SCC did not occur in either of these solutions in additional tests in which circumferentially notched specimens were used and the strain rate was decreased five times with respect to that applied for smooth tensile specimens. Ductile failure accompanied by pitting corrosion was also observed on a smooth specimen tested in 9.1 molal LiCl after being SA (1,200 °C/ 10 min.) and sensitized at 700 °C for 15 hr. Even though the results of thermal stability tests indicate that this heat treatment produces a severely sensitized microstructure with Cr-depleted grain boundary regions (Section 5.4) no significant decrease in SCC resistance was observed.

The addition of a crevice on the gage length of the smooth tensile specimens resulted in an increased susceptibility to SCC for the as-received material as shown in Figure 4-19. Details are provided in Table D-13. In contrast to the results presented above for smooth tensile specimens with a crevice, significant SCC of creviced specimens was observed in 9.1 molal LiCl at 110 °C and 6.2 molal NaCl with the addition of 0.01 M $Na_2S_2O_3$ at 95 °C.

All observations were confirmed by fractographic examination of the failed smooth tensile specimens using the SEM. Several thumbnail-shaped areas exhibiting transgranular quasi-cleavage features were observed along the periphery of the fracture surface of the alloy 825 specimens tested in $MgCl_2$ solution, both at the open-circuit as well as the anodic-applied potential. One of these areas is shown at high magnification in Figure 4-20 confirming the occurrence of SCC. The appearance of numerous secondary cracks on the side surface of these specimens is illustrated in Figure 4-21. The coalescence of deep, slightly branched cracks, growing in different planes, led to the generation of an extremely uneven fracture surface. Transgranular cracking was also noted on creviced specimens tested in 9.1 molal LiCl at 110 °C and 6.2 molal NaCl with the addition of 0.01 M $Na_2S_2O_3$ at 95 °C.

4.3.2.2 Constant-Deflection Tests

The results of all the U-bend tests of alloy 825 are presented in Table D-14 and plotted in Figure 4-22 to indicate the location of the potentials used in the tests with respect to $\boldsymbol{E_p}$ and $\boldsymbol{E_{rp}}$. It is seen that, within the range of chloride concentrations tested, SCC only occurred in 40 percent $MgCl_2$ (14 molal Cl^-) solutions. Cracks were observed on single specimens after 2,016 hr of testing. However, the occurrence of SCC was accompanied by extensive pitting near the vapor/solution interface. SCC was also observed after 2,016 hr of testing on the inner U-bend of double U-bend specimens tested at open-circuit and at applied anodic potentials. It should be noted that the inner U-bend of these specimens was not inspected prior to completing three consecutive 672 hr testing periods. No SCC was observed in any of the 11 U-bend specimens tested, in some cases for a total testing time of 4,536 hr (189 d), in 5.8–9.0 molal chloride solutions (pH 4.0) at 95 °C. Certain specimens were exposed to alternate cycles of full immersion in the concentrated solutions, followed by exposure to the vapor phase just above the vapor/solution interface. However, no SCC was detected under these conditions. Specimens tested under fully immersed conditions for 504 hr (21 d) in both NaCl and LiCl solutions containing 6.0 molal Cl^- at potentials slightly anodic to the open-circuit potential exhibited localized corrosion mostly in the form of small pits located mainly in the legs of the U-bend above the vapor/solution interface. However, these pits did not give rise to cracks upon further exposure.

In summary, SCC of alloy 825 was not observed in chloride solutions using the slow strain rate technique over a wide range of chloride concentrations, except in 40 percent $MgCl_2$ at 120 °C, which corresponds to 14 molal Cl^-. SCC of creviced specimens occurred at lower chloride concentrations, in LiCl as well as in NaCl solutions, with the addition of 0.01 M $Na_2S_2O_3$. SCC of alloy 825 in U-bend tests only occurred in environments which produced SCC in SSRTs.

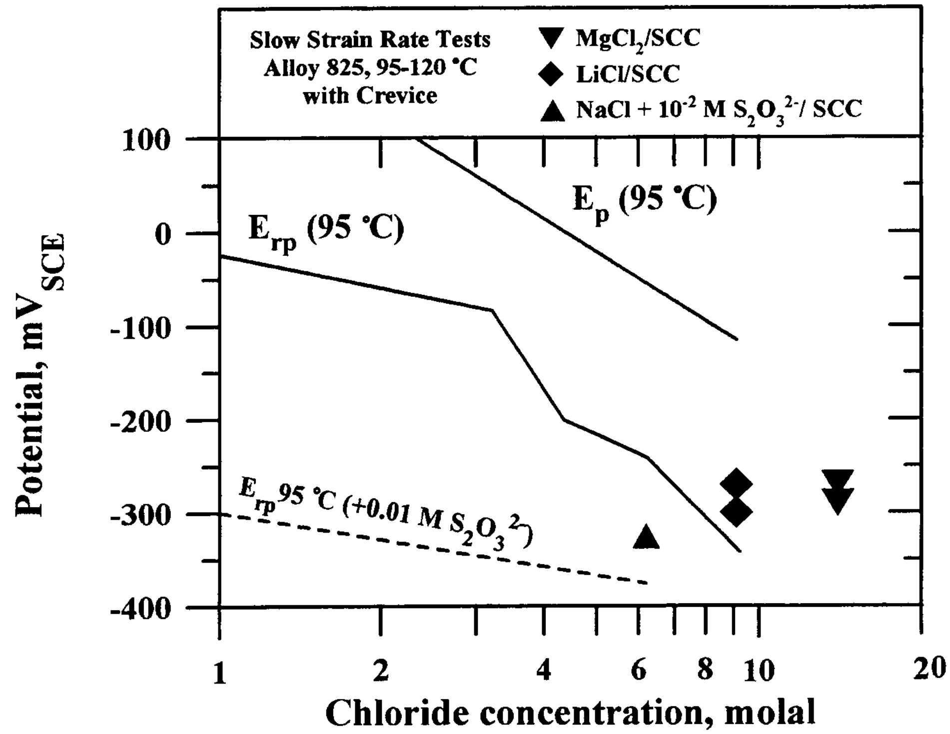

Figure 4-19. Results of slow strain rate tests of alloy 825 using creviced specimens in concentrated chloride solution ($MgCl_2$, LiCl, and NaCl), with and without the addition of thiosulfate, in terms of potential and chloride concentration at temperatures ranging from 95 to 120 °C

4.4 DISCUSSION

4.4.1 Stress Corrosion Cracking of Type 316L Stainless Steel

The results plotted in Figure 4-2 clearly indicate that mill-annealed type 316L SS failed by SCC in SSRTs when exposed to $MgCl_2$ and LiCl solutions at chloride concentrations equal to or greater than 7.2 molal and temperatures above 100 °C. Although SCC was observed under open-circuit conditions, it was significantly enhanced at slightly anodic potentials. The potential range for SCC was bounded by the values of E_p and the E_{rp} obtained in CPP tests. As shown in Figure 4-6, the fracture surfaces exhibited a relatively large proportion of intergranularly cracked area in addition to the transgranular features typical of the SCC of annealed, nonsensitized austenitic SS in concentrated chloride-containing solutions. The important effects of chloride concentration, temperature and potential on the SCC susceptibility, as reflected in the elongation to failure ratios, are shown in Figures 4-10, 4-11, and 4-12. A significant decrease in these values is observed above 7.2 molal of chloride and temperatures above 95 °C. At potentials just above the E_{rp} the elongation to failure ratios decrease. In contrast, even at high Cl^- concentrations, failure by SCC was completely eliminated when the potential of the specimen was maintained below the E_{rp}.

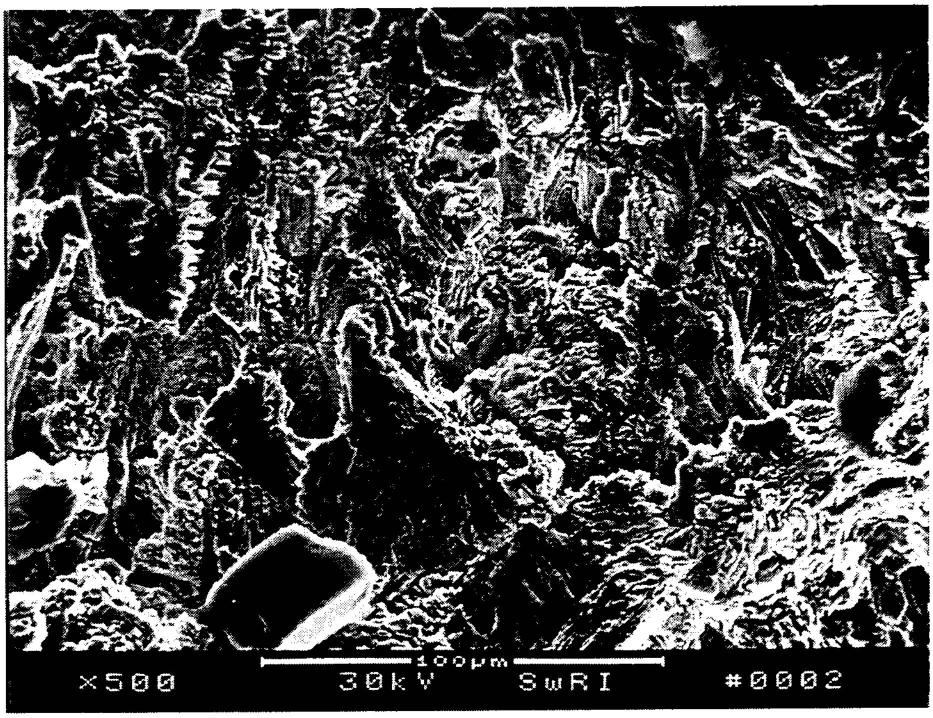

Figure 4-20. Scanning electron microscope fractograph showing the transgranular stress corrosion cracking area of the alloy 825 specimen fractured in a slow strain rate test at an applied potential of −260 mV_{SCE} in 40 percent $MgCl_2$ solution at 120 °C

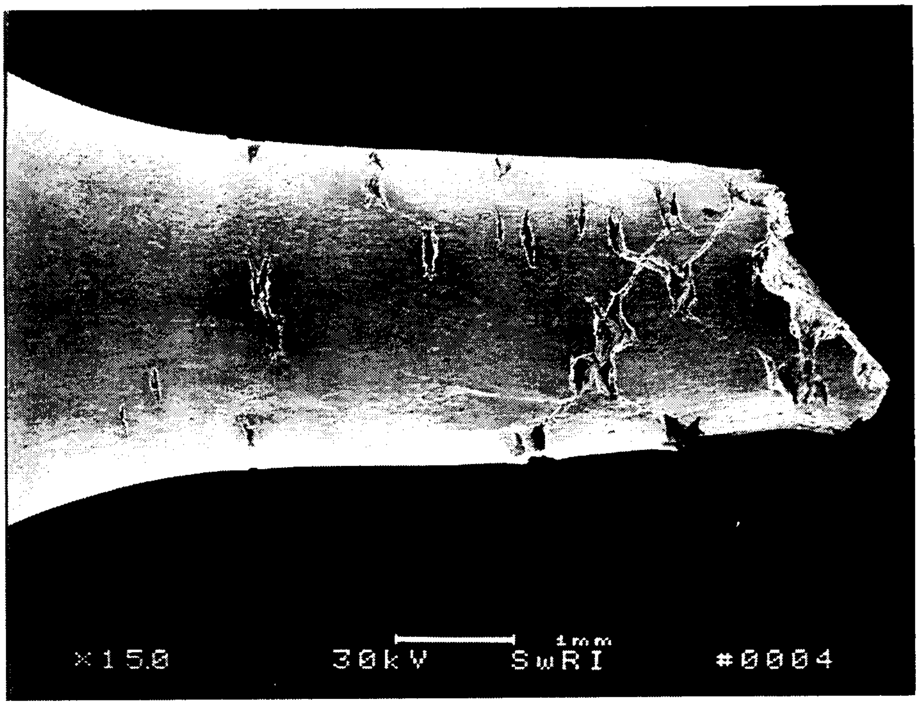

Figure 4-21. Side surface of the alloy 825 specimen tested at an applied potential of −260 mV_{SCE} in 40 percent $MgCl_2$ solution at 120 °C

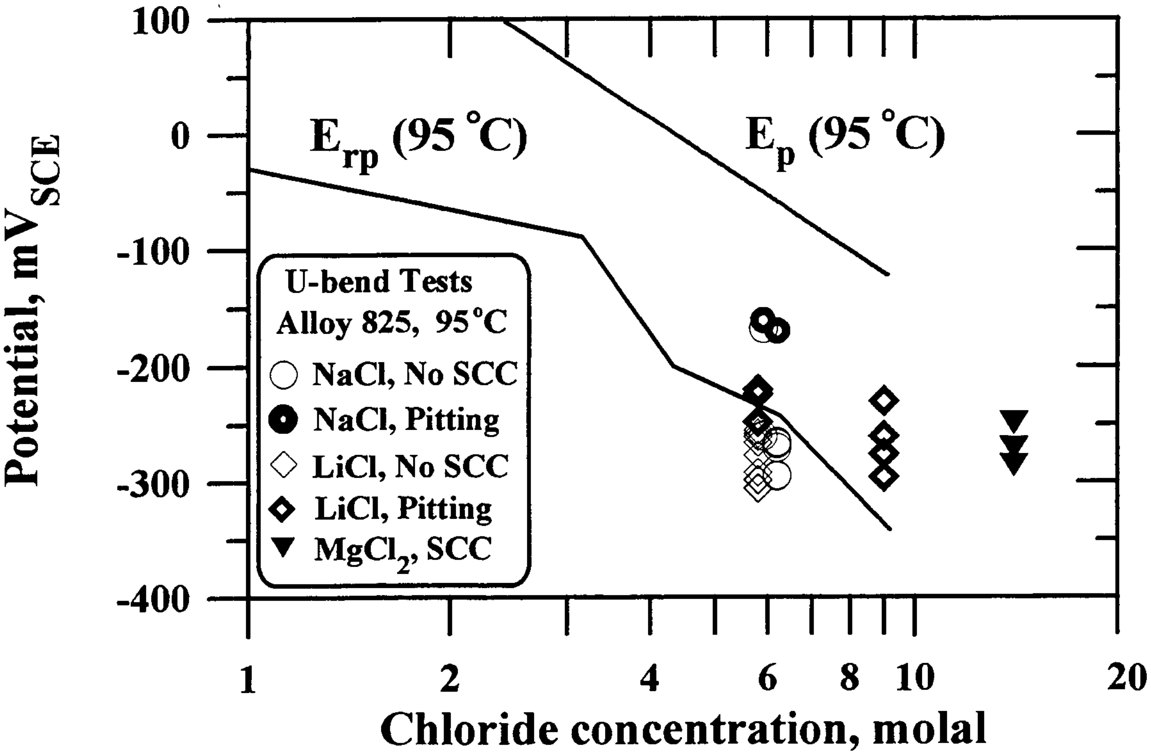

Figure 4-22. Results of constant-deflection tests using U-bend specimens of alloy 825 in concentrated chloride solutions in terms of potential and chloride concentration at 95 °C

Several authors (Takano, 1974; Stalder and Duquette, 1977; Manfredi et al., 1987; Duffo et al., 1988) have reported the simultaneous occurrence of transgranular and intergranular SCC of type 304 SS in SSRTs conducted in concentrated $MgCl_2$ or LiCl solutions at temperatures above 90 °C. The proportion of intergranular to transgranular SCC changes with chloride concentration, temperature, potential, and strain rate, but it is complicated to establish a well-defined pattern as a function of these variables. It appears, however, that the tendency to intergranular SCC increases with decreasing chloride concentration, temperature, and potential, and also with increasing strain rate. Although no similar studies have been conducted with type 316L SS, Okada et al. (1971) have suggested, by studying the SCC behavior of types 304 and 316 SSs, and Fe-16Cr-15Ni-xMo (x=1,2,4) alloys in hot $CaCl_2$ solutions, that the fracture mode became intergranular with higher Mo content. This was attributed by Okada et al. (1971) to the improved corrosion resistance of the alloys brought about by the higher Mo content, which parallels the effect of decreasing corrosivity of the solutions as a result of lower chloride concentrations and temperatures.

On the contrary, as also shown in Figure 4-2, SCC did not occur in plain NaCl solutions in which the chloride concentration was 6.2 molal. This is close to the maximum concentration attainable in NaCl due to solubility limitations. The same results were obtained in LiCl solutions of equivalent chloride concentration. These results indicate that under the experimental conditions used in these tests, particularly in terms of temperature and strain rate, no SCC can be promoted regardless of the cation at chloride concentrations equal to or lower than 6.2 molal, even at acidic pHs. During the course of most of these tests the pH changes from values close to 2.5 initially to values higher than 6.0 at the end of the test, presumably due to the generation of hydroxide ions at the counterelectrode as a consequence of the reduction of water or H^+ ions. However, this explanation is not completely satisfactory because the pH increase was also observed in some tests conducted under open-circuit conditions. It is possible that this increase in pH may render the environment less aggressive in terms of the susceptibility to SCC. When SCC was observed the increase of pH was less pronounced, suggesting that the hydrolysis of metal cations generated at the crack tip tend to neutralize the alkaline build-up of the solution. In these tests, both open-circuit and applied potentials are within the range defined by the pitting potential, E_p, and the repassivation potential, E_{rp}. The corrosion potential for all these tests, in which N_2 was bubbled into the solution, was on average -350 mV_{SCE} with a standard deviation of 10 mV. This potential is very close to the extrapolated value of E_{rp} for a chloride concentration of 6.2 molal (Figure 4-2).

The occurrence of SCC of austenitic SSs is expected in neutral, chloride-containing solutions above 80 °C in the low end of this potential range, just above E_{rp} (Cragnolino and Sridhar, 1992a; Tamaki et al., 1990; Tsujikawa et al., 1994). Instead of SCC, the dominant failure mode in the tests reported above was ductile failure accompanied by pitting corrosion. Since Beavers and Koch (1992) have claimed that the inability to reproduce the SCC of austenitic SSs in dilute chloride solutions using SSRTs may be due to the use of relatively high-extension rates, the strain rate was decreased by almost three times from 1×10^{-6} to 3.6×10^{-7} s^{-1} in specific tests. Nevertheless, cracks were not initiated, and it was found very difficult to avoid the occurrence of pitting as the predominant phenomenon in this chloride concentration range. Although the potentials selected were approximately 100 mV lower than the extrapolation of the line representing the dependence of E_p with chloride concentration, which defines the electrochemical conditions for pit nucleation in potentiodynamic scans, pitting corrosion was observed on all of these specimens (Figure 4-2), after an initiation time of several hours. These observations are in complete agreement with the results presented in Section 3.3.2.1 for alloy 825.

The addition of thiosulfate to the NaCl solutions promoted SCC at a slightly lower chloride concentration (5.8 molal) both at the open-circuit and anodic-applied potentials, as shown in Figure 4-2. The elongation to failure was almost identical for both MA and SA specimens tested under open-circuit conditions (≈-385 mV_{SCE}), and the fracture surface exhibited transgranular and intergranular cracking (Figures 4-13 and 4-14). SCC occurred in the presence of thiosulfate despite that the corrosion potential was approximately 35 mV lower than that in plain chloride solutions. However the potential of this specimen was still above the E_{rp} line for Cl^-+0.01 M $S_2O_3^{2-}$ plotted in Figure 4-2. Significant decreases in the E_{rp} of SSs in Cl^- solutions have previously been reported as a result of thiosulfate additions. Nakayama et al. (1993) have observed that the repassivation potential for crevice corrosion, E_{rcrev}, of type 304 SS decreased by approximately 400 mV when 10 ppm $S_2O_3^{2-}$ was added to a solution containing 100 ppm Cl^-, corresponding to a $S_2O_3^{2-}/Cl^-$ molar ratio of 0.032.

Tsujikawa et al. (1993) reported similar SCC results as those discussed above for SA type 316L SS in 20 percent NaCl solution (4.3 molal) containing 0.001 to 0.1 M $Na_2S_2O_3$ (pH 4.0) at 80 °C. These authors conducted SSRTs at a strain rate of 2.0×10^{-6} s^{-1} and constant load tests at initial applied stresses higher than 1.3 σ_y, where σ_y is the yield strength of the alloy. However, Tsujikawa et al. (1993) only observed the occurrence of transgranular cracking.

Ductile fracture was the single failure mode, even in the presence of thiosulfate, at a lower chloride concentration (1,000 ppm). No SCC was observed in these tests regardless of the increase in thiosulfate concentration, the decrease in strain rate, the application of an anodic potential, or the use of a notched specimen with an O-ring to promote crevice conditions. The $S_2O_3^{2-}/Cl^-$ molar ratio was varied from 0.035 to 0.35 in this set of tests which seems to be the appropriate ratio to have a minimum in the curves of E_p and E_{rcrev} as a function of thiosulfate concentration, as demonstrated for type 304 SS by Newman et al. (1982) and Nakayama et al. (1993), respectively. It was expected, although never observed, that cracks could be initiated from the bottom of incipient pits, produced by the localized breakdown of the oxide film during straining. It is well known that pitting corrosion of austenitic SSs, such as types 304, 304L, and 316L, initiates at MnS inclusions (Szklarska-Smialowska, 1986). Furthermore, the presence of crevice geometries introduced to promote crack initiation, through the localized modification of the environment expected in the occluded region, did not lead to the nucleation of cracks. Lott and Alkire (1989) and Alkire and Lott (1989) have shown that the anodic dissolution of MnS inclusions generates $S_2O_3^{2-}$ ions. These species, in conjunction with chloride, promote initiation of crevice corrosion at induction times that decrease with potential, crevice gap, and areal density of inclusions. It was hypothesized that the exposure time available in SSRTs, limited by the occurrence of ductile failure, was not long enough to facilitate such environmental modification, and therefore, crack initiation. However, no SCC occurred in prolonged tests (>900 hr) conducted under constant elongation conditions at stresses well above the yield strength. Localized corrosion, without signs of crack initiation, was observed both at the corrosion potential and at a slightly anodic potential.

No SCC occurred in the chloride concentration range extending from 1,000 to 10,000 ppm under a wide range of experimental conditions, including the presence of crevice geometries Figure 4-1. A decrease of the strain rate from 1.0×10^{-6} to 2.2×10^{-7} s^{-1} did not induce crack initiation under similar environmental conditions even in the presence of thiosulfate, which is one of the critical species that could be generated inside a crevice by the dissolution of sulfide inclusions. In this chloride concentration range, it was also difficult to avoid the occurrence of pitting as predominant phenomenon. Although the potentials selected were well below the extrapolation of the line representing the dependence of E_p with chloride concentration (Figure 4-1), pitting corrosion was observed in all these specimens.

It must be emphasized, however that Tamaki et al. (1990) were able to initiate cracks in type 316 SS in relatively dilute chloride solutions (180 to 18,000 ppm Cl^-) at 80 °C by using a tapered double-cantilever beam specimen with a sufficiently wide but narrow crevice. Transgranular cracks initiated and grew under applied potentials above E_{rcrev} and stress intensities (K_I) greater than 4.0 $MPa \cdot m^{1/2}$. Transgranular cracking of SA type 316 SS has been observed in SSRTs in the presence of very low (5 ppm) chloride concentrations as NaCl when smooth tensile specimens were tested (Yang et al., 1992) but at temperatures above 150 °C. In addition to the differences in specimen geometry, stressing techniques and other experimental conditions (e.g., temperature), it is entirely possible that the occurrence of SCC observed by Tamaki et al. (1990) and Yang et al. (1992) can be attributed, at least partially, to the higher carbon content of type 316 SS with respect to that of type 316L.

It appears that acidic, high-chloride concentrations are required locally to initiate cracks in type 316L SS at temperatures below 100 °C. In dilute solutions, a tight crevice is necessary to generate such acidic, localized environment sufficiently enriched in chloride ions in the presence of the required tensile stresses. Tsujikawa et al. (1994) used a spot-welded specimen, which had a tight metal/metal crevice and high residual stresses, to demonstrate that cracks are initiated in the creviced area at potentials just above E_{rcrev} in a variety of Fe-18Cr-14Ni alloys, containing other alloying elements, in dilute NaCl solutions at 80 °C. At even higher potentials, crevice corrosion predominated. Several tests conducted in 1 M NaCl solution using specimens with a specially designed crevice-forming device (Table D-3) did not lead to the initiation of cracks, because pitting corrosion predominated in the crevice region. However, the initiation of minor cracks, without any noticeable growth, was noted in a few of the galvanostatic tests. Lowering the applied current reduced the competing effect of localized corrosion propagation but did not result in a significant increase in crack growth. In agreement with the findings of Suleiman and Newman (1995), very minor cracking was observed in the creviced specimens exposed to 1 M NaCl under potentiostatic or galvanostatic conditions in SSRTs. In constant-extension tests in which the testing time was substantially increased, only minor cracking was observed even in the presence of 0.01 M $Na_2S_2O_3$. As discussed by Suleiman and Newman (1995), the main advantage of conducting the tests under galvanostatic conditions is that the tendency to induce severe pitting corrosion outside the crevice area is significantly reduced.

Contrary to the results of SSRTs in dilute chloride solutions, SCC was often observed in constant-deflection tests, even in the absence of thiosulfate. The presence of thiosulfate, however, significantly enhanced SCC susceptibility. Cracks were mostly detected above the vapor/solution interface, indicating that the local environment created as a liquid film on the specimen surface could be more detrimental than the bulk liquid environment. The existence of stagnant conditions, promoted by the elimination of a purging gas, appears to create a more severe environment than that arising from the continuous bubbling of synthetic air. This is apparently reflected in the higher potential obtained without gas purging (-130 mV_{SCE}) with respect to that (<-200 mV_{SCE}) measured in the presence of purged air. It is possible that H_2S, generated by reduction of thiosulfate at the metal surface, could be more easily oxidized by oxygen in a process assisted by the solution agitation promoted by gas bubbling and therefore eliminated from the solution as a cracking promoter. However, additional information is needed to confirm this interpretation.

No convincing explanation can be offered at the present time for the differences observed between the results of slow-strain rate and constant-deflection tests. Explanations based on differences in oxygen concentration, potential distributions at the vapor/solution interface, or exposure times are not considered to be satisfactory. SCC was observed on U-bend specimens of the two heats of 316L after testing in 1,000 ppm Cl^- with and without the addition of thiosulfate. It can be concluded, therefore, that the differences in the results of SSRTs and U-bend tests are not the result of heat to heat variations.

As noted in Figure 4-16, SCC in 1,000 ppm chloride solutions containing thiosulfate occurred at potentials below the E_{rp} line. The explanation for the occurrence of SCC at such low potentials is similar to that offered above for the SSRTs conducted at higher chloride concentrations. However, the occurrence of pitting and even SCC in plain chloride solutions at potentials below that line is not explainable, but it may be attributed to the fact that the potential exhibited significant variations during these prolonged tests. During an extended period, the potential remained above the E_{rp} line.

In more concentrated chloride solutions, SCC of type 316L SS was observed in constant-deflection tests conducted in both LiCl and NaCl solutions at concentrations (5.8 molal) at which no cracking was detected in SSRTs. The addition of thiosulfate further increased the susceptibility to SCC in agreement with the result obtained in the SSRTs.

4.4.2 Stress Corrosion Cracking of Alloy 825

The results shown in Figure 4-18 clearly indicate that MA alloy 825 only failed by SCC in SSRTs when exposed to $MgCl_2$ solutions at a chloride concentration of 14.0 molal and a temperature of 120 °C. In contrast, SCC did not occur in LiCl solutions in which the chloride concentration was equal to 9.1 molal at 110 °C. These results indicate that, under the experimental conditions used in these tests, particularly in terms of temperature and strain rate, SCC cannot be promoted regardless of the cation at chloride concentrations less than or equal to 9.1 molal, even at acidic pHs. Instead of SCC, the dominant failure mode was ductile failure, accompanied by pitting corrosion. Under equivalent testing conditions, MA type 316L SS was found to be susceptible to SCC at chloride concentrations greater than 7.2 molal. In 40 percent $MgCl_2$ solution at 120 °C the elongation to failure for type 316L SS was found to be 7.4 percent at the open-circuit potential and 4.6 percent at a 20-mV anodic overpotential, whereas for alloy 825 the values were 44 and 36 percent, respectively.

The addition of thiosulfate to a 5.8 molal NaCl solution promoted transgranular SCC of type 316L SS. However, as shown in Figure 4-18, no SCC was observed on alloy 825 under the same testing condition or under more severe conditions prompted by the use of a notched specimen at a lower extension rate over a very extended period. Tsujikawa et al. (1993) reported that alloy 825 did not exhibit SCC in 20 percent NaCl solution (4.3 molal) containing 0.001 to 0.1 M $Na_2S_2O_3$ (pH 4.0) at 80 °C by conducting SSRTs and constant-load tests at applied stresses above the yield strength of the alloy. As indicated in Figure 4-18, pitting was observed in the thiosulfate-containing solution. The open-circuit and the anodic potentials used for testing in this environment are well below the plotted values of $\boldsymbol{E_{rp}}$ for plain Cl^- solutions. However, it should be noted that metastable sulfur oxyanions, such as $S_2O_3^{2-}$, induce a significant decrease in $\boldsymbol{E_p}$ and $\boldsymbol{E_{rcrev}}$ for type 304 SS when added to chloride-containing solutions with respect to the plain chloride environment (Newman et al., 1982; Nakayama et al., 1993). A similar effect was observed for alloy 825, as indicated by the $\boldsymbol{E_{rp}}$ line for Cl^-+0.01 M $S_2O_3^{2-}$ solutions shown in Figure 4-18.

The presence of a crevice on the smooth tensile specimen resulted in a substantial increase in the SCC susceptibility of alloy 825. Significant cracking was observed in SSRTs in 6.2 molal NaCl with the addition of 0.01 M $S_2O_3^{2-}$ under anodic applied potential and in 9.1 molal LiCl under both open-circuit and an anodic-applied potential. Since the chloride concentration in these solutions is very high, it seems unlikely that the increase in SCC susceptibility is a only result of an increase in the Cl^- concentration of the occluded region. Substantial decreases in pH in the creviced region may have also been detrimental.

The constant-deflection tests confirmed the results of the SSRTs in the case of alloy 825 in the sense that no SCC was found within the same range of chloride concentrations using both test methods. For uncreviced specimens, SCC was observed only in 40 percent $MgCl_2$ solution at 120 °C using SSRTs. U-bend tests conducted in the same solution at 95 °C also resulted in SCC. However, a longer exposure time was necessary to initiate cracks on the U-bend specimens. This observation further supports the effect of temperature on SCC exhibited by 316L SS. The presence of a mill-finished surface apparently did not result in an increase in SCC susceptibility in this environment, even though a greater degree of pitting corrosion was observed for these specimens. A large number of constant-deflection tests was conducted for extended periods in concentrated chloride solutions close to the solubility of NaCl at 95 °C to confirm the superior resistance to SCC of alloy 825 compared to type 316L SS using a different test technique. As noted above, SCC of type 316L SS was observed in constant-deflection tests in both LiCl and NaCl solutions at concentrations (5.8 molal) at which no cracking was detected in SSRTs. This difference in behavior can be expected from their chemical compositions as discussed before on the basis of literature information (Sridhar and Cragnolino, 1992a). The higher Ni content of alloy 825 combined with the higher levels of Cr and Mo makes this alloy far more resistant to SCC in chloride-containing environments that any of the austenitic SS.

Contrary to the case of type 316L SS in which a significant susceptibility to SCC in constant-deflection tests was detected in the vapor phase under conditions leading to the formation of liquid film on the surface, localized corrosion in the form of pitting was the dominant phenomenon in alloy 825. Due to the significant susceptibility to localized corrosion, long-term SCC tests should be conducted in a wide range of environmental conditions. SCC can occur as a competitive phenomenon when the tendency to localized corrosion becomes marginal. The constant-deflection tests conducted for several months demonstrated that cracks were not readily initiated from pits. However, it was shown in SSRTs that severe SCC can be initiated under crevice conditions. It is presently unclear if the initiation of cracks could be promoted through the alteration of the surface or near-surface conditions by the introduction of very localized plastic deformation via cold work or microchemical modifications through surface depletion of some alloying element or thickening of the passive film by oxidation in air (Dunn et al., 1993). In addition, sensitization to intergranular corrosion promoted by prolonged heat treatment at temperatures above 550 °C (Cragnolino and Sridhar, 1993a) leading to carbide precipitation and presumably to Cr depletion at grain boundaries may have an effect on SCC of alloy 825. Thus far, only limited investigations have been conducted to investigate these effects. These tests on sensitized specimens did not indicate any detectable effect of sensitization on SCC. However, they are too limited to be conclusive.

5 MATERIALS STABILITY AND SENSITIZATION

5.1 INTRODUCTION

Changes in material microstructure and microchemistry, particularly at grain boundaries, can affect its mechanical properties (embrittlement) or its corrosion resistance (sensitization). The term sensitization is generally used to denote the effect of intergranular carbides on corrosion, but can be extended to the effect of other types of intergranular precipitates (e.g., intermetallics) on corrosion. The changes in microstructure and microchemistry of container materials may arise from several factors which can be broadly classified as: (i) fabrication related factors, and (ii) repository emplacement related factors.

Fabrication Related Factors: For the current ACD, the containers will be made by welding of plates both longitudinally and circumferentially. The longitudinal welds will be post-weld annealed during fabrication of the containers. Due to the presence of spent fuel cladding inside, which limits the maximum temperature to 350 °C, the circumferential closure welds may be post-weld annealed by controlling the overall temperature. This can be accomplished by using an induction coil, but size considerations may be a limiting factor. Fusion welding results in segregation of alloying elements such as chromium in the weld metal (Cieslak et al., 1986a,b) resulting in interdendritic corrosion especially in environments promoting localized corrosion (Garner, 1982). In some alloys, welding produces a heat affected zone (HAZ), which has grain boundary carbides, resulting in sensitization. In stabilized alloys, such as alloy 825, the possibility of intergranular carbides and sensitization in a narrow region close to the fusion boundary also exists. This phenomenon has been named knife-line attack (Cowan and Tedmon, 1973), and it has been observed in nuclear fuel reprocessing plants in acid media under highly oxidizing conditions.

Emplacement Related Factors: Depending upon the thermal loading strategy, the waste packages can stay dry at temperatures well above 100 °C for extended periods of time (thousands of years). The possibility exists that carbide or intermetallic precipitation can occur over this time period, even though exposure temperatures below 350 °C are significantly lower than the temperatures generally investigated for sensitization (600 to 800 °C). Such precipitation of carbides can be exacerbated by the presence of prior cold work, ferrite in the weld, or segregation of alloying elements in the weld. In alloys such as alloy 825, electron vacancy and d-band orbital energy calculations (Cragnolino and Sridhar, 1993a) indicate that sigma phase may be a possibility at low temperatures and extended time periods.

In the IWPE project, attention was focused on alloy 825 because this alloy continues to be the focus as a candidate overpack material. However, the extent of mechanistic investigation in this area has been less than for the localized corrosion and SCC because the methodologies developed for investigating sensitization are more material dependent. A combination of corrosion tests and analytical electron microscopy was employed to examine the factors affecting the sensitization of alloy 825.

5.2 EXPERIMENTAL PROCEDURES

5.2.1 Heat Treatments and Intergranular Corrosion Tests

For the determination of a time-temperature-sensitization (TTS) diagram for alloy 825, cubic samples of approximately 12.5 mm (0.5 in.) on each side were cut from a 12.5-mm- (0.5 in.) thick plate of the Heat No. HH4371 FG supplied by INCO Alloys International in the hot-rolled and MA condition. The chemical composition of this heat is given in Table A-1. Long-term sensitization studies were conducted with 3.1-mm- (0.12 in.) thick plate Heat No. HH7004 FK also obtained from INCO Alloys International. The composition of this plate is also shown in Table A-1. The samples were mechanically polished, finishing with 200-grit SiC paper, and degreased with acetone.

The microstructure of the as-received or MA material is shown along with the microstructures obtained after several heat treatments in Appendix E. Previously, it was reported that the MA samples exhibit a dual grain size microstructure, with bands or areas of large grains surrounded by areas of very small grains (Cragnolino and Sridhar 1993a). Orange colored, cuboidal precipitates, which are most probably titanium nitrides or titanium carbonitrides, were observed in the MA microstructure. In addition, of a large number of small particles or precipitates, which are probably mixed titanium/chromium carbides, are clearly visible in some of the grains, while other grains are almost free of precipitates. It should be noted, however, that the grain boundaries are completely devoid of precipitates.

Since the MA samples exhibit a large number of small intragranular precipitates, which are probably carbides, tests were also conducted on specimens which were SA at 1,200 °C for 10 min, in order to dissolve the carbides followed by fast quenching in cold water. It is apparent that the high-temperature treatment, although short, produces significant grain growth. However, the grain boundaries of the SA material are free of precipitates and most of the intragranular precipitates, which were observed in the MA material. The dissolution of the intragranular precipitates confirms that they are actually titanium/chromium carbides. However, the large cuboidal precipitates were not dissolved by the high-temperature treatment, suggesting that they may be titanium nitrides or carbonitrides.

Initially, both MA and SA samples were heat treated at various temperatures ranging from 600 to 800 °C for 0.1, 1.0, and 15.0 hr. Heat treatments were conducted in a Lindberg tube furnace, using a quartz tube in which MA samples and SA samples were thermally treated simultaneously at the desired temperature. A very low air pressure of approximately 1.3×10^{-6} atm was maintained using a vacuum pump to limit the oxidation of the samples. A K-type (Chromel-alumel) thermocouple was introduced in a 1.6 mm (1/16 in.) borehole drilled in the SA sample to monitor the temperature accurately using a previously calibrated Doric Digitrend 235 data logger. Times ranging from 8 to 12 min were required to attain the desired temperature, as recorded from the instant at which the samples were introduced in the preheated furnace.

In addition to the MA and SA specimens, the effect of cold work on the kinetics of sensitization was examined briefly. For this purpose, SA specimens in the form of U-bends were subjected to various aging treatments. The U-bend area was then compared to the straight section which is relatively undeformed. The extent of cold work by this technique is low (about 25 percent) and further studies using cold-rolled specimens must be conducted are necessary.

After completing the sequence of heat treatments, each cubic sample was cut in half using a water-cooled abrasive cut off wheel in order to test duplicate specimens. The specimens were then wet-polished with 220-grit SiC paper, rinsed with double-deionized water, and then dried with an air blower. After measuring all dimensions with a calibrated caliper, the specimens were degreased with acetone, dried, and weighed in an analytical balance to the nearest 0.1 mg.

The alloy 825 specimens were then exposed to boiling 65 percent nitric acid solution according to American Society for Testing and Materials (ASTM) A-262-93a, Standard Practice C (American Society for Testing and Materials, 1994b) to detect their susceptibility to intergranular corrosion.

Exposures were conducted in 1,000-mL Erlenmeyer flasks fitted with Allihn condensers using 450 mL (20 mL/cm^2 of total specimen surface area) of 65 ± 0.2 weight-percent nitric acid solution, prepared with analytical reagent grade acid. Companion specimens, designated A and B, were simultaneously tested using a basket-shaped glass holder or glass cradle (American Society for Testing and Materials, 1994c) in which the specimens were separated by a piece of microscope slide to avoid any contact. Solutions were heated and maintained at the boiling point on hot plates. Specimens were exposed, fully immersed into the boiling nitric acid solution, for a total of 240 hr through five consecutive periods of 48 hr each, the solution being replaced after each period. In some cases, as a result of test scheduling, the second period was shortened to 32 hr, while the third one was extended to 64 hr.

Longer-term material stability tests of alloy 825 were conducted with SA specimens which were heat treated at 550 to 800 °C for times ranging from 15 to 1,000 hr using a Lindberg oven. The heat treatment was conducted in an air environment and the temperature was regularly monitored with an independent calibrated thermocouple meter with a type K thermocouple. After the desired heat treatment time was reached, the specimens were removed and quickly quenched in cold water. The specimens were ground to a 220-grit finish and tested using ASTM A262, Standard Practice C. Some specimens were also tested in accordance with ASTM A262, Standard Practice D (American Society for Testing and Materials, 1994b) using a mixture of 50 percent H_2SO_4+42 g/L $Fe_2(SO_4)_3 \cdot 4H_2O$ at the boiling temperature for a period of 120 hr.

After each test period, the specimens were scrubbed with a nylon brush, washed with double-deionized water, rinsed with acetone, and then dried, prior to being weighed to the nearest 0.1 mg. When testing was completed, selected specimens were mounted for metallographic observation. Electrolytic etching in 5 percent nital was used to reveal grain boundaries, whereas carbide particles were detected by electrolytic etching in 80 percent phosphoric acid.

Alternative tests were also investigated for the purpose of detecting the degree of sensitization of alloy 825 since the ASTM A262 Practice C and D generate large volumes of waste acid and take up to 240 hr to obtain results. The electrochemical potentiokinetic reactivation (EPR) test as described in ASTM G108 was initially developed to determine the degree of sensitization of type 304L SS (ASTM G 108) (American Society for Testing and Materials, 1994d). Both single loop and double loop EPR tests were used. Initially benchmark tests were conducted with both sensitized type 304L SS (621 °C for 24 hours) and nonsensitized type 304L SS (MA) in 0.5 M H_2SO_4+0.01 M KSCN. Alloy 825 was subsequently tested in the same solution as well as in solutions in which the sulfuric acid composition was varied from 1 to 50 percent at temperatures up to 100 °C.

CPP tests were also conducted on sensitized alloy 825 specimens. These tests were conducted in a solution containing 20 to 1,000 ppm Cl^-, 85 ppm HCO_3^-, 20 ppm SO_4^{2-}, 10 ppm NO_3^-, and 2 ppm F^-, with Na^+ as the single cation. Anodic scans were started at the corrosion potential and the potential of the specimen was increased at a rate of 0.167 mV/s until a current density of 5 mA/cm^2 was obtained. The direction of the scan was than reversed and the potential of the specimen was decreased until the original corrosion potential was reached. The E_{rp}, as defined in Chapter 3, was then used to characterize the degree of sensitization.

5.2.2 Scanning Transmission Electron Microscopy Studies

Scanning transmission electron microscopy (STEM) studies were conducted using a Phillips EM420 system. The specimens were prepared from discs cut from cylindrical specimens used for the electrochemical studies. These slices, about 1,000-μm thick, were first mechanically thinned to 40 μm. Discs 3 mm in diameter were then punched out and electropolished in a jet-polishing apparatus (Fisione Jet Polisher) until a small perforation was detected. Based on a literature survey, several electrolytes were tried and the perchloric-ethanol mixture was chosen initially as the most appropriate (Pan et al., 1995). The effect of electropolishing procedure on the carbide analysis will be described in detail later. At least two specimens for every heat treatment condition were examined.

The quantitative X-ray microanalyses were carried out using a 20 nm electron beam diameter. The instrument is capable of going down to 1 nm probe size, however, the problems of beam location and low X-ray intensities place a lower limit of 2 nm probe size. The X-ray intensities were converted to concentration of species using the Cliff-Lorimer procedure (Goldstein and Williams, 1981). In this procedure, the ratio of concentration of species is assumed to be proportional to the ratio of their X-ray intensities, because the X-ray fluorescence and absorption can be neglected due to the thinness of the sample. This relationship is expressed as:

$$\frac{C_{Cr}}{C_{Ni}} = k_{CrNi}\left(\frac{I_{Cr}}{I_{Ni}}\right) \tag{5-1}$$

where C_{Cr} and C_{Ni} refer to the concentrations of Cr and Ni, respectively, and I_{Cr} and I_{Ni} refer to their respective X-ray intensities. The factor, k_{CrNi}, is calculated by conducting the analysis at a location remote from the grain boundary and using the known bulk chemical composition of the alloy. Since, Ni is a major alloying element in alloy 825, it was used as the basis for calculating other alloying elements. The k factors calculated from an area far away from the grain boundaries were compared to the k factors calculated from SA specimens which did not have any grain boundary precipitates. There was a good agreement in the k factors between all the specimens, provided the same jet-polishing procedure was used. For type 304L SS, Fe was used as the basis for calculating the concentrations of the other alloying elements. The errors associated with the Cliff-Lorimer procedure have been discussed by Goldstein and Williams (1981). Their method of estimating the errors (2σ confidence limits) on the calculated composition consists of adding the relative errors of k and I values in Eq. (5-1). Because of the Gaussian nature of the X-ray intensities, the relative errors of the measured intensities are assumed to be proportional to 2(I)-0.5. In the present study, the root mean squares of all the relative errors is used, as shown in Eq. (5-2), rather than the sum of the relative errors (Coleman and Steele, 1989).

$$\varepsilon_{Cr} = \left[(\varepsilon_k)^2 + (\varepsilon_{I_{Ni}})^2 + (\varepsilon_{I_{Cr}})^2\right]^{0.5} \tag{5-2}$$

where the ε values are the relative errors (95 percent confidence interval/average value) of the various terms in Eq. (5-1) and the error in the matrix Ni concentration which is used to normalize the other concentrations is ignored. In Eq. (5-2), k is not a directly measured quantity, but calculated from analyses of matrix far from the grain boundaries and from SA specimens. Based on a number of measurements on alloy 825, the 2σ relative error in k_{Cr} is about 2.8 percent (Dunn et al., 1995a). Based on Eq. (5-2), the relative error in Cr concentration was calculated to be about 15 percent. Generally however, the error calculated by Eq. (5-2) is larger than the errors estimated from replicate measurements of the same specimen (Hall and Briant, 1984). Since the peaks of the desired elements in this investigation are far apart, the errors were estimated from replicate measurements rather than by using Eq. (5-2). The standard deviation (σ) for the measurement of Cr concentration was estimated to be 0.5 at. percent and for Mo about 0.16 at. percent.

5.3 EXPERIMENTAL RESULTS

5.3.1 Intergranular Corrosion Tests

According to ASTM A-262-93a, Standard Practice C, the evaluation of the susceptibility to intergranular corrosion is made by calculating an average corrosion rate over the five test periods. The corrosion rate is calculated as uniform dissolution or penetration, regardless of the localized morphology of the attack, by dividing the weight loss after each test period by the total surface area of the specimen, using the following expressions:

$$CR\ (mm/yr) = 8.76 \times 10^4\ \Delta W\ /\ [A \cdot t \cdot \delta] \tag{5-3}$$

and

$$cr\ \left(mg/dm^2 \cdot day\right) = 2.40 \times 10^6\ \Delta W\ /\ [A \cdot t] \tag{5-4}$$

where ΔW is the weight loss in g, A is the area in cm^2, t is the exposure time in hr, and δ is the density, which is 8.14 g/cm^3 for alloy 825 (American Society for Testing and Materials, 1994c).

Two methods were used to calculate average corrosion rates. In the first one, to be identified as Method 1, corrosion rates were calculated independently for each test period and an average value was obtained from the five exposure periods. In Method 2, corrosion rates were calculated at the end of the fifth period by taking into account the weight loss over the total exposure time from the beginning of the test. As expected, the two methods gave essentially the same results, indicating the absence of errors in the determination of the corrosion rates. However, for the specimens with corrosion rates higher than 0.3 mm/yr, it was noted that corrosion rates increased significantly after the initial exposure period of 48 hr, reaching a maximum or a plateau in subsequent periods.

A complete summary of the results obtained using the ASTM A262 tests is provided in tabular form in the Appendix F. Previously, it was reported that the SA samples became far more sensitized than the MA samples after 15 hr treatment at 700 °C (Cragnolino and Sridhar, 1993a). In order to compare the data for different conditions, corrosion rate in Figures 5-1 and 5-2 are presented in a normalized scale by dividing the corrosion rate of the heat-treated specimens by that of the MA and SA samples, respectively. The corrosion rate in boiling HNO_3 for the MA and SA specimens heat treated at 700 °C for 15 hr was 1.26 and 15.4 mm/yr, respectively (Tables F-1 and F-2). At 750 °C, only 1 hr of heat treatment is required for SA samples to reach a relatively high corrosion rate, with a subsequent smaller increase in corrosion rate for 15 hr treatment. It may be observed that specimens heat treated at 700 °C had the highest corrosion rate. No appreciable increase in the corrosion rate was observed for specimens treated at 600 °C

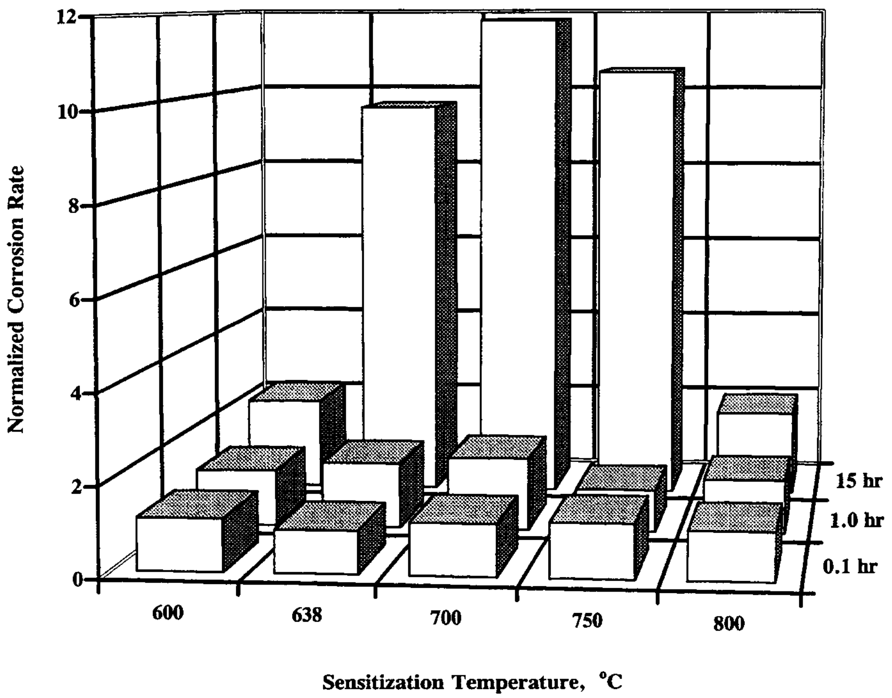

Figure 5-1. Effect of heat treatment temperature and time on the corrosion rate of mill-annealed specimens of alloy 825 in boiling 65 percent nitric acid

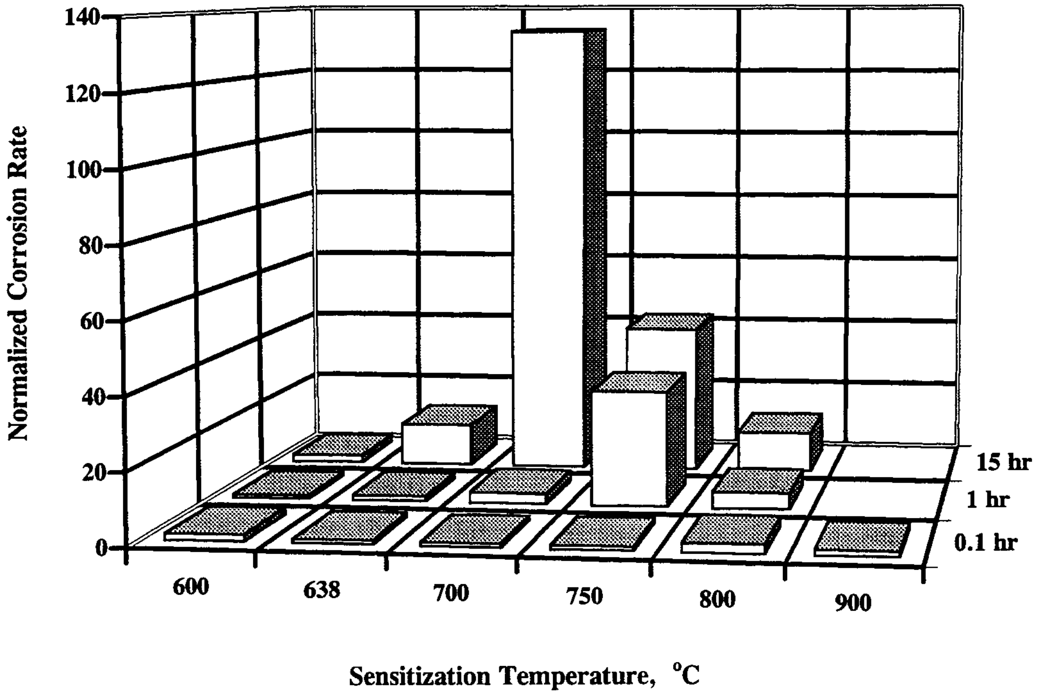

Figure 5-2. Effect of heat treatment temperature and time on the corrosion rate of solution-annealed specimens of alloy 825 in boiling 65 percent nitric acid

even for times of 15 hr. It is also apparent that 0.1 hr heat treatment of MA samples at any temperature is insufficient to produce a microstructure with a corrosion rate significantly higher than that of the original MA sample, since corrosion rates are lower than 0.13 mm/yr for all these MA and heat-treated specimens (Table F-1). It appears, however, that corrosion rates for the SA samples heat treated for 0.1 hr are slightly higher than those of the corresponding MA samples (Table F-2). This observation is in agreement with the slightly greater corrosion rate exhibited by the SA sample without further heat treatment (0.12 mm/yr) with respect to that of the original MA sample (0.10 mm/yr).

The results described above are expressed as corrosion rates in terms of uniform dissolution, following the procedures of the ASTM Standard. However, cross sections of the specimens indicated the development of localized dissolution along the grain boundaries, in the form of intergranular corrosion, for the heat-treated MA samples. Intergranular penetration and the extent of the attack increased with increasing heat treatment time at 700 °C, whereas the original MA sample only exhibited a very slight nonuniform attack. Increasing the temperature to 750 °C had a similar effect. At 800 °C, however, the specimen surface exhibited a very irregular appearance, but with a limited amount of intergranular penetration. In agreement with the corrosion rate measurements, the heat-treated SA samples showed deep intergranular penetration, particularly for the samples heat treated for 15 hr at temperatures of 700 °C or above. No signs of localized attack are shown by the SA sample without additional thermal treatment. Microstructural examinations of the cross sectioned and etched SA specimens revealed that precipitates formed at the grain boundaries after aging for 15 hr at 700 °C. Fewer precipitates were observed as the time and temperature of aging were decreased.

A convenient method for displaying the data of the intergranular corrosion tests is the use of TTS diagrams. The results described above are shown both for heat-treated MA and SA samples in Figure 5-3. A value of 0.3 mm/yr has been adopted as a boundary between the sensitized and the nonsensitized regions of the diagram. Although this value can be considered arbitrary, it is the same as that adopted previously by Raymond (1968). It should be emphasized, however, that the location of the boundary depends on the solution composition and other environmental conditions that are fixed in the ASTM A-262 Standard Practice C. In a different environment, the sensitization domain may be reduced or extended beyond that shown in Figure 5-3.

Longer thermal exposures up to 1,000 hr were conducted on SA specimens of Heat No. HH7004FK to determine if significant sensitization could be attained at lower temperatures and to determine the effects of cold work on the sensitization kinetics. In addition to boiling HNO_3, which promotes intergranular attack as a result of both grain boundary precipitation and chromium depletion, a boiling solution of 50 percent H_2SO_4+42 g/L $Fe_2(SO_4)_3 \cdot 4H_2O$, as described in ASTM A262 Practice D, was also used because it is considered to selectively identify sensitization due to chromium depletion at grain boundaries.

The results of the nitric acid corrosion test for long-term heat-treated specimens are shown in Figure 5-4 in terms of the normalized corrosion rate. For a heat treatment time of 15 hr, the corrosion rates shown here agree with those previously shown for the 12.5-mm-thick material (Tables F-2 and F-3). The addition of 25 percent cold work, as calculated by the method outlined in ASTM G-30 (American Society for Testing and Materials, 1994a), did not seem to increase the corrosion rate at aging temperatures at or above 700 °C. In addition, no significant increase in sensitization as a result of cold work was observed at lower treatment temperatures contrary to the results reported by Park et al. (1994) for alloy 600. The corrosion rate increased by a factor of two as the sensitization time at 700 and 750 °C was increased from 15 to 100 hr. At 640 °C, a slight increase was observed in the corrosion rate from

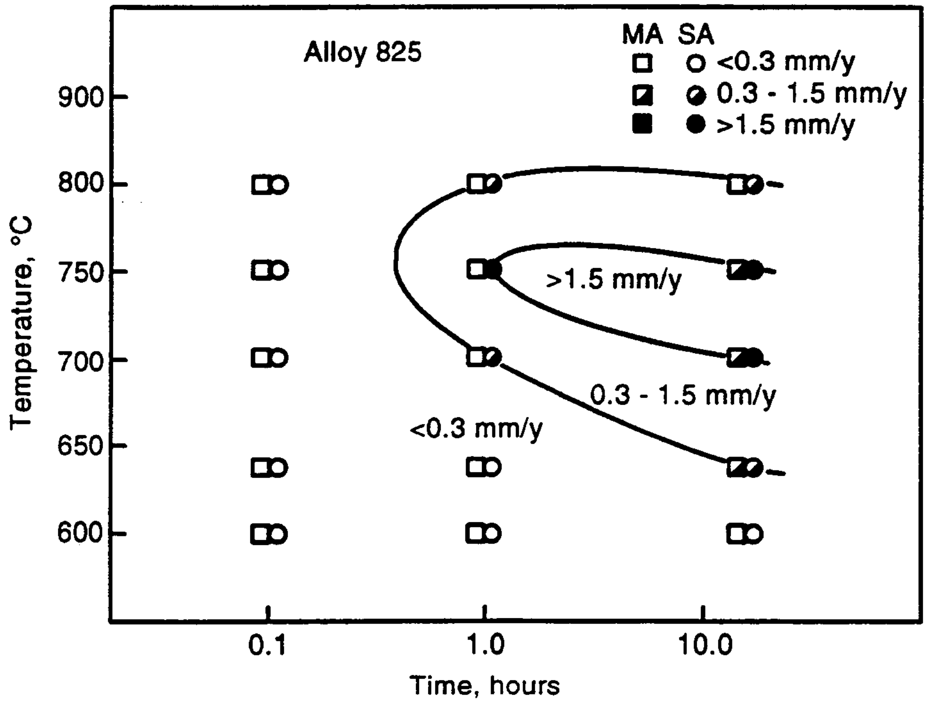

Figure 5-3. Time temperature sensitization diagram for mill-annealed and solution-annealed specimens of alloy 825 in boiling 65 percent nitric acid solution

0.38 mm/yr for the 15-hr aged specimens to 0.67 mm/yr after 100 hr of aging. A significant increase in corrosion rate was observed for specimens heat treated for 1,000 hr, as shown in Figure 5-4, reflecting the relevance of prolonged heat treatments. A fourfold increase in the corrosion rate was observed at 600 °C. After 15 hr of aging at 600 °C, the corrosion rate was 0.10 mm/yr, the same as unaged SA or MA specimens. However after 100 hr the corrosion rate increased to 0.38 mm/yr indicating some degree of sensitization.

Results of the sulfuric acid-ferric sulfate tests are shown in Figure 5-5. Clearly, the corrosion rate in this test was much less than that in boiling nitric acid (Table F-3). However, the trends in this data are the same as observed in the nitric acid test. The maximum corrosion rate was observed in the specimen aged for 1,000 hr at 640 °C. The specimen heat treated at 600 °C for 100 hr had a corrosion rate two times higher than the SA specimen. Again, no increase in sensitization was observed on specimens cold worked prior to thermal aging at 750 °C.

From Figures 5-4 and 5-5, it is apparent that the nitric acid test is much more sensitive to grain boundary precipitation than the sulfuric acid-ferric sulfate test. The differences in the corrosion rates observed in these tests are apparently due to the different sensitivities of these tests to grain boundary chemistry, as discussed by Streicher (1978). The sulfuric acid-ferric sulfate test is sensitive to the extent of the chromium depletion region, both its microstructural width and its minimum Cr concentration. The nitric acid test is sensitive to both Cr depletion and the presence of Cr^{6+} species in the test solution. It has been shown that the higher Cr-containing phases have higher corrosion rates in nitric acid solutions containing Cr^{6+}. If the grain boundary region has some level of Cr depletion, preferential corrosion occurs initially in this region in nitric acid. Once a sufficient concentration of Cr^{6+} species is generated, then

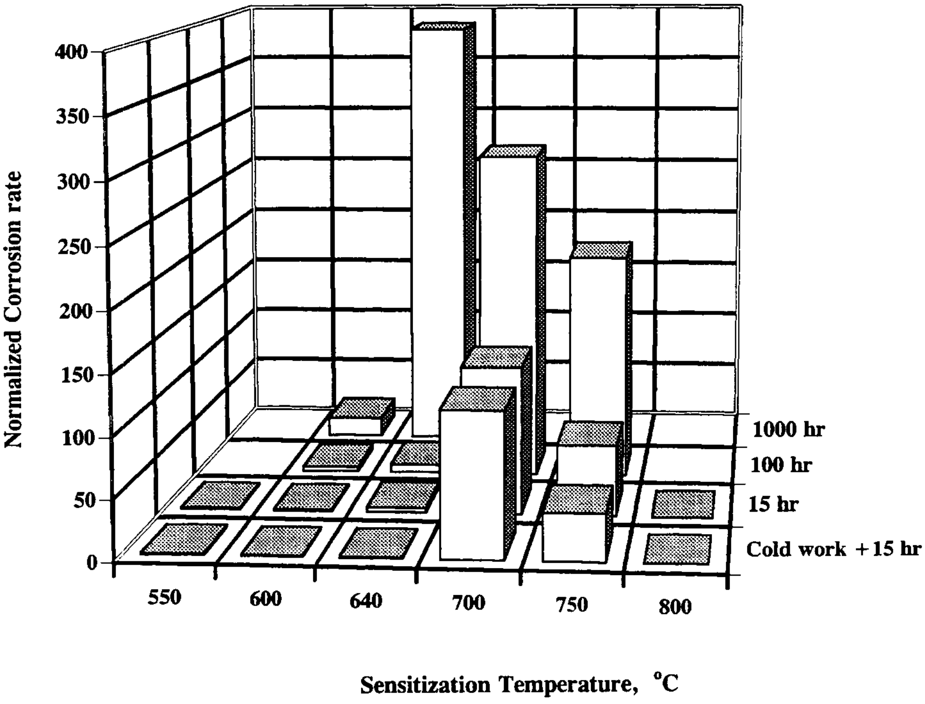

Figure 5-4. Effect of heat treatment temperature and time, including the effect of cold work on the corrosion rate of solution-annealed specimens of alloy 825 in boiling 65 percent nitric acid

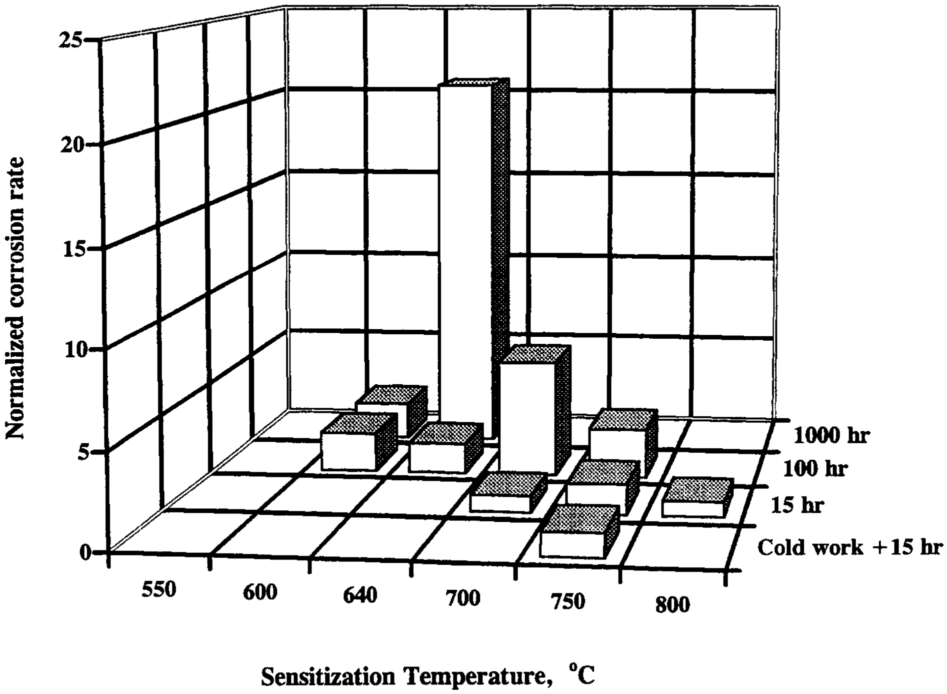

Figure 5-5. Effect of heat treatment temperature and time, including the effect of cold work on the corrosion rate of solution-annealed specimens of alloy 825 in sulfuric acid plus ferric sulfate solution

accelerated corrosion occurs in the grain boundary where there is an enriched Cr phase due to the presence of $M_{23}C_6$. Hence, the observed differences in the corrosion rate of heat-treated alloy 825 in nitric acid compared to that in sulfuric acid-ferric sulfate solution seems to be indicative of a very narrow region of Cr depletion for this alloy. This finding is in agreement with the previous results of Brown (1969) on alloy 825 with a higher carbon (0.03 percent) content and slightly lower (21.24 percent) Cr concentration.

Efforts to find an alternative test to characterize the degree of sensitization of alloy 825 centered around the EPR and CPP tests. EPR tests were first conducted on type 304L SS in both the sensitized (621 °C for 24 hr) and the MA conditions in 0.5 M H_2SO_4 solution with the addition of 0.01 M KSCN. The results of these initial benchmark tests, that agree well with the ASTM G 108-94 round-robin test results (American Society for Testing and Materials, 1994d) are shown in Figure 5-6. It can be seen that for the MA specimen without any sensitization, no reactivation peak is present. For the sensitized material, a large reactivation peak at -202 mV_{SCE} is observed. The result of a double loop EPR test for a sensitized 304L SS specimen is shown in Figure 5-7. It should be noted that the maximum current density of the forward anodic peak (I_a) is 54 mA/cm^2 and the maximum current density of the reactivation peak (I_r) is 10 mA/cm^2. No reactivation peak was observed on the MA material.

Attempts to use either the single loop or the double loop EPR test for characterizing sensitization of alloy 825 were not successful. The single loop method using 0.5 M H_2SO_4 solution with 0.01 M KSCN at 30 °C did not show a reactivation peak for sensitized alloy 825. Additional tests were conducted in up to 50 percent H_2SO_4 with and without the addition of KSCN at temperatures up to 100 °C. Although some grain boundary etching of the sensitized material was observed in 20 to 30 percent H_2SO_4 at 100 °C, no reproducible distinction could be made between the reactivation peaks of the sensitized specimens and the SA specimens (Figure 5-8). In double loop EPR tests conducted in 20 percent H_2SO_4, a small reactivation peak was only observed for sensitized specimens. For this test, shown in Figure 5-9, the I_a was 542 $\mu A/cm^2$ and the I_r was 21 $\mu A/cm^2$. Because of the very small reactivation peak for this well sensitized specimen (15 hr at 750 °C), the characterization of alloy 825 specimens with different degrees of sensitization was not attempted using this technique.

The effect of sensitization on localized corrosion was then examined using CPP tests conducted in a range of chloride concentrations. CPP tests conducted in solutions containing 100 ppm Cl^- were found to be the most sensitive to grain boundary precipitation. The correlation between the nitric acid test results and the repassivation potential, E_{rp}, in chloride solution is shown in Figure 5-10. The E_{rp} values were derived from tests in which pitting was initiated at high potentials. Heat treatment conditions that lead to a high corrosion rate in 65 percent nitric acid resulted in a lower E_{rp} in the dilute chloride solution. Sensitized specimens had pits initiating from grain boundaries whereas nonsensitized specimens showed random pitting, mainly at the grain interiors. The E_{rp} for the MA material was found to be lower than that for the SA material, whereas the nitric acid and sulfuric acid-ferric sulfate tests indicated no significant difference. The MA specimen has some intragranular and intergranular precipitates, which are a combination of TiC and $M_{23}C_6$, whereas the SA microstructure is essentially free of the precipitates. The decrease in the E_{rp} with sensitization was only observed in the 100 ppm Cl^- solution and only when the polarization scan reached potentials above 1.0 V_{SCE}. If pits were initiated potentiostatically at 800 mV_{SCE} in a 100 ppm Cl^- solution no significant effect on E_{rp} was observed. At 20 ppm Cl^-, no consistent pitting was observed. In contrast, in a 1,000 ppm Cl^- solution, pitting was consistently observed but the E_p and the E_{rp} of SA, MA, and sensitized specimens were virtually the same.

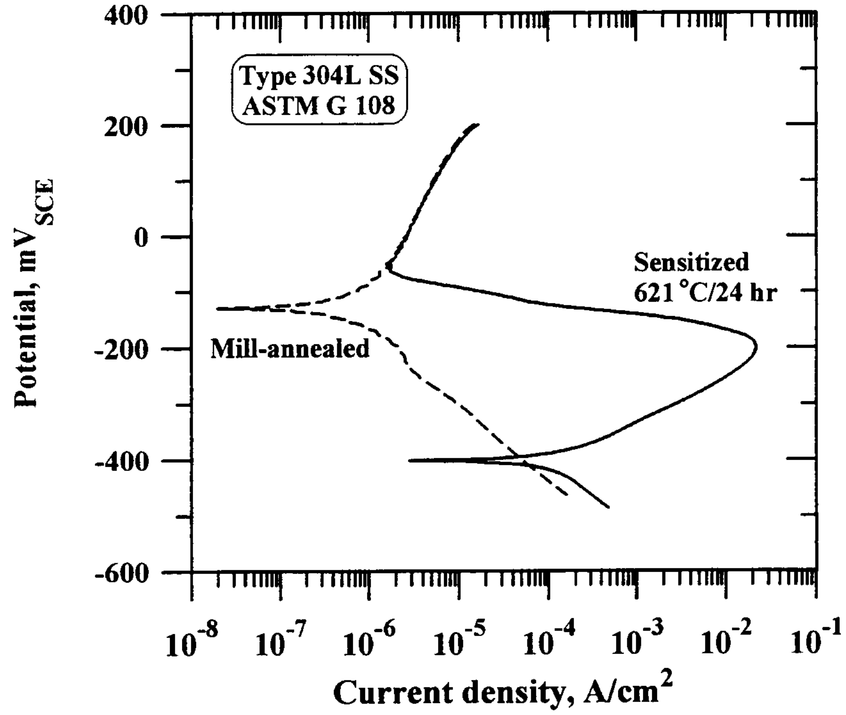

Figure 5-6. Single loop electrochemical potentiokinetic reactivation scans of mill-annealed and sensitized type 304L stainless steel conducted in 0.5 M H_2SO_4+0.01 M KSCN at 30 °C (scan rate: 1.67 mV/s)

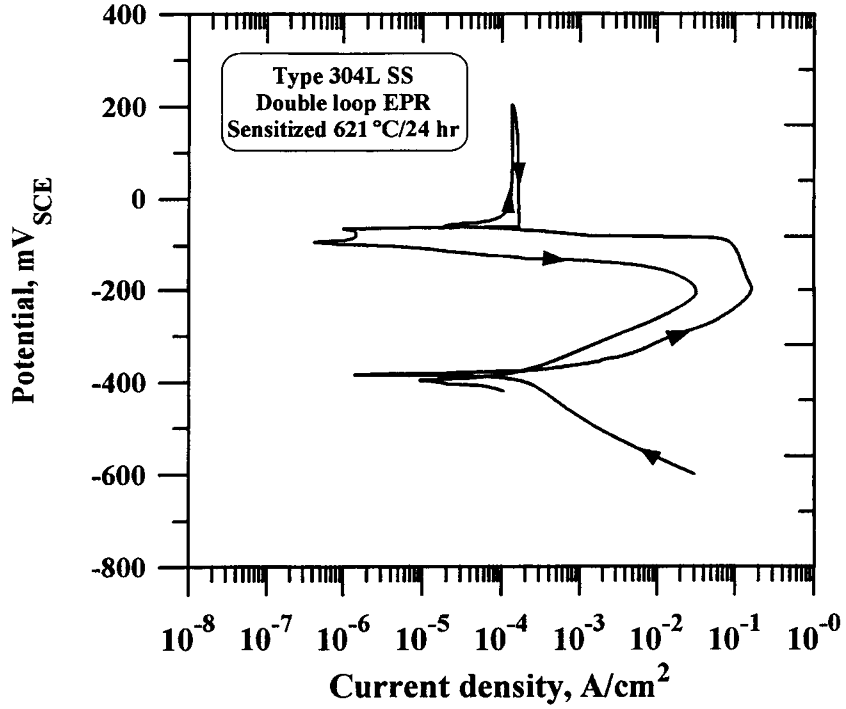

Figure 5-7. Double loop electrochemical potentiokinetic reactivation scans of sensitized type 304L stainless steel conducted in 0.5 M H_2SO_4+0.01 M KSCN at 30 °C (scan rate: 1.67 mV/s)

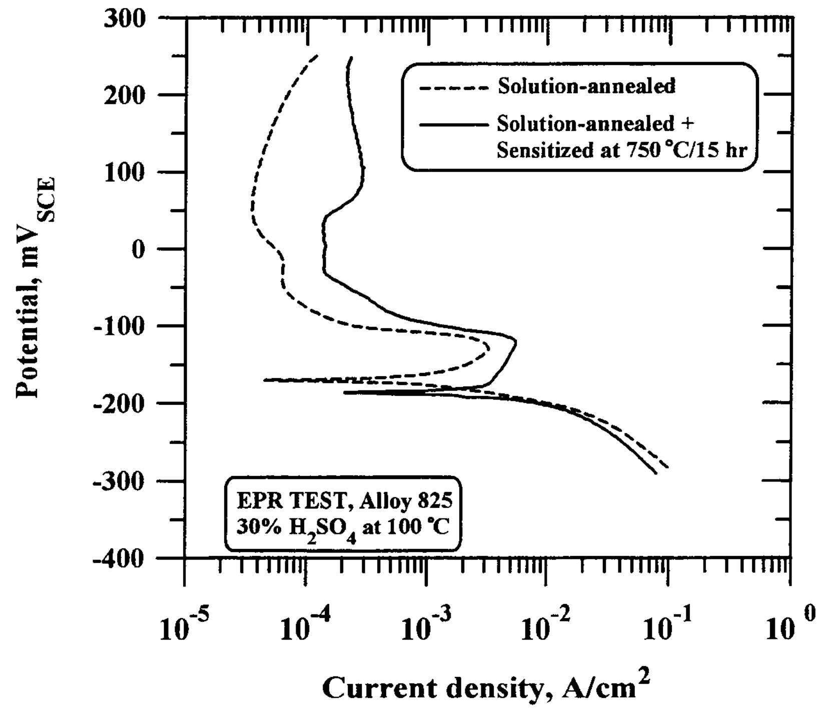

Figure 5-8. Single loop electrochemical potentiokinetic reactivation scans of annealed and sensitized alloy 825 conducted in 30 percent H_2SO_4 at 100 °C (scan rate: 1.67 mV/s)

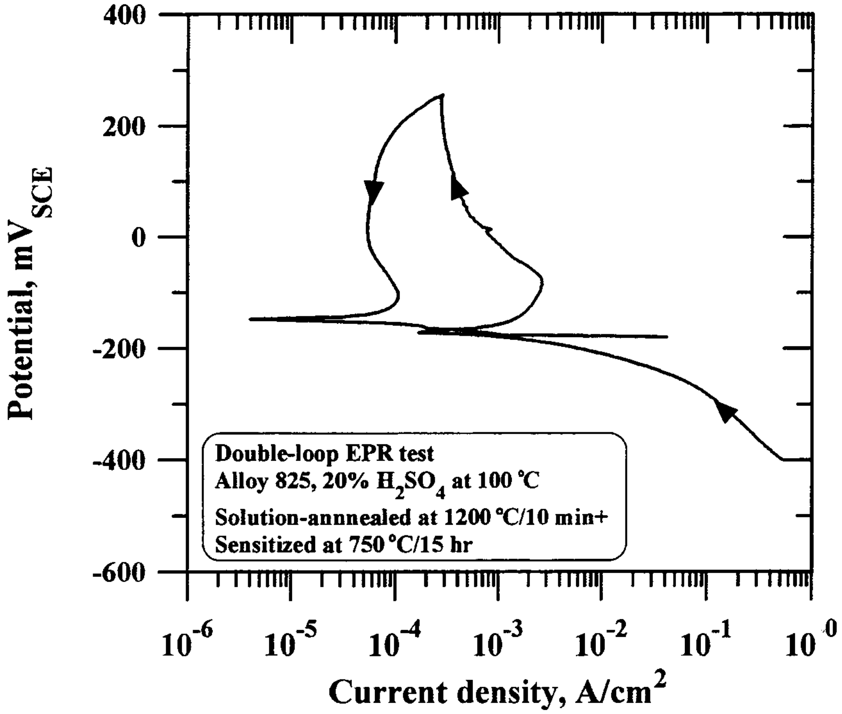

Figure 5-9. Double loop electrochemical potentiokinetic reactivation scans of sensitized alloy 825 conducted in 20 percent H_2SO_4 at 100 °C (scan rate: 1.67 mV/s)

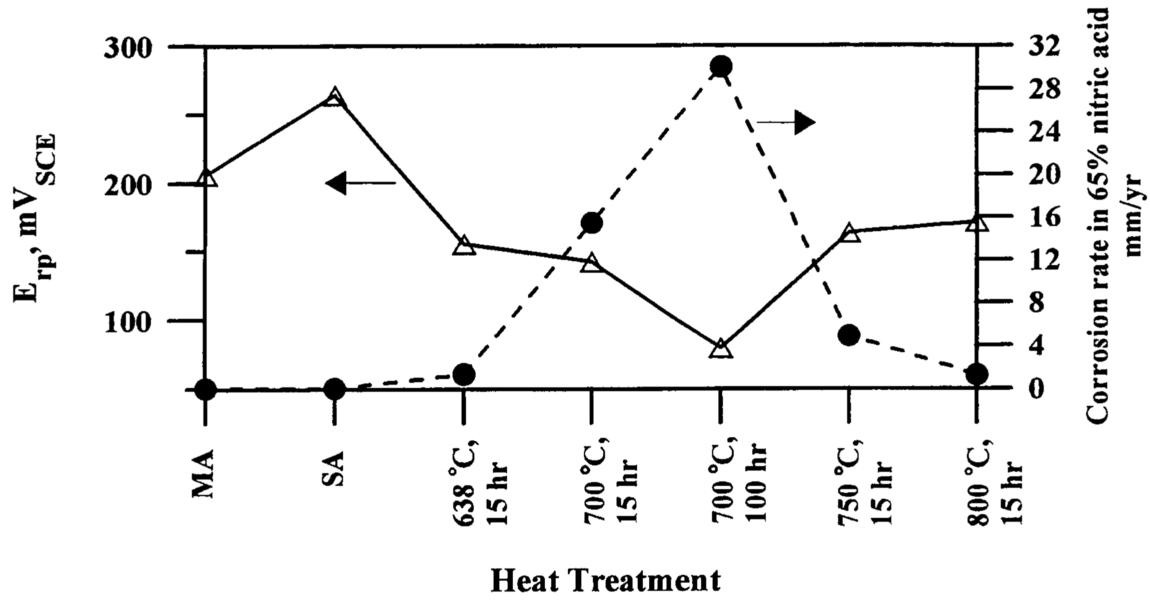

Figure 5-10. A comparison of the repassivation potential measured at a scan rate of 0.167 mV/s in 100 ppm Cl^- solution at 95 °C (shown as the triangles) and the corrosion rate in boiling 65 percent nitric acid (shown as circles) of variously heat-treated alloy 825

5.3.2 Scanning Transmission Electron Microscopy Studies

5.3.2.1 Precipitation Characterization

Only $M_{23}C_6$-type carbide was observed on the grain boundaries at all aging temperatures and times employed in this study. The bright-field image and the selected area diffraction pattern of a SA specimen aged subsequently at 750 °C for 15 hr are shown in Figure 5-11. The globular precipitates were carbides of the $M_{23}C_6$ type, which agrees with the literature findings for this alloy (Raymond, 1968). Lower aging temperatures produced a finer, but more numerous, grain boundary precipitate, but the type of precipitate was still $M_{23}C_6$ (Figure 5-12). The density of precipitates decreased upon aging at 800 °C (Figure 5-13), but their size increased significantly.

5.3.2.2 Effect of Polishing Procedure

As mentioned before, two common electropolishing solutions were used: (i) 80 mL perchloric acid+180 mL ethylene glycol+300 mL methanol and (ii) 15 percent nitric acid + methanol mixture. As shown in Figure 5-14, the Cr profile across a grain boundary is significantly different for the two polishing solutions. This was observed for all aging treatments. The Cr-depleted zone observed in the foil specimen electropolished in a perchloric acid solution is significantly deeper and wider than that electropolished in a nitric acid solution, indicating a surface chemistry artifact as a result of the electropolishing operation. The chemical composition of the grain boundary carbides measured in these thin-foil specimens

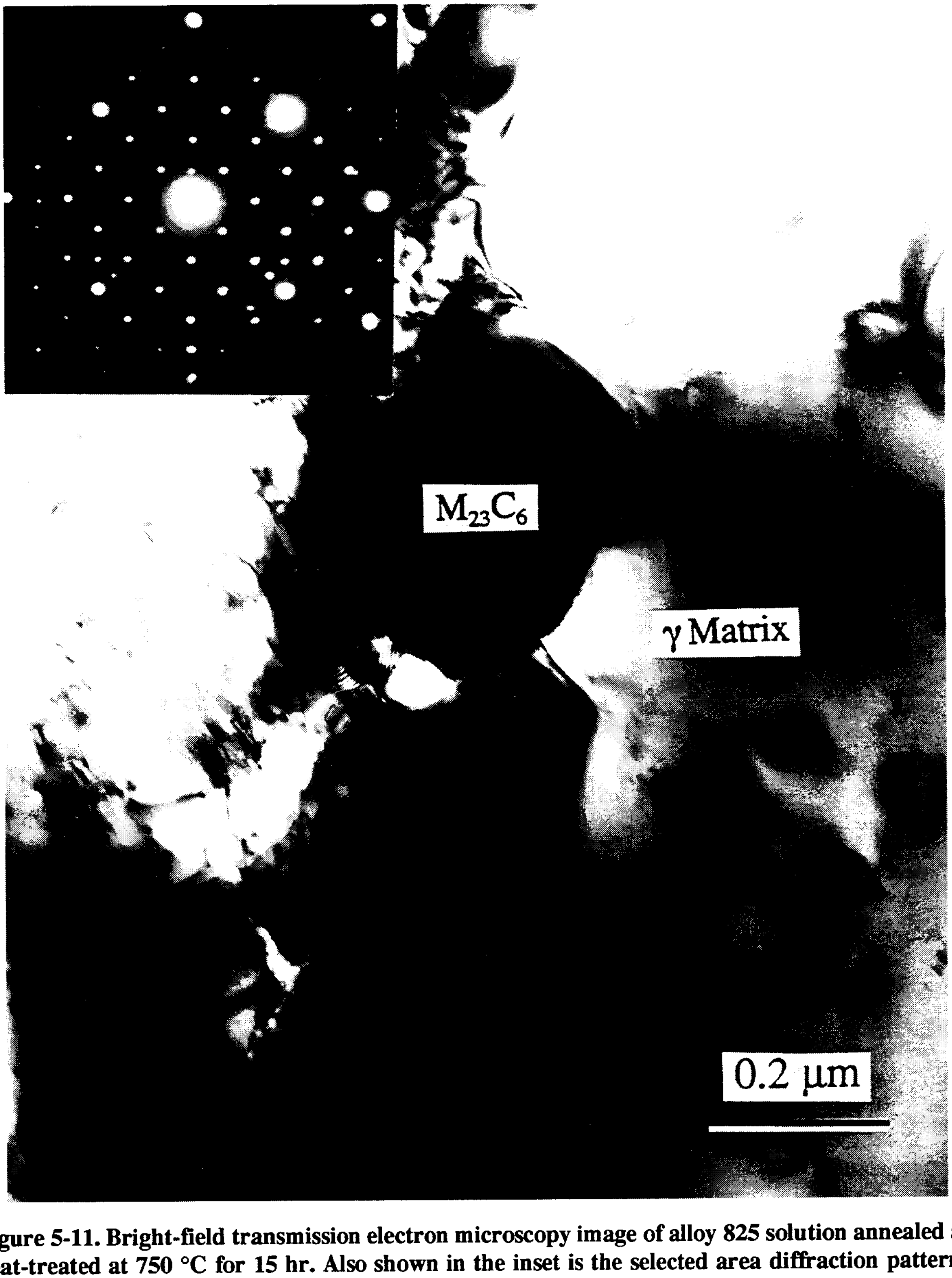

Figure 5-11. Bright-field transmission electron microscopy image of alloy 825 solution annealed and heat-treated at 750 °C for 15 hr. Also shown in the inset is the selected area diffraction pattern of the austenite grain in the [001] zone axis and the grain boundary carbide oriented in the [001] zone axis.

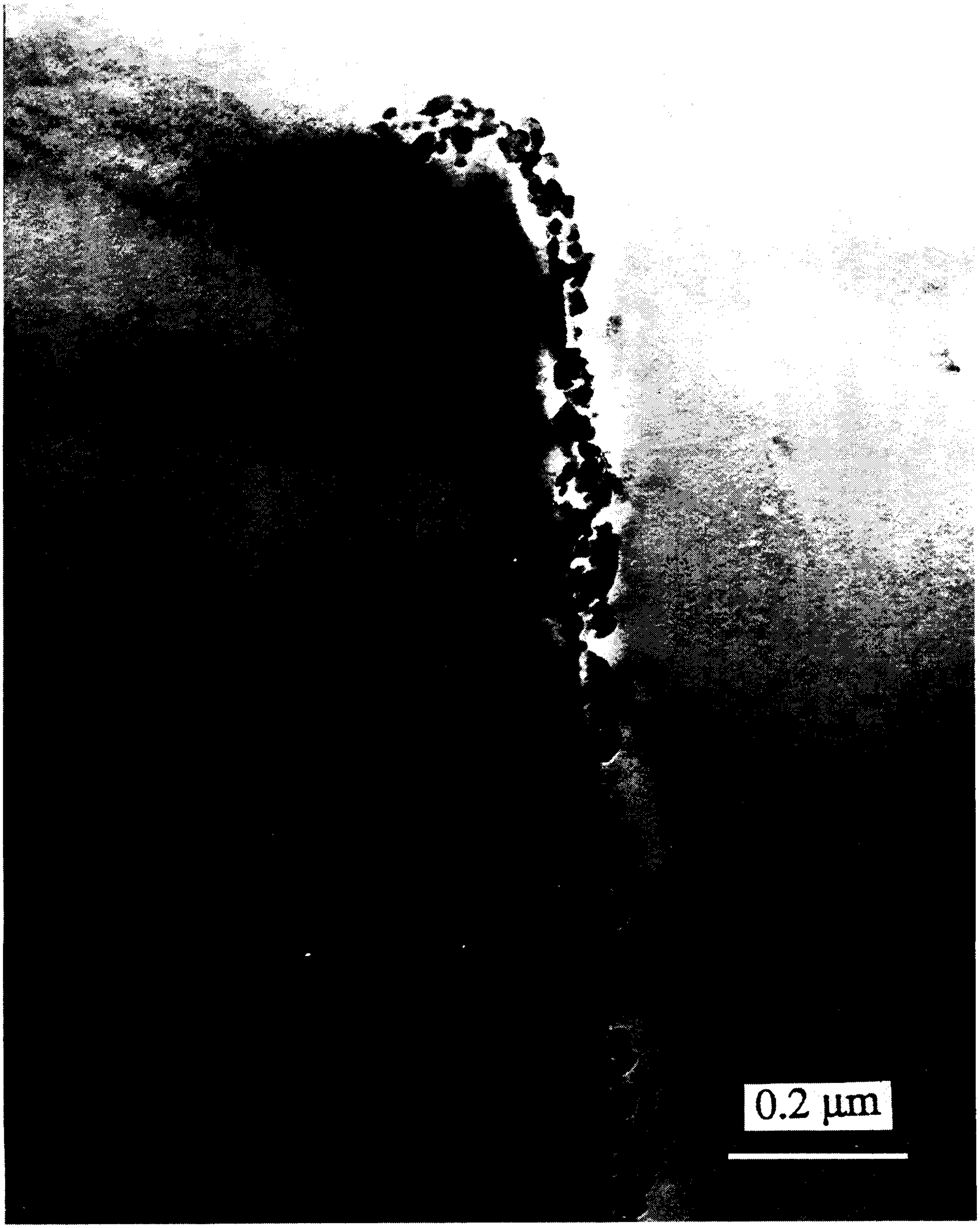

Figure 5-12. Bright-field transmission electron microscopy image of alloy 825 solution annealed and heat-treated at 640 °C for 15 hr showing a fine distribution of $M_{23}C_6$ precipitates at a grain boundary

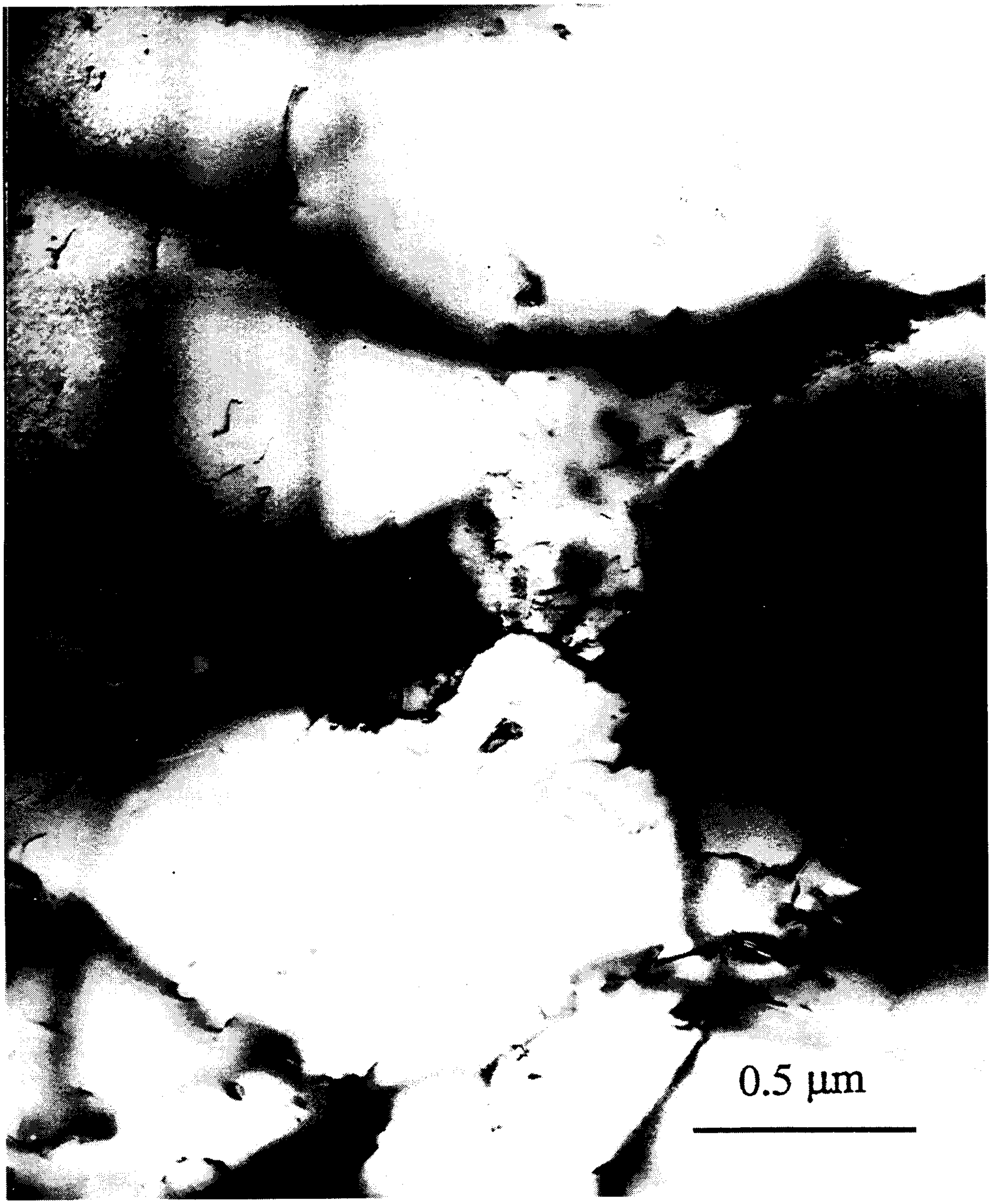

Figure 5-13. Bright-field transmission electron microscopy image of alloy 825 solution annealed and heat-treated at 800 °C for 15 hr showing a coarse precipitate at a grain boundary

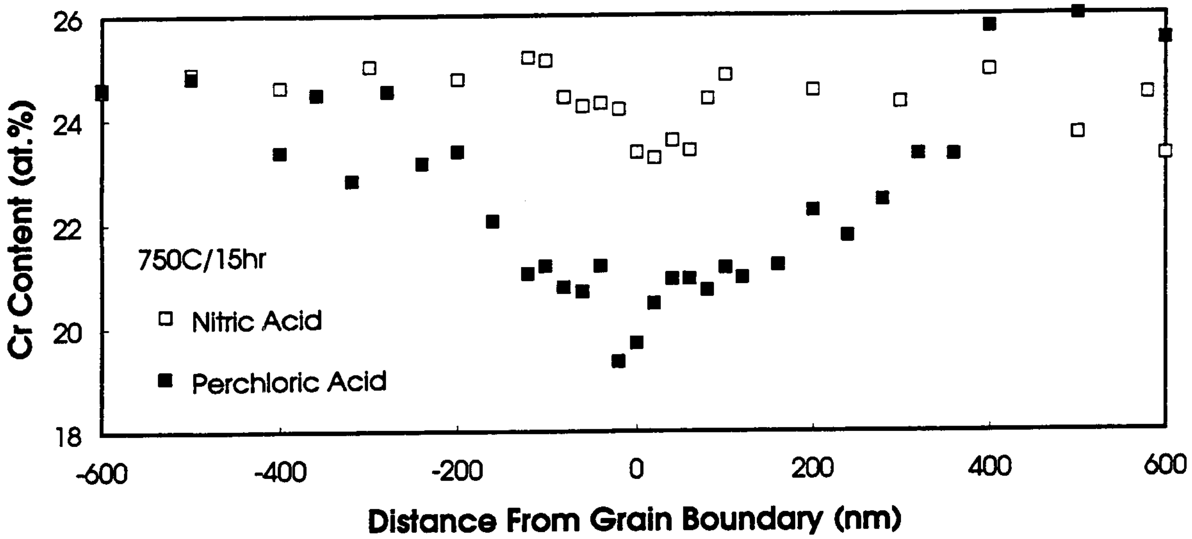

Figure 5-14. Chromium concentration profiles along a grain boundary of alloy 825, heat-treated at 750 °C for 15 hr, containing $M_{23}C_6$ precipitates as measured after electropolishing in nitric acid and in perchloric acid solutions

electropolished in both of the solutions is also presented in Table 5-1. It can be seen that the chromium content of the carbides for the perchloric acid-polished specimens is substantially higher than that for the nitric acid-polished specimens. The Cr content of the carbides in the specimens polished in a perchloric acid solution was found to be more consistent with the literature findings as shown in Table 5-2. In contrast, the Cr content of carbides in specimens prepared by electropolishing in the nitric acid solution was 31 at. percent at Cr. In addition, the Mo content of the precipitates is higher for the perchloric acid polishing solutions.

Table 5-1. Chemical composition of grain boundary carbides in atomic percent (the ± sign indicates the 95 percent confidence interval)

Polishing Solution	Fe	Ni	Cr	Mo
Perchloric Acid	10.1 ± 2.2	9.9 ± 2.5	71.9 ± 4.7	4.7 ± 0.9
Nitric Acid	27.2 ± 1.0	36.4 ± 1.7	31.0 ± 2.1	2.1 ± 0.3

The most likely source of the changes in chromium concentration profile and carbide chemical composition is considered to be a preferential dissolution process at the surface of the grain boundary region during the electropolishing preparation of the thin-foil specimens. It has been reported in intergranular corrosion studies that the high-Cr containing phases corrode faster in nitric acid solutions because of the formation of hexavalent chromium during the corrosion test (Streicher, 1978). In the case

Table 5-2. Chemical compositions of $M_{23}C_6$-type carbides presented in the literature

Alloy	Cr (weight percent)	Reference
316LN	65.0	Hall and Briant, 1984
Alloy 690	88.5	Angeliu and Was, 1990
17Cr-12Ni SS	74.1	Thorvaldsson et al., 1981
IN939	98.2	Smith et al., 1981
316LN	63.1	Mulford et al., 1983
308 SS	75.0	Chen et al., 1990

of Transmission Electron Microscopy (TEM) thin-foil specimens preparation, a stagnant, viscous film is expected to be present on the thin-foil surface during the jet electropolishing operation (Goodhew, 1984; Esteban et al., 1990) and since the grain boundary region has a small chromium depletion, preferential dissolution may occur initially in this region in the nitric acid solution. Because the stagnant layer in jet polishing is thin, the concentration of Cr^{6+} generated in the nitric acid polishing solution may be high. Once sufficient Cr^{6+} is generated in the solution in this polished region, then accelerated polishing occurs in the grain boundary where there is a higher-Cr phase. As a result, accelerated dissolution of chromium in the Cr-rich carbide precipitates and a resultant enrichment of Ni and Fe are observed. It appears that Mo is also preferentially dissolved in nitric acid polishing solutions due to the same kind of mechanism. In a similar way, a shallow Cr-depleted zone is produced in specimens polished in nitric acid solutions because once Cr^{6+} is generated in the polishing solution, the higher-Cr regions in the specimen dissolve faster than the lower-Cr regions. In contrast, the perchloric acid electropolishing does not operate in a sufficiently high potential regime to sustain the formation of Cr^{6+}. This interpretation is a hypothesis since it is not possible to establish the potential difference at the metal/solution interface under the high-applied voltage used in jet electropolishing. Further investigation of grain boundary chemistry was carried out using only the perchloric acid polishing solution.

5.3.2.3 Effect of Aging Treatment of Chromium Depletion Profiles

The profile was taken across the grain boundary in-between precipitates. Several grain boundary areas were examined on different specimens of the same treatment. The effect of aging temperature on the grain boundary depletion of Cr is shown in Figure 5-15. It can be seen that aging at 700 °C produced the lowest grain boundary Cr concentration. The effect of aging time at 700 °C on Cr profile is shown in Figure 5-16. While longer aging time did not appreciably affect the minimum Cr concentration, a widening of the depleted zone is seen in Figure 5-16. Mo depletion was also observed in some specimens, but was never consistent. It is possible that the small concentrations of Mo present in the alloy did not permit an accurate analysis of the profile with the current instrument. The relative error in the determination of the Mo content in the matrix is close to 30 percent. It must be noted, however, that the carbide precipitates consistently exhibited a higher Mo content than the matrix.

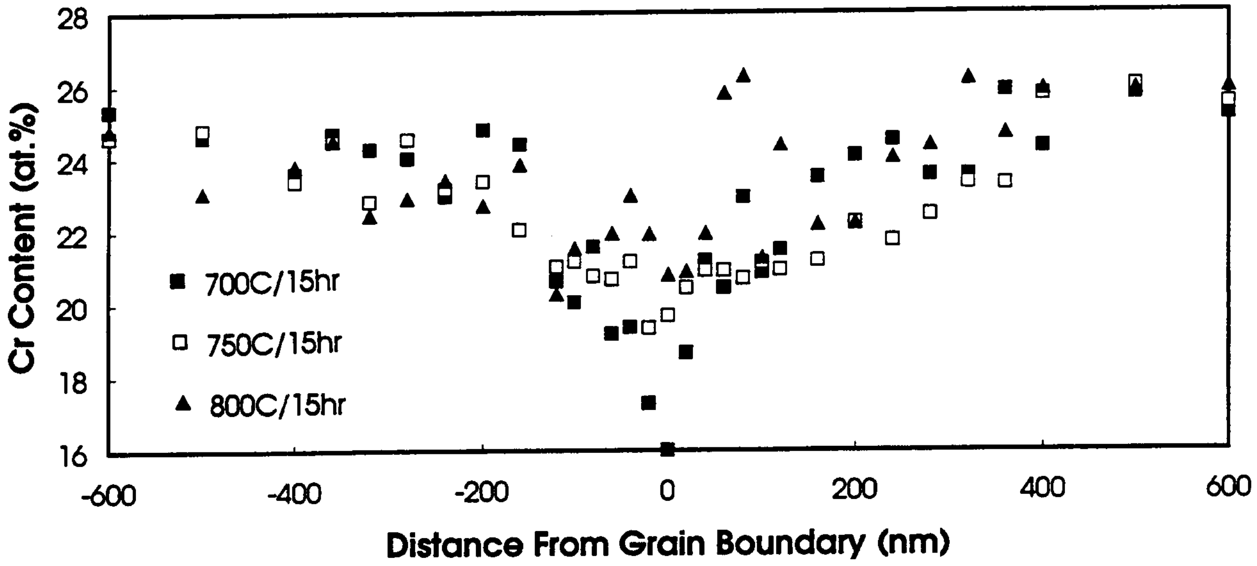

Figure 5-15. Chromium concentration profiles along a grain boundary of alloy 825 containing $M_{23}C_6$ precipitates after heat treatment for 15 hr at various temperatures

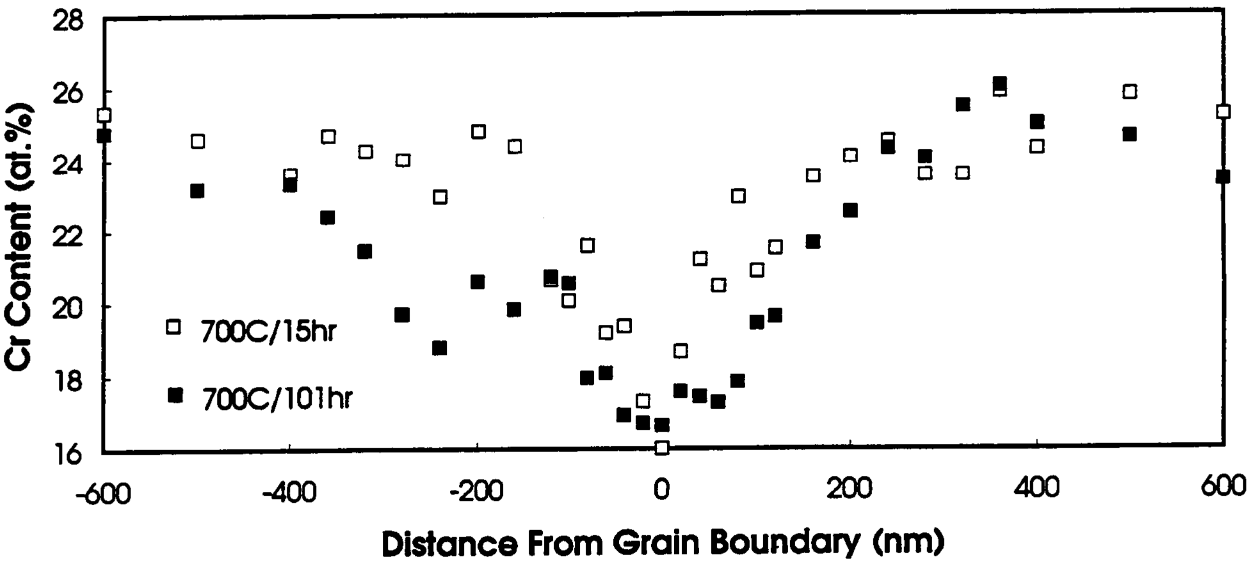

Figure 5-16. Effect of heat treatment time on the chromium concentration profiles along a grain boundary of alloy 825 thermally treated at 700 °C

5.4 DISCUSSION

5.4.1 Kinetics of Aging Effects

The results described in the previous section essentially confirm the findings reported by Raymond (1968) regarding the temperature range for sensitization and the location of the "nose" in the TTS diagram for alloy 825. The SA material indicated a much higher degree of sensitization than the MA material. This was rationalized by Raymond (1968) in terms of the redissolution of matrix $M_{23}C_6$ carbides rather than the Ti(C,N) and reprecipitation of these carbides along the grain boundaries. The practical importance of the analysis of the SA material arises from the presence of a narrow zone exhibiting the SA microstructure adjacent to weldments.

However, for a material SA at 1,204 °C and then annealed at 940 °C for 1 hr (temperature of the current stabilizing treatment for MA samples), Raymond (1968) found a much larger sensitization domain, in terms of time and temperature, than that found in the current investigation. In addition, it should be noted that, in the present work, a corrosion rate as high as 15.5 mm/yr was attained in SA samples after 15 hr of heat treatment at 700 °C, (Table F-2) whereas approximately the same rate was obtained by Raymond (1968) after just 0.2 hr. The simplest explanation for the greater degree of sensitization of the material studied by Raymond (1968) is related to the higher carbon content of the original composition of alloy 825. Raymond (1968) tested a heat of alloy 825 with a carbon content of 0.03 weight percent, whereas the heat used in the present study contains only 0.01 weight percent. The effect of the higher carbon content on the sensitization of alloy 825 is understandable in terms of chromium depletion as determined by the equilibrium chromium concentration at the carbide–matrix interface. This will be discussed in greater detail later in this section. Chromium carbides precipitate initially along grain boundaries at sensitization temperatures because the solubility of carbon in alloy 825 is about 0.01 weight percent (Raymond, 1968). This is the value measured at about 980 °C, but it could be even slightly smaller at lower temperatures.

In order to evaluate potential sensitization effects at lower temperatures, corrosion rates measured in SA samples heat treated for 15 hr at temperatures ranging from 600 to 700 °C were plotted on a logarithmic scale as a function of the reciprocal of the heat treatment temperature, as shown in Figure 5-17. A typical Arrhenius behavior was observed with an apparent activation energy of approximately 292.6 kJ/mole (69.9 kcal/mole). This value is relatively close to the activation energy for matrix diffusion of chromium in a nickel-based alloy such as alloy 600 (Ni-15%Cr-6%Fe), in which a value of 277.7 kJ/mole has been measured by Pruthi et al. (1977). Data for binary Ni-Cr alloys, reported also by Pruthi et al., indicate that the activation energy increases with increasing chromium content, reaching about 290.4 kJ/mole for Ni-29.7%Cr. This effect of the chromium content on the activation energy for chromium diffusion may be the reason of the high value for the activation energy obtained in the present study, since the chromium content of alloy 825 is higher than that of alloy 600. It appears that the corrosion rates measured in the thermally-treated SA samples can be related, at least qualitatively, to the degree of sensitization, as given by the level of chromium depletion and the width of the depleted zone. The width of the depleted zone is approximately given by $2(Dt)^{1/2}$, where D is the matrix diffusion coefficient of chromium at the temperature of interest and t is time. A detailed experimental study of Cr depletion profiles in alloy 825, as affected by heat treatment temperature and time, would be required to confirm that suggestion, coupled with the application of thermodynamic and kinetics models for the interpretation of chromium depletion.

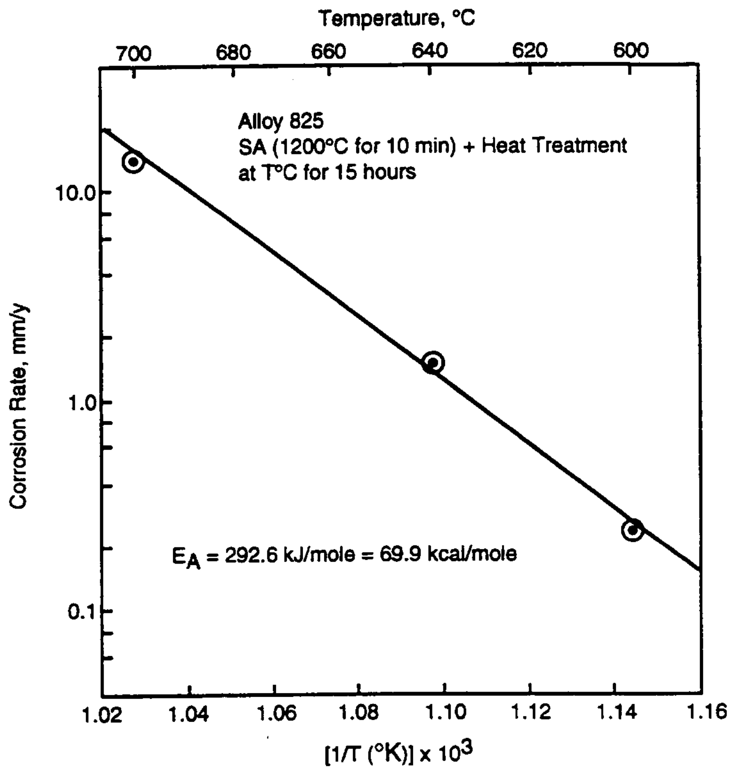

Figure 5-17. Corrosion rates for solution-annealed specimens of alloy 825 in boiling 65 percent nitric acid solution as a function of the reciprocal of the heat-treatment temperature

Leaving aside any mechanistic interpretation of the activation energy values discussed above, it is apparent, however, that such high values indicate a very strong temperature dependence. A decrease in temperature from 600 to 400 °C implies a decrease of at least five orders of magnitude in the rate of the controlling process (i.e., chromium diffusion) if there is no change in the mechanism with respect to that prevailing in the 600 to 700 °C range. This implies that heat treatments extended for more than 18 yr will be required at 400 °C to obtain the degree of sensitization observed in the high-temperature range. In order to study the thermal stability of alloy 825 at temperatures closer to those expected under repository conditions within a realistic time frame, it would be necessary to enhance metallurgical processes responsible for sensitization, such as carbide precipitation and chromium diffusion, among others. This can be accomplished by introducing a higher dislocation density in the γ matrix of SA samples through cold work prior to the sensitization treatments. It is known that cold work (up to 20 percent) prior to sensitization increases significantly the degree of sensitization of type 304 SS (Pednekar and Smialowska, 1980). However, cold-working of austenitic SSs results in the formation of martensite, which is not the case of alloy 825. This is an additional incentive to evaluate the influence of cold work on the low-temperature behavior of alloy 825, because the effect cannot be predicted simply by comparing with that of SS. It should be noted that Park et al. (1994) found that cold work preceding heat treatment accelerates the precipitation of M_7C_3 carbides in alloy 600. The effect of cold work on thermal stability is also important from a practical point of view. Surface and near-surface areas of the HLW containers could be affected by cold work arising from sudden mechanical loads, impingement by wall-rock shear offsets, and other interactions leading to localized plastic deformation. Initial investigations using U-bend specimens of SA material, however, did not indicate any effect of cold work on sensitization kinetics (Figures 5-4 and 5-5). This may indicate that the amount of cold work in the U-bend was inadequate or alloy 825 is relatively insensitive to cold work as compared to type 304 SS.

5.4.2 Approach to Modeling Sensitization

The effects of aging time and temperature on corrosion and E_{rp} may be better understood if combined with the STEM analyses. For this purpose, the size of the chromium depletion zone and the level of Cr were considered together as an equivalent Cr depletion zone width as suggested by Was et al. (1981). The area of the depletion profiles shown in Figures 5-15 and 5-16 below various Cr concentrations were calculated. This area was then divided by the bulk Cr concentration to obtain an equivalent width of the Cr depletion zone (in nanometers). It must be noted that the chromium concentration here refers to atomic percent. The corrosion rate in boiling 65 percent nitric acid is plotted as a function of the equivalent Cr depletion size for various Cr levels in Figure 5-18. It can be seen that a good correlation is obtained between the corrosion rate and depletion size below a Cr concentration of 20 to 21 atomic percent. The regression coefficient for the 19 percent Cr depletion widths is deceptively high because of the fewer points associated with it. Figure 5-18 suggests that the corrosion rate in boiling nitric acid is determined by the size of the depletion zone below a critical Cr concentration of about 21 atomic percent (about 19 weight percent). The effect of Cr depletion zone size on the E_{rp} is shown in Figure 5-19. The correlation is poorer than that for the corrosion rate in nitric acid. This poor correlation presumably arises from the fact that localized corrosion resistance is a function of both Cr and Mo. The STEM analyses of Mo did not indicate significant depletion although the carbide analyses showed higher Mo. This observation may be due to a lack of resolution of the Mo analyses, low Mo concentrations, or the result of a very narrow Mo profile. The poorer correlation in Figure 5-19 may be a result of considering only Cr depletion. Another possibility is that a linear correlation of Cr depletion to E_{rp} is not valid. It can be observed in Figure 5-19 that below a depletion zone size of about 5 nm, the E_{rp} levels off, indicating pitting in the matrix.

It must be noted that the degree of sensitization in this study was not as high as that investigated for alloy 600 by Was et al. (1981). Additionally, other factors such as P segregation can affect the corrosion rate, especially in nitric acid (Briant, 1987). In contrast, the corrosion rate in boiling nitric acid and E_{rp} did not correlate well with minimum Cr concentration at the grain boundaries. For example, both aging treatments at 700 °C, for 15 hr and 100 hr, showed the same minimum Cr concentration, but the latter treatment resulted in significantly higher sensitization.

In order to determine whether sensitization can significantly affect the corrosion resistance of alloy 825 under repository time-temperature conditions, the kinetics of Cr+Mo depletion must be modeled and coupled with empirical data correlating the depletion zone width to E_{rp} in various environments of interest to the repository. The current data set is limited in nature, but establishes a methodology for predicting the effect of sensitization on localized corrosion and possibly SCC, assuming that E_{rp} is the bounding parameter for SCC in the sensitized material. Modeling of Cr+Mo depletion kinetics has been attempted by numerous investigators and reviewed by Bruemmer (1990). The formation of $M_{23}C_6$ carbide can be represented by the following overall reaction:

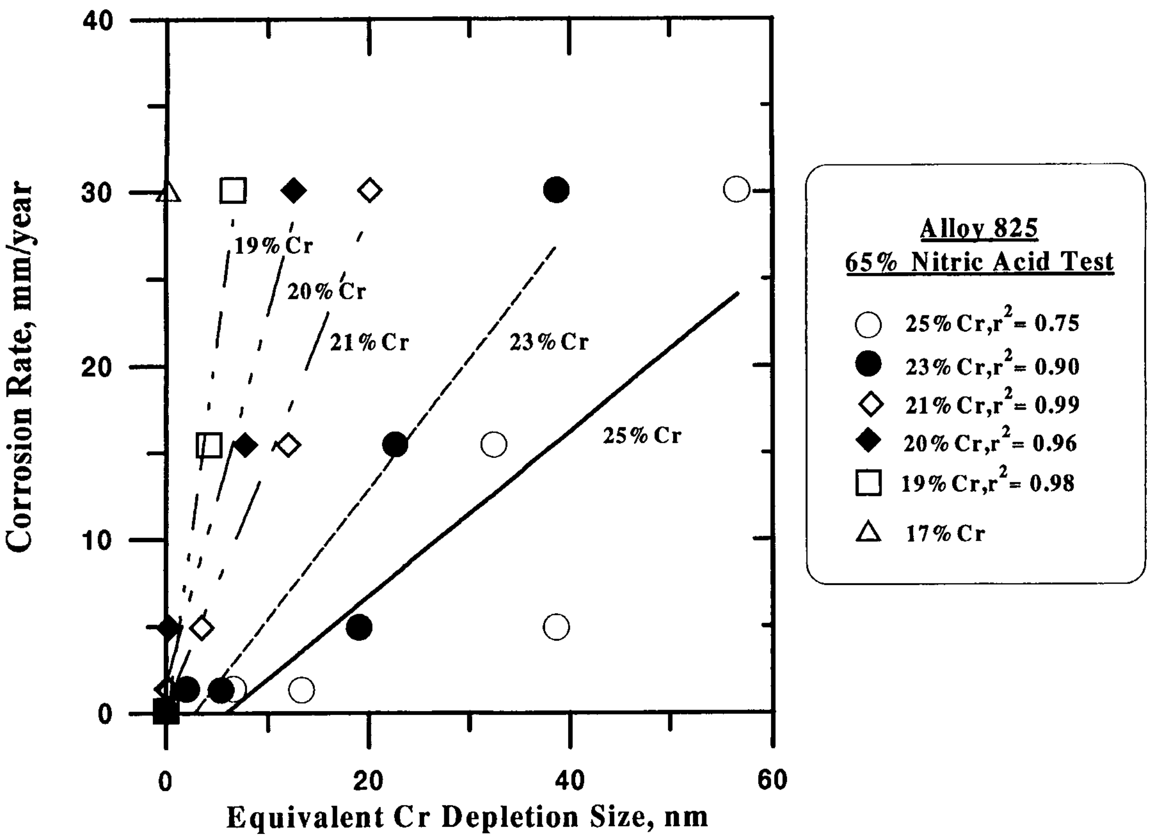

Figure 5-18. Corrosion rates in boiling 65 percent nitric acid as a function of equivalent chromium depletion zone size (nm) below various Cr levels for alloy 825 after solution annealing followed by various heat treatments

$$M_{23}C_6 \rightleftharpoons 23\,M + 6\,C \tag{5-5}$$

where M is mostly Cr, but can contain some Mo, Ni, and Fe. The equilibrium constant for this reaction is written as:

$$K = \exp\left(-\frac{\Delta G}{RT}\right) = \frac{a_{M_{23}C_6}}{(a_M)^{23}(a_C)^6} \tag{5-6}$$

Therefore, a higher carbon content in the alloy implies a lower chromium activity or concentration at the interface. The equilibrium constant in Eq. (5-6) decreases with decreasing temperature (Bruemmer, 1990). The activities in Eq. (5-6) can be written in terms of the appropriate concentrations by:

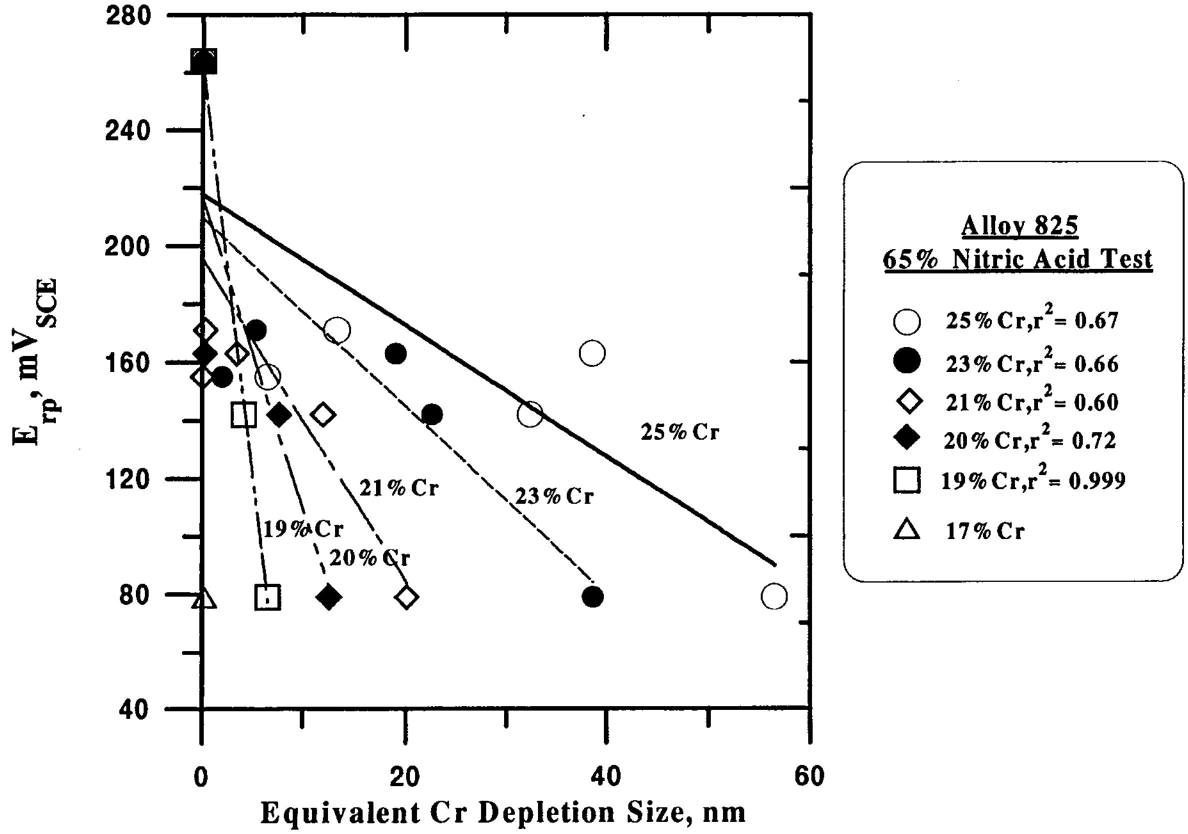

Figure 5-19. Repassivation potential in a 100 ppm chloride solution at 95 °C as a function of equivalent chromium depletion zone size (nm) below various Cr levels for alloy 825 variously heat-treated after solution annealing (scan rate: 0.167 mV/s)

$$a_{Cr*} = \gamma_{Cr*} X_{Cr*}; \quad a_C = \gamma_C X_C \tag{5-7}$$

where the M is replaced by an equivalent Cr concentration, $Cr*$, that includes the effect of Mo. The γs are the activity coefficients, and the Xs are the concentrations of the elements of interest. The activity of the carbide in Eq. (5-6) can be assumed to be equal to 1 under standard conditions. The activity coefficient of carbon in solid-solution has been reviewed by Hillert and Qui (1991) and Natesan and Kassner (1973). The activity coefficient for Cr can be calculated either by the approach of pairwise interaction parameters given by Was and Kruger (1985) or by empirical equations as employed by Bruemmer (1990). The current data for $M_{23}C_6$ carbides indicate then that the equilibrium Cr concentration at the matrix-carbide interface must decrease with decrease in temperature (Bruemmer, 1990; Angelieu and Was, 1990). The experimental results presented in Figures 5-15 and 5-16, are consistent with this prediction for the temperature range of 800 °C to 700 °C. However, the Cr concentration at the grain boundaries of the 640 °C aged specimen was higher than those of the 700 °C aged specimens. One possible reason for this discrepancy may be the morphology of carbides for the 640 °C aged specimens. The carbides for this aging treatment were small, but more continuously distributed along the grain boundaries. Hence, it was difficult to find a grain boundary area devoid of precipitation in order to determine the interfacial Cr concentration under these conditions. The electron beam intersected the overlying carbides and the analysis was skewed by the presence of carbides.

Whereas the chromium concentration at the carbide/matrix interface is thermodynamically determined, the profile of the chromium concentration gradient is dominated by diffusional factors. The depletion zone width has been predicted to increase with aging temperature (Bruemmer, 1990; Was and Kruger, 1985) from 600 °C to 700 °C for both austenitic SS ($M_{23}C_6$ carbides) and alloy 600 (M_7C_3 carbides). Beyond this temperature, the depletion zone width increases, but the minimum Cr concentration also increases. Thus, the total volume of depleted material below a certain critical Cr concentration decreases. These predictions are essentially confirmed by the present set of experiments.

6 MICROBIALLY INFLUENCED CORROSION

6.1 INTRODUCTION

The literature on microbially influenced corrosion (MIC) of the candidate container materials for the proposed repository site at Yucca Mountain was reviewed by Geesey (1993), as the initial activity in this task. A brief summary is presented in this chapter. In addition to the SCP design alloys mentioned in Section 2, alternate corrosion resistant alloys, such as alloy C-4 (Ni-16Cr-16Mo-3Fe-1Ti) and Titanium Grade 12 (Ti-0.7Ni-0.3Mo), were considered in the review. MIC of alloys currently proposed for the outer disposal overpack in the ACD, such as carbon steels and alloy 400 (Ni-32Cu-1Fe), was also reviewed.

The ubiquitous nature of bacteria and other microorganisms was noted, indicating that some of them have survived, and even grown, at temperatures above 100 °C (Stetter et al., 1986) or under high radiation fields as those encountered in the damaged core of the failed nuclear reactor at Three Mile Island (Booth, 1987; Miller et al., 1988). Another important aspect discussed as part of the general considerations on MIC is the fact that microorganisms tend to form biofilms on any nontoxic substrate exposed to aqueous environments, particularly those with a high surface area to volume ratio. The rock environment, like any porous medium, exhibits an extremely high surface area to volume ratio. Thus, the vast majority of microorganisms found in this environment may be expected to form biofilms over the surfaces of the rock particles, in the pore spaces between particles, and on other surfaces buried in the soil horizon. Both the French and United States research programs on low-level radioactive waste suggest that biofilms on the inorganic matrix are an important factor in the distribution of the microorganisms in the radioactive waste (Rosevear, 1991). These biofilms are composed of complex assemblages of distinct microbial species attached to the substrate through a matrix of extracellular polymeric substances (EPS). The importance of microbial biofilms was emphasized in terms of heterogeneous cell distribution and metabolism-driven chemical gradients at or near metal/solution interfacesn, which may lead to the occurrence of localized corrosion. The influence of biofilm formation in the modification of the corrosion potential established at a metal/solution interface and its eventual effect on the occurrence of localized corrosion were noted. This aspect is reviewed in the context of recently available information in Section 6.2 of this report.

6.2 MICROORGANISMS IN SUBSURFACE ENVIRONMENTS

The characteristics of microorganisms in subsurface environments were discussed at length by Geesey (1993). The discussion relied heavily on information obtained in recent years in various DOE sites, revealing that an abundant, diverse, and active microbial population exists under subsurface conditions. Relevant information obtained at Savannah River Plant, Idaho National Engineering Laboratory, Hanford, Rainier Mesa at the Nevada Test Site, and Pajarito Plateau in New Mexico, was summarized as an introduction to a discussion of biotransformations by subsurface microorganisms. It was noted that the body of information describing the microbiology of deep subsurface environments is still limited to only a few sites, none of which has been exhaustively characterized. It is likely that a diversity of microorganisms will be present in the geologic formation in which the HLW repository is proposed at Yucca Mountain. Only a small fraction of the total numbers and physiological types of microorganisms present in subsurface environments has been cultured, and even fewer identified. Those microorganisms present in the subsurface repository environment can be expected to exhibit a wide range of metabolic capabilities for both aerobic (use of molecular oxygen as terminal electron acceptor) and anaerobic (use of molecules or ions other than molecular oxygen as electron acceptor) respiration, with their energy needs met by either heterotrophy (requirement of organic compounds as source for cell carbon) or lithotrophy (usage of reduced inorganic compounds as energy source). The data from deep subsurface vadose zones suggest that total organic carbon is an important control on the culturability, activity, and diversity of microorganisms in this environment. The fact that small increases in water potential stimulate microbial growth and activity suggests that water availability also controls microbial metabolism.

It was emphasized that it is difficult to predict biological activities based on measured carbon turnover in low-nutrient environments. Carbon can be directed to various metabolic pathways, each with different byproducts, depending on the types of nutrients available and the prevailing environmental conditions. If the subsurface microbial population is demonstrated to be active, there is a high likelihood that such activity has had significant impacts on the geochemistry of the site and movement of nutrients at depth. Predictions of the types and activities of subsurface microorganisms should be based on the physical and chemical characteristics of the particular site. It was concluded that the presence of any particular microorganism cannot be ruled out simply because the repository is located several hundred meters below the surface under unsaturated conditions. The key question is whether specific corrosive activities are likely to proceed at rates that will compromise container integrity over a 300- to 1,000-yr period.

Although bacteria, as a group of living microorganisms, can function over a wide range of water activity, pH, salinity, temperature, and oxygen concentrations, it was noted that a given species is limited to a substantially narrower range of these parameters for growth. A discussion on the effect of those environmental factors, as well as the presence of electron acceptors and nutrient availability were summarized in a recent publication (Geesey and Cragnolino, 1995), following the previous review by Geesey (1993). A variety of aerobic and anaerobic microorganisms known to be implicated in MIC were discussed, emphasizing the type of metabolic products that their activity generates, as well as their nutrient requirements. At Yucca Mountain, the activity of man will undoubtedly result in the introduction of nutrients in the vicinity of the repository. An estimated 15 million gal. of drilling fluids were released into the Topopah Spring block a short distance from the anticipated repository site (West, 1988). Lateral movement of these drilling fluids may potentially reach the proposed repository. In addition to the drilling fluids now in the formation, many more gallons are expected to be introduced directly to the site during construction, along with lesser amounts of diesel fuels, hydraulic fluids, and gaseous exhausts (Hersman, 1987). This increased nutrient load is expected to stimulate microbial growth and activity at the repository (Hersman, 1987). No detailed experimental work on the nutritional or energetic value of the proposed backfill material to microorganisms is known. This is an important area that requires more research.

The examination of the energy requirements to maintain microbial growth under repository conditions was also considered in the review. In the examined case of a Swiss repository (McKinley et al., 1985), it was concluded that the main energy-producing reaction would be the corrosion of the steel container and that the amount of energy available would be a greater limiting factor than the nutrient availability. This preliminary estimation led to the conclusion that microbial action was unlikely to be a significant problem in a HLW repository. A comparable type of analysis has been conducted for the Canadian repository program (Stroes-Gascoyne, 1989). However, it has been pointed out (Arter et al., 1991) that the current models are too simplistic to describe the complex microbial processes that may occur on metallic surfaces exposed to repository environments.

6.3 MICROBIALLY INFLUENCED CORROSION OF CONTAINER MATERIALS

6.3.1 Introduction

It was noted in the review that MIC manifests itself primarily as localized corrosion in the form of pitting. During biofilm development, discrete microcolonies of distinct bacteria are found as a heterogeneous and patchy distribution on the metal surface, occluding some areas and leaving others fully exposed to the bulk aqueous phase. Even mature biofilms with near full coverage of the metallic substrate have channels allowing the transport of dissolved oxygen and the establishment of differential aeration cells (Costerton et al., 1994). This uneven accessibility of the reducible species present in solution to the metal surface (i.e., oxygen under aerobic conditions) leads to the formation of electrochemical cells characterized by the physical separation of cathodic and anodic areas. The depletion of the cathodic reactant (i.e., oxygen) in the occluded area under the biofilm enhances the anodic dissolution of this area, promoting acidification as a result of the hydrolysis of the metal cations, increasing the concentration of aggressive anions (i.e., chloride) and fostering the oxidative dissolution of detrimental species from the metal (i.e., sulfur species from MnS inclusions). In turn, these physicochemical processes tend to increase even more the rate of localized anodic dissolution.

In certain cases of MIC, as discussed for sulfate-reducing bacteria (SRB) in the review, the modification of the local environment by metabolic products (i.e., reduced sulfur species) arising from bacterial activity may decrease the critical potential for the initiation of localized corrosion. The localized environments in these occluded areas are far more complex in the case of MIC than those present under abiotic (absence of living microorganisms) conditions in crevices or beneath deposits. This complexity is the result of the multiple biochemical reactions associated with the generation of metabolic products through bacterial activities. For these reasons, it was emphasized that inclusion of appropriate controls to account for all other abiotic corrosion reactions is a necessary requirement for the experimental demonstration of microbial involvement in a given corrosion process. Bacterial biofilms can also inhibit corrosion (Angell et al., 1994). From the point of view of predicting long-term resistance to MIC, it is extremely important to determine if a threshold potential also exists in localized corrosion processes influenced by microorganisms. If such threshold potential exists and it is related to the repassivation potential for crevice corrosion, its application as a bounding parameter for performance assessment should be more fully explored. The existence of a repassivation potential for crevice corrosion is well documented in the case of carbon steels, Fe-Cr-Ni-Mo alloys, and titanium alloys exposed to abiotic chloride-containing waters.

6.3.2 Microbially Influenced Corrosion of Mild- and Low-Alloy Steels

A very extensive literature exists on MIC of steels in soil and aqueous systems under aerobic and anaerobic conditions. The roles of anaerobic SRB, aerobic sulfur-oxidizing bacteria, and iron-oxidizing and iron-reducing bacteria in the corrosion of mild steel have been discussed by many authors with special consideration of environmental factors, such as salinity, temperature, pH, and water potential, as well as mechanistic interpretation of the different steps in the electrochemical corrosion process. A number of excellent reviews have been published, including those by Miller and Tiller (1970) and Ford and Mitchell (1990b).

SRB are considered to be the most important mediators of anaerobic corrosion of steel. Fifty percent of the failures of underground pipe are thought to be due to microbial action (Booth, 1964). Dissimilatory SRB most commonly associated with corrosion of steel are distributed into the genera *Desulfovibrio, Desulfotomaculum, Desulfobulbus, Desulfobacter, Desulfobacterium, Desulfococcus, Desulfosarcina*, and *Desulfomonas*. The genus *Desulfotomaculum* is often isolated from deep subsurface oil production fluids. The thermophilic species *Desulfotomaculum nigrificans* is likely to promote corrosion of mild steel that comes in contact with the produced fluids from oil reservoirs.

Other important groups of bacteria associated with corrosion of steel are the autotrophic (capable of using CO_2 as source for cell carbon) iron- and sulfur-oxidizing bacteria. Organisms such as *Thiobacillus thiooxidans* and *Sulfolobus* sp. have the ability to oxidize reduced forms of sulfur to meet their energy needs with the subsequent production of sulfuric acid. The sulfuric acid destabilizes the protective iron oxide films that form on carbon steel (Miller and Tiller, 1970). Acidification also facilitates corrosion by shifting the corrosion potential in a more noble direction.

The bacteria *Thiobacillus ferrooxidans* and *Sulfolobus* sp. oxidize Fe(II) to Fe(III) to obtain energy for growth. The oxidation of passivating or protective Fe(II) films promotes oxidation of the metallic iron in steels (Miller and Tiller, 1970). Another group of iron-oxidizing bacteria often associated with corrosion of iron, carbon steel, and SSs is the iron-precipitating sheathed bacteria. This group includes the genera *Gallionella, Leptothrix, Crenothrix, Clonothrix*, and *Lieskeella* (Ehrlich, 1981). These bacteria appear in tubercles or deposits under which various type of corrosion can occur. These organisms promote the oxidation of Fe(II) to Fe(III) under slightly reducing conditions at pH greater than 5. The Fe (III) hydroxides precipitate around the outside of the cell forming sheath. It is believed that at least some of the iron oxidation that occurs in the presence of these microorganisms is the result of biochemical reactions, such as ammonia production and excretion, that raise the pH of the solution (Ehrlich, 1981).

Iron-reducing bacteria also appear to be important in the corrosion of mild steel. Some species of *Pseudomonas sp.* have been reported to reduce Fe(III) to Fe(II) (Obuekwe et al., 1981a,b,c; Sorensen, 1982). These organisms have been recovered from oil production facilities as well as various freshwater and marine environments. They appear to utilize Fe(III) as an alternative electron acceptor when oxygen becomes depleted in their environment. They are heterotrophs in that they utilize short-chain organic acid such as lactate as a carbon source.

Other aerobic and facultatively (not obligatorily) anaerobic organisms that have been implicated in the corrosion of steels through their ability to produce and excrete organic acids include: *Escherichia coli, Bacillus megaterium, Serratia marcescens*, and *Salmonella typhimurium* (Umbreit, 1976). Other investigators (Booth and Wormwell, 1962) report that the hydrogenase enzyme synthesized by some SRB promotes corrosion of steel by removing hydrogen from the metal surface, causing cathodic depolarization. Methanogenic bacteria have also been implicated in the corrosion of iron and steel in anaerobic environments (Daniel et al., 1987; Boopathy and Daniel, 1991). *Methanococcus thermolithotrophicus* and *Methanosarcina bakeri* normally use molecular hydrogen and carbon dioxide to produce methane, but can use elemental iron in mild steel as a source of electrons to produce energy for the reduction of carbon dioxide to cellular material and methane. As mentioned previously, methanogens are routinely isolated from deep subsurface environments.

The availability of oxygen determines in large part the types of microorganisms and their metabolic activities and products. In the absence of oxygen and at nominally negative redox potentials, corrosive microbial reactions such as sulfate reduction, Fe^{+3} reduction, production of organic acids by facultative anaerobes, and methanogenesis will be favored. In the presence of oxygen at positive redox potentials, oxygen-respiring chemoheterotrophic bacteria utilize a wide variety of reduced organic carbon compounds and convert them to products that serve as electron donors to SRB and facultatively anaerobic bacteria. In addition, iron oxidizers will be active under aerated conditions.

Fluctuating oxygen concentration influences the types of sulfur products formed at the steel surface that initially appeared as hydrogen sulfide released from the SRB (Hamilton, 1990). In the absence of oxygen, protective iron sulfides such as mackinawite (FeS_{1-x}), greigite (Fe_3S_4), and smythite (Fe_3S_{4-x}) are formed. If oxygen is introduced to the system, the formation of pyrite (FeS_2) and elemental sulfur are favored. In addition, the introduction of oxygen favors the anodic dissolution of iron in the steel in the form of Fe^{+2} ions. These ions react with oxygen in solution to form Fe(III) hydroxides. Hydrolysis reactions promote the formation of hydrated Fe(III) oxide, $Fe_2O_3 \cdot x\ H_2O$, and Fe(III) oxyhydroxide, FeOOH, which react with the hydrogen sulfide generated by the SRB when oxygen is absent to form elemental sulfur and iron sulfide (Nielsen et al., submitted for publication). Oxygen will also react directly with iron sulfide to produce elemental sulfur and iron oxide. Both molecular oxygen and elemental sulfur can depolarize the cathode by reacting with electrons to form hydroxyl ions or hydrogen sulfide, respectively.

Deposition of iron sulfide on a steel surface results in the formation of a galvanic cell. Iron sulfide is cathodic to the underlying iron in the steel, causing the iron to dissolve as Fe at the anode and react with the oxygen and hydroxyl ions present at the cathode. Finally, transient introduction of oxygen to the system provides an additional cathodic reaction on the adjacent surface. As mentioned previously, SRB utilize a rather narrow range of reduced organic compounds. Aerobic and facultatively anaerobic heterotrophs, on the other hand, can utilize a wide range of reduced organic compounds present in the system and convert them to lactate, acetate, butyrate, and propionate, all of which serve as electron donors for the SRB. Thus, SRB activity during periods of anaerobiosis is stimulated by the accumulation of electron donors in the biofilm provided by the aerobic and facultatively anaerobic bacteria during periods of oxygen availability.

The temperature range over which microbial corrosion of mild steel occurs is quite broad. The SRB *Desulfotomaculum* grows over a temperature range of 30–70 °C (Ehrlich, 1981). Iron-oxidizing bacteria such as *Sulfolobus* sp. are active at temperatures of 50–85 °C but not at 90 °C (Ehrlich, 1981). While most strains are mesophilic (able to grow at moderate temperatures) with an optimum temperature of 15–30 °C, some strains of *T. ferrooxidans* oxidize iron without growth at 37 °C, and one strain reportedly is active at 40 °C. Brock (1978) described a pink bacteria growing on the surface of glass slides after 2 d immersed in boiling water. Generation times ranging from 2.5–3 hr were observed at 91 °C.

The pH range over which steel-corroding bacteria are active is also very broad. *T. ferrooxidans* exhibits optimal iron oxidation at pH 3–3.6, optimal growth at pH 2.5–5.8, and tolerates pH over the range 1.4–6.0 (Ehrlich, 1981). *Sulfolobus* sp. function over the pH range 0.9–5.8. Salinities of up to 3.5 percent are typical in estuarine and marine waters. Corrosion of mild steel submerged in waters of salinities ranging from 0–3.5 percent have, in some cases, been accelerated by bacteria. Little work has been done on MIC of mild steel under low water potentials.

Walch and Mitchell (1986) have proposed a role for microorganisms in hydrogen embrittlement of steel. Many bacteria produce molecular hydrogen as a byproduct of fermentative metabolism, which may be dissociated into atomic hydrogen and adsorbed into the steel by dissociative chemisorption. Other bacteria produce hydrogen ions along with organic or mineral acids, which may be reduced at cathodic sites to atomic hydrogen. SRB produce hydrogen sulfide, which impedes formation of molecular hydrogen. The adsorption of atomic hydrogen at the surface of the steel promotes absorption into the metal. Ford and Mitchell (1989, 1990a) reported that when high-strength steel was exposed to hydrogen-producing bacteria, longitudinal cracks appeared on the upper surface of the steel. Some initiation of cracking was apparent on control steel, but to a much lesser degree than steel exposed to the bacteria. Possible mechanisms of the involvement of the organisms in the cracking process proposed by the authors were similar to those for hydrogen embrittlement.

The repository corrosion research program in the United Kindgom has included studies on microbially mediated corrosion of steel (Philip and Taylor, 1987). The program has concentrated on gas and acid production caused by microbial degradation of the organic and inorganic components of the waste (Pugh et al., 1989). A mathematical model that simulated microbial processes in the repository environment was developed. The model simulates gas production through metal corrosion (Colasanti et al., 1989). The worst microbial case was encompassed by the limits established for chemical degradation and corrosion. The current research is focusing on the manner in which microorganisms form biofilms and survive high pH.

The main microbiological concern related to intermediate- and low-level waste in Sweden was the corrosion of steel packages (Rosevear, 1991). Carbon steel has been tested as a candidate container material in the HLW Swiss program, as well. Laboratory vessels were filled with synthetic groundwater simulating that around a Swiss repository and some were inoculated with microorganisms, including SRB, iron-oxidizing bacteria, sulfur-oxidizing bacteria, and alkalinophilic bacteria and incubated for up to 18 months in the presence of cement and iron coupons. During this time, the pH increased to 11.5–12, E_h decreased to $-100\ \mathrm{mV_{SHE}}$, and there was evidence of cement degradation. The final population of microorganisms was the same regardless of inoculation. The population appeared to be capable of surviving alkaline conditions (West et al., 1992). Steel coupons all exhibited signs of corrosion but no sterile controls were apparently maintained. Detailed metallographic observations revealed that the corrosion was localized as deep pits. Corrosion products appeared to be Fe(III) oxyhydroxide and magnetite. This type of corrosion was considered to be a microbial influence (West et al., 1992).

If conditions for microbial activity develop at the surface of the wrought steel overpack, these activities could either accelerate abiotic corrosion reactions or promote MIC under anaerobic conditions. Further work needs to be done to estimate the rate of localized corrosion in a simulated repository environment. It should be noted, however, that experience in the oil industry has revealed that laboratory simulations usually underestimated corrosion rates observed in the field.

6.3.3 Microbially Influenced Corrosion of Stainless Steels

The section on MIC of austenitic SSs is based on several recent studies that were prompted by many failures due to localized corrosion observed in auxiliary systems of nuclear power plants. Although SSs are very resistant to general corrosion, they are particularly vulnerable to localized corrosion in those systems in which the water is stagnant or the flow is low or intermittent (Licina, 1988; Wolfram et al., 1988; Kearns and Borenstein, 1991).

Tatnall (1981) suggested that iron-oxidizing bacteria such as *Gallionella* tend to concentrate iron, manganese, and chlorides, with the result that their deposits are rich in Fe(III) and Mn(IV) chlorides.

These acidic, oxidizing chloride salts cause rapid pitting of SSs that penetrates walls of piping and other structures within weeks at ambient temperature. The pits appear as pinholes at the surface, which expand into cavities in the bulk metal.

Stainless steels are susceptible to pitting corrosion in the presence of SRB or their metabolites (Moreno et al., 1992). SRB may have an anodic or cathodic effect, depending on the specific conditions at a surface. SRB are generally considered to be the major culprits of localized pitting corrosion, which is the most common type of corrosion to occur on SSs (Hamilton, 1985; Ibars et al., 1992; Duquette and Ricker, 1986; Scott et al., 1991; Iverson, 1987). SRB generally produce open pitting or gouging on SS, whereas along the edges of gasket joints, SRB produce shallow crevice corrosion (Tatnall, 1981). The production of sulfides such as HS^- and H_2S in localized high concentrations in chloride-containing media causes the breakdown potential to move toward more negative values (Newman et al., 1982).

Pitting of 304 SS in freshwater environments has been proposed to occur indirectly through reactions catalyzed by SRB-containing biofilms (Newman et al., 1991). H_2S, produced by SRB metabolism, reacts with sulfate ions to produce thiosulfate ions. Pitting occurs even in the absence of chloride ions, so long as the ratio $[SO_4^{2-}/S_2O_3^{2-}]$ ranges from approximately 10 to 30. Pitting has been observed at thiosulfate concentrations as low as 1 ppm (10^{-5} M). The aggressiveness of thiosulfate as compared to sulfide is due to its anionic nature: it is attracted into pits along with Cl^- and SO_4^{2-} by electromigration, whereas sulfide as H_2S is uncharged at the acidic pH encountered inside pits (Newman et al., 1989). In environments containing SRB, the rapid failures experienced by SS must involve a locally anaerobic environment, with maintenance of an oxidizing potential through access of oxygen to remote areas. Pitting corrosion of SSs in a uniformly anaerobic environment is not likely, as the potential would be lower than any value at which corrosion has been observed. It is incorrect to assume that a lowering of the potential in itself increases the likelihood of corrosion. In SSs, there is no active loop in neutral solution, and acidification at the anode can only be achieved if there is a remote cathode. SRB-induced pitting of SSs is proposed to be an H_2S-catalyzed dissolution process in a locally anaerobic microenvironment, driven by remote reduction of oxygen or another cathodic reductant (Newman et al., 1991).

When bacteria colonize a surface, a patchy biofilm develops (Costerton et al., 1987). The respiratory activities of the bacteria limit oxygen access to the underlying metal surface and promote establishment of an oxygen concentration cell on the surface. Once a biofilm on a SS substratum has been established, it has the ability to trap and entrain certain species of chemicals that may be particularly aggressive towards SS (Videla and Characklis, 1992). Chloride concentrations have been found to be surprisingly high within an established tubercle, even when the chloride concentration in the surrounding medium is quite low (Borenstein, 1991). Chloride ions have the ability to permeate the passive film, thus initiating or enhancing the electrochemical reactions that are responsible for localized corrosion (Fan and Bard, 1989). Costerton and Geesey (1986) have proposed the formation of a corrosion cell in which there are distinctively localized anodic and cathodic sites due to microbial activity concentrated at the surface.

EPS produced by the biofilm-forming bacteria may prevent the corrosive metabolites from diffusing across the surface or into the bulk aqueous phase, thereby accumulating at localized sites near the substratum surface. Beech et al. (1991) and Nivens et al. (1986) showed that *Desulfovibrio desulfuricans* and *Vibrio natrigens*, respectively, produced exopolymer during colonization of SS. The EPS produced by many bacteria found in aquatic and terrestrial environments, including the deep subsurface, contain uronic acid subunits. These polyanionic polysaccharides could produce an acidic environment at specific locations on the surface or create metal concentration cells on the SS surface as a result of differential binding of metal ions. Slime-forming pseudomonads have been associated with some cases of SS pitting (Pope et al., 1984). Species of bacteria that have been associated with slime-related SS corrosion include: *Vibrio natrigens*, *Clostridium*, *Flavobacterium*, *Bacillus*, *Desulfovibrio*, and *Desulfotomaculum* sp.

Bacteria may contribute to anodic dissolution by production of acidic substances, such as CO_2, or organic acids such as acetate, butyrate, and other short-chain fatty acids. The production of these substances decreases the local pH by increasing the proton concentration (Hamilton, 1985; Dowling et al., 1992; Iverson, 1987). Biofilms of acetic acid-producing bacteria grown in aerated artificial seawater destabilize or dissolve the protective calcareous film that forms on SSs during cathodic polarization (Little et al., 1987b). The presence of the bacterial biofilm led to an increase in current density when the surface was polarized to $-900\ mV_{SCE}$. Cathodic depolarization has often been cited as the mechanism of MIC to explain an undefined change in electrochemical response of a system containing microorganisms (Little et al., 1987b).

Bacteria can colonize those areas of the surface at which the protective oxide layer has been breached by mechanical or halide attack, produce a slime layer composed of cells and matrix exopolysaccharide, and prevent the penetration of oxygen to the surface and subsequent passivation (Pope et al., 1984). The growth of SRB in oxygen-depleted regions of a respiring microbial biofilm also prevents passivation of the protective oxide layer where breaches have occurred.

For reasons that are not entirely understood, MIC seems to be more likely to occur at or near a weld than at any other area on a SS surface (Borenstein, 1991; Licina, 1988; Ibars et al., 1992). Welding of some austenitic SS leads to a duplex microstructure because the filler metal is chosen to promote the formation of delta ferrite. Under oxidizing acidic conditions, the austenitic matrix is preferentially attacked (Ibars et al., 1992). Similar preferential attack of the austenitic phase has been observed in type 316L weld metal (Licina, 1988). However, there are cases in which the delta ferrite is preferentially removed and the austenite is unattacked. As a rule, the duplex condition seems to be more susceptible to MIC than the austenitic condition alone, particularly in the proximity of the weld fusion line. The heat-affected zone (HAZ) has also been shown to be susceptible to MIC (Licina, 1988; Ibars et al., 1992).

6.3.4 Microbially Influenced Corrosion of Nickel Alloys

Pure nickel and nickel alloys are vulnerable to MIC, as discussed in some detail on the basis of reviewed data (Geesey, 1993). A brief summary is included here to consider essentially the three nickel-base alloys currently considered as candidate waste package materials. They are alloys 400, 825 and C-22.

Mollica et al. (1990) have shown that formation of a biofilm on passive alloys such as nickel-chromium and nickel-copper in seawater can promote depolarization of the cathodic reduction of oxygen. Depolarization produces an increase of the free corrosion potential for alloys in the passive state which, in turn, may result in increased susceptibility to localized corrosion. However, nickel and alloy 400 are not so passive in seawater as those nickel-base alloys containing chromium as the main alloying element For those nonpassivating metals, the corrosion potential increases by only a few tens of millivolts, even though the biofilm catalyzes the oxygen-reduction reaction. The rates of anodic dissolution were found to increase by two orders of magnitude. There was a 3-mg weight loss for a nickel specimen exposed for 40 d to sterile seawater as compared to a 600-mg weight loss in biologically active seawater. A similar effect was observed for alloy 400.

Alloy 400 experienced pitting under a multilayer scale after exposure to estuarine water for 6 months (Little et al., 1990). Surface scales appeared as blisters containing corrosion products and bacterial cells. SRB were typically present in densities of 10^4 cells/cm^2. A black layer within the pits was enriched in sulfur and chlorine. Regions under the biofilm were depleted in nickel and iron and enriched in copper. Differential aeration cells appeared to have formed with low oxygen concentrations under the deposits suitable for SRB activity. The surface area under the deposit became anodic and corroded, while the electrons generated from the dissolution of the metal are consumed by the reduction of oxygen outside the deposit. A spongy, copper-rich material accumulated in the base of the pits.

Alloy 400 is fouled to a similar extent by SRB in seawater as Corten A steel (Fe-0.12C-1Cr-0.4Cu) (Sanders and Maxwell, 1983). However, it takes SRB much longer (150–288 d) to achieve a stable sulfate reduction rate (20–27 nmol SO_4/coupon/day) on alloy 400 than on the steel. Corrosion rates (8–12 mg/dm^2 ·d) were similar, however. Severe deep pitting was observed.

An extensive study on alloy 400 exposed to Arabian Gulf seawater for up to 4 months and also exposed to cultures of active sulfate-reducing bacteria was conducted by Gouda et al. (1993). The Arabian Gulf seawater contains organic carbon concentrations of 8 ppm. The active SRB was cultured on a rich nutrient medium, enriched with anaerobic sewage sludge, and then deaerated in an atmosphere of hydrogen and carbon dioxide prior to exposure to the metal substratum. After 10 to 21 d exposure of the alloy 400 to the active SRB culture in deaerated seawater in the laboratory, a sulfide layer containing a bacterial biofilm had formed on the metal surface. The biofilm contained actively growing cells of *Desulfotomaculum* sp. as well as other possible genera of SRB including *Desulfovibrio* sp. These bacteria were surrounded by EPS. After 3-weeks exposure to anaerobic laboratory conditions, corrosion was slight. However, when air was introduced for 1 week into the system, localized corrosion was observed. The effect of oxygen on the corrosion behavior of alloy 400 mimics to some extent that observed with mild steel. The localized areas that had been attacked contained a cracked layer that exposed the grain boundaries of the alloy. Intergranular attack by the SRB was observed at this time and became more severe with further incubation. Intergranular corrosion has been observed in the presence of microorganisms in freshwater (Stoecker, 1984) and seawater environments (Schiffrin and de Sanchez, 1985). According to the authors, the response of the alloy 400 to aeration also implicate a differential aeration cell as the mechanism of corrosion. Some authors have suggested that the sulfide generated by the SRB promotes the breakdown of the oxide films on nickel alloys (Schumacher, 1979).

Exposure of alloy 400 to chlorinated Arabian Gulf seawater for 10 d at different temperatures resulted in the development of a few small black nodules, circular in shape (Gouda et al., 1993). These nodules developed from discrete microcolonies of bacteria growing on the metal surface. After 1 month, the black layer became covered with green deposits. The size and number of nodules were greater at 30 °C than at 19 or 50 °C. The number of nodules increased significantly at all temperatures after 4 months exposure. Two types of corrosion attack were identified: deep localized attack that produced cavities and irregular shaped, shiny, shallow and broad attack that was spread all over the surface at all temperatures studied. Intergranular corrosion attack occurred inside the cavities, very similar in appearance to that produced in the presence of the active SRB culture. The other type of attack resembled the etching attributed to chloride pitting corrosion. Prolonged exposure to the Arabian Gulf seawater under laboratory conditions for up to 4 months resulted in pit propagation and severe intergranular corrosion. In summary, the laboratory seawater studies demonstrated that even though the water was not deaerated and contained 0.2 ppm free residual chlorine, SRB-associated localized corrosion occurred within a 3-month period.

Immersion of alloy 400 surfaces in unchlorinated or chlorinated natural Arabian Gulf seawater for 50 d resulted in the appearance of nodular deposits (1 mm dia) on the metal surface similar to those observed in the laboratory immersion tests (Gouda et al., 1993). The deposits were made up of a black layer composed of one or more iron nickel sulfides $(Fe,Ni)_xS_y$ overlayed with a green layer of $CuCl_2 \cdot 3Cu(OH)_2$ and $NiCl_2$. The areas under the deposits displayed severe intergranular attack below which a copper-rich matrix was detected. These results suggest preferential attack of iron and nickel by SRB. Although deposit density was not reported, the numbers and size of the deposits were reported to be much greater in unchlorinated seawater than in chlorinated seawater. After 50 d exposure to chlorinated and unchlorinated seawater, 1.6×10^2 SRB/cm^2 and 6×10^1 SRB/cm^2 were recovered from the metal surfaces. After 70 d exposure, the SRB cell densities increased to 3.3×10^2 and 5.1×10^3/cm^2. The authors clearly indicated that the biofilm population rather than the planktonic cell population was responsible for the observed corrosion. They further indicated that chlorination at the levels applied (0.5 ppm) in their studies was ineffective in keeping the SRB cell densities in the biofilm under control. No controls were described, however, that considered the role of abiotic reactions in these corrosion studies.

Gouda et al. (1993) concluded that both active laboratory cultures of SRB or from naturally occurring microorganisms in Arabian Gulf seawater produced similar forms of attack on alloy 400. This alloy was reported to be more susceptible to MIC than brass, 70/30 Cu-Ni alloy (CDA 715), Sanicro 28, alloy 825, or Ti when exposed to the same environmental conditions. They indicated that failure and leaking of alloy 400 heat exchange tubes can take place whenever SRB are present, irrespective of their densities. Through-wall perforations (2 mm thickness) occurred within 3–8 months of the time the tubes were placed in service.

Alloy 400, when submerged in quiescent seawater, developed evidence of corrosion in crevices (Klein et al., 1991). Treatment of the seawater with 1 mg of chlorine per liter of seawater rendered the alloy more resistant to crevice corrosion in the presence of microorganisms. After 180 d exposure, depths of attack were about half of that observed in unchlorinated natural seawater. In the absence of chlorination, it appeared that biological activity present in natural seawater promotes an increase of the corrosion potential and, consequently, pitting of alloy 400.

Soracco et al. (1988) reviewed the susceptibility to MIC of various alloys used in many components in the power-generating industry, including carbon steels, SSs, and copper alloys. According to their survey, no cases of MIC of nickel-chromium alloys had yet been documented. However, very few studies of MIC of nickel-chromium alloys had been carried out at that point. Indeed, the lack of relevant information for a particular alloy of interest led to the consideration of related alloys in the review whenever possible (Geesey, 1993). Nickel-based alloys containing chromium as the main alloying element (i.e., alloys 825 and C-4) were a particular problem because published information, even for related alloys, was extremely limited.

Heat exchanger tubing made of alloy 800 (Ni-21Cr-46Fe-0.02Cu) suffered from under-deposit pitting corrosion on the lakewater (Lake Ontario) side of the tubing (Brennenstuhl et al., 1990). Model heat exchanger test rigs were rapidly colonized (in few days) by a biofilm. Initially, the biofilm was almost completely organic in nature. After maturation, however, inorganic deposits from the surrounding environment accumulated in the film. After 2 months exposure, a calcareous layer eventually covered the film. Microbial biomass contributed approximately 10 percent of the total deposit mass. The exopolymers excreted by the bacteria in the biofilm trapped the inorganic particles, which acted as nuclei for calcium carbonate deposition. The calcareous layer, along with the sediment material, led to the formation of crevices where localized breakdown of the passive oxide layer occurred.

Electrochemical noise measurements suggested that negligible attack occurred on alloy 800 during initial stages of biofilm buildup in the presence of lakewater (Brennenstuhl et al., 1990). Over a period of several months, passivity was still maintained as long as sufficient water was circulated over the tube surface to provide an adequate supply of oxygen to the metal surface. Passivity breakdown occurred after 6 months when flow was interrupted for a short time. One year after the tubing had become heavily fouled, the corrosion current remained high during both normal and low-water flow operation. The environment at the tube surface had become sufficiently aggressive to ensure pit propagation. The authors felt that bacteria had an important role in the pitting process (Brennenstuhl et al., 1990).

Similar studies with alloy 825 and Sanicro 28 (Ni-27Cr-36Fe-3.5Mo-0.6Cu) indicated that they experienced pitting corrosion after 3 yr (Brennenstuhl et al., 1990). These two alloys contained Mo, whereas alloy 800 did not. Pitting was always more prevalent at the hot end of the tubing. The material extracted from the pits and bulk deposits formed on alloy 800 was enriched in chromium (63 percent) and calcium (16 percent). Pits may have initiated at TiC inclusions. Examination of the pits suggested crystallographic attack indicating an activation controlled dissolution process. Ca, Fe, and S were enriched in the vicinity of the pits. The Fe/S ratio was as high as 2.4. P and Cl were also enriched but not to the extent of S. Cl^- and SO_4^{2-} concentrations in the lakewater were 35 and 25 ppm, respectively. It is believed that oxygen respiration by aerobic bacteria and anaerobes such as SRB assist in the formation of microgalvanic cells, which leads to accelerated attack. Chloride ions are likely to be involved in the breakdown of passivity of the protective oxide film.

The initiation of crevice attack on alloy 825 at 25 °C was found to be four times more severe in natural seawater than in synthetic seawater after 30 d exposure using a multiple crevice assembly (Dexter et al., 1986). However, for type 304 SS, natural seawater was slightly more aggressive than synthetic seawater; whereas for type 316 SS, natural seawater was not as corrosive as synthetic seawater. When tests were conducted at 50 °C, no difference in corrosivity was noted between natural and synthetic seawater, which suggests that bacteria present in the natural seawater are not able to survive at 50 °C.

In summary, nickel alloys containing copper and iron as alloying elements are susceptible to similar types of microbial attack as copper-nickel alloys. Sulfide, chloride, and acids produced by microorganisms will accumulate in biofilms on the metal surface and, through various proposed mechanisms, initiate or promote localized corrosion of the metal. In the case of nickel-copper alloys, attack is focused at the grain boundaries. Nickel alloys are therefore ranked similar to copper alloys in terms of resistance to MIC.

6.3.5 Summary and Conclusions

Based on a survey of the current literature, it appears that there have been no in-depth studies on MIC of Ni-Fe-Cr-Mo alloys, such as alloys 825 and C-22. In separate studies, however, pitting and crevice corrosion of alloy 825 were observed in lakewater and natural seawater, respectively. Bacteria were found to be involved in both cases. Considerable research still needs to be conducted to evaluate the resistance to MIC of Ni-Fe-Cr-Mo alloys in the repository environment because the information and data available on these alloys are very limited. Most of the information available in the literature refers to commercial nickel and alloy 400. This alloy has been found extremely susceptible to localized corrosion in the presence of SRB, as encountered in polluted seawater.

Although Ti is currently not considered as an alternate container material in the ACD, the apparent resistance of Ti and its alloys to MIC should be noted. Titanium is prone to fouling in natural seawater, but it appears to be extremely resistant to localized corrosion in particularly severe microbial environments, as concluded by comparing the effects of these environments on other corrosion-resistant alloys.

No studies on MIC of the candidate container materials have been conducted in an unsaturated subsurface soil or rock environment, and this review suggests that all the materials considered may be susceptible to MIC, with the possible exception of titanium and its alloys. As discussed previously (Geesey, 1993; Geesey and Cragnolino, 1995), it appears that microbiologically mediated processes of degradation will not occur if the temperature at the waste package surface is above 100 °C and the moisture content remains below 60 percent over the 300- to 1,000-yr containment period. On the other hand, it is concluded that sufficient nutrients and microbial life are likely to be present in the near-field to promote MIC if the temperature of the waste package drops below 100 °C and the moisture content rises above 60 percent for any period of time. Specific recommendations are included if the latter conditions become dominant, even in the presence of radiation fields, high salinity, or low pH, because these factors are not considered limiting factors for the occurrence of MIC. The specific recommendations comprise development and studies in the following areas: (i) monitoring techniques for MIC, (ii) nutrient availability in the near-field, (iii) bioenergetics of container corrosion, and (iv) production of gaseous by-products by microorganisms. It is recommended that site-specific studies that will determine the tolerance of microorganisms to repository conditions be performed.

6.4 THE EFFECT OF BIOFILMS ON THE CORROSION POTENTIAL

6.4.1 Background

A review of the current literature detailing the effects of microorganisms on corrosion potential (E_{corr}) has been compiled due to the interest in using E_{corr} measurements for the monitoring and prediction of corrosion on HLW containers. As discussed in the following, it is not possible to determine whether localized corrosion has occurred or if corrosion rates have increased or decreased based on the measurement of E_{corr} alone. Various authors have shown that microbially influenced pitting is preceded by an increase in E_{corr} (usually termed ennoblement in the literature; this term will, therefore, be used in this report to represent an increase in E_{corr}) while others have shown that a decrease in E_{corr} is indicative of initiation of microbial attack. Yet others have shown that the presence of a biofilm can lead to a slight potential increase without any initiation of localized corrosion or increase in corrosion rates.

6.4.2 Ennoblement of Stainless Steels in Seawater

A number of investigators (Mollica and Travis, 1976; Mollica et al., 1984; Motoda et al., 1990; Audouard et al., 1995) have shown that SSs exposed to natural seawater undergo a rapid ennoblement from −100 (±100) mV_{SCE} to above 300 mV_{SCE}. On the contrary, others (Johnson and Bardal, 1985; Dexter and Gao, 1988) found potential rises from −100 to −250 mV_{SCE} to only 50 to 300 mV_{SCE} for SSs in seawater (Figure 6-1). A major concern with such work is the lack of suitable sterile controls. When some level of control was attempted, it was achieved by filtration through a 0.2 µm filter which has been shown to be ineffective (Buchanan et al., 1991; Little et al., 1987a). Other metals such as nickel and alloy 400 (Mollica et al., 1987) and copper based alloys (99Cu, 90Cu10Ni, 70Cu30Ni, admiralty brass and

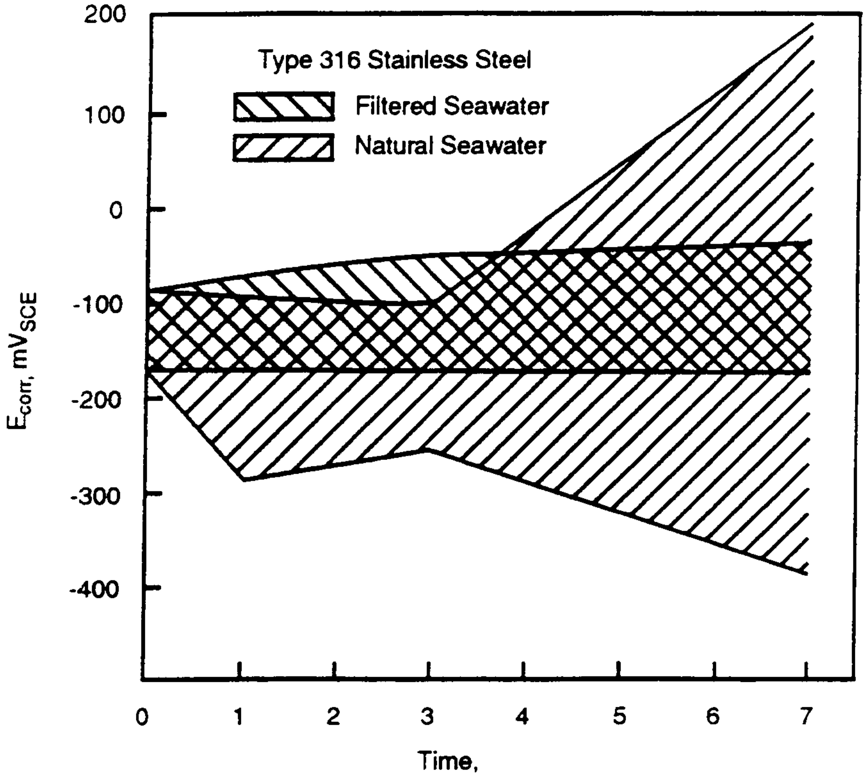

Figure 6-1. Corrosion potential as a function of time for type 316 stainless steel during exposure to natural and filtered seawater (Dexter and Gao, 1988)

aluminum bronze) (Little and Mansfeld, 1991) did not show an increase in the E_{corr} upon exposure to natural seawater. Despite a hundredfold increase in weight loss, as reported by Mollica et al. (1987) for nickel and nickel alloy samples exposed to natural water over "sterile" water, the corrosion potential remained negative (Mollica et al., 1989). Copper presents an interesting case in relation to corrosion potentials. King et al. (1995) showed that clay-covered copper electrodes are 100 mV more positive (noble) than those measured in a bulk solution of the same chloride and oxygen concentration. This ennoblement was attributed to restrictive mass-transport conditions, resulting in a change of both the rate of anodic and cathodic reactions. Both reactions become transport controlled, with the clay acting as a barrier to the diffusive transport of both the copper (II) chloride ions that controls the anodic reaction and oxygen controlling the cathodic reaction, and resulting in an increase in corrosion potential. Biofilms may play a similar role in altering the transport of species, but additional factors are possibly involved associated with the generation of metabolic products.

6.4.3 Studies Attempting to Show Ennoblement as a Result of Microbial Action

Despite the lack of controls, it is generally accepted that the ennoblement seen on SSs is a result of microbial activity. Mollica et al. (1984) showed that removal of the biofilm with a nylon brush resulted in a transitory loss of ennoblement (corrosion potential decrease). The level of biofilm removed with the brush is not known. From other studies, it is known that this procedure is possibly limited to the removal of loosely attached material and not the irreversibly attached biofilm (Dickinson and Lewandowski, 1995).

This concern seems to be confirmed by the rapidity with which the high E_{corr} values were reestablished. Motoda et al. (1990) showed that removing the loosely attached cells of a biofilm on an ennobled sample did not result in the loss of ennoblement. However, subsequent microscope examination revealed that a thin film rich in oxygen and carbon was still present on the surface, suggesting an attached microbial biofilm. Once this film was removed the ennoblement was lost.

Initially Mollica and Travis (1976) showed data in which they suggested there was a linear correlation between biomass and level of ennoblement. However, Mollica et al. (1987) suggested a different explanation when they found that the addition of sodium azide to a biofilmed, ennobled titanium coupon led to the loss of ennoblement. Their contention was that as sodium azide is a metabolic inhibitor, it showed that the ennoblement was a result of metabolic activity. It needs to be noted that although sodium azide is indeed an inhibitor of aerobic metabolism blocking the electron transport chain at the terminal transfer point, it has also been shown to inhibit the growth of SRB while, at the same time increasing the rate of sulphate reduction and hydrogen production. It is possible that an increase in hydrogen production would lead to an increased polarization of the cathodic reaction and a corresponding decrease in E_{corr}. The interpretation of the sodium azide data is therefore inconclusive. More recently, an extensive study by Audouard et al. (1995), in which a number of SSs were exposed at various sites around Europe, showed that there was no correlation between level of ennoblement, and either biofilm wet weight or other environmental conditions such as temperature. There was a large variation in the initial E_{corr} values ($\approx$+75 to -125 mV_{SCE}) depending on exposure location. However, a correlation was suggested between the level of EPS produced and the level of ennoblement, with no ennoblement at EPS levels below 100 $ng \cdot cm^{-2}$. The overall conclusion of Audouard et al. (1995) was that level of ennoblement was dependent not on the biomass but rather on metabolic activity.

Mollica et al. (1989) investigated the effect of temperature on biofilm metabolism and ennoblement of SSs. Ennoblement was seen at all temperatures measured below 40 °C. Monitoring of the electron transport system (ETS) activity (reportably a measure of living biomass) confirmed that there was no correlation between biomass and ennoblement as ETS levels were the same at all temperatures after about 7 d, while there was a significant difference in E_{corr} (none at 40 °C). Adenosine triphosphate (ATP) levels within the biofilm were also measured as an index of physiological activity. The ATP levels measured at 20 d were roughly equal for all temperatures, but there was no ennoblement at 40 °C. Also, at the 7- and 11-d points, the activity as measured by ATP at 35 °C was nearly double that seen at the lower temperatures, but the ennoblement was less. These observations seem to suggest that ennoblement was not a factor of either biomass or physiological activity, contrary to the claims made in the paper. It might be possible to make a link between a threshold level of activity (as measured by ATP) and ennoblement as suggested by the following observations of the data presented. After 7 d, 1 ng cm^{-2} of ATP was present for the 25 °C exposure resulting in an increase of E_{corr} to about 200 mV_{SCE} whereas at 40 °C no variation of E_{corr} above 0 mV_{SCE} can be correlated to a maximum ATP level attained of approximately 0.75 ng cm^{-2}. This suggests that a threshold level between 0.75 and 1.0 ng cm^{-2} of ATP exists to have an effect on E_{corr}.

6.4.4 Exposure of Stainless Steel to Seawater with no Ennoblement

Other authors have shown that exposure of SSs to natural seawaters does not necessarily result in ennoblement (Little et al., 1991; Little and Mansfeld, 1991; Mansfeld et al., 1992). SS samples exposed to either Gulf of Mexico or Pacific Ocean water underwent only a slight ennoblement from –150±50 mV_{SCE} to 70 mV_{SCE} which was equivalent to that seen in carefully sterilized natural or synthetic seawater (instant ocean™, and 3 percent NaCl) (Figure 6-2). There was a strong correlation seen between the low level of ennoblement and light levels. Ennoblement was seen in natural water with natural light levels and attributed to the presence of photosynthetic diatoms. Under reduced light levels ennoblement was seen in carefully sterilized seawater, instant ocean™, and 3 percent NaCl solutions probably related to the formation of a more protective passive film but not in natural seawater. Microprobe analysis of the biofilms formed under the various lighting conditions showed that the lit systems had uniform oxygen and pH profiles throughout the biofilm, whereas the reduced light biofilm had heterogenous pH levels and a sharp gradient in dissolved oxygen levels through the biofilm. Abiotic studies showed that a decrease in the pH lead to an increase in the E_{corr} of SS. The ennoblement was therefore thought to be dependent on the microenvironment at the metal/microbe interface (pH and dissolved oxygen levels) in which photosynthetic organisms played a large part.

6.4.5 Ennoblement of Stainless Steel in Freshwater

Similar results were seen in a study by Buchanan et al. (1991) for SS exposed to Tennessee River water. Samples exposed to unfiltered water underwent ennoblement while those exposed to filtered water did not. Microbiological examination of the samples revealed that a major effect of the filter was to remove diatoms but not bacteria. The difference in ennoblement was therefore attributed to the presence or absence of photosynthetic diatoms. Further evidence for this effect was presented when ennobled samples were placed in dark conditions. After ennoblement was lost, light conditions were returned accompanied by ennoblement. Similar abiotic experiments to those of Little et al. (1991) were presented showing that a drop in pH to 3.5 could result in the levels of ennoblement seen in the exposed systems, whereas dissolved oxygen levels seemed to have little effect on the E_{corr} values. Approximately 60 mV difference was noted between air sparging and nitrogen sparging. The ennoblement was again attributed to diatom activity possibly causing a change in the local pH at the biofilm metal interface.

6.4.6 Mechanistic Studies

Laboratory studies using a mixed community incorporating a photosynthetic cyanobacteria showed that E_{corr} is a function of the level of illumination (Dowling et al., 1992). The evolution of oxygen (1–7 mg/L^{-1}) correlated with an ennoblement of 2 to 15 mV. It was concluded that this level of oxygen production resulting from photosynthesis was not sufficient to account for the levels of ennoblement seen in natural systems, but revealed that photosynthetic microorganisms within a biofilm play a role by modifying the local environment. It should be noted that many of the papers which report an ennoblement of SS assume that the biofilms create anaerobic conditions whereas, as shown above, this is not necessarily true due to the action of photosynthetic microorganisms.

It is generally agreed that the observed ennoblement is due to either thermodynamic reasons (a positive shift of the reversible potential of the oxygen electrode associated with changes in the dissolved oxygen concentration) or kinetic reasons (increase of the exchange current density and/or a decrease in the charge transfer coefficient for the oxygen reduction reaction), or a combination of the two. Various mechanisms for the enhancement of the oxygen reduction have been put forward which include (i) a decrease in the pH, (ii) macrocyclic organo–metallic catalysts, or (iii) bacterially produced enzymatic catalysis. The action of pH has already been noted above. A decrease in pH results in an increase of the

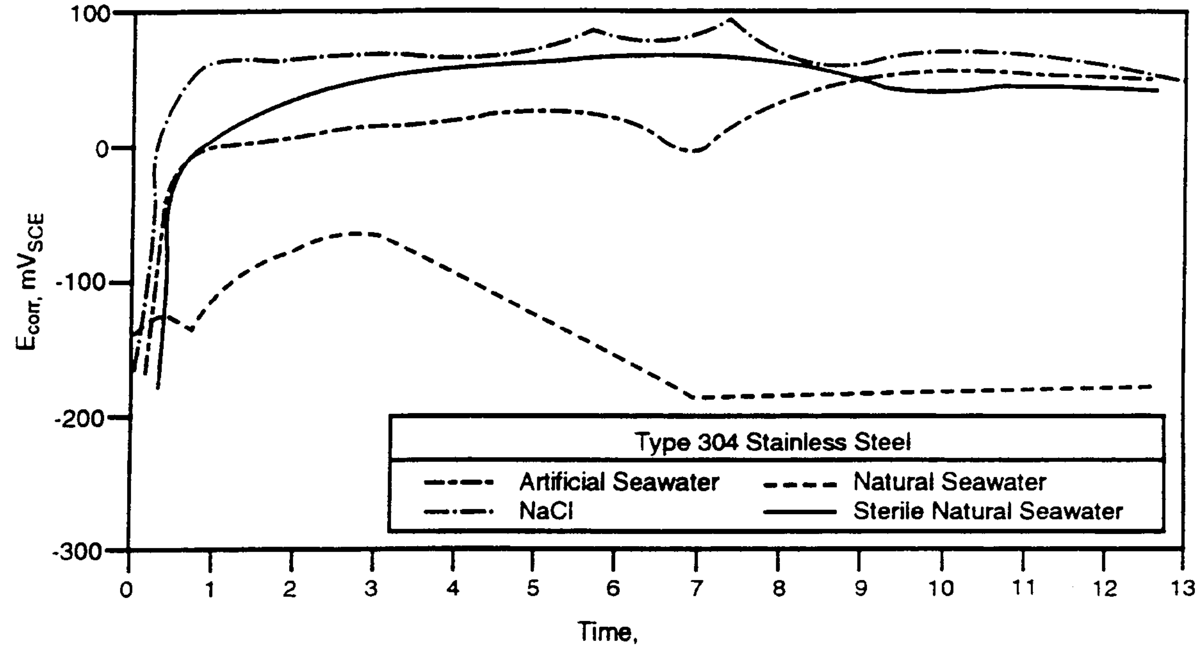

Figure 6-2. Corrosion potential as a function of time for type 304 stainless steel exposed to various chloride-containing media under dark conditions (Little et al., 1991)

reversible potential for the oxygen electrode. Although a number of workers have put forward elaborate schemes for the production of macrocyclic organo–metallic catalysts, no real evidence has demonstrated their existence in biofilms or their role (Johnson and Bardal, 1985).

Chandrasekaran and Dexter (1993a) suggested that a decrease in pH alone was not sufficient to account for the level of ennoblement seen in some natural systems. They were able to culture bacteria isolated from biofilms on pH indicating plates and show that many were able to produce pH levels below 3. Also, using enzymic strips, they were able to show an elevated level of hydrogen peroxide (1.3 to 6.6 mM) within biofilms compared to the bulk waters. Using cyclic voltammetry on ennobled biofilm samples, it was suggested (Chandrasekaran and Dexter, 1993a) that peaks for the oxidation of hydrogen peroxide and reduction of hydrogen could be identified. In abiotic experiments, similar curves were only obtained at a pH of 2.8–2.9, with 8.2–9.8 mM hydrogen peroxide, and an oxygen concentration below 0.6 ppm. In a later study (Chandrasekaran and Dexter, 1993b), it was seen that the addition of 2.4 mM hydrogen peroxide had no effect on the E_{corr}, at pH 5, whereas at pH 2.9, the addition of a similar level of hydrogen peroxide resulted in an additional ennoblement of 40 mV. Tests on the effect of adding active and deactivated catalase on ennobled biofilms were inconclusive with loss of ennoblement in both.

A detailed investigation by Dickinson and Lewandowski (1995) showed that hydrogen peroxide was not necessary for ennoblement. A number of type 316L SS samples were exposed to flowing river water, half of which became ennobled to 350 mV_{SCE} within 17 d, whereas the other half never reached a level above 110 mV_{SCE} (again showing the known variability in ennoblement). A plot of the final E_{corr} against E_{corr} measured after 10 hr showed that those samples which had an E_{corr} of less than −110 mV after 10 hr did not develop high levels of ennoblement (above 110 V_{SCE}). Microbiological examination of all the samples, by light and laser confocal microscopy, showed similar biofilms with a coverage of 50 percent and thickness between 20 and 400 μm. Aggregates of cells were found within a gel of exopolymers. Analysis of the films with microelectrodes showed uniform dissolved oxygen levels, hydrogen peroxide levels below the limit of detection of 2 μM, and no variation in E_{corr} values within the biofilm. Removal of all but a 20-μm adherent portion of the biofilm only resulted in a loss of ennoblement of less than 12 mV, consistent with the findings reported previously. Creation of anaerobic conditions within the biofilm by the addition of glucose, promoting growth of aerobic bacteria and depletion of dissolved oxygen levels, caused a drop in E_{corr} by more then 600 mV. E_{corr} was again ennobled when the carbon limiting conditions were restored. It was concluded from these results that ennoblement is not necessarily related to the presence of anaerobic biofilms.

A preliminary report on the MIC of SS weldments by SRB (Peterson and Taylor, 1995) showed that a drop in E_{corr} (−300 mV_{SCE}) in the presence of a mixed community incorporating SRB was correlated to a decrease in the polarization resistance, indicating the corrosion was occurring at a higher rate in the presence of the bacteria under presumably anaerobic conditions. A similar result was obtained by Franklin et al. (1991) in an actively aerated system in which pitting of mild steel by a *Pseudomonas*-like bacteria was being observed with the scanning vibrating electrode. The initiation of stable (nonrepassivated) pits was marked by a drop in the E_{corr} from −200 to −600 mV_{SCE}. A similar drop was seen over a longer timeframe when a similar concentration of formaldehyde fixed cells were added. However, if ten times the number of fixed cells were added the E_{corr} drop was similar to that seen with live cells. Therefore, Franklin et al. (1991) suggested that the resultant drop in E_{corr} was not solely due to metabolic activity. However, it should be noted that a certain level of metabolic products would have been present within the fixed cells which would have been released with time.

In a type 316L SS tubular flow system in which a mixed biofilm was generated and no evidence of pitting was noted, the colonization of the metal by *Vibrio natriegens* was correlated to a rise in E_{corr} to 100 mV_{SCE}. Subsequent addition of the SRB *Desulfovibrio vulgaris*, after steady E_{corr} values had been maintained for 170 hr, resulted in a further ennoblement to 250 mV_{SCE} which was correlated with the colonization of the biofilm by the SRB (Benbouzid-Rollet et al., 1991). Feron (1991) showed that E_{corr} for type 316L and 430Ti (16Cr-0.44Ti) SSs was strongly dependent on sulphide concentration rather than the numbers of SRB or strain used. Sulphide at concentrations above 30 mg/L^{-1} resulted in a drop of E_{corr}.

6.4.7 Electrochemical Anomalies in Ennoblement Studies

In discussing the corrosion potential rises associated with microbial colonization of SSs, a number of unusual features are evident. This is apparent when values of E_{corr} are compared with E_p and the potential range within which pitting can occur. A number of the studies reviewed above reported potentials well within the pitting range, without any evidence of corrosion occurring, while others, like that of Dexter and Gao (1988), demonstrate variability with some samples reaching relatively high potentials without any pitting and others where pitting/crevice corrosion occurred with a corresponding drop in E_{corr} (Mansfeld and Little, 1991).

The typical scenario was illustrated by Sridhar and Dunn (1994) who monitored current density of an artificial crevice on 304 SS in which the applied potential was increased stepwise. The current density was stable until a potential of 159 mV_{SCE} was reached, at which point crevice corrosion was initiated as evidenced by a rise in the current density and a subsequent drop in the potential inside the crevice.

From the above literature it would appear that microbial biofilms can result in a shift of E_{pit} to higher potentials. Little and Mansfeld (1991), using CPP, reported that E_{pit} for 304 SS in a deareated 3.5 percent NaCl solution was a function of pH and ranged from 300 mV_{SCE} at pH 8 down to 0 mV_{SCE} at pH 2 (consistent with the Pourbaix diagram, Starr et al., 1976). This, therefore, would create a paradox with regard to ennoblement of SS following colonization by microorganisms, as it is generally accepted that a decrease in pH is at least partially responsible for the increase seen in E_{corr}. But the Pourbaix diagram and the data above suggest that decreasing the pH would result in lowering E_{pit}, making pitting more likely to occur at lower pH.

In an attempt to address this problem, Zang and Dexter (1995) examined the effect of a biofilm on E_{pit} for types 304 and 316 SS. It was seen that the presence of a biofilm increased E_{pit} for type 304 but not for type 316 SS. It was suggested that the production of corrosion inhibitors by the biofilm, such as nitrate, sulphate, and phosphate, is the cause of this increase. However, no evidence for the presence of elevated concentrations of these species was presented to justify that argument.

6.4.8 Conclusion and Further Study

From the above literature survey, it is evident that E_{corr} is the easiest electrochemical measurement to perform, but other electrochemical and nonelectrochemical measurements are needed in order to attain a mechanistic understanding of microbially induced pitting. It is further evident that microorganisms may have varied effects on E_{corr}. It is, therefore, suggested that a careful and systematic study be undertaken in which E_{corr} is monitored and correlated to microbial activity, as determined by pH changes, dissolved oxygen consumption/production (not likely in underground repository), sulfide production, thiosulfate/sulfate reduction, and hydrogen peroxide production. This approach can be combined with the use of other electrochemical methods, such as electrochemical impedance spectroscopy (EIS). This can be achieved with controlled batch culture studies. Later, chemstate studies in which growth and metabolism can be maintained in steady state should provide further insight into the microbial role in changes of E_{corr}.

7 HYDROGEN ABSORPTION AND EMBRITTLEMENT OF CONTAINER MATERIALS

7.1 INTRODUCTION

It was mentioned in Chapter 2 that the DOE advanced conceptual design for waste packages has evolved to a multiwall design with a carbon steel outer overpack surrounding an austenitic alloy (e.g., alloy 825) inner overpack. Such a design necessitates consideration of other failure modes in addition to the ones discussed heretofore. A detailed discussion of these alternate designs and failure modes may be found elsewhere (Sridhar et al., 1994a). One of these failure modes is hydrogen embrittlement of the inner alloy overpack.

The hydrogen embrittlement and transport study at the CNWRA actually predated the advanced conceptual designs. The experimental investigation was performed at The Ohio State University (OSU), with the specific purpose of developing a methodology for determining hydrogen transport parameters at the temperatures of interest in the repository. A more detailed discussion of these results may be found in another report (Sridhar et al., 1991a) and two theses (Miller, 1990; Kesavan, 1991). The salient points of these reports are presented here, with a focus on the austenitic alloys.

7.2 ANTICIPATED SOURCES OF HYDROGEN

Hydrogen embrittlement, as an important degradation mode for the containers in the proposed Yucca Mountain repository, has not been investigated experimentally by DOE thus far. However, the effects of hydrogen on the candidate materials have been reviewed as part of an extensive survey of degradation modes by Gdowski and Bullen (1988). A main limitation of their report is that the sources of hydrogen in the proposed repository site at Yucca Mountain and the waste package design are not analyzed. Four potential sources of hydrogen in the repository may be identified:

(i) Galvanic Coupling: The higher alloy inner overpack material may come into contact with the carbon steel outer overpack, rendering the inner overpack cathodic if an aqueous environment contacts both.

(ii) Crevice Corrosion: It is well established that the pH inside a crevice is quite acidic (approximately 2 or lower for some SSs). Hence, depending upon the potential drop within the crevice, hydrogen evolution within the crevice is possible and has been observed in some cases. This effect can be coupled with the previous galvanic effect to increase hydrogen reduction and, consequently, hydrogen uptake on the inner alloy overpack.

(iii) Microbially Influenced Effects: It has been shown that some microorganisms can evolve hydrogen at metal surfaces independent of corrosion reactions.

(iv) Radiolysis Products of the Surrounding Environment: It has been argued that radiolysis of water and water vapor can form hydrogen free radicals, which may then diffuse to the metal surface to be absorbed by the metal.

Note that sources 1 and 2 require the presence of an aqueous phase. Source 3 depends on the characteristics of the microorganism. The microorganism investigated so far, *Clostridium Acetobutylicum*, has been grown in aqueous, anaerobic conditions (Walch et al., 1989). Source 4 can function in both aqueous and gaseous media, but the products of radiolysis are different.

7.2.1 Galvanic Coupling

Galvanic coupling of higher alloys with carbon steel has been shown to cause hydrogen embrittlement in many applications, particularly in the oil and gas field. Most of these environments are more severe than the projected environmental conditions at the Yucca Mountain repository site. For example, the cracking of Monel K-500 (Ni-29Cu-2Fe-2.7Al-0.6Ti) bolts in off-shore applications has been established to be due to hydrogen generated by galvanic coupling of this Ni-Cu alloy with aluminum components (Efird, 1985). In this case, the galvanic potential was estimated to be -1.0 V_{SHE}, and the hydrogen concentrations in the failed bolts were as high as 18 ppm. Galvanic coupling of the same Ni-Cu alloy to steel components has been reported to be the cause of failure in down-hole oil and gas components (Erlings et al., 1986), and hydrogen concentrations as high as 200 ppm have been reported in failed components. In the latter case, the presence of sulfur compounds, such as H_2S, enhances the entry of hydrogen into the metal by limiting (poisoning) the recombination of adsorbed hydrogen atoms.

The rate of hydrogen generation due to galvanic coupling under repository conditions can be estimated if the anodic and cathodic polarization curves of the candidate container material and carbon steel under identical environmental conditions are known. Unfortunately, polarization curves for carbon steel and candidate container materials under identical environmental conditions simulating those of the Yucca Mountain repository are not available. Galvanic corrosion in sea water at low temperatures has been examined in detail by Hack and Scully (1984). For a HY80 steel–alloy 625 (Ni-22Cr-5Fe-9Mo-4Nb) galvanic couple, the predicted galvanic current density was 4 $\mu A/cm^2$ while the measured value was 9 $\mu A/cm^2$. Mansfeld and Kenkel (1975) measured the galvanic current density between various couples in 3.5 percent NaCl at 21 °C. For a 304L SS–4130 steel couple, the galvanic current density was 9.53 $\mu A/cm^2$. Rhodes (1986) estimated the galvanic current density of carbon steel coupled to many Ni-base alloys in a 4 percent $NaCl+H_2S$ (1 atm) environment to be 10–100 $\mu A/cm^2$. Since the repository environment is not expected to be as severe, the galvanic current density and, hence, the rate of hydrogen evolution may be assumed to be of the order of 10 $\mu A/cm^2$. Though this rate is low (by an order of magnitude) compared to the typical current densities used for short-term tests, long-term embrittlement has been observed at these low-charging current densities. However, these embrittlement phenomena have been mainly confined to low temperatures (about 25–30 °C). The effect of temperature will be examined later.

7.2.2 Crevice Corrosion Induced Hydrogen Evolution

It is well recognized that the environmental conditions inside a crevice or an occluded area in electrolytic contact with the bulk environment tend toward the more acidic. Because of deoxygenation, acidic conditions, and the potential drop along the crevice, reducing conditions prevail in the crevice, promoting hydrogen ion reduction as the cathodic process. This reduction reaction has been shown to occur in plain carbon steel by performing permeation studies on a creviced sample (Cottis et al., 1986). Hydrogen permeation inside a crevice in a bulk solution of 3.5 percent NaCl solution increases when the external potential is either anodic or cathodic. Although similar experiments have not been tried for SSs or Ni-base alloys, Ohnaka and Furutani (1990) have attempted to establish the conditions in which hydrogen evolution inside a crevice is possible in SSs. They established that detectable permeation occurred only at applied potentials lower than the equilibrium potentials for hydrogen evolution for the calculated pH at temperature. They noted that for a solution of pH3.8, permeation of hydrogen did not occur above a potential of $-0.2\ V_{SCE}$. Turnbull (1983) has shown that the measured potential inside crevices for SSs is only slightly below the external potential. The measured potential of 304L SS in an aerated, tuff-conditioned J-13 solution augmented with a NaCl concentration of 1,000 ppm at 95 °C is $-0.15\ V_{SCE}$ (Glass et al., 1984). If the solution is deaerated, the corrosion potential drops to about $-0.5\ V_{SCE}$. Hence, hydrogen evolution inside crevices cannot be ruled out for 304L SS under repository environmental conditions. Since similar potential and crevice solution compositions are expected for the other Ni-Fe-Cr-Mo alloys, hydrogen evolution in crevices is a viable mechanism.

7.2.3 Microbially Influenced Hydrogen Evolution

Some microorganisms have been shown to generate hydrogen (Walch et al., 1989; Ford and Mitchell, 1990a). The growth of the organism, *Clostridium Acetobutylicum* on one surface of a steel sample has been shown (Walch et al., 1989) to correspond with an increase in permeation current measured on the other surface of the steel sample. This increase in permeation current did not occur in the presence of a nonhydrogen-producing bacterium, *Clostridium Limosum*, or with *Desulfovibrio Desulfuricans ssp. Astuarii*. The permeation current densities, about 10 $\mu A/cm^2$, can be considered significant, although the data shown by Walch et al. (1989) exhibited high background current densities. The hydrogen-producing bacterium had to be maintained in an anoxic medium, whereas the environmental conditions in the repository are aerobic. However, anoxic conditions can exist underneath biofilms that themselves may survive in aerobic conditions. An additional factor that needs to be evaluated is the survivability of this or other hydrogen-producing strains in the radiation and thermal field. Hence, further information is needed before considering microorganisms to be important sources of hydrogen. However, it should be noted that thermophilic SRB could grow in the near field producing H_2S, which may diffuse toward the metal surfaces to promote hydrogen adsorption (Greesey, 1993).

7.2.4 Radiolysis Products

Ionizing radiations produce activated neutral species as well as ions and free radicals. In aqueous systems, such species include, among others, $H^{\cdot}$, $OH^{\cdot}$, H^+, OH^-, e_{aq}^-, and H_2O_2. The steady-state concentrations of various species depend among many factors on pH, aeration, temperature, and concentration of solute species such as Cl^-, Fe^{2+}, etc. (Spinks and Woods, 1990). In near neutral solutions, e_{aq}^- (solvated electrons), $OH^{\cdot}$ (hydroxyl radical), and H_2O_2 dominate. In the presence of aeration, both solvated electrons and hydrogen radicals will be converted to hydrogen peroxide, which will be the predominant species. A further confirmation of this analysis is the measurement of open-circuit potential (Glass et al., 1986) of type 316L SS in J-13 water while it was exposed to gamma irradiation (dose rate: 3.3×10^6 rad/hr or 9.2 Gy/sec), which showed that potential increased by about 200 mV. This increase in potential is due to the presence of an oxidizing species and was simulated in separate experiments without irradiation by the addition of H_2O_2. Kim and Oriani (1987a,b) examined the open-circuit behavior of Grade-12 Ti in a deaerated brine solution and found a similar increase in open-circuit potential that could be simulated by the addition of H_2O_2. Increase in redox potential of brine environments by gamma irradiation has also been documented by Gray (1987). The formation of chlorine from chloride has been indicated by Spinks and Woods (1990) but has not been reported by the foregoing investigations in brine environments.

The effect of gamma radiation on hydrogen uptake by Grade-12 Ti was also investigated by Kim and Oriani (1987a, b). Gamma irradiation (dose rate: 0.42 Gy/sec) reduced the absorbed hydrogen concentration. Similar reduction was also noted in an unirradiated environment when H_2O_2 was added to the solution or when the solution was purged with H_2 or O_2. The authors hypothesized that the reduction in hydrogen absorption due to irradiation was due to the reduction in concentration of $H^\cdot$ (hydrogen radical) by conversion to H_2 and H_2O_2. The presence of H_2O_2 also acted to reduce the electrolytic generation of hydrogen by increasing the corrosion potential.

Radiolysis of water vapor plus air mixtures have been reviewed by Reed and van Konynenburg (1987). In the presence of both nitrogen and oxygen, nitric acid is the predominant species. While these authors did not indicate the yield of hydrogen radical in these systems, it can be assumed to be negligible. In any case, presence of nitric acid can be expected to increase the redox potential, and thus preclude electrolytic evolution of hydrogen. Additionally, nitric acid may be expected to strengthen the passive film of stainless alloys, thus decreasing permeation of hydrogen further.

From the foregoing discussion, it is clear that radiolytic generation of hydrogen radical in aqueous solutions, water vapor, and two-phase mixtures will be minimal. However, in creviced areas, acidic conditions and lack of oxygen (which is consumed by corrosion reactions) may favor hydrogen radical generation, and the possibility needs to be examined further.

7.3 HYDROGEN EMBRITTLEMENT OF CANDIDATE CONTAINER ALLOYS

Embrittlement due to hydrogen can manifest itself in a variety of ways. These processes include embrittlement due to: (i) absorbed atomic hydrogen (usually called hydrogen embrittlement), (ii) hydride formation in reactive materials such as Ti, Nb, Ta, and Zr, and (iii) absorbed hydrogen, which reacts with carbides or oxides to create internal methane or steam bubbles (called hydrogen attack or hydrogen sickness), and pressure build-up from formation of molecular hydrogen in internal cavities. Embrittlement due to absorbed atomic hydrogen, termed from here on as hydrogen embrittlement, is the focus of this section. While hydride formation has been claimed to be the cause of embrittlement in Ni-base alloys, it has not been established unequivocally nor is it necessary to consider it as a separate phenomenon for the current candidate materials. Hydrogen attack is more important in higher carbon materials than in the austenitic alloys currently being considered for the inner overpack, at least in the temperatures that are anticipated to prevail in the repository. However, because of the long time periods involved, it cannot be ruled out as a possible embrittlement mechanism. It will be considered in the next phase of this project.

The extent of research activities on hydrogen embrittlement of SSs and Ni-base alloys in the past 40 yr has been considerable. The effect of environmental and microstructural variables on hydrogen embrittlement of these two classes of alloys is briefly reviewed in the following section.

7.4 A BRIEF REVIEW OF THE HYDROGEN EMBRITTLEMENT OF STAINLESS STEELS AND Ni-BASE ALLOYS

7.4.1 Role of Environmental Variables

The three most important environmental variables affecting hydrogen embrittlement are the surface hydrogen fugacity (cathodic charging current density in the case of electrolytic source of hydrogen), presence of recombination "poisons" (e.g., S, P, As, Sb, Sn), and temperature. Other environmental variables that can affect embrittlement include presence of oxidizing species that can either reduce cathodic hydrogen current or increase resistance of passive film to entry of hydrogen. In this section, only the first three environmental factors are considered.

Hydrogen Fugacity

The effect of gaseous hydrogen pressure on embrittlement has been examined with respect to high-strength steels and Ni-base alloys. Generally, a steep dependance on pressure is noted at low pressures, followed by a region of cracking that is independent of pressure. In the case of embrittlement by electrolytic charging of hydrogen, a monotonic decrease in time to failure or increase in crack growth rate with charging current density has been noted (Sridhar et al., 1980). Longer times and lower current densities have been studied by Kane (1978) for many Ni- and Co-base alloys. Two points are worthy of note in this work: (i) alloy G (Ni-22Cr-20Fe-6Mo-2Nb), which contains higher iron (20 percent Fe) is much more resistant to cracking than alloy 625 (3 percent Fe) and (ii) at current densities typical of cathodic coupling with carbon steel, cracking can occur at room temperature within a relatively short time provided the applied stresses approach the 0.2 percent yield strength.

Recombination Poisons

It is by now well established that minor concentrations of impurities in the environment or alloy can greatly influence the entry of hydrogen into the metal. It is not the intent to review the rather extensive literature available in this area (for example, McCright, 1977). Typically, these poisons aid the entry of adsorbed hydrogen into the metal by inhibiting the recombination of hydrogen adatoms to form hydrogen gas, which can then escape. In sour gas environments, for example, hydrogen permeation has been shown to be increased by the presence of H_2S (Kane, 1985). Such recombination poisons are not known to be present in the repository environment. However, the presence of SRB may lead to the generation of H_2S in the near field, as noted before. The effect of impurity elements present inside the alloy is much more debatable. Many investigators have shown that the presence of alloying impurities such as P (Berkowitz and Kane, 1980), Sb and Sn (Latanision and Opperhauser, 1975), and S (Jones et al., 1980) cause increased embrittlement of austenitic SSs and Ni-base alloys. The cause of the increased embrittlement has been hypothesized to be due either to the direct action of these impurities on grain-boundary cohesion or indirectly, to their enhancement of hydrogen entry in the metal. From the high-level waste container point of view, the interest in these impurities is in their segregation to grain boundaries due to prolonged exposure to temperatures in the range of 200–300 °C (Berkowitz and Kane, 1980).

Effect of Temperature

Hydrogen embrittlement has been known to decrease with an increase in temperature from the earliest investigations of this phenomenon. In high-strength steels, embrittlement has been shown to have a three-stage behavior: at low temperatures below about 0 °C, embrittlement increases with temperature; at intermediate temperatures around 0 °C, there is a plateau region followed by a decrease in embrittlement with an increase in temperature (Williams and Nelson, 1969; Wei and Gao, 1985). The temperature at which maximum embrittlement is observed depends on the composition and microstructure of the alloy. Though Williams and Nelson rationalized this three-stage behavior in terms of hydrogen adsorption kinetics, other explanations based on a multiplicity of rate-controlling processes have been advanced (Wei and Gao, 1985). For example, in the low-temperature regime, the embrittlement can be transport controlled. Hence, increasing the temperature results in greater availability of hydrogen to the critical stress region (e.g., plastic zone/elastic region transition area). In the higher temperature regime, the rate of accumulation of incoming hydrogen at these sites may be offset by the rate of diffusion away from these sites. In austenitic materials with a face-centered cubic crystal structure, the diffusivity of hydrogen is low. Therefore, diffusion enhanced by the movement of dislocations has been proposed. In this case, increasing the temperature can be shown to result in less accumulation of hydrogen at the dislocation site, and hence less embrittlement. In the case of Ni-base alloys, the three-stage behavior has not been observed, perhaps because sufficiently low temperatures have not been explored. However, the decrease in cracking tendency with an increase in temperature has been reported in many alloy systems (Price and King, 1985).

From the above discussion, the degree of hydrogen embrittlement may be concluded to be reduced significantly by the high temperatures expected to prevail in the repository. It must be emphasized, however, just as in other degradation processes, that the data suggesting lack of embrittlement at higher temperatures are relatively short term in nature. Recent investigations (Singh and Alstetter, 1982) have shown that the crack-tip hydrogen concentration is the most important factor and that embrittlement can be obtained at higher temperatures if the crack-tip hydrogen concentration is high enough. Modeling of the rate-controlling processes of hydrogen embrittlement in combination with experimental data may be needed to predict the long-term behavior. Such models have been advanced for steels (e.g., Wei and Gao, 1985), and for metastable austenitic alloys (Singh and Alstetter, 1982). A critical review of the available models of hydrogen embrittlement and their limitations is needed.

7.4.2 Role of Microstructure

The most important microstructural feature governing the hydrogen embrittlement susceptibility in austenitic alloys and Ni-base alloys is the deformation mode (Thompson and Bernstein, 1976). Other microstructural factors affecting embrittlement include grain size, segregation of impurities, inclusions and second-phase particles, and grain boundary precipitation of carbides or intermetallic phases. The last factor, while important for SCC and intergranular corrosion, is less significant for hydrogen embrittlement.

Deformation mode is controlled by alloy composition and precipitation of coherent phases and, in turn, controls formation of secondary phases during plastic deformation. Plastic deformation can occur in a planar mode in which the dislocation motion occurs along certain preferred combinations of crystallographic planes (slip planes) and directions. Plastic deformation can also occur by extensive cross-slip in which dislocations can "circumvent" obstacles in a given slip plane by moving on to another slip plane that intersects the original slip plane on which the dislocation was moving. One consequence of planar deformation mode is the pile-up of dislocations at an obstacle, such as a grain boundary, resulting in the build-up of stress concentrations. If cross-slip were to occur, the stress concentration will be relieved by the movement of dislocations onto another slip plane. Another consequence of planar deformation mode in the case of hydrogen embrittlement is the dislocation-assisted transport of hydrogen. Tensile triaxial stresses associated with dislocations can result in the segregation of hydrogen at dislocations. This process has been verified visually by autoradiographic images of tritium segregation to triaxially stressed regions at crack tips and, indirectly, by observations of hydrogen trapping in heavily cold-worked metals containing numerous dislocations. Motion of dislocations upon plastic deformation causes migration of the associated hydrogen cloud, which can result in greater penetration than by diffusion alone. While this mechanism has not been universally accepted, dislocation drag of hydrogen can explain many of the observations related to the effects of strain rate, temperature, and deformation mode on embrittlement. For example, if dislocation motion enhances the penetration of hydrogen to critically strained regions, then planar deformation would tend to enhance the accumulation of hydrogen at these regions compared to cross-slip deformation, which would tend to carry away hydrogen as much as bring hydrogen to these locations. This mechanism of dislocation-assisted/enhanced transport of hydrogen is not universally accepted, as revealed by the work of Zakrozcymski (1985). The effect of test techniques on observation of dislocation transport must be examined since observations favoring dislocation transport have come from a variety of techniques, including electrochemical permeation studies. The only observations disfavoring dislocation transport have come from electrochemical permeation tests. Whether one accepts this mechanism or not, it has been shown rather conclusively that materials within the same class suffer greater hydrogen embrittlement (and SCC) if they deform by planar slip (Thompson and Bernstein, 1976).

Planar slip can be brought about by a number of factors such as low-stacking fault energy (SFE), precipitation of coherent phases, short- and long-range ordering, clustering, and low temperature. Stacking faults, which are planar defects contained by two dislocations, force planar deformation mode because cross-slip would entail creation of new interfaces on other slip planes, thus requiring greater energy. Decreasing stacking fault energy results in greater planarity of deformation. Precipitation of coherent precipitates (i.e., precipitates whose crystal plane spacing matches that of the parent crystal) also tends to force planar deformation. This planar deformation occurs because once deformation initiates on a plane, the precipitate is cut, creating surfaces with other orientations that may not match up with the parent crystal planes. Creating new surfaces entails expenditure of energy, hence favoring continued deformation on the same plane rather than new planes. Thus, age-hardening in Ni-base alloys or Cu-base alloys causes coherent precipitation and planar deformation and leads to an increase in embrittlement. Similarly, precipitation of short- and long-range ordered domains can cause planarity of slip. This slip planarity occurs in the Ni-base alloys containing low Fe upon prolonged exposure to temperatures in the 200–500 °C range (Sridhar et al., 1980). The behavior of alloy C-22 is similar to that of alloy C-276 in the presence of hydrogen. Addition of Fe to Ni-base alloys beyond about 10 percent suppresses ordering reactions considerably, and hence low-temperature aging has much less effect on hydrogen embrittlement in alloys such as alloy G (Kargol and Ladna, 1982) and alloy 825. Since segregation of deleterious impurities such as phosphorus also occurs in this temperature range, the effects of ordering and segregation cannot be separated in the low-Fe alloys. However, the available data indicate that segregation has less deleterious effects than ordering. From a repository point of view, the higher Fe containing Ni-base alloys (e.g., 825, G, G-3, etc.) are less susceptible to hydrogen embrittlement and low-temperature aging than the low Fe-containing alloys (e.g., C-276, C-22, 625).

In the case of the austenitic SSs, it is well established that the SSs that are marginally stable are the ones that are most susceptible to hydrogen embrittlement (e.g., Singh and Alstetter, 1982). In these SSs, plastic deformation induces formation of martensite, with the low stacking fault energy alloys having a greater tendency to form martensite. While the role of the martensite has not been clarified, steels with deformation-induced martensite have been shown to exhibit greater susceptibility to hydrogen embrittlement. Thus, type 304 SS is more susceptible to hydrogen embrittlement than type 310 or 316 SSs.

7.5 HYDROGEN PERMEATION AND EMBRITTLEMENT STUDIES ON AUSTENITIC ALLOYS

The focus of the research program at the OSU funded by the CNWRA was establishing methodologies for obtaining hydrogen transport parameters and generating some initial data on the kinetics of hydrogen permeation at various temperatures. Description of the electrochemical permeation technique and the permeation data on some of the candidate alloys are presented elsewhere (Sridhar et al., 1991a). The emphasis on these OSU investigations was on measuring θ, the fraction of the surface covered by hydrogen that will be absorbed. Diffusivities of hydrogen for various alloys have been calculated and compared to literature values. Some preliminary data on the hydrogen embrittlement susceptibility using SSRT are also described.

7.5.1 Hydrogen Permeation Studies

7.5.1.1 Experimental Procedures

The austenitic alloys investigated in this program (Kesavan, 1991) were essentially alloys 825 and C-22, although some preliminary investigation was also carried out on type 316L SS. Alloy 825 was purchased as a 1.6 mm (0.063 in.) sheet, then cold rolled through a series of steps to a final thickness of 0.16 mm (6.3 mils). It was then annealed in argon at 980 °C for 40 min and air cooled. Alloy C-22 was purchased as a 1.6-mm- (0.063 in.) thick sheet, then cold rolled to final thicknesses of 0.076, 0.1, and 0.13 mm (3, 4, and 5 mils). It was final annealed in Argon at 1120 °C for 20 min and air cooled. The chemical compositions of these materials are given in Table 7-1, as they are different from those used in the other studies.

Table 7-1. Chemical compositions (weight percent) of alloys 825 and C-22 foils used in the hydrogen permeation studies

Alloy	C	Cr	Fe	Ni	Mo	Others
Alloy 825	0.014	20.6	28.7	40.6	3*	Cu: 2.1 Ti: 0.72
Alloy C-22	0.004	22.0	4.3	Balance	13.6	W: 3.1 P: 0.009
* – Nominal value						

The permeation measurements were carried out using a modified version of the Devanathan-Stachurski cell (Kesavan, 1991). The foil specimen was sandwiched between two glass cells. Hydrogen was charged from one side (entry side) by cathodic polarization. Part of the hydrogen evolving at this side then was absorbed into the metal and diffused through the foil. The hydrogen flux diffusing through and emerging from the other side of the foil after a breakthrough time was measured by anodic oxidation, while monitoring the current density. Because this is a faradaic process, the measured anodic current density is then proportional to the flux of hydrogen permeating through the foil. The technique has been described extensively in the literature (e.g., McBreen et al., 1966).

Both cells were fitted with condensers to minimize electrolyte loss, a Luggin probe with a salt bridge for the reference electrode, counter electrodes, and gas spargers. The whole apparatus was placed in a convection oven controlled by a proportional temperature controller with an accuracy of ±1 °C. Ag/AgCl external reference electrodes were used with correction for thermal diffusion potential. The electrolyte used for charging hydrogen was 0.1 N NaOH, without any recombination poison. The output side was anodically polarized to oxidize any hydrogen permeating through. In order to measure this current, which is then related to the flux of hydrogen permeating through the foil, it is imperative that any other current due to other anodic or cathodic reactions be minimized (Mezzanotte et al., 1980). This is typically done by purifying the electrolyte of any organic contaminants (pre-electrolyzing) and by protecting the anodic side of the foil surface so that anodic dissolution does not occur. Typically, a Pd coating is applied to this surface to minimize anodic dissolution. In these studies, the Pd coating on the alloys was found to be nonadherent, thus giving rise to a high background current density. However, it was found that the background current density (Figure 7-1) was minimized by using 0.1 M Na_2SO_4 as the exit side electrolyte.

7.5.1.2 Results

The hydrogen permeation current is shown for alloy 825 in Figure 7-2. It can be seen that after a breakthrough time of about 20 hr, there is a rise in the anodic transient and a final leveling off relating to a steady-state hydrogen permeation. The steady-state permeation current density versus charging current density relationship is shown in Figure 7-3 for alloy 825. The calculated diffusivity of hydrogen from rise and decay transients at 95 °C is shown in Figure 7-4. The effect of temperature on apparent diffusivity in alloy C-22 is shown as an Arrehenius plot in Figure 7-5.

Methods for analyzing electrochemical hydrogen permeation transients have been described by Kesavan (1991). The Iyer-Pickering-Zamanzadeh (IPZ) approach (Iyer et al., 1989; Iyer and Pickering, 1990) was used to analyze the parameters related to transport of hydrogen. In this model, the following assumptions are made regarding the intermediate steps involved in the hydrogen absorption:

- Hydrogen evolution reaction occurs by a discharge-recombination mechanism involving single electron transfer
- The recombination step is not rate limiting
- Adsorption follows Langmuir isotherm
- Adsorption--absorption reaction is under local equilibrium
- Permeation involves no trapping and only steady-state conditions are considered

The IPZ model then provides the following relationships:

$$i_\infty = \left(\frac{k''}{b}\right)(Fk_3)^{-0.5}\sqrt{i_r} \tag{7-1}$$

$$i_c e^{a\alpha\eta} = -\left(\frac{b i_0'}{k''}\right) i_\infty + i_0' \tag{7-2}$$

$$(k'')^{-}1 = \left(\frac{k_{ads}}{k_{abs}}\right) + \left(\frac{D}{k_{abs}}\right)(L)^{-1} \tag{7-3}$$

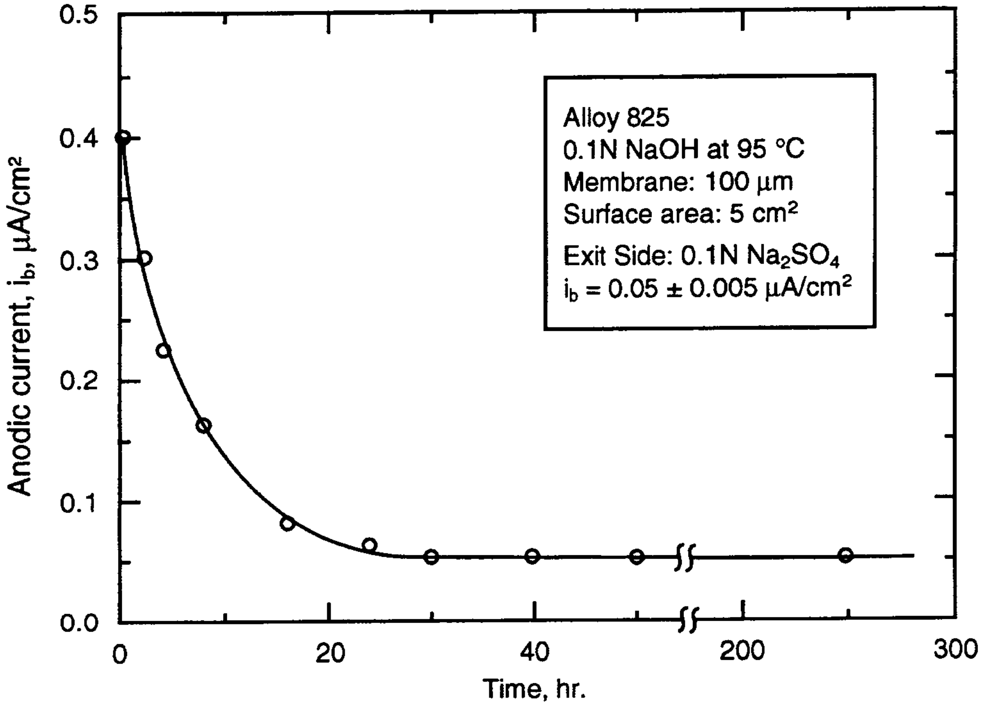

Figure 7-1. Background current density versus time plot for alloy 825 in 0.1 M Na_2SO_4 solution at 95 °C

$$i_0' = \frac{i_0}{(1-\theta)} \tag{7-4}$$

where i_0 is the exchange current density for hydrogen evolution, i_c is the cathodic charging current density, i_∞ is the steady-state permeation current density, and $i_r = i_c - i_\infty$. Other parameters in the above equations are: F = Faradays constant; k'' = thickness dependent adsorption-absorption constant; $b = L/FD$; k_{ads} = adsorption rate constant; k_{abs} = absorption rate constant; k_3 = recombination rate constant; D = Lattice diffusivity of hydrogen; L = foil thickness; $a = F/RT$; α = transfer coefficient for proton discharge; η = overpotential; and θ = equilibrium hydrogen surface coverage.

By measuring the steady-state permeation current density as a function of charging current density and thickness of foil, and measuring the parameters for the kinetics of hydrogen evolution reaction independently (Table 7-2), the parameters in Eqs. (7-1) through (7-4) can be derived. Of most interest to this study was the hydrogen surface coverage, θ. The values of the hydrogen surface coverage so derived are shown in Tables 7-3 and 7-4 (Kesavan, 1991).

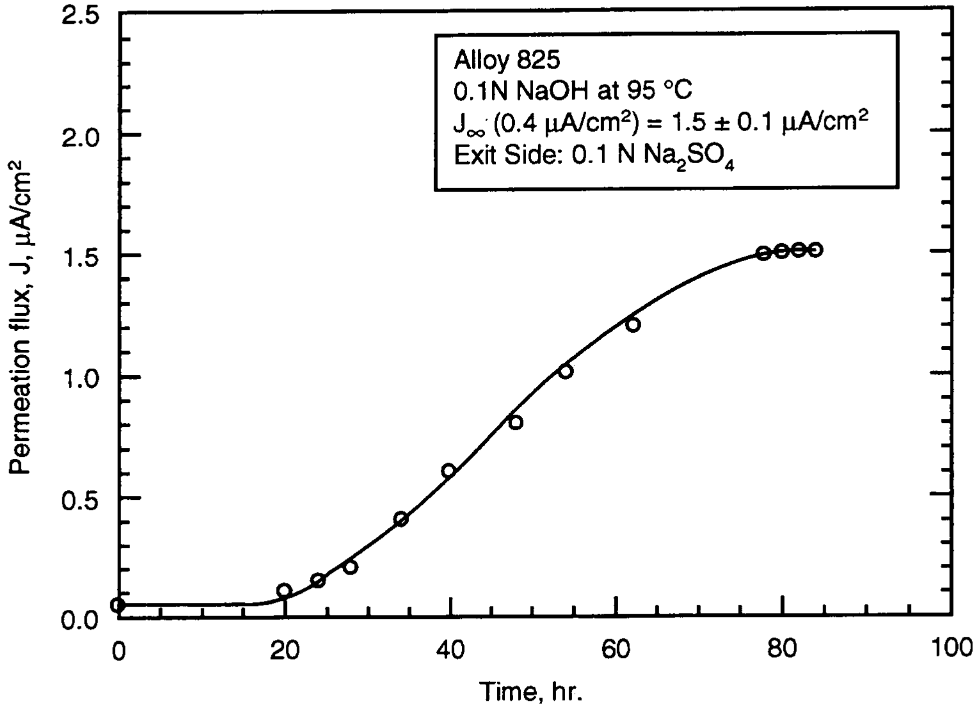

Figure 7-2. Hydrogen permeation curve obtained on alloy 825 in 0.1 M Na_2SO_4 solution at 95° C

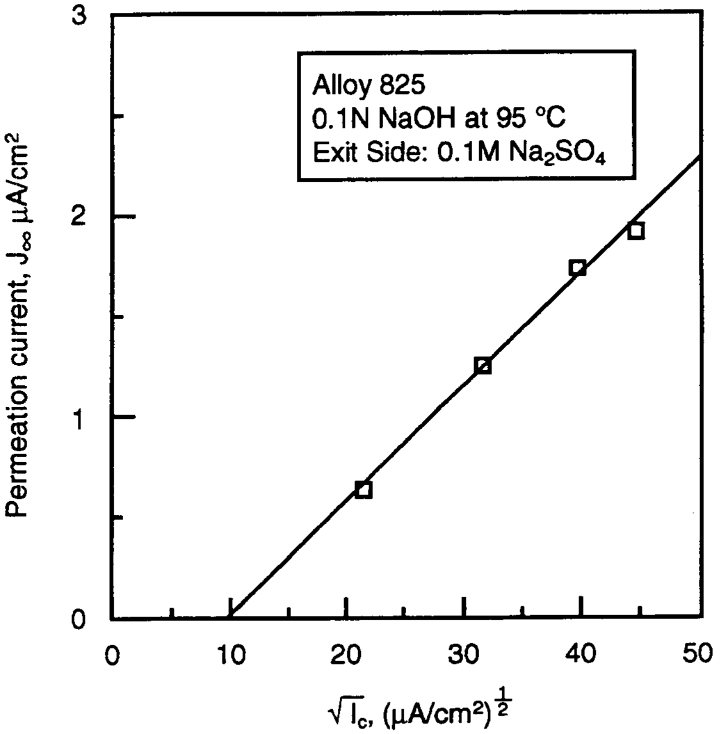

Figure 7-3. Permeation current-charging current relationship for alloy 825 at 95 °C

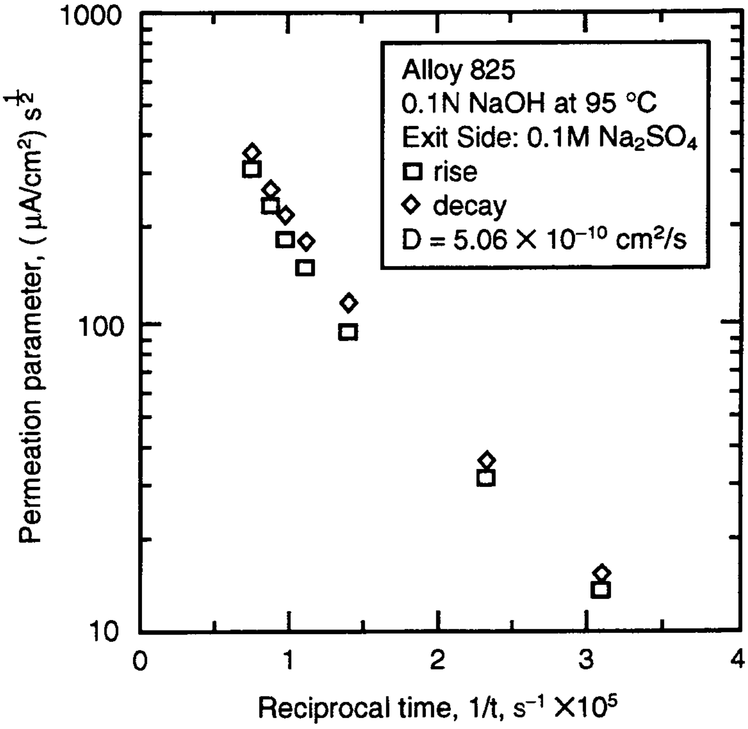

Figure 7-4. Diffusivity of hydrogen from rise and decay transients for alloy 825 at 95 °C

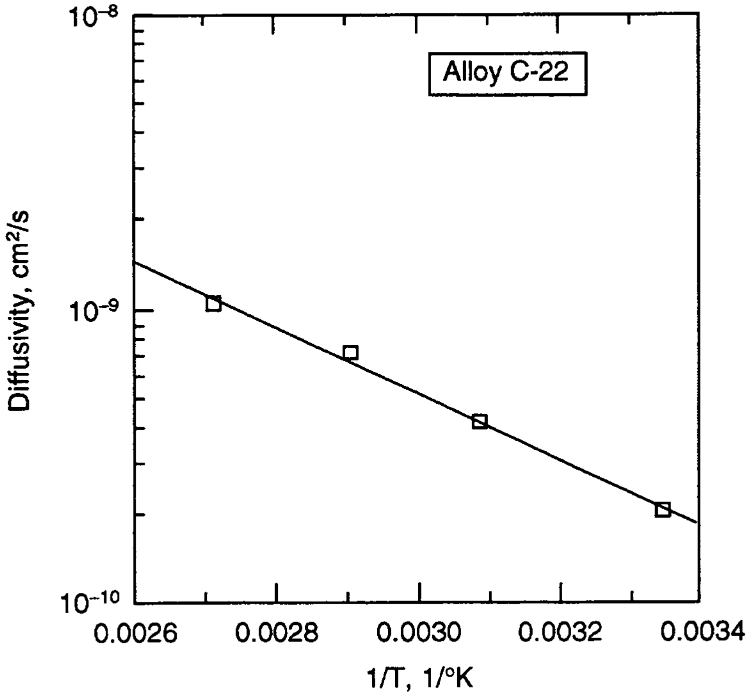

Figure 7-5. Plot of apparent diffusivity of hydrogen as a function of temperature for alloy C-22

Table 7-2. Summary of hydrogen evolution reaction parameters calculated from cathodic polarization curves

Alloy	Temp, (°K)	i_o, H_2 ($\mu A/cm^2$)	α	β_c (mV/dec.)
C-22	368	60	0.43	−170
825	368	50	0.41	−178
316L	368	30	0.41	−180
C-22	298	30	0.41	−145
C-22	323	40	0.43	−150
825	298	28	0.40	−146
825	323	38	0.43	−150

Table 7-3. Summary of Iyer-Pickering-Zamanzadeh analysis of permeation data

Alloy	D_H (cm^2/s)	α	i_o ($\mu A/cm^2$)	θ ($i_c = 1\ mA/cm^2$)	k_{abs}
C-22	9×10^{-10}	0.43	61.1	0.053	0.982
825	5.1×10^{-10}	0.41	49.1	0.073	0.991
316L	3×10^{-10}	0.41	29.5	0.113	1.001

Table 7-4. Surface coverage of hydrogen (θ) as a function of charging current density

Alloy	k_{abs}	$\theta = f(i_c)$ (i_c, $\mu A/cm^2$)		
		200	400	800
C-22	0.982	0.013	0.028	0.044
825	0.991	0.029	0.039	0.062
316L	1.001	0.058	0.071	0.101

7.5.2 Hydrogen Embrittlement Studies

These studies were conducted on cylindrical waisted specimens machined from 12 mm plate of the same heat as that used for the other studies in the IWPE project (Table A-1). Slow strain rate tests were conducted on 24-hr hydrogen precharged specimens that were also charged continuously during the test. The nominal strain rate was 4×10^{-6} per s, and the specimens were oriented such that stress was applied perpendicular to the rolling direction. The results are summarized in Table 7-5 (Kesavan, 1991). It can be seen that alloy C-22 suffered a significant reduction in ductility at 25 and 50 °C, but not at 85 °C. Numerous secondary cracking was observed on the hydrogen-charged alloy C-22 at the two lower temperatures, but not at the highest temperature. The alloy 825 did not exhibit any signs of embrittlement at any test temperature.

Table 7-5. Summary of slow strain rate results on alloys C-22 and 825

Alloy	Temp (°C)	i_c (mA/cm^2)	Time to failure (hours)	Max. Load (ksi)	% reduction in area
C-22	25	0	165	112.58	74.62
C-22	25	20	118.4	103.50	42.88
C-22	50	20	135.25	105.24	47.54
C-22	85	20	159.5	111.77	64.20
825	25	0	99	97.90	71.34
825	25	20	95	95.04	67.87
825	50	20	95.5	95.45	69.63
825	80	20	94	95.70	68.6

7.5.3 Discussion

The diffusion coefficients for hydrogen in pure metals Fe and Ni have been assembled and evaluated by Võlkl and Alefeld (1978). The lattice diffusivity of hydrogen in Ni is remarkably reproducible over a wide temperature range spanning from about 0 to 1,400 °C. This range is particularly noteworthy considering the multitude of test techniques used to measure diffusivity. The diffusivity for hydrogen in Ni follows the Arrhenius relationship given below:

$$D(\mathrm{cm}^2/\mathrm{sec}) = 4.8.10^{-3} e^{-\frac{9690\ \mathrm{cal/mole}}{RT}} \qquad (7\text{-}5)$$

The diffusivity reported in Fe, however, has varied considerably (sometimes over three orders of magnitude) among investigators. This variation has been attributed to surface-controlled processes, which can affect the measurements (Võlkl and Alefeld, 1978). Based on the number of data that agree with each other, the diffusivity up to about 600 °C may be given as:

$$D(\mathrm{cm}^2/\mathrm{sec}) = 7.5.10^{-4} e^{-\frac{2{,}490\ \mathrm{cal/mole}}{\mathrm{RT}}} \tag{7-6}$$

Equations (7-5) and (7-6) indicate that diffusivity of hydrogen in the body-centered cubic iron is considerably higher than that in the face-centered cubic Ni. However, when Fe is added to Ni while maintaining a face-centered cubic crystal structure (up to about 60 percent wt), the diffusivity is lowered, while the solubility is only slightly affected. The permeability, which is a product of diffusivity and solubility, is also lowered by the addition of Fe (Beck et al., 1971). After the solubility limit for Fe in Ni is exceeded, body-centered cubic phase starts precipitating, and the diffusivity increases. This type of behavior has been verified by others in Ni-Fe alloys as well as Ni-Fe-Cr-Mo alloys (Thompson and Bernstein, 1976). The findings of the research at the OSU are in agreement with this behavior, since the diffusivity of alloy 825 calculated from the permeation rise transient at 95 °C (5.06×10^{-10} cm^2/sec) is lower than that of alloy C-22 at the same temperature (9×10^{-10} cm^2/sec). The diffusivity of type 316L SS from the permeation rise transient is found to be 3×10^{-10} cm^2/sec. The values from these measurements are in reasonable agreement with values reported for similar alloys in the literature. For example, Ohnaka and Furutani (1990) measured a value of diffusivity for 304 SS at 95 °C to be 1.4×10^{-10} cm^2/sec. Mezzanotte et al. (1980) measured the value of diffusivity at 90 °C for alloy C-276 (an alloy similar to alloy C-22) to be 7×10^{-10} cm^2/sec. The activation energy for diffusivity for alloy C-22 calculated from Figure 7-5 is 21.2 kJ/mole (5 kcal/mole), which is significantly lower than the activation energy measured for Ni and alloy C-276 (Mezzanotte et al., 1980).

The preliminary tests conducted to date reinforce the literature findings that alloy 825, being a higher iron-containing Ni-base alloy, is less susceptible to hydrogen embrittlement than alloy C-22. It must be noted that alloy 825 would also be expected to be less susceptible to order-disorder transformation at repository temperatures than alloy C-22. Ordering, as indicated before, increases the tendency to hydrogen embrittlement. Higher temperatures resulted in lower embrittling susceptibility, as would be expected.

From the perspective of hydrogen embrittlement, it may be tempting to conclude that the greater resistance of the higher Fe-containing Ni-base alloys is due to their lower diffusivity for hydrogen. Indeed, Coyle et al. (1977) constructed an index that they termed Hydrogen Affinity Index, which was proportional to the solubility divided by the diffusivity. They showed that a Ni-base alloy containing 20 percent Fe (alloy G) had a higher affinity index (lower diffusivity, higher solubility) and concomitantly lower susceptibility to embrittlement to hydrogen than a 5 percent Fe alloy (alloy C-276). However, this correlation should be used with care since the diffusivity and embrittlement are affected by many microstructural features. For example, in alloy C-276, long-term aging at 500 °C results in lower diffusivity (Mezzanotte et al., 1980) but increased embrittlement (Sridhar et al., 1980).

8 SUMMARY AND RECOMMENDATIONS

The IWPE Research Project was undertaken with the broad objective of attaining an adequate understanding of the long-term performance of radioactive waste packages in the context of the NRC role as reviewer of the license application and licensing authority for the proposed HLW repository at Yucca Mountain, Nevada. A more specific objective of the project was to assess test methodologies for evaluation of various material degradation processes affecting HLW container materials and the applicability of parameters derived from these tests for long-term performance prediction. The material degradation processes that may affect the performance of the waste package include those promoted by the presence of a liquid environment in contact with the waste package leading to various forms of aqueous corrosion, as well as those induced by thermomechanical effects arising from the thermal-loading conditions that will prevail in the repository. The fundamental approach guiding the experimental work in this project has been the use of short-term test techniques to evaluate the effects of various environmental factors on the different degradation processes under consideration (i.e., localized corrosion, SCC) and then to examine the applicability of these parameters to long-term prediction. The effect of high-temperature thermal treatments on material behavior has also been studied in an attempt to provide a basis for predicting the long-term performance at lower temperatures.

Although the DOE conceptual design has changed and the material selection for the waste package is still evolving, the focus of the IWPE project on the austenitic Fe-Cr-Ni-Mo alloys is deemed to be appropriate. This class of alloys is being considered in the ACD for important components of the waste package, such as the MPC and the inner disposal overpack, as indicated in Table 2-1. Despite the current DOE approach that relies on maintaining the waste package dry over a very extended period (several hundred to thousand of years) under the unsaturated conditions of the repository horizon, the strong possibility of having an aqueous, saline environment contacting the containers at shorter times is emphasized in the report. The evolution in the chemical composition of the environment by a combination of processes, including the effects of heat on rock-water interactions, evaporation and condensation of groundwater on container surfaces, formation of radiolytic species, and modifications due to microbial activity and presence of corrosion products, is discussed briefly to explain the reasons for studying a wide range of environmental conditions. The consideration of such a range has demonstrated to be useful for evaluating the effect of several influential environmental factors on the various corrosion processes covered in this report. A summary of the main findings of the experimental investigations and the conclusions of the literature reviews is presented below according to the various tasks of the IWPE project. This summary is followed by a series of recommendations for future work on waste package materials and designs.

8.1 SUMMARY OF RESULTS AND CONCLUSIONS

8.1.1 Localized Corrosion

Assuming that the containers will be exposed to aqueous environments, the interactive effects of environmental factors on localized corrosion over limited ranges of anion concentrations and temperatures, as defined by a full-factorial test matrix, were investigated using the cyclic potentiodynamic polarization test technique. The environmental factors examined were Cl^- (6–1,000 ppm), SO_4^{2-} (20–1,000 ppm), NO_3^- (10–1,000 ppm), F^- (2–200 ppm), and temperature (60–95 °C). For alloy 825, the electrochemical parameters derived from CPP curves, the E_p and the E_{rp}, did not always provide adequate information on the propensity to localized corrosion. This limitation was especially true in rather benign environments in which pitting did not initiate until high potentials were reached. Hence, a LCI was defined to include visual information on the occurrence of localized corrosion. When LCI was used as the measured parameter and when the environmental factors were chosen carefully, the correlation coefficient of the analysis was very high. Chloride was the most important promoter and nitrate was the most important inhibitor of localized corrosion for alloy 825. There was a strong interaction between chloride and nitrate. Temperature, sulfate, and fluoride did not affect localized corrosion significantly. For type 316L SS, there was a good correlation between visual observation of localized corrosion and electrochemical parameters. In this case, chloride was the only factor of importance in promoting localized corrosion, whereas the other anionic species were not important within the concentration ranges studied. The effect of temperature was not examined for this alloy.

The factorial analyses are limited to the ranges of the environmental factors studied within which linearity is assumed. Hence, additional experiments were conducted to define the true functional relationship between the electrochemical parameters for localized corrosion and chloride concentration. In addition to E_p, it was found that E_{rp} also exhibits a linear relationship with the logarithm of the chloride concentration, but the slope was smaller than that corresponding to E_p. Other environmental factors such as pH, bicarbonate, silicate and Mg^{+2} concentration did not have an effect on these parameters, whereas thiosulfate decreased the value of E_{rp} significantly. The presence of oxidizing agents, such as H_2O_2, increased the E_{corr} of alloy 825 such that it becomes higher than E_{rp} at chloride concentrations above 100 ppm. If these conditions are found to prevail in the proposed repository environment, alloy 825 may be only marginally better with respect to type 316L SS as a choice of container material. In aerated solutions corresponding to mild oxidizing conditions (E_{corr} close to -300 mV_{SCE} at 95 °C) alloy 825 should be expected to be resistant to localized corrosion even in concentrated chloride solutions, except in the presence of thiosulfate. However, long-term exposures under natural corrosion conditions are necessary to corroborate this observation. It was observed that E_{corr} values are dependent on surface conditions. The presence of an oxide film formed in air under dry conditions at temperatures above 100 °C, increased significantly the value of E_{corr}, particularly in deaerated environments.

The use of E_{rp} as a predictive parameter for localized corrosion was examined in detail. The extent of prior pit growth was not a factor in determining E_{rp} of alloy 825 and type 316L SS, although it affects repassivation time. An important observation is that E_{rp} for pitting corrosion is almost identical to that observed for crevice corrosion, indicating that a common mechanistic interpretation is valid for both phenomena. The mechanistic aspects of E_{rp} were examined. By using measurements of pH, chloride concentration, and potential inside artificial crevices, it was concluded that the initiation of crevice corrosion is the result of pitting localized on isolated spots within the crevice area. The stochastic nature of crevice corrosion initiation was discussed in terms of prevailing ideas for the initiation of pitting corrosion, which attribute its stochastic nature to véry localized fluctuations of pH and chloride concentration.

Surface chromium depletion has a profound effect on the corrosion behavior of alloy 825. Specimens with surface Cr depletion exhibited pitting even in a 6 ppm chloride solution at 95 °C. More importantly, high rates of uniform dissolution were noted at low potentials in the 1,000 ppm chloride solutions, but the behavior of alloy 825 is reestablished as soon as this outer layer is corroded away, allowing the bulk properties to determine the electrochemical response of the alloy.

Preliminary experiments with alloy C-22 suggest that this alloy is considerably more resistant to localized corrosion than alloy 825. The alloy could not be pitted even at high potentials in solutions with up to 10,000 ppm chloride concentration and 10,000 ppm sulfate concentration at 95 °C. However, the cyclic polarization curves exhibited a hysteresis loop, which is not consistent with the appearance of the specimens. Hence, the applicability of the CPP tests to determine E_{rp} for this type of alloy is questionable, and further studies are needed to develop an appropriate technique for measuring the E_{rp} of this alloy.

By measuring repassivation and initiation times of alloy 825 in 1,000 ppm chloride solution at 95 °C using pitted and creviced specimens in experiments conducted over 18 months, it was concluded that the E_{rp} for deep pits measured by the slow-scan rate technique can be used to predict the long-term occurrence of localized corrosion. A wide range of applied potentials was used in these experiments to define an unique potential, E_u, above which the alloy is prone to localized corrosion whereas below it is immune. Prolonged tests using different oxidants as cathodic reactants are needed to confirm the validity of this conclusion under natural corroding conditions.

Finally, field experience and laboratory data were compared on the basis of information reported in the literature and assumptions about E_{corr} values when they were not provided. This preliminary analysis indicates that the concept of E_{rp} as a lower limit for the occurrence of localized corrosion seems to be valid over an extended range of alloys and applications.

8.1.2 Stress Corrosion Cracking

Slow strain rate tests and constant deflection tests on type 316L SS and alloy 825 were used to define environmental conditions, in terms of solution composition, pH, and temperature, as well as potential ranges that may promote SCC. The environments studied are chloride-containing solutions that simulate variations of groundwater environments produced by evaporation of water and concentration of salts.

The results generated so far are consistent with the assumption that the E_{rp} for localized corrosion constitutes a lower limit for the critical potential for SCC in the case of type 316L SS. However, the range of chloride concentrations over which SCC occurred seems to be dependent on the test technique. In SSRTs, SCC of type 316L SS was observed when exposed to $MgCl_2$ and LiCl solutions at chloride concentrations equal to or greater than 7.2 molal temperatures above 100 °C. Although SCC occurred under open-circuit conditions, it was significantly enhanced at slightly anodic potentials. On the contrary, SCC did not occur by decreasing the potential below E_{rp}, which in concentrated chloride solutions is close to E_{corr}. In addition, SCC did not occur in NaCl and LiCl solutions in which the chloride concentration was 6.2 molal at 95 °C. This value is close to the maximum concentration attainable in NaCl due to solubility limitations. These results indicate that under the experimental conditions used in these tests, particularly in terms of temperature and strain rate, no SCC can be promoted regardless of the cation at chloride concentrations equal to or lower than 6.2 molal, even at acidic pHs. The addition of thiosulfate promoted SCC in 5.8 molal chloride solutions both at the open-circuit and anodic-applied potentials, but not at lower chloride concentrations.

No SCC of type 316L SS occurred in the chloride concentration range extending from 1,000 to 10,000 ppm at 95 °C, under a wide range of experimental conditions, including the presence of crevice geometries and the addition of thiosulfate, at potentials at which SCC should be expected. In this chloride concentration range, pitting occurred as the predominant phenomenon, although potentials were well below the line representing the dependence of E_p on chloride concentration as measured in CPP tests. Incipient cracks were observed in galvanostatic tests under crevice conditions in 1 M NaCl solution (≈35,500 ppm chloride). Although the failure was ductile, and accompanied by pitting corrosion, this result suggests that SCC may be promoted in SSRTs under crevice conditions at this chloride concentration over a very narrow range of potentials. In a constant extension test, incipient cracks were detected but substantive growth was not observed even in the presence of thiosulfate.

Contrary to the results of strain rate tests, SCC of type 316L SS occurred in constant deflection tests in dilute chloride solutions (1,000 ppm) at 95 °C and potentials ranging from −130 to −240 mV_{SCE}, with and without the addition of thiosulfate. The presence of thiosulfate, however, enhanced the SCC susceptibility significantly. Cracks were mostly detected above the vapor/solution interface, indicating that the local environment created as a liquid film on the specimen surface could be more detrimental than the bulk liquid environment. In more concentrated chloride solutions, SCC was observed in constant deflection tests conducted in both LiCl and NaCl solutions at concentrations (5.8 molal) at which no cracking was detected in SSRTs. The addition of thiosulfate increased even further the susceptibility to SCC, in agreement with the result obtained in the SSRTs.

Alloy 825 only failed by SCC in SSRTs when exposed to $MgCl_2$ solutions at a chloride concentration of 14.0 molal at a temperature of 120 °C. In contrast, SCC did not occur in LiCl and NaCl solutions in which the chloride concentration was equal to 9.3 molal or lower at temperatures below 110 °C. These results indicate that under the experimental conditions used in these tests, particularly in terms of temperature and strain rate, SCC cannot be promoted regardless of the cation at chloride concentrations less than or equal to 9.3 molal, even at acidic pH levels. Instead of SCC, the dominant failure mode was ductile failure, accompanied by pitting corrosion. SCC did not occur by the addition of thiosulfate to a solution containing 5.8 molal chloride even under severe conditions prompted by the use of a notched specimen at a lower extension rate over a very extended period. However, under crevice conditions SCC was promoted in all these conditions. The constant deflection tests confirmed the results of the SSRTs in the case of alloy 825 in the sense that no SCC was found within the same range of chloride concentrations using both test methods. Contrary to the case of type 316L SS in which a significant susceptibility to SCC in constant deflection tests was detected in the vapor phase under conditions leading to the formation of liquid film on the surface, localized corrosion in the form of pitting was the dominant phenomenon in alloy 825.

8.1.3 Materials Stability

The results of this experimental study indicate that alloy 825, despite the low carbon content attained with new production methods and the introduction of an appropriate stabilization treatment, is still susceptible to sensitization. Hence, intergranular corrosion becomes possible under specific environmental conditions if the alloy is thermally treated in the 600 to 800 °C range for times sufficient to precipitate chromium-rich carbides at grain boundaries.

As expected, solution annealing, prior to these thermal treatments, enhanced the degree of sensitization significantly, leading to high corrosion rates in the boiling 65 percent nitric acid solution.

Corrosion rates were significantly lower in the ferric sulfate-sulfuric acid tests, but intergranular corrosion was nevertheless observed. Cold work (up to an estimated 25 percent) of SA specimens prior to thermal treatment did not affect the degree of sensitization, but further studies are necessary to confirm this finding, particularly at low temperatures.

Attempts to apply several variations of the EPR tests for the detection of sensitization were unsuccessful because the electrochemical parameters used in these tests (i.e., reactivation charge, peak current ratio) did not exhibit a noticeable difference between sensitized and annealed specimens.

The most effective assessment of the effect of sensitization through electrochemical methods was performed by measuring E_{rp} in CPP tests conducted in a 100 ppm chloride solution at 95 °C. A significant decrease of E_{rp}, greater than 100 mV with respect to that for MA or SA specimens was observed for specimens sensitized for 100 hr at 700 °C. These results correlate well with those obtained in the boiling nitric acid test. Localized attack developed along grain boundaries in the sensitized specimens.

The sensitization process was found to be strongly dependent on temperature, with an apparent activation energy of approximately 292 kJ/mole in the 600 to 750 °C range, which indicates that very prolonged heat treatments may be required to induce sensitization at lower temperatures.

Grain boundary chromium-depletion of sensitized specimens was confirmed by STEM studies. X-ray diffraction patterns confirmed that $M_{23}C_6$ was the single identified precipitate in grain boundaries, in which chromium (72 at. percent) was the predominant metallic component. Chromium concentration profiles were obtained revealing that the minimum Cr content was approximately 20 at. percent in the most severely sensitized condition attained at 700 °C for at least 15 hr. The extent of the chromium depletion was quantified and approximately correlated with the corrosion rate from the nitric acid tests and E_{rp} measured in chloride solutions.

8.1.4 Microbially Influenced Corrosion

The potential for MIC of the candidate and alternate container materials is briefly summarized on the basis of an extensive review of the literature prepared early in this project. A brief description of the characteristics of microbial life in subsurface environments is included to emphasize energy and nutrient requirements to sustain bacterial growth. The effect of various environmental parameters involved, such as salinity, water availability, temperature, pH, and the presence of electron acceptors is noted. In the discussion on MIC, separate consideration is given to different classes of metallic materials, including mild and low-alloy steels, austenitic SSs, and nickel alloys. It was concluded that all the alloys reviewed, with the possible exception of titanium, may be susceptible to MIC. The lack of relevant information on Ni-Fe-Cr-Mo alloys is emphasized.

With the understanding that no studies on MIC of the candidate container materials have been conducted in an unsaturated subsurface soil or rock environment, it is pointed out that all the alloys would be resistant to microbially mediated processes if the temperature at the waste package surface is above 100 °C and the moisture content remains below 60 percent over the 300- to 1,000-yr containment period. On the other hand, it is concluded that sufficient nutrients and microbial life are likely to be present in the near field to promote MIC if the temperature of the waste package drops below 100 °C and the moisture content rises above 60 percent for any period of time.

The effect of microbial activity on the E_{corr} is also reviewed. While an increase in the E_{corr} in the presence of biofilms has been observed in seawater, the magnitude of the effect and the mechanism are still matters of controversy. Prediction of such an effect is critical for evaluating waste package performance taking into consideration that increases in the E_{corr} above E_{rp} would lead to the occurrence of localized corrosion or eventually SCC for Ni-Fe-Cr-Mo alloys.

8.1.5 Hydrogen Absorption and Embrittlement

The anticipated sources of hydrogen in the repository were examined. The most likely sources of hydrogen include crevice environments and galvanic coupling with the carbon steel disposal overpack. Microbially influenced generation of hydrogen cannot be precluded, but the survivability, in the repository environment, of organisms known to generate hydrogen on steels or other organisms with similar capabilities is yet to be demonstrated. However, the SRB could form H_2S in the proximity of the waste packages leading to hydrogen absorption by the containers. Radiolytic generation of hydrogen from vapor sources is unlikely because of the predominance of the oxidizing species so generated, as well as the reactions of hydrogen radical with oxygen present in the unsaturated zone of the Yucca Mountain site. Radiolytic generation of hydrogen from aqueous environments inside crevices is a possibility because of the acidic and anoxic conditions prevailing in these regions. However, shielding of γ-radiation could prevent water radiolysis in the current ACD.

Assuming hydrogen is generated in sufficient concentrations, the susceptibility to embrittlement of candidate container materials under repository thermal conditions was examined. The hydrogen embrittlement characteristics of the austenitic alloys are relatively well understood, at least, phenomenologically. Among the austenitic SSs and Ni-base alloys, 304/304L is the least resistant, followed by the high-Ni alloys such as alloy C-276, C-22, or 625. The higher Fe-containing Ni-base alloys, such as alloy 825, are the most resistant of this class. All these alloys show a decreasing tendency to embrittle as the temperature is raised above room temperature. Long-term exposure to repository thermal conditions can be deleterious to the room temperature embrittlement susceptibility of the low-Fe, Ni-base alloys such as alloy C-22 because of ordering reactions. No embrittlement has been observed at the anticipated repository temperatures.

The hydrogen permeability techniques investigated at the OSU enable measurement of hydrogen diffusivity and surface coverage in aqueous solutions up to boiling point and can be adapted for measurement at higher temperatures. Comparison of the initial data to data from the literature at the same temperatures indicates quite good agreement for all the alloys.

8.2 RECOMMENDATIONS

Although several fundamental aspects of relevance to the KTUs identified in Chapter 1 have been addressed in this project, further experimental studies are needed in certain critical areas in order to: (i) address issues related to the performance of new DOE strategies, designs, and materials, and (ii) increase the confidence in the use of parameters such as E_{rp} for long-term prediction. This effect of environment on long-term performance includes not only the effect of the chemical composition and physicochemical properties of the changing environment on the corrosion resistance of the waste package materials, but also their thermomechanical stability as a result of the prolonged exposure at temperatures well above ambient temperatures.

Since any experiment, irrespective of its duration, is going to be shorter than the required lifetime of the waste package, performing experiments under natural corroding conditions in environments resembling those anticipated under repository conditions will only serve to eliminate materials that fail quickly. A concept traditionally used in corrosion studies consists in the modification of the environmental conditions by increasing the concentration of aggressive species, increasing the temperature, or decreasing the pH to accelerate the corrosion process of interest. However, the extent of the acceleration cannot be judged in the absence of operational experience, and even then, only if the component fails in service. In addition, certain accelerating factors that can be used, such as temperature and potential, may not always accelerate the specific corrosion process but decrease its rate by altering the mechanism of the process under study. Instead, the approach adopted in the IWPE project for long-term prediction of materials performance is based on the use of critical potentials for localized corrosion, such as the E_{rp}.

Initial steps in the mechanistic modeling of the E_{rp} has been taken by measuring chemical and potential changes in simulated crevices that are being used to define conceptually the appropriate mechanism and provide input to a mathematical model, which is an activity carried out in parallel with the IWPE project in the EBS element. E_{rp} values for localized corrosion derived from short-term electrochemical testing, in addition to being applied to define the occurrence of SCC, are being evaluated through on-going potentiostatic experiments extended to date up to 18 months.

The following experimental work is recommended for the future project on waste package as an extension of the work reported herein.

- Since tests in the current IWPE project have been performed under isothermal conditions, it is necessary to conduct experiments under heat transfer conditions simulating the evaporation of groundwater around the waste package and formation of concentrated saline solutions to assess corrosion of waste package materials. The possibility of periodic wet-dry cycles should be considered, as well as the effect of corrosion products (i.e., Fe(II) and Fe(III) species formed by the dissolution of the outer disposal overpack). Parameters of interest to be measured included E_{corr}, Eh, pH, and concentration of anionic species, particularly chloride, and the relative humidity in the surrounding environment. This activity should include the materials currently considered in the ACD and the evaluation of the anticipated corrosion processes, such as general corrosion, localized corrosion, and SCC, with the main purpose of defining scale-up criteria and attaining a conceptual description of the controlling processes at the repository scale.

- The long-term corrosion and stress corrosion experiments should be extended to durations of several years. These experiments, in addition to the potentiostatic tests currently underway, should include tests at open-circuit potentials evaluating a range of oxidizing conditions provided by the presence of different redox couples. The aim of these experiments is to confirm the validity of the E_{rp} concept for long-term prediction of localized corrosion and SCC, including materials tested in the current IWPE project and those proposed as candidate materials for the waste package in the ACD phase of the DOE program.

Specific activities that should be included in this area are, as follows:

- Continuation of tests using fracture mechanics specimens to evaluate the effect of stress intensity on crack growth rate and to determine the value of K_{Iscc}. These tests should cover a range of environmental conditions, in terms of chloride concentration, temperature, presence of thiosulfate and potential, using modified wedge-opening loading (WOL) specimens in which cracks, once initiated at potentials higher than the critical potential for SCC, can be arrested by decreasing the potential below that value.
- Measurement of specific electrochemical parameters, such as exchange current density, reaction orders, and transfer coefficients of cathodic reactions for input in modeling of the E_{corr} and galvanic coupling.
- Although hydrogen embrittlement may be considered to be less important than other degradation processes such as crevice corrosion, SCC, etc., on the basis of short-term testing, the potential for embrittlement over long-time periods should be evaluated using existing models, particularly for the carbon steel overpack.

- The thermal stability and eventual embrittlement of candidate materials for overpacks, MPC, and internal components of MPC must be investigated. The potential for low-temperature embrittlement of type 316L weldments, due to α' precipitation, must be examined to evaluate eventual decreases in fracture toughness of the MPC at temperatures ranging from repository to ambient temperatures. Similarly, the effect of phosphorus segregation to grain boundaries in the base and weld metal on the embrittlement of steels must be explored. Review of the literature should precede the initiation of experimental work in this area, but the need for long-term prediction of embrittlement problems, particularly at welds, makes this activity crucial. Studies on sensitization of alloy 825 or other Ni-base alloys that may be proposed as the focus for the inner overpack should be continued at temperatures closer to repository temperatures by substantially extending the exposure times.

- The experimental work recently initiated on the effect of microbial colonies on the modification of the environment near the waste package surface should be continued. Emphasis on the availability of nutrients in the near field and the bioenergetics of container corrosion should set the basis for studying the effect of microorganisms on the localized corrosion of container materials. Specific effort should be devoted to understanding the effect of biofilm formation on the evolution of the E_{corr} and the possibility of extending the concept of the E_{rp} to MIC. Specific attention should be given to the effect of microbial activity on the integrity of welds.

- The experimental work, devoted only to container materials in the current project, should be extended to the waste form. The rate-controlling process in the release rate of matrix elements from simulated spent fuel should be experimentally studied. The formation of secondary minerals, which may control the dissolution rate, must be experimentally investigated, taking into consideration the chemical composition of the near-field environment. These investigations will be coordinated with other research projects that are underway at the CNWRA.

9 REFERENCES

Abraham, T., H. Jain, and P. Soo. 1986. *Stress Corrosion Cracking Tests on High-Level Waste Container Materials in Simulated Tuff Repository Environments.* NUREG/CR-4619. Washington, DC: Nuclear Regulatory Commission.

Alavi, A., and R.A. Cottis. 1987. The determination of pH, potential and chloride concentration in corroding crevices on 304 stainless steel and 7475 aluminum alloy. *Corrosion Science* 27: 443–451.

Alkire, R.C., and S.E. Lott. 1989. The role of inclusions on initiation of crevice corrosion of stainless steel. II. Theoretical studies. *Journal of the Electrochemical Society* 136: 3,256–3,262.

American Society for Testing and Materials. 1994a. G 30-94, Standard practice for making and using U-bend stress-corrosion test specimens. *Annual Book of Standards.* Philadelphia, PA: American Society for Testing and Materials: 03.02: 97–103.

American Society for Testing and Materials. 1994b. A 262-93a, Standard practices for detecting susceptibility to intergranular attack in austenitic stainless steel. *Annual Book of Standards.* Philadelphia, PA: American Society for Testing and Materials: 03.02: 1–16.

American Society for Testing and Materials. 1994c. G 28-94, Standard test methods of detecting susceptibility to intergranular attack in wrought, nickel-rich, chromium-bearing alloys. *Annual Book of Standards.* Philadelphia, PA: American Society for Testing and Materials: 03.02: 92–96.

American Society for Testing and Materials. 1994d. G 108-94, Standard test method for electrochemical reactivation (EPR) for detecting sensitization of AISI Type 304 and 304L stainless steels. *Annual Book of Standards.* Philadelphia, PA: American Society for Testing and Materials: 03.02: 457–464.

American Society for Testing and Materials. 1994e. G 61-86, Standard test method for conducting cyclic potentiodynamic polarization measurements for localized corrosion susceptibility of iron-, nickel-, or cobalt-based alloys. *Annual Book of Standards.* Philadelphia, PA: American Society for Testing and Materials: 03.02: 238–241.

American Society for Testing and Materials. 1994f. G 31-72, Standard practice for laboratory immersion corrosion testing of metals. *Annual Book of Standards.* Philadelphia, PA: American Society for Testing and Materials: 03.02: 104–110.

Audouard, J.P., C. Compere, N.J.E. Dowling, D. Feron, D. Festy, A. Mollica, T. Rogne, V. Scotto, U. Steinsmo, C. Taxen, and D. Thierry. 1995. Effect of marine biofilms on stainless steels—Results from a European exposure program. Paper No. 3. *1995 International Conference on Microbially Influenced Corrosion.* Houston, TX: NACE International.

Angeliu, T.M., and G.S. Was. 1990. Grain boundary chemistry and precipitation in controlled purity alloy 690. *Proceedings of the Fourth International Symposium on Environmental Degradation of*

Materials in Nuclear Power Systems-Water Reactors. D. Cubicciotti, ed. Houston, TX: National Association of Corrosion Engineers: 5-64–5-78

Angell, P., J.-S. Luo, and D.C. White. 1994. High resolution microbial pitting corrosion studies utilizing a two-dimensional scanning vibrating electrode microscope (SVEM) system. *Proceedings of the Tri Service Corrosion Conference*. T. Naguy, ed. Washington, DC: Department of Defense: 161–181.

Arter, H.E., K.W. Hanselmann, and R. Backofen. 1991. Modelling of microbial degradation processes; the behavior of microorganisms in a waste repository. *Experientia* 47: 578–583.

ASM International. 1988. Forming and forging. *Metals Handbook*. Metals Park, OH: ASM International 19(14): 616–623.

Asphahani, A.I. 1980. Localized corrosion of high performance alloys. *Materials Performance* 19(8): 9–21.

Bates, R.G. 1964. *Determination of pH: Theory and Practice*. New York, NY: J. Wiley & Sons.

Batista, W., A.M.T. Louvisse, O.R. Mattos, and L. Sathler. 1988. The electrochemical behaviour of Incoloy 800 and AISI 304 stainless steel in solutions that are similar to those within occluded corrosion cells. *Corrosion Science* 28: 759–768.

Beavers, J.A., N.G. Thompson, and W.V. Harper. 1990. Potentiodynamic polarization studies of candidate container materials in simulated tuff repository environments. *Scientific Basis for Nuclear Waste Management XIII*. V.M. Oversby and P.W. Brown, eds. Pittsburgh, PA: Materials Research Society: 176: 533–540.

Beavers, J.A., and N.G. Thompson. 1990. *Environmental Effects on Corrosion in the Tuff Repository*. NUREG/CR-5435. Washington, DC: Nuclear Regulatory Commission.

Beavers, J.A., N.G. Thompson, and C.L. Durr. 1992. *Pitting, Galvanic, and Long-Term Corrosion Studies on Candidate Container Alloys for the Tuff Repository*. NUREG/CR-5709. Washington, DC: Nuclear Regulatory Commission.

Beavers, J.A., and C.L. Durr. 1992. *Stress Corrosion Cracking Studies on Candidate Container Alloys for the Tuff Repository*. NUREG/CR-5710. Washington, DC: Nuclear Regulatory Commission.

Beavers, J.A., and G.H. Koch. 1992. Limitations of slow strain rate test for stress corrosion cracking testing. *Corrosion* 48: 256-264.

Beck, W., J.O'M. Bockris, M.A. Genshaw, and P.K. Subramanyan. 1971. Diffusivity and solubility of hydrogen as a function of composition in Fe-Ni alloys. *Metallurgical Transactions* 2: 883-888.

Beech, I.B., C.C. Gaylarde, J.J. Smith, and G.G. Geesey. 1991. Exopolysaccharide from *Desulfovibrio desulfuricans* and *Pseudomonas fluorescens* in the presence of mild and stainless steel. *Applied Microbiology and Biotechnology* 35: 65–71.

Benbouzid-Rollet, N.D., J. Guezennec, M. Conte, and D. Prieur. 1991. Experimental biofilms containing sulphate-reducing and fermentative bacteria on stainless steel in a laboratory tubular flow-system. *Microbially Influenced Corrosion and Biodeterioration.* N.J.E. Dowling, M.W. Mittelman, and J.C. Danko, eds. Knoxville, TN: The University of Tennessee: 3–47 to 3–63.

Berkowitz, B.J., and R.D. Kane. 1980. The effect of impurity segregation on the hydrogen embrittlement of a high-strength nickel base alloy in H_2S environments. *Corrosion* 36: 24–29.

Bernhardsson, S., and R. Mellström. 1983. Performance of a highly alloyed stainless steel in marine environments. Paper No. 72. *Corrosion '83*. Houston, TX: National Association of Corrosion Engineers.

Bogaerts, W.F., and A.A. van Haute. 1985. Chloride pitting and water chemistry control in cooling or boiler circuits. *Corrosion Science* 25: 1,149–1,161.

Boopathy, R., and L. Daniel. 1991. Effect of pH on anaerobic mild steel corrosion by methanogenic bacteria. *Applied and Environmental Microbiology* 57: 2,104–2,108.

Booth, G.H. 1964. Sulfur bacteria in relation to corrosion. *Journal of Applied Bacteriology* 27: 174–181.

Booth, W. 1987. Postmortem on Three Mile Island. *Science* 238: 1,342–1,345.

Booth, G.H., and F. Wormwell. 1962. Corrosion of mild steel by sulfate-reducing bacteria. Effect of different strains of organisms. *Proceedings of First International Congress on Metallic Corrosion,* London, U.K.: Butterworths: 341–344.

Borenstein, S.W. 1991. Microbially influenced corrosion of austenitic stainless steel weldments. *Materials Performance* 30(1): 52–54.

Box, G.E.P., W.G. Hunter, and J.S. Hunter. 1978. *Statistics for Experimenters*. New York, NY: John Wiley & Sons.

Brennenstuhl, A.M., P.E. Doherty, P.J. King, and T.G. Dunstall. 1990. The effects of biofouling on the corrosion of nickel heat exchanger alloys at Ontario Hydro. *Microbially Influenced Corrosion and Biodeterioration.* N.J. Dowling, M.W. Mittelman, and J.C. Danko, eds. Knoxville, TN: The University of Tennessee: 4-25 to 4-31.

Briant, C.L. 1987. Grain boundary segregation of phosphorus and sulfur in types 304L and 316L stainless steel and its effect on intergranular corrosion in the Huey test. *Metallurgical Transactions* 18A: 691–699.

Brock, T.D. 1978. *Thermophilic Microorganisms and Life at High Temperatures.* New York, NY: Springer-Verlag.

Brookes, H.C., and F.J. Graham. 1989. Influence of the electrolyte and alloy composition on the pitting behavior of stainless steel alloys. *Corrosion* 45: 287–293.

Brown, M.H. 1969. The relationship of heat treatment to the corrosion resistance of stainless alloys. *Corrosion* 25: 438–443.

Bruemmer, S.M. 1990. Quantitative modeling of sensitization development in austenitic stainless steel. *Corrosion* 46: 698–709.

Buchanan, R.A., P. Li, X. Zhang, N.J.E. Dowling, E.E. Stansbury, J.C. Danko, and D.C. White. 1991. *Electrochemical Studies of Microbially Influenced Corrosion.* Project 2939-5. Final Report. Palo Alto, CA: Electric Power Research Institute.

Cavanaugh, M.A., J.A. Kargol, J. Nickerson, and N.F. Fiore. 1983. The anodic dissolution of a Ni-base superalloy. *Corrosion* 39: 144–150.

Chandrasekaran, P., and S.C. Dexter. 1993a. Mechanism of potential ennoblement on passive metals by seawater biofilms. Paper No. 493. *Corrosion/93*. Houston, TX: NACE International.

Chandrasekaran, P., and S.C. Dexter. 1993b. Factors contributing to ennoblement of passive metals due to seawater biofilms. Paper No. 479. *Proceedings of the 12th International Corrosion Congress.* Houston, TX: National Association of Corrosion Engineers.

Chen, J.S., V. Radmilovic, and T.M. Devine. 1990. A comparison of the chromium concentration on grain boundaries in sensitized stainless steel measured by analytical electron microscopy and an electrochemical technique. *Corrosion Science* 30: 477-494.

Cieslak, M.J., G.A. Knorovsky, T.J. Headley, and A.D. Romig. 1986b. The use of new PHACOMP in understanding the solidification microstructure of nickel base alloy weld metal. *Metallurgical Transactions* 17A: 2,107–2,116.

Cieslak, M.J., T.J. Headley, and A.D. Romig. 1986a. The welding metallurgy of Hastelloy alloys C-4, C-22, and C-276. *Metallurgical Transactions* 17A: 2,035–2,047.

Colasanti, R., D. Coutts, S.Y.R. Pugh, and A. Rosevear. 1989. *Microbiology and Radioactive Waste Disposal; Review of the Nirex Research Programme–January 1989.* United Kingdom Atomic Energy Administration Report NSS/R131. Oxfordshire, UK: Harwell Laboratory.

Coleman, H.W., and W.G. Steele, Jr. 1989. *Experimentation and Uncertainty Analysis for Engineers*. New York: John Wiley & Sons.

Costerton, J.W., and G.G. Geesey. 1986. Microbial ecology of surface colonization and consequent corrosion. *Biologically Induced Corrosion.* S.C. Dexter, ed. Houston, TX: National Association of Corrosion Engineers: 223–232.

Costerton, J.W., K.-J. Chen, G.G. Geesey, T.I. Ladd, J.C. Nickel, M. Dasgupta, and T.J. Marrie. 1987. Bacterial biofilms in nature and disease. *Annual Review of Microbiology* 41: 435–464.

Costerton, J.W., Z. Lewandowski, D. DeBeer, D. Caldwell, D. Korber, and G. James. 1994. Biofilms, the customized microniche. *Journal of Bacteriology* 176: 2,137–2,142.

Cottis, R.A., K.R. Gowers, M. Haji-Ghassemi, and E.A. Taqi. 1986. The application of hydrogen permeation measurements to the study of corrosion fatigue crack growth in steels. *Electrochemical Methods in Corrosion Research.* M. Duprat, ed. Materials Science Forum. Aedermannsdorf, Switzerland: Trans Tech Publications Ltd.: 8: 243–252.

Cowan II, R.L., and C.S. Tedmon Jr. 1973. Intergranular corrosion of iron-nickel-chromium alloys. M.G. Fontana and R.W. Staehle, eds. *Advances in Corrosion Science and Technology.* New York, NY: Plenum Press: 3: 293-400.

Coyle, R.J., A. Atrens, N.F. Fiore, J.J. Bellina, and M. Jolles. 1977. Effect of metallurgical variables on hydrogen solubility in high alloys. *Environment Sensitive Fracture of Engineering Materials.* Z.A. Foroulis, ed. Warrendale, PA: The Metallurgical Society of AIME: 431–439.

Cragnolino, G., and N. Sridhar. 1991a. *A Review of Localized Corrosion of High-Level Nuclear Waste Container Materials—I.* CNWRA 91-004. San Antonio, TX: Center for Nuclear Waste Regulatory Analyses.

Cragnolino, G.A., and N. Sridhar. 1991b. Integrated waste package experiments. *Report on Research Activities for Calendar Year 1990.* W.C. Patrick, ed. NUREG/CR-5817, CNWRA 91-01A. Washington, DC: Nuclear Regulatory Commission.

Cragnolino, G., and N. Sridhar. 1991c. Localized corrosion of a candidate container material for high-level nuclear waste disposal. *Corrosion* 47: 464–472.

Cragnolino, G., and N. Sridhar. 1991d. Integrated waste package experiments. *Report on Research Activities for the Quarter January 1 through March 31, 1991.* W.C. Patrick, ed. CNWRA 91-01Q. San Antonio, TX: Center for Nuclear Waste Regulatory Analyses.

Cragnolino, G.A., and N. Sridhar. 1992a. *A Review of Stress Corrosion Cracking of High-Level Nuclear Waste Container Materials—I.* CNWRA 92-021. San Antonio, TX: Center for Nuclear Waste Regulatory Analyses.

Cragnolino, G.A., and N. Sridhar. 1992b. Integrated waste package experiments. *Report on Research Activities for Calendar Year 1991.* W.C. Patrick, ed. NUREG/CR-5817. Vol. 2. CNWRA 91-01A. San Antonio, TX: Center for Nuclear Waste Regulatory Analyses.

Cragnolino, G., and N. Sridhar. 1993a. *Long-Term Stability of High-Level Nuclear Waste Container Materials I—Thermal Stability of Alloy 825.* CNWRA 93-003. San Antonio, TX: Center for Nuclear Waste Regulatory Analyses.

Cragnolino, G.A., and N. Sridhar. 1993b. Integrated waste package experiments. *NRC High-Level Radioactive Waste Research at CNWRA, January–June 1992.* W.C. Patrick, ed. CNWRA 92-01S, NUREG/CR-5817, Vol. 3, No. 1. San Antonio, TX: Center for Nuclear Waste Regulatory Analyses.

Cragnolino, G.A., D. Dunn, and N. Sridhar. 1994a. *Environmental Effects on Stress Corrosion Cracking of Type 316L Stainless Steel and Alloy 825 as High-Level Nuclear Waste Container Materials.* CNWRA 94-028. San Antonio, TX: Center for Nuclear Waste Regulatory Analyses.

Cragnolino, G.A., N. Sridhar, and D. Dunn. 1994b. Integrated waste package experiments. *NRC High-Level Radioactive Waste Research at CNWRA, January 1 Through June 30, 1994.* B. Sagar, ed. CNWRA 94-01S. San Antonio, TX: Center for Nuclear Waste Regulatory Analyses.

Cragnolino, G.A., D. Dunn, and N. Sridhar. 1995. Environmental factors in the stress corrosion cracking of type 316L stainless steel and alloy 825 in chloride solutions. Accepted for publication in *Corrosion.*

Crolet, J.L., L. Séraphin, and R. Tricot. 1976. Influence de la teneur en chlorure sur le pH de dépassivation des aciers inoxydables. *Mémoires Scientifiques Revue Métallurgie* 73(1): 1–8.

Daniel, L., N. Belay, B.S. Rajagopal, and P.J. Weimer. 1987. Bacterial methanogenesis and growth from CO_2 with elemental iron as the sole source of electrons. *Science* 237: 509–511.

Dexter, S.C., and G.Y. Gao. 1988. Effect of seawater biofilms on corrosion potential and oxygen reduction of stainless steel. *Corrosion* 44: 717–723.

Dexter, S.C., K.E. Lucas, and G.Y. Gao. 1986. The role of marine bacteria in crevice corrosion initiation. *Biologically Induced Corrosion.* S.C. Dexter, ed. Houston, TX: National Association of Corrosion Engineers: 144–153.

Dexter, S.C., and G.Y. Gao. 1988. Effect of seawater biofilms on corrosion potential and oxygen reduction of stainless steel. *Corrosion* 44: 717–723.

Dickinson, W., and Z. Lewandowski. 1995. Electrochemical and microelectrode studies of stainless steel ennoblement. Paper No. 223. *Corrosion/95.* Houston, TX: NACE International.

Dowling, N.J.E., J. Guezennec, J. Bullen, B.J. Little, and D.C. White. 1992. Effect of photosynthetic biofilms on open-circuit potential of stainless steel. *Biofouling* 5: 315–322.

Dowling, N.J.E., A.A. Brooks, T.J. Phelps, and D.C. White. 1992. Effects of selection and fate of substrates applied to anaerobic bacteria in the corrosion of pipeline steel. *Journal of Industrial Microbiology* 10: 207–215.

Duffo, G.S., I.A. Maier, and J.R. Galvele. 1988. The influence of temperature on the susceptibility of type 304 stainless steel to intergranular and transgranular stress corrosion cracking in LiCl solutions. *Corrosion Science* 28: 1,003–1,018.

Dunn, D.S., N. Sridhar, and G.A. Cragnolino. 1993a. The effect of surface conditions on the localized corrosion of a candidate high-level waste container material. *Proceedings of the 12th International Corrosion Congress.* Houston, TX: NACE International: 5B: 4,021–4,028.

Dunn, D.S., N. Sridhar, and G.A. Cragnolino. 1993b. Effects of surface conditions on the localized corrosion of alloy 825 high-level waste container material. Paper No. 94-138. *Corrosion/94.* Houston, TX: NACE International.

Dunn, D.S., N. Sridhar, and G.A. Cragnolino. 1995a. Integrated waste package experiments. *NRC High-Level Radioactive Waste Research at CNWRA, July–December 1994.* B. Sagar, ed. CNWRA 94-02S. San Antonio, TX: Center for Nuclear Waste Regulatory Analyses.

Dunn, D.S., N. Sridhar, and G.A. Cragnolino. 1995b. Effects of surface chromium depletion on the localized corrosion of alloy 825 as a high-level nuclear waste container material. Accepted for publication in *Corrosion.*

Duquette, D.J., and R.E. Ricker. 1986. Electrochemical aspects of microbially influenced corrosion. *Biologically Induced Corrosion.* S.C. Dexter, ed. Houston, TX: National Association of Corrosion Engineers: 121–130.

Efird, K.D. 1985. Failure of Monel Ni-Cu-Al Alloy K-500 bolts in seawater. *Materials Performance* 25(4): 37–40.

Ehrlich, H.L. 1981. *Geomicrobiology.* New York, NY: Marcel Dekker.

Erlings, J.G., H.W. deGroot, and J.F.M. van Roy. 1986. Stress corrosion cracking and hydrogen embrittlement of high-strength nonmagnetic alloys in brines. *Materials Performance*: 26(10): 28–34.

Esteban, J.M., G.S. Hickey, and M.E. Orazem. 1990. The impinging jet electrode: Measurement of the hydrodynamic constant and its use for evaluating film persistency. *Corrosion* 46: 896–901.

Fan, F.F., and A.J. Bard. 1989. *In situ* scanning tunneling microscopy study of corrosion of type 304L stainless steel in aqueous media. *Journal of the Electrochemical Society* 136: 166–170.

Farmer, J.C., R.A. van Konynenburg, R.D. McCright, and D.B. Bullen. 1988a. *Survey of Degradation Modes of Candidate Materials for High-Level Radioactive Waste Disposal Containers. Volume 3, Localized Corrosion and Stress Corrosion Cracking of Austenitic Alloys.* UCID–21362, Vol. 3. Livermore, CA: Lawrence Livermore National Laboratory.

Farmer, J.C., R.A. van Konynenburg, R.D. McCright, and G.E. Gdowski. 1988b. *Survey of Degradation Modes of Candidate Materials for High-Level Radioactive-Waste Disposal Containers. Volume 4, Stress Corrosion Cracking of Copper-Based Alloys.* UCID–21362, Vol. 4. Livermore, CA: Lawrence Livermore National Laboratory.

Farmer, J.C., R.A. van Konynenburg, R.D. McCright, and G.E. Gdowski. 1988c. *Survey of Degradation Modes of Candidate Materials for High-Level Radioactive-Waste Disposal. Volume 5, Localized Corrosion of Copper-Based Alloys.* UCID-21362, Vol. 5. Livermore, CA: Lawrence Livermore National Laboratory.

Feron, D. 1991. Chemical and electrochemical aspects of the corrosion of stainless steels in the presence of sulphate-reducing bacteria. *Microbially Influenced Corrosion and Biodeterioration.* N.J.E. Dowling, M.W. Mittelman, and J.C. Danko, eds. Knoxville, TN: The University of Tennessee: 5–73 to 5–83.

Ford, T.E., and R. Mitchell. 1989. Hydrogen embrittlement: A microbiological perspective. *Corrosion '89.* Paper No. 189. Houston, TX: National Association of Corrosion Engineers.

Ford, T., and R. Mitchell. 1990b. The ecology of microbial corrosion. *Advances in Microbial Ecology* 11: 231–262.

Ford, T., and R. Mitchell. 1990a. Metal embrittlement by bacterial hydrogen—An overview. *Marine Technology Society Journal* 24(3): 29–35.

Franklin, M.J., D.C. White, and H.S. Isaacs. 1991. Effect of bacterial biofilms on carbon steel pit propagation in phosphate containing medium. *Microbially Influenced Corrosion and Biodeterioration.* N.J.E. Dowling, M.W. Mittelman, and J.C. Danko, eds. Knoxville, TN: The University of Tennessee: 3–35 to 3–46.

Fujimoto, S., T. Shibata, M. Minamida, and S. Udaka. 1994. A statistical evaluation of crevice corrosion on type 304 stainless steel. *Corrosion Science* 36: 1575–1583.

Fukuda, T., and M. Akashi. 1992. The effect of chloride concentration for the crevice corrosion initiation of c.p.- titanium used for nuclear waste package. *Proceedings of the Annual Corrosion Conference. Corrosion '92.* Paper No. 92. Houston, TX: National Association of Corrosion Engineers.

Galvele, J.R. 1981. Transport processes in passivity breakdown—II. Full hydrolysis of the metal ions. *Corrosion Science* 21: 551-579.

Garner, A. 1982. Corrosion of high alloy austenitic stainless steel weldments in oxidizing environments. *Materials Performance* 21(8): 9-14.

Gaudet, G.T., W.T. Mo, T.A. Hatton, J.W. Tester, J. Tilly, H.S. Isaacs, and R.C. Newman. 1986. Mass transfer and electrochemical kinetic interactions in localized pitting corrosion. *AIChE Journal* 32: 949–958.

Gdowski, G. 1991. *Survey of Degradation Modes of Four Nickel-Chromium-Molybdenum Alloys.* UCRL-ID-108330. Livermore, CA: Lawrence Livermore National Laboratory.

Gdowski, G.E., and D.B. Bullen. 1988. *Survey of Degradation Modes of Candidate Materials for High-Level Radioactive Waste Disposal Containers. Volume 6. Effects of Hydrogen in Austenitic and Copper-Based Materials.* UCID-21362, Volume 6. Livermore, CA: Lawrence Livermore National Laboratory.

Geesey, G. 1993. *A Review of the Potential for Microbially Influenced Corrosion of High-Level Nuclear Waste Containers.* G.A. Cragnolino, ed. CNWRA 93-014. San Antonio, TX: Center for Nuclear Waste Regulatory Analyses.

Geesey, G., and G.A. Cragnolino. 1995. A review of the potential for microbially influenced corrosion of high-level nuclear waste containers in an unsaturated repository site. Paper No. 76. *1995 International Conference on Microbially Influenced.* Houston, TX: NACE International.

Glass, R.S., G.E. Overturf, R.E. Garrison, and R.D. McCright. 1984. *Electrochemical Determination of the Corrosion Behavior of Candidate Alloys Proposed for Containment of High-Level Nuclear Waste in Tuff.* UCID-20174. Livermore, CA: Lawrence Livermore National Laboratory.

Glass, R.S., G.E. Overturf, R.A. van Konynenburg, and R.D. McCright. 1986. Gamma radiation effects on corrosion—I. Electrochemical mechanisms for the aqueous corrosion processes of austenitic stainless steels relevant to nuclear waste disposal in tuff. *Corrosion Science* 26: 577–590.

Glassley, W.E. 1989. Evaluation of the post-emplacement environment of high level radioactive waste packages at Yucca Mountain, Nevada. *Waste Management '89*. R.G. Post, ed. Tucson, AZ: Arizona Board of Regents: 1: 477–483.

Goldstein, J.L., and D.B. Williams. 1981. X-ray microanalysis of thin specimens. *Quantitative Microanalysis with High Spatial Resolution.* G.W. Lorimer et al., eds. London, U.K.: The Metals Society: 5-14.

Goodhew, P.J. 1984. Specimen preparation for transmission electron microscopy. *Royal Microscopical Society Handbook No. 3.* Oxford, U.K.: Oxford University Press.

Gouda, V.K., I.M. Banat, W.T. Riad, S. Mansour. 1993. Microbially induced corrosion of UNS NO4400 in seawater. *Corrosion* 49: 63-73.

Gray, W.J. 1987. Effects of radiation on the oxidation potential of salt brine. *Scientific Basis for Nuclear Waste Management XI.* M.J. Apted and R.E. Westerman, eds. Pittsburgh, PA: Materials Research Society: 112: 405–413.

Hack, H.P., and J.R. Scully. 1986. Galvanic corrosion prediction using long- and short-term polarization curves. *Corrosion* 42: 79–90.

Hack, H.P. 1982. Crevice corrosion behavior of 45 molybdenum-containing stainless steels in seawater. Paper No. 65. *Corrosion '82*. Houston, TX: National Association of Corrosion Engineers.

Hakkarainen, T. 1990. Electrochemical conditions inside growing pits in stainless steel. *Advances in Localized Corrosion.* H. Isaacs et al., eds. Houston, TX: National Association of Corrosion Engineers: 277-282.

Hall, E.L., and C.L. Briant. 1984. Chromium depletion in the vicinity of carbides in sensitized austenitic stainless steels. *Metallurgical Transactions* 15A: 793–811.

Hamilton, W.A. 1985. Sulfate-reducing bacteria and anaerobic corrosion. *Annual Review of Microbiology* 39: 195–217.

Hamilton, W.A. 1990. Sulfate-reducing bacteria and their role in corrosion. *Biofouling and Biocorrosion in Industrial Water Systems.* H.C. Flemming and G.G. Geesey, eds. Berlin: Springer–Verlag: 187–193.

Hersman, L.E. 1987. *Biodegradation of Drilling Fluids: Effects on Water Chemistry.* Nevada Nuclear Waste Storage Investigation Milestone Report. Los Alamos, NM: Los Alamos National Laboratory.

Hicks, P.D., and C.J. Alstetter. 1992. Hydrogen-enhanced cracking of superalloys. *Metallurgical Transactions* 23A: 237–249.

Hillert, M., and C. Qui. 1991. A thermodynamic assessment of the Fe-Ni-Cr-C system. *Metallurgical Transactions* 22A: 2,187-2,198.

Ibars, J.R., D.A. Moreno, and C. Ranninger. 1992. Microbially influenced corrosion of stainless steels—A technical review on the influence of microstructure. *International Biodeterioration and Biodegradation* 29: 343–355.

International Organization for Standardization. 1989. *Corrosion of Metals and Alloys—Stress Corrosion Testing. Part 7: Slow Strain Rate Testing.* ISO7539-7:1989E. Geneva, Switzerland: International Organization for Standardization.

Iverson, W.P. 1987. Microbial corrosion of metals. *Advances in Applied Microbiology* 32: 1–36.

Iyer, R.N., H.W. Pickering, and M. Zamanzadeh. 1989. Analysis of hydrogen evolution and entry into metals for the discharge-recombination process. *Journal of the Electrochemical Society* 136: 2,463–2,470.

Iyer, R.N., and H.W. Pickering. 1990. Current developments in modeling and characterizing electrochemically influenced hydrogen evolution and entry into metals. *Hydrogen Effects on Materials Behavior.* N.R. Moody and A.W. Thompson, eds. Pittsburgh, PA: The Minerals, Metals, and Materials Society: 195–209.

Johnson, R., and E. Bardal. 1985. Cathodic properties of different stainless steels in natural seawater. *Corrosion* 41: 296–302.

Jones, R.H., S.M. Bruemmer, M.T. Thomas, and R.D. Baer. 1980. Grain-boundary chemistry, fracture mode and ductility comparisons for iron, nickel tested at cathodic potentials. *Hydrogen Effects in Metals.* I.M. Bernstein and A.W. Thompson, eds. Pittsburgh, PA: The Materials Society: 369.

Kain, R.M. 1993. Seawater testing to assess the crevice corrosion resistance of stainless steels and related alloys. *Proceedings of the 12th International Corrosion Congress* Houston, TX: NACE International: 3B: 1,889–1,900.

Kane, R.D. 1985. Role of H_2S in behavior of engineering alloys. *International Metals Reviews* 30: 291–301.

Kane, R.D. 1978. Accelerated Hydrogen Charging of Ni-base and Co-base alloys. *Corrosion* 34: 442–445.

Kargol, J.A., and B. Ladna. 1982. The roles of ordering and impurity segregation on the hydrogen assisted crack propagation in nickel base alloys. *Scripta Metallurgica* 16: 191–195.

Kearns, J.R., and S.W. Borenstein. 1991. MIC testing of welded stainless alloys for nuclear plant service water systems. *Corrosion '91*. Paper No. 279. Houston, TX: National Association of Corrosion Engineers.

Kerrisk, J.F. 1987. *Groundwater Chemistry at Yucca Mountain, Nevada, and Vicinity*. LA-10929-MS. Los Alamos, NM: Los Alamos National Laboratory.

Kesavan, S. 1991. *The Kinetics of Hydrogen Evolution and Absorption on High-Nickel Alloys at Elevated Temperatures*. Ph.D. Dissertation. Columbus, OH: The Ohio State University.

Kim, Y.J., and R.A. Oriani. 1987a. Corrosion properties of the oxide film formed on grade 12 titanium in brine under gamma radiation. *Corrosion* 43: 85–91.

Kim, Y.J., and R.A. Oriani. 1987b. Brine radiolysis and its effect on the corrosion of grade 12 titanium. *Corrosion* 43: 92–97.

King, F., Y. Tang, M.J. Quinn, and C.D. Litke. 1995. The effects of dissolved oxygen concentration and mass-transport conditions on the dissolution behaviour of copper nuclear waste containers. Paper No. 424. *Corrosion '95*. Houston, TX: National Association of Corrosion Engineers.

Klein, P.A., R.A. Hays, and R.J. Ferrara. 1991. The effect of electrolytic chlorination on the crevice corrosion behavior of 70/30 copper-nickel and nickel-copper alloy 400. Paper No. 509. *Corrosion '91*. Houston, TX: National Association of Corrosion Engineers.

Knauss, K.G., W.J. Beiriger, and D.W. Peifer. 1985. *Hydrothermal Interaction of Crushed Topopah Spring Tuff and J-13 Water at 90, 150, and 250°C Using Dickson-Type, Gold-bag Rocking Autoclaves*. UCRL-53630. Livermore, CA: Lawrence Livermore National Laboratory.

Knauss, K.G., T.J. Wolery, and K.J. Jackson. 1990. A new approach to measuring pH in brines and other concentrated electrolytes. *Geochimica et Cosmochimica Acta* 54: 1,519–1,523.

Kosaki, A., and H. Komada. 1991. Corrosion life-time assessment of carbon steel and stainless alloys for geological disposal facility. *Proceedings of the Fourth Annual International High-Level Radioactive Waste Management Conference*. La Grange Park, IL: American Nuclear Society 1: 1,754–1,760.

Laliberté, L.H., and A. Garner. 1981. Corrosion protection of bleach plant washers by electrochemical potential control. *Tappi, The Journal of the Technical Association of Pulp and Paper Industry* 64(1): 47–51.

Latanision, R.M., and H. Opperhauser. 1975. The intergranular embrittlement of Ni by hydrogen: Effect of grain boundary segregation. *Metallurgical Transactions* 5A: 483–493.

Leckie, H.P., and H.H. Uhlig. 1966. Environmental factors affecting the critical potential for pitting in 18-8 stainless steel. *Journal of the Electrochemical Society* 113: 1,262–1,267.

Licina, G.J. 1988. A review of microbially influenced corrosion in nuclear power plant systems. Paper No. 268. *Corrosion '88*. Houston, TX: National Association of Corrosion Engineers. Paper No. 268.

Linke, W.F. 1965. *Solubilities: Inorganic and Metal Organic Compounds*. Washington, DC: American Chemical Society: 959.

Little, B.J., and F. Mansfeld. 1991. The corrosion behavior of stainless steels and copper alloys exposed to natural seawater. *Werkstoffe und Korrosion* 42: 331–340.

Little, B.J., S.M. Gerchakov, and L. Udey. 1987a. A method for sterilization of natural seawater. *Journal of Microbial Methods* 7: 193–200.

Little, B.J., P. Wagner, and D. Duquette. 1987b. Microbiologically induced cathodic depolarization. Paper No. 370. *Corrosion '87*. Houston, TX: National Association of Corrosion Engineers.

Little, B.J., P. Wagner, R. Ray, and M. McNeil. 1990. Microbiologically influenced corrosion in copper and nickel seawater piping systems. *Marine Technology Society Journal* 24(3): 10–17.

Little, B.J., R. Ray, P. Wagner, Z. Lewandowski, W.C. Lee, and W.G. Characklis. 1991. Impact of biofouling on the electrochemical behaviour of 304 stainless steel in natural seawater. *Biofouling* 3: 45–59.

Lott, S.E., and R.C. Alkire. 1989. The role of inclusions on initiation of crevice corrosion of stainless steel. I. Experimental studies. *Journal of the Electrochemical Society* 136: 973–979.

Lukezich, S.J. 1989. *The Corrosion Behavior of Ni-Base High Performance Alloys in Simulated Repository Environments*. M.S. Thesis. Columbus, OH: The Ohio State University.

Luo, J.L., Y.C. Lu, and M.B. Ives. 1992. Use of microelectrodes to determine local conditions within active pits. *Materials Performance* 31(10): 44–47.

Maiya, P.S. 1989. *A Review of Degradation Behavior of Container Materials for Disposal of High-Level Nuclear Waste in Tuff and Alternative Repository Environments*. ANL-89/14. Argonne, IL: Argonne National Laboratory.

Maiya, P.S., W.J. Shack, and T.F. Kassner. 1990. Stress corrosion cracking of candidate material for nuclear waste containers. *Corrosion* 46: 954–963.

Manfredi, C., I.A. Maier, and J.R. Galvele. 1987. The susceptibility of AISI type 304 stainless steel to transgranular and intergranular SCC in 40% $MgCl_2$ solution at 100 °C. *Corrosion Science* 27: 887–903.

Mansfeld, F., and J.V. Kenkel. 1975. Laboratory studies of galvanic corrosion—I. Two-metal couples. *Corrosion* 31: 298–302.

Mansfeld, F., and B.J. Little. 1991. A technical review of electrochemical techniques applied to microbiologically influenced corrosion. *Corrosion Science* 32: 247–272.

Mansfeld, F., R. Tsai, H. Shih, B.J. Little, R. Ray, and P. Wagner. 1992. An electrochemical and surface analytical study of stainless steels and titanium exposed to natural seawater. *Corrosion Science* 33: 445–456.

Marcus, Y. 1989. Determination of pH in highly saline waters. *Pure and Applied Chemistry* 61: 1,133-1,138.

Mason, R.L., R.F. Gunst, and J.L. Hess. 1989. *Statistical Design and Analysis of Experiments.* New York, NY: John Wiley & Sons.

McBreen, J., L. Nanis, and W. Beck. 1966. A method for determination of the permeation rate of hydrogen through metal membranes. *Journal of the Electrochemical Society* 113: 1,218–1,222.

McCright, R.D. 1977. Effects of environmental species and metallurgical structure on the hydrogen entry into steel. *Stress Corrosion Cracking and Hydrogen Embrittlement of Iron-base Alloys.* R.W. Staehle, J. Hochmann, R.D. McCright, and J.E. Slater, eds. Houston, TX: National Association of Corrosion Engineers: 306–325.

McCright, R.D. 1988. *An Annotated History of Container Candidate Material Selection.* UCID-21472. Livermore, CA: Lawrence Livermore National Laboratory.

McCright, R.D. 1990. Container materials for high-level nuclear waste proposed Yucca Mountain site. *Scientific Basis for Nuclear Waste Management XIV.* T.A. Abrajano, Jr., and L.H. Johnson, eds. Pittsburgh, PA: Materials Research Society. 212: 249–260.

McKinley, I.G., J.M. West, and H.A. Grogan. 1985. *An Analytical Overview of the Consequence of Microbial Activity in a Swiss HLW Repository.* Report EIR-Bericht No. 562. Switzerland. NAGRA NTB 85-43.

Mezzanotte, D.A., J.A. Kargol, and N.F. Fiore. 1980. Hydrogen transport in a Ni-base superalloy. *Scripta Metallurgica* 14: 219–223.

Miller, R.L., J.H. Wolfram, and A.L. Ayers. 1988. *Studies of Microbially Influenced Corrosion on TMI Canister.* Department of Energy Report No. EG&G MS T 7744. U.S. Department of Energy: Washington, DC.

Miller, J.D.A., and A.K. Tiller. 1970. Corrosion in industrial situations by mixed microbial flora. *Microbial Aspect of Metallurgy.* J.D.A. Miller, ed. New York: Elsevier: 107–128.

Miller, C.T. 1990. *Electrochemical Studies of Hydrogen Diffusion and Evolution on Copper Alloys.* M.S. Thesis. Columbus, OH: The Ohio State University.

Mollica, A., and A. Travis. 1976. The influence of microbiological film on stainless steels in natural seawater. *Proceedings of 4th International Congress on Marine Corrosion and Fouling*. Boulogne, France. Centre de Recherches et d'Etudes Oceanographique: 351–365.

Mollica, A., A. Travis, E. Traverso, G. Ventura, V. Scotto, G. Alabiso, G. Marcenaro, V. Montini, G. de Carolis, and R. Dellepiane. 1984. Interaction between biofouling and oxygen reduction rate on stainless steel in seawater. *Proceedings of 6th International Congress on Marine Corrosion and Fouling*. Athens, Greece: 269–281.

Mollica, A., G. Ventura, E. Traverso, and V. Scotto. 1987. Cathodic behaviour of nickel and titanium in natural seawater. *Seventh International Biodeterioration Symposium*. Cambridge, U.K.

Mollica, A., A. Travis, E. Traverso, G. Ventura, G. de Carolis, and R. Dellepiane. 1989. Cathodic performance of stainless steels in natural seawater as a function of microorganism settlement and temperature. *Corrosion* 45: 48–56.

Mollica, A., G. Ventura, and E. Traverso. 1990. On the mechanism of corrosion induced by biofilm growth on the active-passive alloys in seawater. *Microbially Influenced Corrosion and Biodeterioration*. N.J. Dowling, M.W. Mittelman, and J.C Danko, eds. Knoxville, TN: The University of Tennessee: 2-25 to 2-31.

Moreno, D.A., J.R. Ibars, C. Ranninger, and H.A. Videla. 1992. Use of potentiodynamic polarization to assess pitting of stainless steels by sulfate-reducing bacteria. *Corrosion* 48: 226–229.

Motoda, S., Y. Suzuki, T. Shinohara, and S. Tsujikawa. 1990. The effect of marine fouling on the ennoblement of electrode potential for stainless steels. *Corrosion Science* 31: 515–520.

Mulford, R.A., E.L. Hall, and C.L. Briant. 1983. Sensitization of austenitic stainless steels II. Commercial purity alloys. *Corrosion* 39: 132–143.

Nakayama, T., and K. Sasa. 1976. Effect of ultrasonic waves on the pitting potentials of 18-8 stainless steel in sodium chloride solution. *Corrosion* 32:283-285.

Nakayama, G., and M. Akashi. 1991. The critical condition for initiation of localized corrosion of mild steel used for nuclear waste package. *Scientific Basis for Nuclear Waste Management XIV*. T. Abrajano and L.H. Johnson, eds. Pittsburgh, PA: Materials Research Society: 212: 279–286.

Nakayama, G., H. Wakamatsu, and M. Akashi. 1993. Effects of chloride, bromide, and thiosulfate ions on the critical conditions for crevice corrosion of several stainless alloys as a material of geological disposal package for nuclear wastes. *Scientific Basis for Nuclear Waste Management XVI*. C.G. Interrante and R.T. Pabalan, eds. Pittsburgh, PA: Materials Research Society. 294: 323–328.

Natesan, K., and T.F. Kassner. 1973. Thermodynamics of carbon in nickel, iron-nickel and iron-chromium-nickel alloys. *Metallurgical Transactions* 4: 2,557–2,787.

Newman, R.C., and E.M. Franz. 1984. Growth and repassivation of single corrosion pits in stainless steel. *Corrosion* 40: 325–330.

Newman, R.C., H.S. Isaacs, and B. Alman. 1982. Effects of sulfur compounds on the pitting behavior of type 304 stainless steel in near-neutral chloride solutions. *Corrosion* 38: 261–265.

Newman, R.C., W.P. Wong, H. Ezuber, and A. Garner. 1989. Pitting of stainless steels by thiosulfate ions. *Corrosion* 45: 282–287.

Newman, R.C., B.J. Webster, and R.G. Kelly. 1991. The electrochemistry of SRB corrosion and related inorganic phenomena. *ISIJ International* 31(2): 201–209.

Nielsen, P.H., W. Lee, Z. Lewandowski, M. Morison, and W.G. Characklis. 1993. Corrosion of mild steel in an alternating oxic and anoxic biofilm system. *Biofouling* 7: 267–284.

Nivens, D.E., P.D. Nichols, J.M. Henson, G.G. Geesey, and D.C. White. 1986. Reversible acceleration of the corrosion of 304 stainless steel exposed to seawater induced by growth and secretions of *Vibrio natriegens*. *Corrosion* 42: 204–210.

Obuekwe, C.O., D.W.S. Westlake, J.A. Plambeck, and F.D. Cook. 1981a. Corrosion of mild steel in cultures of ferric iron reducing bacterium isolated from crude oil. I. Polarization characteristics. *Corrosion* 37: 461–467.

Obuekwe, C.O., D.W.S. Westlake, J.A. Plambeck, and F.D. Cook. 1981b. Corrosion of mild steel in cultures of ferric iron reducing bacterium isolated from crude oil. II. Mechanisms of anodic depolarization. *Corrosion* 37: 632–637.

Obuekwe, C.O., D.W.S. Westlake, J.A. Plambeck, and J.W. Costerton. 1981c. Surface changes in mild steel coupons from the action of corrosion-causing bacteria. *Applied and Environmental Microbiology* 41: 766–774.

Ohnaka, N., and Y. Furutani. 1990. Electrochemical investigation of hydrogen absorption of type 304 stainless steel in 0.05 M Na_2SO_4 solutions of different pH at 95 °C. *Corrosion* 46: 129–135.

Okada, H., Y. Hosio, and S. Abe. 1971. Scanning electron microscopic observations of fracture surfaces of austenitic stainless steels in stress corrosion cracking. *Corrosion* 27: 424–428.

Okada, T. 1984. Considerations of the stability of pit repassivation during pitting corrosion of passive metals. *Journal of the Electrochemical Society* 131: 1,026–1,032.

Okayama, S., Y. Uesugi, and S. Tsujikawa. 1987a. The effect of alloying elements on the repassivation potential for crevice corrosion of stainless steels in 3% NaCl solution. *Corrosion Engineering* 36: 157–168.

Okayama, S., S. Tsujikawa, and K. Kikuchi. 1987b. The effects of alloying elements on stainless steel depassivation pH. *Corrosion Engineering* 36: 631–638.

Oldfield, J.W., and W.H. Sutton. 1978a. Crevice corrosion of stainless steels—I. A mathematical model. *British Corrosion Journal* 13: 13-22.

Oldfield, J.W., and W.H. Sutton. 1978b. Crevice corrosion of stainless steels—II. Experimental studies. *British Corrosion Journal* 13: 104–111.

Oversby, V.M. 1985. *The Reaction of Topopah Spring Tuff with J-13 Water at 150°C—Samples from Drill Cores USW G-1, USW GU-3, USW G-4, and UE-25h#1*. UCRL-53629. Livermore, CA: Lawrence Livermore National Laboratories.

Pabalan, R.T., W.M. Murphy, and P. Bertetti. 1990. Unsaturated mass transport (Geochemistry). *Report on Research Activities for the Quarter July 1 Through September 30, 1990*. CNWRA 90-03Q. San Antonio, TX: Center for Nuclear Waste Regulatory Analyses.

Pabalan, R.T., and W. Murphy. 1991. Geochemical modeling. *Report on Research Activities for Calendar Year 1990*. W.C. Patrick, ed. NUREG/CR-5817. Washington, DC: Nuclear Regulatory Commission: 2–24 to 2–25.

Pan, Y.-M., N. Sridhar, D.S. Dunn, and G.A. Cragnolino. 1995. Effect of specimen preparation procedures on chromium depletion and precipitation chemistry in alloy 825 by analytical electron microscopy. *Journal of Materials Science Letters*. Submitted for publication.

Park, J.Y., W.J. Shack, and R.D. Diercks. 1991. Crack-growth testing of candidate waste-container materials. *Proceedings of the Topical Meeting on Nuclear Waste Packaging. FOCUS '91*. La Grange Park, IL: American Nuclear Society: 163–169.

Park, J.Y., P.S. Maiya, W.K. Soppet, D.R. Diercks, W.J. Shack, and T.F. Kassner. 1992. *Stress Corrosion Cracking of Candidate Waste Container Materials—Final Report*. ANL-92/28. Argonne, IL: Argonne National Laboratory.

Park, J.Y., W.J. Shack, and R.D. Diercks. 1994. Crack-growth behavior of candidate waste-container materials in simulated underground water. *Application of Accelerated Corrosion Tests to Crevice Life Prediction of Materials*. ASTM STP 1194. G. Cragnolino and N. Sridhar, eds. Philadelphia, PA: American Society for Testing and Materials: 188–203.

Park, J.M., W.S. Ryu, and Y.H. Kang. 1994. DSC study on carbide precipitation on reaction on Inconel 600. *Journal of Nuclear Materials* 209: 221–225.

Patrick, W.C. 1986. *Spent Fuel Test—Climax: An Evaluation of the Technical Feasibility of Geologic Storage of Spent Nuclear Fuel in Granite—Final Report*. UCRL-53702. Livermore, CA: Lawrence Livermore National Laboratory.

Pednekar, S., and S. Smialowska. 1980. The effect of prior cold work on the degree of sensitization in type 304 stainless steel. *Corrosion* 36: 565–577.

Petersen, T.A., and S.R. Taylor. 1995. The effects of sulphate reducing bacteria on stainless steel and Ni-Cr-Mo alloy weldments. Paper No. 56. *1995 International Conference on Microbially Influenced Corrosion.* Houston, TX: NACE International.

Philip, J.C., and K.J. Taylor. 1987. *The Effect of Sulfate Reducing Bacteria on the Corrosion of Mild Steel Embedded in Bentonite Graphitic Groundwater Paste.* Report AERE R12388. United Kingdom Atomic Energy Administration (UKAEA) Report 12388. Report DOE/RW/86/090. U.K. Department of Environment. Oxfordshire, U.K.: Harwell Laboratory.

Pope, D.H., D.J. Duquette, A.H. Johannes, and P.C. Wayner. 1984. Microbial influenced corrosion of industrial alloys. *Materials Performance* 23(4): 14–18.

Postgate, J.R. 1979. *The Sulphate-Reducing Bacteria.* Cambridge, England: Cambridge University Press: 81.

Postlethwaite, J., R.J. Scoular, and M.H. Dobbin. 1988. Localized corrosion of molybdenum-bearing nickel alloys in chloride solutions. *Corrosion* 44: 199–203.

Pourbaix, M., L. Klimzack-Mathieiu, Ch. Mertens, J. Meunier, Cl. Vanleugen-Haghe, L. de Munck, J. Laureys, L. Neelemans, and M. Warzee. 1963. Potentiokinetic and corrosimetric investigations of the corrosion behaviour of alloy steels. *Corrosion Science* 3: 239–259.

Price, C.E., and R.N. King. 1985. The embrittlement of Monel 400 by hydrogen and mercury as a function of temperature. *Corrosion Cracking.* V.S. Goel, ed. Materials Park, OH: ASM International: 81–88.

Pruthi, D.D., M.S. Anand, and R.P. Agarwala. 1977. Diffusion of chromium in Inconel 600. *Journal of Nuclear Materials* 64: 206–210.

Pugh, S.Y.R., R.L. Colasanti, and D.A.P. Coutts. 1989. Should we landfill waste? The biotechnology implications. *Proceedings, Third International Conference on New Frontiers for Hazardous Waste Management.* Pittsburgh, PA.

Raymond, E.L. 1968. Mechanism of sensitization and stabilization of Incoloy nickel-iron-chromium alloy 825. *Corrosion* 24: 180–188.

Reed, D.T., and R.A. van Konynenburg. 1987. Effect of ionizing radiation on moist air systems. *Scientific Basis for Nuclear Waste Management XI.* M.J. Apted and R.E. Westerman, eds. Pittsburgh, PA: Materials Research Society: 112: 393–404.

Reed, D.T., and R.A. van Konynenburg. 1990. Progress in evaluating the corrosion of candidate high-level waste container metals in irradiated air-steam mixtures. *Proceedings of the Topical Meeting on Nuclear Waste Packaging—Focus '91.* La Grange Park, IL: American Nuclear Society: 185–192.

Reed, D.T., and R.A. van Konynenburg. 1991. Corrosion of copper-based materials in irradiated moist-air systems. *Scientific Basis for Nuclear Waste Management XIV.* T.A. Abrajano, Jr., and L.H. Johnson, eds. Pittsburgh, PA: Materials Research Society 212: 317–325.

Rhodes, P.R. 1986. Stress cracking risks in corrosive oil and gas wells. Paper No. 322. *Corrosion '86*. Houston, TX: National Association of Corrosion Engineers.

Rosenfeld, I.L., I.S. Danilov, and R.N. Oranskaya. 1978. Breakdown of the passive state and repassivation of stainless steels. *Journal of the Electrochemical Society* 125: 1,729–1,735.

Rosenfeld, I.L., and I.S. Danilov. 1967. Electrochemical aspects of pitting corrosion. *Corrosion Science* 7: 129–142.

Rosevear, A. 1991. *Review of National Research Programmes on the Microbiology of Radioactive Waste Disposal*. Report NSS/R263. Oxfordshire, U.K.: Harwell Laboratory, United Kingdom Atomic Energy Administration.

Russell, E.W., R.D. McCright, and W.C. O'Neal. 1984. *Containment Barrier Metals for High-level Waste Packages in a Tuff Repository*. UCRL-53449. Livermore, CA: Lawrence Livermore National Laboratory.

Sanders, P.F., and S. Maxwell. 1983. Microfouling, macrofouling and corrosion of metal test specimens in seawater. *Microbial Corrosion*. London, England: The Metals Society. 74–83.

Schiffrin, D.J., and S.R. de Sanchez. 1985. The effect of pollutants and bacterial microfouling on the corrosion of copper based alloys in seawater. *Corrosion* 41: 31–38.

Schumacher, M., ed. 1979. *Seawater Corrosion Handbook*. Park Ridge, NJ: Noyes Data Corporation: 494.

Schwartzkopf, W., E. Smialos, and R. Koster. 1992. *In-situ* corrosion on cast-steel high-level waste containers plated with titanium/nickel alloys. *Scientific Basis for Nuclear Waste Management XV*. C.G. Interrante and R.T. Pabalan, eds. Pittsburgh, PA: Materials Research Society: 257: 423–430.

Scott, P.J.B., J. Goldie, and M. Davies. 1991. Ranking alloys for susceptibility to MIC—A preliminary report on high-Mo alloys. *Materials Performance* 30(1): 55–57.

Scotto, V. 1988. Electrochemical studies of biocorrosion of stainless steels in seawater. *Microbial Corrosion: 1988 Workshop Proceedings*. G.J. Licina, ed. Palo Alto, CA: Electric Power Research Institute.

Scotto, V., R. Di Cinio, and G. Marcenaro. 1985. The influence of marine aerobic microbial film on stainless steel corrosion behaviour. *Corrosion Science* 25: 185–194.

Scully, J.C. 1971. Fractographic aspects of stress corrosion cracking. *Theory of Stress Corrosion Cracking in Alloys*. J.C. Scully, ed. Brussels, Belgium: North Atlantic Treaty Organization: 127–166.

Shaw, B.A., P.J. Moran, and P. Gartland. 1993. Crevice corrosion of a nickel-based superalloy in natural and chlorinated seawater. *Proceedings of the 12th International Corrosion Congress*. Houston, TX: NACE International: 3B: 1,915–1,928.

Shibata, T., and H. Takamiya. 1986. Effect of pH and [Cl⁻] on the stochastic process of pitting corrosion of Mo-containing stainless steels. *Critical Issues in Reducing the Corrosion of Steels.* H. Leidheiser, Jr., and S. Haruyama, eds. Houston, TX: National Association of Corrosion Engineers: 17–27.

Shinohara, T., S. Tsujikawa, and N. Masuko. 1990. In-situ measurement for crevice corrosion of high purity 18Cr-14Ni steel under optical glass in 3%NaCl solutions. *Corrosion Engineering* 39: 255–269.

Shinohara, T., N. Masuko, and S. Tsujikawa. 1993. Moire method to measure penetration depth profiles on unevenly corroded metal surfaces. *Corrosion Science* 35: 785–789.

Silcock, J.M., and P.R. Swann. 1979. Nucleation and growth of transgranular stress corrosion cracks in austenitic stainless steels. *Environment-Sensitive Fracture of Engineering Materials.* Z.A. Foroulis, ed. Warrendale, PA: The Metallurgical Society of AIME: 133–152.

Singh, S., and C. Alstetter. 1982. Effects of hydrogen concentration on slow crack growth in stainless steels. *Metallurgical Transactions* 13A: 1,799–1,808.

Smialos, E., W. Schwartzkopf, R. Köster, B. Fiehn, and G. Halm. 1990. *Corrosion Testing of Selected Packaging Materials for Disposal of High-Level Waste Glass in Rock Salt Formations.* KfK 4723 (EUR–13672). Karlsruhe, Germany: Kernforschungszentrum Krlsruhe GmbH.

Smith, G.D.W., A.J. Garratt-Reed, and J.B. Vander Sande. 1981. Comparison between atom probe and STEM microanalysis. *Quantitative Microanalysis with High Spatial Resolution.* G.W. Lorimer et al., eds. London, U.K.: The Metals Society: 238–249.

Soracco, R.J., D.H. Pope, J.M. Eggers, and T.N. Effinger. 1988. Microbially influenced corrosion investigations in electric power generating stations. Paper No. 83. *Corrosion '88.* Houston, TX: National Association of Corrosion Engineers.

Sorensen, J. 1982. Reduction of ferric ion in anaerobic marine sediment and interaction with reduction of nitrate and sulfate. *Applied and Environmental Microbiology* 43: 319–324.

Sorensen, N.R., and M.A. Molecke. 1992. Summary of the WIPP materials interface interactions test—Metal corrosion. *Workshop on In Situ Tests on Radioactive Waste Forms and Engineered Barriers.* Corsendok, Belgium. SAND92-1921C. Albuquerque, NM: Sandia National Laboratory.

Spinks, J.W.T., and R.J. Woods. 1990. *Introduction to Radiation Chemistry.* 3rd Edition. New York, NY: John Wiley & Sons.

Sridhar, N., J.A. Kargol, and N.F. Fiore. 1980. Effect of low-temperature aging on hydrogen-induced crack growth in a nickel-base superalloy. *Scripta Metallurgica* 14: 1,257–1,260.

Sridhar, N., G.A. Cragnolino, and F.F. Lyle. 1990. *Progress Report of Activities and Recommendations in the Integrated Waste Package Experimental Program. May 1988–April 1990.* CNWRA Task

Activity 20-3704-042-005-900. San Antonio: TX: Center for Nuclear Waste Regulatory Analyses.

Sridhar, N., B.E. Wilde, C. Manfredi, S. Kesavan, and C. Miller. 1991a. *Hydrogen Absorption and Embrittlement of Candidate Container Materials—I.* CNWRA 91-008. San Antonio, TX: Center for Nuclear Waste Regulatory Analyses.

Sridhar, N., and G.A. Cragnolino. 1993a. Integrated waste package experiments. *NRC High-Level Radioactive Waste Research at CNWRA, July–December 1992.* B. Sagar, ed. NUREG/CR-5817. V. 3, No. 2. CNWRA 92-02S. Washington, DC: Nuclear Regulatory Commission.

Sridhar, N., and G.A. Cragnolino. 1993b. Applicability of repassivation potential for long-term prediction of localized corrosion of alloy 825 and type 316L stainless steel. *Corrosion* 49: 885–894.

Sridhar, N., and G.A. Cragnolino. 1993c. Effects of environment on localized corrosion of copper-based high-level waste container materials. *Corrosion* 49: 967–976.

Sridhar, N., G.A. Cragnolino, and D.S. Dunn. 1993a. *Experimental Investigations of Localized Corrosion of High-Level Waste Container Materials.* CNWRA 93-004. San Antonio, TX: Center for Nuclear Waste Regulatory Analyses.

Sridhar, N., G.A. Cragnolino, and D. Dunn. 1993b. Integrated Waste Package Experiments. *NRC High-Level Radioactive Waste Research at CNWRA January-June 1993.* B. Sagar, ed. CNWRA 93-01S. San Antonio, TX: Center for Nuclear Waste Regulatory Analyses.

Sridhar, N., J.C. Walton, G.A. Cragnolino, and P.K. Nair. 1993c. *Engineered Barrier System Performance Assessment Codes (EBSPAC) Progress Report—October 1, 1992, through September 25, 1993.* CNWRA 93-021. San Antonio, TX: Center for Nuclear Waste Regulatory Analyses.

Sridhar, N., and D.S. Dunn. 1994. Effect of applied potential on changes in solution chemistry inside crevices on type 304L stainless steel and alloy 825. *Corrosion* 50: 857–872.

Sridhar, N., G.A. Cragnolino, D.S. Dunn, and H.K. Manaktala. 1994a. *Review of Degradation Modes of Alternate Container Designs and Materials.* CNWRA 94-010. San Antonio, TX: Center for Nuclear Waste Regulatory Analyses.

Sridhar, N., G.A. Cragnolino, and D. Dunn. 1994b. Integrated Waste Package Experiments. *NRC High-Level Radioactive Waste Research at CNWRA July-December 1993.* B. Sagar, ed. CNWRA 93-02S. San Antonio, TX: Center for Nuclear Waste Regulatory Analyses.

Sridhar, N., G.A. Cragnolino, H. Pennick, and T.Y. Torng. 1994c. Application of a Transient Crevice Corrosion Model to the Prediction of Performance of High-level Nuclear Waste Container Materials. *Life Prediction of Corrodible Structures.* R.N. Parkins, ed. Houston, TX: National Association of Corrosion Engineers: 1: 429–453.

Stalder, F., and D.J. Duquette. 1977. Slow strain rate stress corrosion cracking of type 304 stainless steels. *Corrosion* 33: 67–72.

Starr, K.K., E.D. Verink, Jr., and M. Pourbaix. 1976. The significance of the protection potential for Fe-Cr alloys at room temperature. *Corrosion* 32: 47–51.

Steinsmo, U., and H.S. Isaacs. 1993. Dissolution and repassivation kinetics of Fe-Cr alloys in pit solutions. *Journal of the Electrochemical Society* 140: 643–653.

Stetter, K.O., A. Segerer, W. Zillig, G. Huber, G. Fiala, R. Huber, and H. Konig. 1986. Extreme thermophilic sulfur-metabolizing archaebacteria. *Systematic and Applied Microbiology* 7: 393–397.

Stoecker, J.G. 1984. Guide for the investigation of microbially induced corrosion. *Materials Performance* 23(8): 48–55.

Strehblow, H.H. 1984. Breakdown of passivity and localized corrosion: Theoretical concepts and fundamental experimental results. *Werkstoffe und Korrosion* 35: 437–448.

Streicher, M.A. 1978. Theory and application of evaluation tests for detecting susceptibility to intergranular attack in stainless steels and related alloys—problems and opportunities. *Intergranular Corrosion of Stainless Alloys.* ASTM STP 656. R.F. Steigerwald, ed. Philadelphia, PA: American Society for Testing and Materials: 3–84.

Stroes-Gascoyne, S. 1989. *The Potential for Microbial Life in a Canadian High-Level Nuclear Fuel Disposal Vault: A Nutrient and Energy Source Analyses.* AECL-9574. Pinawa, Manitoba, Canada: Atomic Energy of Canada Limited.

Stumm, W., and J.J. Morgan. 1981. *Aquatic Chemistry.* 2nd. ed. New York, NY: John Wiley & Sons.

Sugimoto, K., and K. Asano. 1990. Analysis of localized corrosion on stainless steel by micro-complex pH-pCl electrode. *Advances in Localized Corrosion.* H. Isaacs et al., ed. Houston, TX: National Association of Corrosion Engineers: 375–379.

Suleiman, M.I., and R.C. Newman. 1995. Galvanostatic, creviced stress corrosion test for austenitic stainless steel in hot chloride solutions. *Corrosion* 51: 171–176.

Suzuki, T., M. Yamabe, and Y. Kitamura. 1973. Composition of anolyte within local anode of stainless steel. *Corrosion* 29: 18–22.

Szklarska-Smialowska, Z. 1986. *Pitting Corrosion of Metals.* Houston, TX: National Association of Corrosion Engineers: 327–338.

Takano, M. 1974. Effect of strain rate on stress corrosion cracking of austenitic stainless steel in $MgCl_2$ solutions. *Corrosion* 30: 441–446.

Tamaki, K., S. Tsujikawa, and Y. Hisamatsu. 1990. Development of a new test method for chloride stress corrosion cracking of stainless steel in dilute NaCl solutions. *Advances in Localized Corrosion.* H.S. Isaacs, U. Bertocci. J. Kruger, and S. Smialowska, eds. Houston, TX: National Association of Corrosion Engineers: 207–214.

Tatnall, R.E. 1981. Fundamentals of bacteria induced corrosion. *Materials Performance* 20(9): 32–38.

Thompson, A.W., and I.M. Bernstein. 1976. *The role of metallurgical variables in hydrogen-assisted environmental fracture*. Report No. SC-PP-75-63. Thousand Oaks, CA: Science Center, Rockwell International.

Thompson, N.G., and B.C. Syrett. 1992. Relationship between conventional pitting and protection potentials and a new, unique pitting potential. *Corrosion* 48: 649–659.

Thompson, N.G., J.A. Beavers, and C.L. Durr. 1992. *Potentiodynamic Polarization Studies on Candidate Container Alloys for the Tuff Repositories*. NUREG/CR-5708. Washington, DC: U.S. Nuclear Regulatory Commission.

Thorvaldsson, T., H. Rubinsztein-Dunlop, H-O. Andren, and G.L. Dunlop. 1981. Analytical electron microscopy of carbide precipitates in a stabilized austenitic stainless steel. *Quantitative Microanalysis with High Spatial Resolution*. G.W. Lorimer et al., eds. London, United Kingdom: The Metals Society: 250–255.

Tromans, D., and L. Frederik. 1984. Effect of thiosulfate on crevice corrosion of stainless steels. *Corrosion* 40: 633–639.

Tsujikawa, S., and Y. Hisamatsu. 1984. Repassivation potential as a crevice corrosion characteristic for austenitic and ferritic stainless steels. *Improvement of Corrosion Resistance of Structural Materials in Aggressive Media*. Ya. M. Kolotyrkin, ed. Moscow: Russia: Nauka Publishers.

Tsujikawa, S., T. Shinohara, and Y. Hisamatsu. 1985. The role of crevices in comparison to pits in initiating stress corrosion cracks of type 310 stainless steel in different concentrations of $MgCl_2$ solutions at 80°C. *Corrosion Cracking*. V.S. Goel, ed. Metals Park, OH: American Society for Metals (ASM): 35–42.

Tsujikawa, S., Y. Soné, and Y. Hisamatsu. 1987. Analysis of mass transfer in a crevice region for a concept of the repassivation potential as a crevice corrosion characteristic. *Corrosion Chemistry within Pits, Crevices, and Cracks*. A. Turnbull, ed. London, U.K.: Her Majesty's Stationery Office: 171–186.

Tsujikawa, S., A. Miyasaka, M. Uedo, S. Ando, T. Shibata, T. Haruna, M. Katahira, Y. Yamane, T. Aoki, and T. Yamada. 1993. Alternative for evaluating sour gas resistance of low-alloy steels and corrosion-resistant alloys. *Corrosion* 49: 409–419.

Tsujikawa, S., T. Shinohara, and W. Lichang. 1994. Spot-welded specimen potentiostatically kept just above the crevice repassivation potential to evaluate stress corrosion cracking susceptibility of improved type 304 stainless steels in NaCl solutions. *Applications of Accelerated Corrosion Tests to Service Life Prediction of Materials*. G. Cragnolino and N. Sridhar, eds. ASTM STP 1194. Philadelphia, PA: American Society for Testing and Materials: 340–354.

Turnbull, A. 1983. The solution composition and electrode potential in pits, crevices, and cracks. *Corrosion Science* 23: 833–870.

U.S. Department of Energy. 1988. *Site Characterization Plan for the Yucca Mountain Site, Nevada Research and Development Area, Nevada.* DOE/RW-0199. Vol. III, Part A, Chap. 7. Washington, DC: U.S. Department of Energy.

U.S. Department of Energy. 1993. *A Preliminary Evaluation of Using Multi-Purpose Canisters Within the Civilian Radioactive Waste Management System. Revision 0.* CRWMS M&O Document No. A00000000-AA-07-00002. Vienna, VA: TRW Environmental Safety Systems, Inc.

U.S. Department of Energy. 1994. *Initial Summary Report for Repository/Waste Package Advanced Conceptual Design. Revision 00.* CRWMS M&O Document DOC No. B00000000-01717-5705-00015. Las Vegas, NV: TRW Environmental Safety Systems, Inc.

Umbreit, W.W. 1976. The oxidation of metallic iron by *Escherichia coli* and other common heterotrophs. *Developments in Industrial Microbiology* 17: 265–268.

van Konynenburg, R.A. 1986. *Radiation Chemical Effects in Experiments to Study the Reaction of Glass in an Environment of Gamma-Irradiated Air, Groundwater, and Tuff.* UCRL-53719. Livermore, CA: Lawrence Livermore National Laboratory.

Videla, H.A., and W.G. Characklis. 1992. Biofouling and microbially influenced corrosion. *International Biodeterioration and Biodegradation* 29: 195–212.

Võlkl, J., and G. Alefeld. 1978. Diffusion of hydrogen in metals. *Hydrogen in Metals—I.* G. Alefeld and J. Võlkl, eds. Berlin, Germany: Springer-Verlag.

Walch, M., and R. Mitchell. 1986. Microbial influence on hydrogen uptake by metals. *Biologically Induced Corrosion.* S.C. Dexter, ed. Houston, TX: National Association of Corrosion Engineers: 201–208.

Walch, M., T.E. Ford, and R. Mitchell. 1989. Influence of hydrogen-producing bacteria on hydrogen uptake by steel. *Corrosion* 45: 705–709.

Walton, J.C. 1993. Effects of evaporation and solute concentration on presence and composition of water in and around the waste package at Yucca Mountain. *Waste Management* 13: 293–301.

Walton, J.C., and S.K. Kalandros. 1992. *TWITCH—A Model for Transient Diffusion, Electromigration, and Chemical Reaction in One Dimension.* CNWRA 92-019. San Antonio, TX: Center for Nuclear Waste Regulatory Analyses.

Wanklyn, J.N. 1981. The role of molybdenum in the crevice corrosion of stainless steels. *Corrosion Science* 21: 211–225.

Was, G.S., and R.M. Kruger. 1985. A thermodynamic and kinetic basis for understanding chromium depletion in Ni-Cr-Fe alloys. *Acta Metallurgica* 33: 841–854.

Was, G.S., H.H. Tischner, and R.M. Latanision. 1981. The influence of thermal treatment on the chemistry and structure of grain boundaries in Inconel 600. *Metallurgical Transactions* 12A: 1,397–1,408.

Watson, M., and J. Postlethwaite. 1990. Numerical simulation of crevice corrosion of stainless steels and nickel alloys in chloride solutions. *Corrosion* 46:522–530.

Wei, R.P., and M. Gao. 1985. Chemistry, microstructure and crack growth response. *Hydrogen Degradation of Ferrous Alloys.* R.A. Oriani, J.P. Hirth, and M. Smialowski, eds. Park Ridge, NJ: Noyes Publications: 579–607.

West, J.M., M. Cave, J.J.W. Higgo, A.E. Milodowski, C.A. Rochelle, and C.A.M. Ross. 1992. The effect of microbial activity on the near and far fields of a Swiss Type B repository. *Scientific Basis for Nuclear Waste Management XV.* C.G. Sombret, ed. Pittsburgh, PA: Materials Research Society. 257: 729–736.

West, K.A. 1988. *Nevada Nuclear Waste Storage Investigation Exploratory Shaft Facility Fluids and Materials Evaluation.* LA-11398-MS. Los Alamos, NM: Los Alamos National Laboratory.

Westerman, R.E., S.G. Pitman, and J.H. Haberman. 1987. *Corrosion Testing of 304L Stainless Steel in Tuff Groundwater Environments.* UCRL-21005. Livermore, CA: Lawrence Livermore National Laboratory.

Wilde, B.E. 1974. On Pitting and Protection Potentials: Their use and possible misuses for predicting localized corrosion resistance of stainless alloys in halide media. *Localized Corrosion.* R.W. Staehle, B.F. Brown, J. Kruger, and A. Agrawal, eds. Houston, TX: National Association of Corrosion Engineers: 342–352.

Wilde, B.E., and E. Williams. 1971. The relevance of accelerated electrochemical pitting tests to the long-term pitting and crevice corrosion behavior of stainless steel in marine environments. *Journal of the Electrochemical Society* 118: 1,057–1,062.

Wilde, M.H., and B.E. Wilde. 1993. Some observations on the mechanism of corrosion to be encountered in nuclear waste repositories located in tuffaceous rock. *Corrosion Science* 34: 433–443.

Williams, D.E., C. Westcott, and M. Fleischmann. 1985a. Stochastic models of pitting corrosion of stainless Steels. I. Modeling of the initiation and growth of pits at constant potential. *Journal of the Electrochemical Society* 132: 1,796–1,804.

Williams, D.E., C. Westcott, and M. Fleischmann. 1985b. Stochastic models of pitting corrosion of stainless Steels. II. Measurement and interpretation of data at constant potential. *Journal of the Electrochemical Society* 132: 1,804–1,811.

Williams, D.P., and H.G. Nelson. 1969. Embrittlement of 4130 steel by low-pressure gaseous hydrogen. *Metallurgical Transactions* 1A: 63–68.

Wolfram, J., R.D. Rogers, and B.J. Buescher. 1988. A summary of microbially influenced corrosion in nuclear power plants. *Pressure Vessels and Piping Conference*. New York, NY: American Society of Mechanical Engineers.

Yang, W., J. Conglenton, O. Kohneh-Chari, and P. Sajdl. 1992. The strain for stress corrosion crack initiation in type 316 stainless steel in high temperature water. *Corrosion Science* 33: 735–750.

Yashiro, H., and K. Tanno. 1990. The effect of electrolyte composition on the pitting and repassivation behavior of AISI 304 stainless steel at high temperature. *Corrosion Science* 31: 485-490.

Yunker, W.H. 1990. *Corrosion Behavior of Copper-base Materials in a Gamma-irradiated Environment, Final Report.* WHC-EP-0188. Richland, WA: Westinghouse Hanford Co.

Zakrozcymski, T. 1985. The effect of straining on the transport of hydrogen in iron, nickel, and stainless steel. *Corrosion* 41: 485–489.

Zhang, H-J., and S.C. Dexter. 1995. The effect of biofilms on critical pitting potentials for stainless steels S30400 and S31600 in seawater. Paper No. 70. *1995 International Conference on Microbially Influenced Corrosion.* Houston, TX: NACE International.

Zhang, X., R.A. Buchanan, E.E. Stansbury, and N.J.E. Dowling. 1989. Electrochemical responses of structural materials to microbially influenced corrosion. Paper No. 512. *Corrosion '89*. Houston, TX: National Association of Corrosion Engineers.

APPENDIX A

MATERIALS USED IN THE INTEGRATED WASTE PACKAGE EXPERIMENTS PROJECT

Table A-1. Chemical compositions of austenitic alloys tested in the Integrated Waste Package Experiments program

Alloy	Material Type (Heat No.)	Elemental Composition, wt percent										
		Al	**C**	**Cr**	**Cu**	**Fe**	**Mn**	**Mo**	**Ni**	**P**	**S**	**Others**
Type 304L SS	12 mm plate (T0954-A64B)	—	0.022	18.3	—	Bal.	1.46	—	9.14	0.026	0.005	Si: 0.47 N: 0.07
Type 316L SS	12 mm plate (P80746)	—	0.014	16.35	0.27	Bal.	1.58	2.07	10.04	0.026	0.018	Si: 0.49 N: 0.06
	3 mm sheet (853252)	—	0.019	16.30	—	Bal.	1.90	2.13	10.18	0.030	0.001	Si: 0.50 N: 0.03
Alloy 825	12 mm plate (HH4371FG)	0.07	0.010	22.09	1.79	30.41	0.35	3.21	41.06	—	—	Si: 0.19 Ti: 0.82
	3 mm sheet (HH7004FK)	0.09	0.010	22.07	1.72	29.69	0.40	3.49	41.22	—	—	Si: 0.29 Ti: 1.02
Alloy C-22	12 mm plate (2277-8-3175)	—	0.004	21.40	—	3.80	0.12	13.60	Bal.	0.008	—	Si: 0.03 W: 3.00 V: 0.15

Table A-2. Chemical compositions of copper-based alloys tested in the Integrated Waste Package Experiments program

Alloy	Elemental Composition, wt percent								
	Al	C	Cu	Fe	Mn	Ni	P	S	Others
CDA-102	—	—	99.95	—	—	—	—	—	—
CDA-715	—	0.013	69.20	0.54	0.57	29.57	0.004	0.006	Pb: 0.010
CDA-613	6.66	—	90.61	2.44	—	0.03	0.006	—	Sn: 0.3

APPENDIX B

SOLUTION PREPARATION FOR LOCALIZED CORROSION EXPERIMENTS

SOLUTION PREPARATION FOR LOCALIZED CORROSION EXPERIMENTS

B.1 PREPARATION OF SIMULATED J-13 SOLUTIONS

Studies were conducted on simulated J-13 well water to test its stability as a function of time and to identify possible sources of error or uncertainties in the preparation procedure.[1] Based on this study, the procedure for preparation of simulated J-13 water and its modifications was formulated (Sridhar et al., 1990). The CNWRA Technical Operating Procedure (TOP)-010, shown below, is followed in preparing these solutions.

- Preparation of Stock Solution A

  Add 1.377 g of $CaSO_4 \cdot 2H_2O$ to 900 mL of high purity water at room temperature and stir until dissolved. Then add 0.944 g of $Ca(NO_3)_2 \cdot 4H_2O$, 0.119 g of KCl, and 0.569 g of $MgCl_2 \cdot 6H_2O$ to the solution and stir until dissolved completely. Care should be taken to add magnesium chloride quickly since it is hygroscopic. Pour into a 1,000 mL flask and dilute to volume with water.

- Preparation of Stock Solution B

  Add 6.720 g of $NaHCO_3$, and 0.376 g of $KF \cdot 2H_2O$ to 900 mL of high purity water at room temperature and stir until dissolved. Care should be taken in adding KF since it is hygroscopic. Pour solution into a 1,000 mL flask and dilute to volume with water.

- Preparation of Solution

  Mix 25 mL of stock Solution A and 25 mL of stock Solution B with 925 mL of high purity water in a 1,000 mL volumetric flask. Add more water to dilute to 1,000 mL. Augmentation of chloride shall be accomplished by addition of appropriate amounts of KCl to stock Solution A.

B.2 MODEL SOLUTION PREPARATION AND ANALYSES

These solutions were primarily used to study the effect of anionic species and were prepared with only sodium salts. In the solutions with the initial room temperature pH of 8.2, the initial bicarbonate concentration was 85 ppm. However, during the heat-up and test periods, some of the bicarbonate was lost as CO_2, and the resulting pH increased to 9.5. The simulated crevice solutions, containing high ionic concentrations (0.5 M to 4 M), were prepared without the addition of nitrate or fluoride salts. In solutions with pH lower than 6, HCl was added to adjust the pH. Bicarbonate was not added since this is unstable and would have evolved as CO_2.

---

[1] Pabalan, R.T. *Test of Technical Procedure for Preparing Simulated and Modified J-13 Well Water.* Internal Memorandum dated August 10, 1989. San Antonio, TX: Center for Nuclear Waste Regulatory Analyses.

B.2.1 Measurement of Bicarbonate Concentration in Aqueous Solutions

Most of the studies on localized corrosion of the candidate container materials included in this task involved aqueous solutions containing bicarbonate ions. Thus, an appropriate method must be applied for the determination of the HCO_3^- concentration, particularly for long-term tests where this concentration may vary with time. A simple technique for this purpose is described in ASTM D 513-88: Standard for Total and Dissolved Carbon Dioxide in Water, Test Method A—Gas Sensing Electrode Test Method. The total concentration of dissolved carbonate species present as CO_2, H_2CO_3, HCO_3^-, and CO_3^{2-} in water are determined potentiometrically by using a carbon dioxide electrode. Volatile weak acids, such as HNO_2, H_2SO_3, acetic acid, and formic acids, are known as potential interferences in this method. This matter is not of concern because these anions are not included in the model solutions to be tested. By knowing the total concentration of dissolved carbonate species, the pH of the solution, and the partial pressure of CO_2 in equilibrium with the solution, the concentration of each species can be calculated by using the thermodynamic constants for the various equilibria involved. These equilibria were briefly discussed in a previous report (Cragnolino and Sridhar, 1991d).

In addition to bicarbonate, the model solutions may eventually contain other anions, such as chloride, sulfate, nitrate, and fluoride, which are the predominant anionic species in the groundwaters in the proximity of the proposed Yucca Mountain repository site. For this reason, a test matrix including 10 solutions (Table B-1) was designed to measure the HCO_3^- ion concentration in the presence of various concentrations of those anions to confirm whether interference by the various anions can be disregarded. Additionally, for each solution, the pH and the chloride concentration were measured. The measurements were conducted using a Model 95-02 Orion carbon dioxide electrode, a Model 94-17B Orion chloride electrode, and a Model 81-02 Orion pH combination electrode in conjunction with a Model 720 Orion pH-ion selective electrode meter.

Following the procedure described in ASTM D 513-88, the carbon dioxide electrode was calibrated within the specified range of 0 to 400 ppm CO_2. The CO_2 concentration was measured in all the solutions, but a dilution factor of 1:20 was used for solutions 5 to 10. For the measurement of the chloride concentration, a dilution factor of 1:100 was applied to solutions 2 and 7.

Results of the measurements of HCO_3^- and Cl^- concentrations for each solution as well as the corresponding pH values are summarized in Table B-2. Triplicate measurements were conducted for each solution, and the values reported are the mean of those measurements. In addition, triplicate samples were prepared in the specific case of solutions 1 and 5, as denoted by the suffixes -a, -b, and -c.

The mean value of the HCO_3^- concentration for solutions 1-a to 1-c is 94.2 ppm with a standard deviation of 1.0 ppm. For solutions 2 to 4, the mean value is 101.2 ppm with a standard deviation of 1.1 ppm. Since the 95 percent confidence interval for solutions 1-a to 1-c is ± 2.4, it can be concluded that the addition of 10,000 ppm chloride, sulfate, or nitrate affects the determination of the bicarbonate concentration at the low bicarbonate concentration level, probably through their effect on the ionic strength of the solutions. On the other hand, for solutions 6 to 9, the mean value is 9,048 ppm with a standard deviation of 425 ppm. In this case the nominal bicarbonate composition of 8,800 ppm lies within the 95 percent confidence interval for the measurements, which is 446 ppm. It can be concluded that the presence of chloride, sulfate, and nitrate at the high bicarbonate concentration level does not affect the determination of the bicarbonate concentration.

Table B-1. Nominal composition of the bicarbonate-containing solutions for HCO_3^-, Cl^-, and pH measurements

Solution	HCO_3^- (ppm)	Cl^- (ppm)	SO_4^{2-} (ppm)	NO_3^- (ppm)	F^- (ppm)
1	88	6	20	10	2
2	88	10,000	20	10	2
3	88	6	10,000	10	2
4	88	6	20	10,000	2
5	88	6	20	10	200
6	8,800	6	20	10	2
7	8,800	10,000	20	10	2
8	8,800	6	10,000	10	2
9	8,800	6	20	10,000	2
10	8,800	6	20	10	200

According to Table B-2, the measured values of the HCO_3^- concentration in the presence of 200 ppm fluoride (solutions 5 and 10) lie outside the 95 percent confidence limits for solutions 2 to 4 and 6 to 9, which are ±2.7 and ±446 ppm, respectively. These results seem to indicate that fluoride interferes with the determination of bicarbonate, presumably through an effect similar to that mentioned above for weak volatile acids. It should be noted that the pK of HF is 3.45, whereas that of HNO_2 is 3.37, suggesting that both anions (F^- and NO_2^-) may have a very similar effect if their volatility is comparable. For example, a 10 percent positive error in the determination of 61 ppm HCO_3^- (10^{-3} M) is caused by 160 ppm NO_2^- (3.5×10^{-3} M) according to ASTM D 513. Additional work is needed to identify beyond doubt the nature of the interference and to determine the possibility of using a correction term.

The mean pH values were found to be 8.26±0.16 and 8.19±0.09 for the nominal bicarbonate concentration of 88 and 8,800 ppm, respectively. Obviously, under conditions of equilibrium of the solutions with the partial pressure of CO_2 in the atmosphere, the HCO_3^- anion constitutes more than 99 percent of the total concentration of dissolved carbonate species. No variation of pH should be expected in that concentration range. The reason is that the pH value should be practically equal to the arithmetic mean of the pK values for the two successive dissociation or acidity constants of dissolved carbon dioxide, which are 6.35 and 10.33 at 25 °C (Stumm and Morgan, 1981). Therefore, by assuming infinite dilution conditions, a pH of 8.34 should be expected, which is very close to that measured.

The mean value of the chloride concentration for all the solutions, with the exception of solutions 2 and 7, was 8.6 ppm with a standard deviation of 1 ppm. No statistical significance can be attributed to the difference in the mean values between both sets of solutions containing 88 and 8,800 ppm bicarbonate.

Table B-2. Values of HCO_3^- concentration, Cl^- concentration, and pH for solutions included in Table B-1

Solution	HCO_3^- (ppm)	Cl^- (ppm)	pH
1-a	93.3	10.6	8.17
1-b	94.0	9.3	8.35
1-c	95.2	10.1	8.41
2	101.0	11,000	8.16
3	102.3	8.6	8.09
4	100.2	8.5	8.51
5	108.1	7.6	8.13
6-a	8,263	7.5	8.21
6-b	8,928	8.6	8.29
6-c	9,372	8.6	8.28
7	9,261	12,500	8.05
8	9,067	7.8	8.13
9	9,400	8.1	8.14
10	10,120	8.3	8.25

It is apparent that higher values than the nominal chloride concentration were measured in all solutions, including those containing 10,000 ppm chloride.

B.2.2 Evolution of pH with Time in Model Solutions

As mentioned previously, the pH in near-neutral solutions evolved from about 8 to about 9. This condition was modeled (Pabalan et al., 1990) in terms of the exsolution of CO_2. The time evolution of pH was monitored in a test solution containing 8,500 ppm HCO_3^-, 1,000 ppm Cl^-, 1,000 ppm SO_4^{2-}, 10 ppm NO_3^-, and 2 ppm F^-. In one series of experiments, two batches of the solution (approximately 900 mL) were placed in polypropylene bottles and loosely covered. The bottles were then placed in a shaker bath at 25 °C at 30 rpm. The pH readings (three readings per sample) were taken on samples that were withdrawn at periodic intervals for up to 20 days. The experiments were repeated for two other solutions, the first containing 85 ppm HCO_3^- and other anions at the same concentration as above, and the second containing only 8,500 ppm HCO_3^-. The results are shown in Figure B-1. In both the 8,500 ppm HCO_3^- solutions, the pH increased slowly from 8.1 to 9.1 over 480 hr (20 d). Correspondingly,

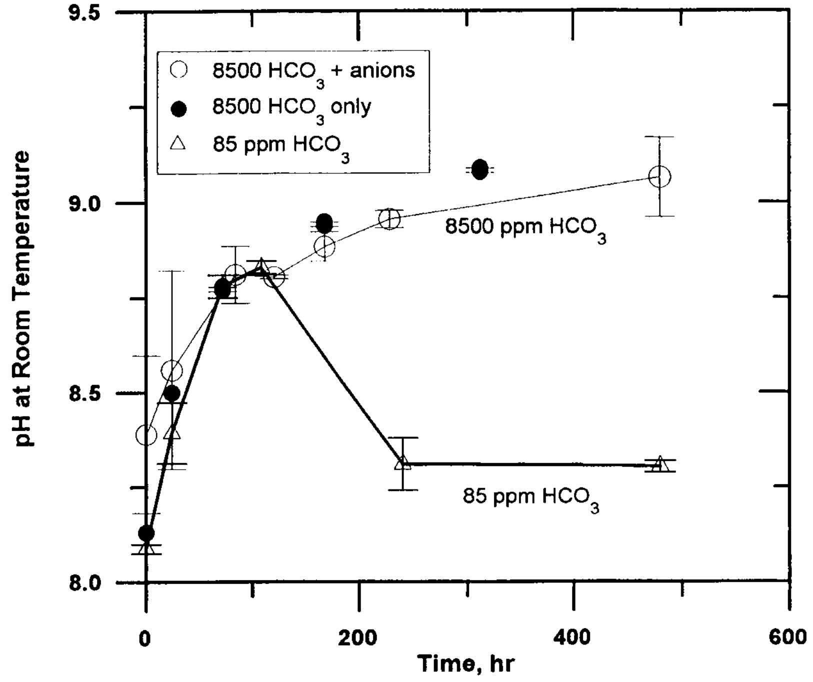

Figure B-1. Change in pH measured at room temperature as a function of time. Solution maintained at 25 °C in a loosely covered polypropylene bottle in a shaker bath.

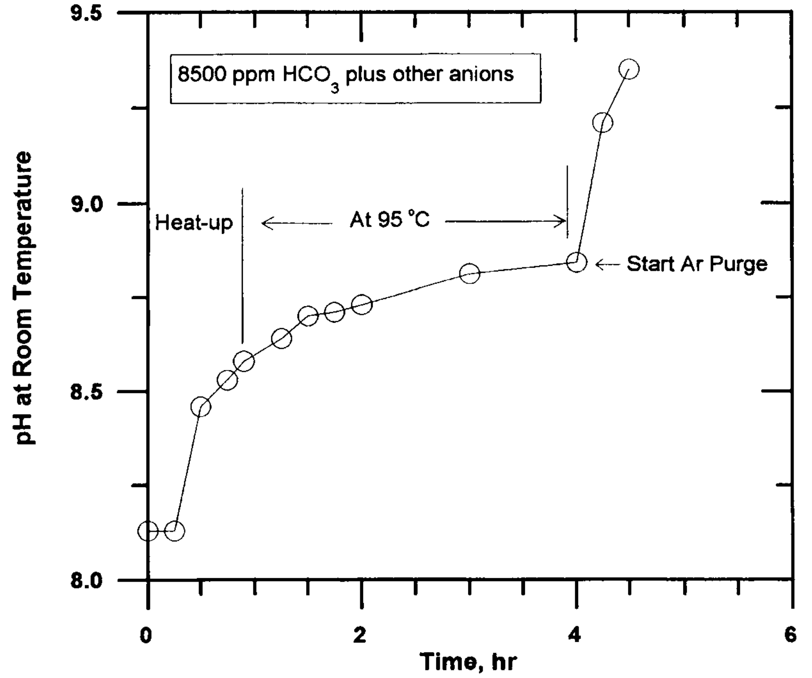

Figure B-2. Change in pH of a solution heated to 95 °C from room temperature. All pH measured at room temperature from solutions withdrawn from glass test cell.

the total carbonate (in terms of the bicarbonate equivalent) decreased (Table B-3). For the 85 ppm HCO_3^- solution, there was a maximum in pH after about 100 hr (5 d). Correspondingly, the total carbonate concentration measured by the electrode increased slightly (Table B-3). It can also be seen from Table B-3 that nitrogen purging accelerated the decrease in bicarbonate concentration.

The effect of heating and purging on the change in pH can be seen in Figure B-2. The change in pH is more rapid due to the faster exsolution of CO_2 and the resulting pH is higher due to the lower solubility of CO_2 at the higher temperature. In the localized corrosion experiments conducted at 95 °C, the pH of the solution can be assumed to be essentially 9.2 since the rise in pH is rapid. For the localized corrosion tests at room temperature, the pH evolves more slowly. However, purging with argon/nitrogen is expected to result in a more rapid increase in pH than shown in Figure B-1.

Table B-3. Measured bicarbonate concentration before and after the 20-day exposure to ambient conditions. Temperature: 25 °C. Solutions were diluted 20:1 for analysis unless otherwise specified.

Solution	HCO_3^- Concentration, ppm	
	Initial	Final
8,500 ppm HCO_3^-, 1,000 ppm Cl^-, 20 ppm SO_4^{2-}, 10 ppm NO_3^-, 2 ppm F^- (20 d)	8,013 8,207	7,458 7,348
8,500 ppm HCO_3^- only (20 d); 200:1 dilution for analysis	9,316	7,237
85 ppm HCO_3^-, 1,000 ppm Cl^-, 20 ppm SO_4^{2-}, 10 ppm NO_3^-, 2 ppm F^- (20 d)	91	113
8,500 ppm HCO_3^-, 1,000 ppm Cl^-, 20 ppm SO_4^{2-}, 10 ppm NO_3^-, 2 ppm F^-, (24 hr); 200:1 dilution for analysis	8,873	7,126
8,500 ppm HCO_3^-, 1,000 ppm Cl^-, 20 ppm SO_4^{2-}, 10 ppm NO_3^-, 2 ppm F^-, (24 hr); Nitrogen purge	7,985	5,129

APPENDIX C

CYCLIC POLARIZATION EXPERIMENTS ON THE AUSTENITIC ALLOYS—DATA TABLES

Table C-1. Summary of results of cyclic potentiodynamic polarization tests on alloy 825 using a two-level full factorial experimental design

Trial	Cl^- (ppm)	T (°C)	F^- (ppm)	NO_3^- (ppm)	SO_4^{2-} (ppm)	E_{corr} (mV_{SCE})	E_p (mV_{SCE})	E_{rp} (mV_{SCE})	E_p–E_{rp} (mV)	Visual Rating	LCI
1	6	60	2	10	20	–413	820	756	64	2	15.6
2	1,000	60	2	10	20	–343	678	38	640	4	377.6
3	6	95	2	10	20	–447	782	758	24	0	0.0
4	1,000	95	2	10	20	–555	626	82	544	4	347.6
5	6	60	200	10	20	–372	807	577	230	0	0.0
6	1,000	60	200	10	20	–541	709	187	522	4	294.5
7	6	95	200	10	20	–432	737	610	127	0	0.0
8	1,000	95	200	10	20	–460	593	–87	680	3	344.0
9	6	60	2	1,000	20	–429	812	679	133	2	49.1
10	1,000	60	2	1,000	20	–453	1061	889	172	2	32.4
11	6	95	2	1,000	20	–602	736	662	74	2	30.2
12	1,000	95	2	1,000	20	–509	712	672	40	0	0.0
13	6	60	,200	1,000	20	–461	776	612	164	0	0.0
14	1,000	60	200	1,000	20	–443	778	566	212	0	0.0
15	6	95	200	1,000	20	–590	716	535	181	0	0.0

Table C-1. Summary of results of cyclic potentiodynamic polarization tests on alloy 825 using a two-level full factorial experimental design (cont'd)

Trial	Cl^- (ppm)	T (°C)	F^- (ppm)	NO_3^- (ppm)	SO_4^{2-} (ppm)	E_{corr} (mV_{SCE})	E_p (mV_{SCE})	E_{rp} (mV_{SCE})	E_p–E_{rp} (mV)	Visual Rating	LCI
16	1,000	95	200	1,000	20	–593	717	560	157	0	0.0
17	6	60	2	10	1,000	–428	769	644	125	2	32.5
18	1,000	60	2	10	1,000	–449	764	108	656	4	343.5
19	6	95	2	10	1,000	–647	715	715	0	0	0.0
20	1,000	95	2	10	1,000	–492	713	–3	716	4	401.7
21	6	60	200	10	1,000	–609	765	568	197	0	0.0
22	1,000	60	200	10	1,000	–450	743	179	564	4	303.6
23	6	95	200	10	1,000	–419	730	574	156	1	21.4
24	1,000	95	200	10	1,000	–523	698	–2	700	4	401.2
25	6	60	2	1,000	1,000	–471	895	815	80	2	26.8
26	1,000	60	2	1,000	1,000	–474	759	631	128	2	33.7
27	6	95	2	1,000	1,000	–478	723	707	16	0	0.0
28	1,000	95	2	1,000	1,000	–555	703	662	41	0	0.0
29	6	60	200	1,000	1,000	–437	776	548	228	0	0.0

Table C-1. Summary of results of cyclic potentiodynamic polarization tests on alloy 825 using a two-level full factorial experimental design (cont'd)

Trial	Cl^- (ppm)	T (°C)	F^- (ppm)	NO_3^- (ppm)	SO_4^{2-} (ppm)	E_{corr} (mV_{SCE})	E_p (mV_{SCE})	E_{rp} (mV_{SCE})	E_p–E_{rp} (mV)	Visual Rating	LCI
30	1,000	60	200	1,000	1,000	−419	666	567	99	0	0.0
31	6	95	200	1,000	1,000	−617	721	560	161	0	0.0
32	1,000	95	200	1,000	1,000	−554	691	583	108	0	0.0
33	300	95	2	10	1,000	−509	728	55	673	4	369.8
34	1,000	80	2	10	20	−503	686	−10	696	4	405.8
35	1,000	95	2	10	200	−470	751	−17	768	4	409.1
36	1,000	95	100	10	20	−545	725	−101	826	4	455.7
37	1,000	95	2	100	20	−488	709	−20	729	4	411.3

$[HCO_3^-]$ = 85.5 ppm ($[NaHCO_3]$ = 122 ppm)
Initial pH of Solutions: 8.15±0.08 (1σ) Final pH: 9.34±0.27 (1σ)

Table C-2. Results of two-level full factorial experiments on type 316L stainless steel

Trial Number	Chloride (ppm)	Nitrate (ppm)	Fluoride (ppm)	Sulfate (ppm)	E_{corr} (mV_{SCE})	E_p (mV_{SCE})	E_{rp} (mV_{SCE})	Visual Rating	LCI
1	6	10	2	20	–739	510	62	4	351.4
2	1,000	10	2	20	–680	97	–171	4	1,105.2
3	6	1,000	2	20	–602	740	740	0	0.0
4	1,000	1,000	2	20	–721	204	–136	4	666.7
5	6	10	200	20	–513	749	680	0	0.0
6	1,000	10	200	20	–666	179	–242	4	940.8
7	6	1,000	200	20	–637	705	633	0	0.0
8	1,000	1,000	200	20	–454	283	–61	3	364.7
9	6	10	2	1,000	–642	728	728	0	0.0
10	1,000	10	2	1,000	–701	176	–224	3	681.8
11	6	1,000	2	1,000	–682	700	700	0	0.0
12	1,000	1,000	2	1,000	–596	333	–11	3	309.9
13	6	10	200	1,000	–683	711	647	0	0.0
14	1,000	10	200	1,000	–502	187	–286	4	1,011.8
15	6	1,000	200	1,000	–626	732	676	0	0.0
16	1,000	1,000	200	1,000	–663	266	–83	3	393.6

Table C-2. Results of two-level full factorial experiments on type 316L stainless steel (cont'd)

Trial No.	Chloride (ppm)	Nitrate (ppm)	Fluoride (ppm)	Sulfate (ppm)	E_{corr} (mV_{SCE})	E_p (mV_{SCE})	E_{rp} (mV_{SCE})	Visual Rating	LCI
REPEAT RUNS									
17	6	10	2	20	−705	577	12	4	391.7
18	3.6	10	2	20	−454	787	755	0	0.0
19	3.6	10	2	20	−625	785	785	0	0.0
20	20	10	2	20	−647	771	771	0	0.0
21	20	10	2	20	−652	746	746	0	0.0
22	20	10	2	20	−622	764	—	2	—
23	100	10	2	20	−656	313	−63	4	480.5
24	100	10	2	20	−657	340	−68	4	480.0
25	100	10	2	20	−638	435	−49	4	445.1
26	300	10	2	20	−661	188	−68	4	544.7
27	300	10	2	20	−607	282	−46	4	465.2
28	300	10	2	20	−578	231	−85	4	547.2

$[HCO_3^-]$ = 85.5 ppm ($[NaHCO_3]$ = 122 ppm)
Temperature = 95 °C

Table C-3. Analysis of variance (anova) table for the factorial experiments on alloy 825 for localized corrosion index (blocking was not considered)

Factor	Effect	Coefficient	Std. Error	95% C.I.	p-value
Average	95.5	95.5	2.49	—	—
Cl	169.0	84.5	4.99	12.2	0.00
T	2.3	1.1	4.99	12.2	0.67
F	−20.4	−10.2	4.99	12.2	0.01
NO_3	−169.4	−84.7	4.99	12.2	0.00
SO_4	4.6	2.3	4.99	12.2	0.40
Cl*T	11.4	5.7	4.99	12.2	0.06
Cl*F	−3.8	−1.9	4.99	12.2	0.49
Cl*NO_3	−174.0	−87.0	4.99	12.2	0.00
Cl*SO_4	6.4	3.2	4.99	12.2	0.25
T*F	18.8	9.4	4.99	12.2	0.01
T*NO_3	−16.3	−8.1	4.99	12.2	0.02
T*SO_4	8.2	4.1	4.99	12.2	0.15
F*NO_3	−1.2	−0.6	4.99	12.2	0.83
F*SO_4	6.4	3.2	4.99	12.2	0.25
NO_3*SO_4	−11.0	−5.5	4.99	12.2	0.07
Cl*T*F	4.4	2.2	4.99	12.2	0.43
Cl*T*NO_3	−14.0	−7.0	4.99	12.2	0.03
Cl*T*SO_4	8.6	4.3	4.99	12.2	0.13
Cl*F*NO_3	8.8	4.4	4.99	12.2	0.13
Cl*F*SO_4	−0.8	−0.4	4.99	12.2	0.89
Cl*F*NO_3*SO_4	0.4	0.2	4.99	12.2	0.95
T*F*NO_3	−4.8	−2.4	4.99	12.2	0.39
T*F*SO_4	0.5	0.2	4.99	12.2	0.93
T*NO_3*SO_4	−9.4	−4.7	4.99	12.2	0.11

$R^2 = 0.998$
Adjusted $R^2 = 0.991$

Table C-4. Analysis of variance (anova) table for the factorial experiments on type 316L stainless steel for localized corrosion index (blocking was not considered)

Factor	Effect	Coefficient	Std. Error	95% C.I.	p-value
F*NO_3*SO_4	0.03	0.013	4.99	12.2	1.00
Average	364.12	364.12	15.17	—	—
Cl	640.39	320.20	30.34	385.6	0.03
NO_3	–294.51	–147.26	30.34	385.6	0.06
F	–50.51	–25.26	30.34	385.6	0.34
SO_4	128.96	–64.48	30.34	385.6	0.15
Cl*NO_3	–206.66	–103.33	30.34	385.6	0.09
Cl*F	37.34	18.67	30.34	385.6	0.43
Cl*SO_4	–41.11	–20.56	30.34	385.6	0.40
NO_3*F	–4.06	–2.03	30.34	385.6	0.92
NO_3*SO_4	46.99	23.50	30.34	385.6	0.36
F*SO_4	153.94	76.97	30.34	385.6	0.12
Cl*NO_3*F	–91.91	–45.96	30.34	385.6	0.20
Cl*NO_3*SO_4	–40.86	–20.43	30.34	385.6	0.40
Cl*F*SO_4	66.09	33.05	30.34	385.6	0.27
NO_3*F*SO_4	–57.51	–28.76	30.34	385.6	0.30

R^2 = 0.998
Adjusted R^2 = 0.977

Table C-5. Results of cyclic potentiodynamic polarization tests on alloy 825 in simulated J-13 solutions modified to various chloride levels at 95 °C

Test No.	Chloride (ppm)	E_p (mV_{SCE})	E_{peak} (mV_{SCE})	E_{rp} (mV_{SCE})	E_{corr} (mV_{SCE})	(E_p — E_{rp}) (mV)	Initial pH	Final pH
34	0	783	382	741	–579	42	8.31	9.73
27	6	767	377	717	–480	50	8.23	9.78
30	6	768	355	706	–522	62	8.31	9.69
32	6	760	351	698	–534	62	8.30	9.76
33	6	743	322	685	–547	58	8.21	9.85
29	6	769	356	705	–557	64	8.30	9.61
31	6	747	322	681	–527	66	8.32	9.89
24	20	736	327	675	–570	61	8.31	9.86
8	20	773	380	707	–565	66	8.28	9.61
14	20	735	339	687	–470	48	8.30	9.85
22	20	739	335	683	–506	56	8.34	9.72
21	20	738	349	682	–588	56	8.28	9.56
23	20	761	352	697	–573	64	8.29	9.50
12	20	646	374	121	–543	525	8.27	9.48
16	100	740	323	366	–542	374	8.30	9.65
19	100	729	316	669	–637	60	8.25	9.72
9	100	754	361	688	–576	66	8.05	9.59
18	100	742	341	656	–592	86	8.32	9.64
17	100	726	329	672	–520	54	8.23	9.71
15	100	739	350	417	–563	322	8.30	9.66
20	100	739	334	309	–571	430	8.26	9.56
26	200	728	315	415	–526	313	8.40	9.85
10	200	746	353	152	–600	594	8.05	9.52
13	200	723	334	377	–579	346	8.27	9.67
25	200	740	335	335	–546	405	8.28	9.70
11	300	579	347	34	–566	545	8.05	9.52
47	300	628	316	103	–589	525	8.32	9.52
48	300	729	320	51	–585	678	8.38	9.41
5	1000	691	282	–35	–655	726	8.08	—
3	1000	699	294	–46	–647	745	8.12	9.50
4	1000	679	298	–63	–631	742	8.11	9.49
6	1000	467	291	–26	–610	493	8.10	9.48
2	1000	669	284	135	–657	534	8.09	9.71
1	1000	682	277	–48	–668	730	8.14	9.66
7	1000	699	306	–42	–643	741	8.11	9.65

Table C-6. Electrochemical parameters from cyclic potentiodynamic polarization curves of alloy 825 in simulated crevice solutions

Test	Environment	Temp. (°C)	E_{corr} (mV_{SCE})	E_p (mV_{SCE})	E_{rp} (mV_{SCE})	i_{pass} A/cm^2	i_{peak} A/cm^2
38	4M Cl^-, pH 8.17	95	−624	−7	−200	7×10^{-7}	1.5×10^{-6}
37	4M Cl^-, pH 2.54	95	−321	−40	−141	1×10^{-6}	1×10^{-6}
37R	4M Cl^-, pH 3.10	95	−365	−44	−137	1×10^{-6}	1×10^{-6}
17	4M Cl^-, pH 1.1	95	−340	−39	−120	2×10^{-5}	4×10^{-3}
18	4M Cl^-, pH 0.03	95	−282	Active Corrosion			
18R	4M Cl^-, pH 0.06	95	−288	Active Corrosion			
39	4M Cl^-, pH 2.91	60	−337	56	−61	8×10^{-7}	8×10^{-7}
40	4M Cl^-, pH 1.13	60	−332	73	−24	4×10^{-6}	3×10^{-4}
41	4M Cl^-, pH 0.0	60	−291	−47	−51	2.5×10^{-4}	3×10^{-2}
22	4M Cl^-, pH 2.0	30	−323	770	757	1×10^{-6}	6×10^{-6}
19	4M Cl^-, pH 0.01	30	−284	913	913	2×10^{-5}	1.5×10^{-3}
21	4M Cl^-, pH −0.36	30	−287	Active Corrosion			
42	0.5M Cl^-, pH 6.08	95	−448	269	12	1.5×10^{-6}	5×10^{-6}
23	0.5M Cl^-, pH 1.0	95	−301	248	19	8×10^{-6}	5×10^{-4}
25	0.5M Cl^-, pH 0.1	95	−292	Active Corrosion			
27	0.5M Cl^-, pH 1.02	30	−269	816	791	1×10^{-6}	4×10^{-6}
29	0.5M Cl^-, pH 0.17	30	−284	869	864	4×10^{-6}	3×10^{-4}

Table C-6. Electrochemical parameters from cyclic potentiodynamic polarization curves of alloy 825 in simulated crevice solutions (cont'd)

Test	Environment	Temp. (°C)	E_{corr} (mV_{SCE})	E_p (mV_{SCE})	E_{rp} (mV_{SCE})	i_{pass} A/cm²	i_{peak} A/cm²
43	3 M Cl^-, pH 3.08	95	−349	32	−85	1.5×10^{-6}	1.5×10^{-6}
31	3M Cl^-+0.25M SO_4^{2-}, pH 1.1	95	−277	96	−77	2×10^{-6}	2×10^{-6}
33	3M Cl^-+0.25M SO_4^{2-}, pH 0.03	95	−289	Active Corrosion			
35	3M Cl^-+0.25M SO_4^{2-}, pH 1.1	30	−290	835	835	1×10^{-6}	1×10^{-6}

Table C-7. Effect of other anions on cyclic potentiodynamic polarization behavior of alloy 825. The pH values reported are final room temperature values unless otherwise noted.

Environment	**Temp. (°C)**	**E_{corr} (mV_{SCE})**	**E_p (mV_{SCE})**	**E_{rp} (mV_{SCE})**
1,000 ppm Cl^- + 85 ppm HCO_3^- + 20 ppm SO_4^{2-} + 10 ppm NO_3^- + 2 ppm F^-, pH 8.9	**30**	−416	817	165
1,000 ppm Cl^- + 85 ppm HCO_3^- + 20 ppm SO_4^{2-} + 10 ppm NO_3^- + 2 ppm F^-, pH 8.2	95	−555	626	82
10,000 ppm Cl^- + 85 ppm HCO_3^- + 20 ppm SO_4^{2-} + 10 ppm NO_3^- + 2 ppm F^-, pH 8.9	**30**	−533	864, 387	−20, −1
10,000 ppm Cl^- + 85 ppm HCO_3^- + 20 ppm SO_4^{2-} + 10 ppm NO_3^- + 2 ppm F^-, pH 9.1	**50**	−495	606	46
10,000 ppm Cl^- + 85 ppm HCO_3^- + 20 ppm SO_4^{2-} + 10 ppm NO_3^- + 2 ppm F^-, pH 9.32	95	−477	418	−77*
SJ-13 water + 0.0232g/l sodium metasilicate	95	−565, −555	773, 763	729, 719
SJ-13 water + 300 ppm Cl^- + 0.023g/l sodium metasilicate	95	−545, −518	713, 731	40, 31
1,000 ppm Cl^- (added as $MgCl_2 \cdot 6H_2O$) + 85 ppm HCO_3^- + 20 ppm SO_4^{2-} + 10 ppm NO_3^- + 2 ppm F^-, pH 8.1	95	−644, −659	605, 546	−4, −75
10,000 ppm Cl^- + 85 ppm HCO_3^- + 20 ppm SO_4^{2-} + **1,000 ppm NO_2^-** + 2 ppm F^-, pH 8.9	95	−432	577	577

* This value was chosen instead of a lower value derived from the intersection of forward and backward scan because of the heavy crevice corrosion.

Bold characters indicate the species factor that was changed with respect to the reference environment of 1,000 ppm Cl^- + 20 ppm SO_4^{2-} + 10 ppm NO_3^- + 2 ppm F^- + 85 ppm HCO_3^- at 95 °C

SJ-13 — Simulated J-13 water

Table C-7. Effect of other anions on cyclic potentiodynamic polarization behavior of alloy 825. The pH values reported are final room temperature values unless otherwise noted. (cont'd)

Environment	Temp. °C	E_{corr} (mV_{SCE})	E_p (mV_{SCE})	E_{rp} (mV_{SCE})
1,000 ppm Cl^- + 85 ppm HCO_3^- + 20 ppm SO_4^{2-} + **1,000 ppm NO_3^-** + 2 ppm F^-, pH 8.9, **Nitrate added at +979 mV_{SCE}**	95	–521	733	188
1,000 ppm Cl^- + 85 ppm HCO_3^- + 20 ppm SO_4^{2-} + **1,000 ppm NO_3^-** + 2 ppm F^-, pH 8.9, **Nitrate added at +592 mV_{SCE}**	95	–493	728	676
1,000 ppm Cl^- + **1,000 ppm HCO_3^-** + 20 ppm SO_4^{2-} + 10 ppm NO_3^- + 2 ppm F^-, pH 10.2	95	–512, –498	657, 673	–167, –303
1,000 ppm Cl^- + **2,000 ppm HCO_3^-** + 20 ppm SO_4^{2-} + 10 ppm NO_3^- + 2 ppm F^-, pH 10.1	95	–537, –532	660, 673	–29, 9
1,000 ppm Cl^- + 85 ppm HCO_3^- + **20,000 ppm SO_4^{2-}** + 10 ppm NO_3^- + 2 ppm F^-, pH 9.5	95	–445	672	400
3.6 ppm Cl^- + 85 ppm HCO_3^- + 20 ppm SO_4^{2-} + 10 ppm NO_3^- + 2 ppm F^-, **1 atm. CO_2, pH 5.3**	95	–472	926	878
1,000 ppm Cl^- + 85 ppm HCO_3^- + 20 ppm SO_4^{2-} + 10 ppm NO_3^- + 2 ppm F^-, **1 atm. CO_2, pH 5.3**	95	–507	586	–315

Bold characters indicate the species factor that was changed with respect to the reference environment of 1,000 ppm Cl^- + 20 ppm SO_4^{2-} + 10 ppm NO_3^- + 2 ppm F^- + 85 ppm HCO_3^- at 95 °C

Table C-8. Effect of other anions on cyclic potentiodynamic polarization behavior of alloy type 316L stainless steel. The pH values are final room temperature values unless otherwise noted.

Environment	Temp. (°C)	E_{corr} (mV_{SCE})	E_p (mV_{SCE})	E_{rp} (mV_{SCE})
1,000 ppm Cl^- + 85 ppm HCO_3^- + 20 ppm SO_4^{2-} + 10 ppm NO_3^- + 2 ppm F^-	95	−680	97	−171
1,000 ppm Cl^- + 85 ppm HCO_3^- + 20 ppm SO_4^{2-} + **10,000 ppm NO_3^-** + 2 ppm F^-, pH 9.7	95	−652	746	746
1,000 ppm Cl^- + 85 ppm HCO_3^- + 20 ppm SO_4^{2-} + **1,000 ppm NO_3^-** + 2 ppm F^-, pH 9.5	**60**	−425	—	96
1,000 ppm Cl^- + **2,000 ppm HCO_3^-** + 20 ppm SO_4^{2-} + 10 ppm NO_3^- + 2 ppm F^-	95	−536	433	−16
1,000 ppm Cl^- + 85 ppm HCO_3^- + **20,000 ppm SO_4^{2-}** + 10 ppm NO_3^- + 2 ppm F^-, pH 7.99 (initial)	**60**	−341	836	−137
1,000 ppm Cl^- + 85 ppm HCO_3^- + **20,000 ppm SO_4^{2-}** + 10 ppm NO_3^- + 2 ppm F^-, pH 7.94 (initial)	95	−420	417	−163
3.6 ppm Cl^- + 85 ppm HCO_3^- + 20 ppm SO_4^{2-} + 10 ppm NO_3^- + 2 ppm F^-, **1 atm. CO_2, pH 5.4**	95	−560	926	926
1,000 ppm Cl^- + 85 ppm HCO_3^- + 20 ppm SO_4^{2-} + 10 ppm NO_3^- + 2 ppm F^-, **1 atm. CO_2, pH 5.5**	95	−510	−13	−358
1,000 ppm Cl^- + 85 ppm HCO_3^- + 20 ppm SO_4^{2-} + 10 ppm NO_3^- + 2 ppm F^-, **1 atm. CO_2, pH 5.5**	**60**	−321	263	−64

Bold characters indicate the species factor that was changed with respect to the reference environment of 1,000 ppm Cl^- + 20 ppm SO_4^{2-} + 10 ppm NO_3^- + 2 ppm F^- + 85 ppm HCO_3^- at 95 °C

Table C-9. Results of cyclic potentiodynamic polarization tests on alloy C-22 at 95 °C

Solution	pH	E_p (mV_{SCE})	E_{rp} (mV_{SCE})	Appearance
0 ppm Cl^- + SJ-13 solution	8.34	737	588	dark spots
6 ppm Cl^- + SJ-13 solution	8.28	727	507	bronze; spots; pits?
6 ppm Cl^- + SJ-13 solution	8.27	681	531	dark spots
6 ppm Cl^- + SJ-13 solution	8.41	729	559	gold spots; no pits
6 ppm Cl^- + SJ-13 solution	8.38	722	557	gold color w/dark spots; no pits
6 ppm Cl^- + SJ-13 solution	7.88	761	513	yellowish; many small pits
300 ppm Cl^- + silicate	8.90	716	355	gold colored; no pits
1,000 ppm Cl^- (as KCl) + SJ-13 solution	8.27	666	346	bronze color
1,000 ppm Cl^- + SJ-13 solution	8.29	542	346	bronze; spots faded away
1,000 ppm Cl^- + SJ-13 solution	8.42	661	332	bronze; spots faded away
1,000 ppm Cl^- + SJ-13 solution	8.43	679	326	uniform gold color
1,000 ppm Cl^- + SJ-13 solution	8.45	682	378	uniform gold color; no pits
1,000 ppm Cl^- + 0.01 M $S_2O_3^{2-}$	4.00	860	689	deep pits; green color in pits
10,000 ppm Cl^- + SJ-13 solution	7.94	618	406	uniform gold color
10,000 ppm Cl^- + 1,000 ppm SO_4^{2-} + SJ-13 solution	8.33	619	363	uniform gold color

Table C-9. Results of cyclic potentiodynamic polarization tests on alloy C-22 at 95 °C (cont'd)

Solution	pH	E_p (mV_{SCE})	E_{rp} (mV_{SCE})	Appearance
1 molal Cl^- + 0.01 M $S_2O_3^{2-}$	4.00	550	550	thick bronze color; maybe a few small pits
4 molal Cl + 85 ppm HCO_3 + 20 ppm SO_4^{2-} + 10 ppm NO_3^- + 2 ppm F^-	7.40	792	392	bronze; small pits
4 molal Cl^-	4.00	911	−119	many small fine pits; a few larger pits; grain boundaries appear visible
4 molal Cl^-	1.00	785	785	a few small spots
4 molal Cl^-	9.00	560	337	bronze film uneven in thickness; many spots
6.2 molal Cl^-	4.00	656	626	bronze; spots
6.2 molal Cl^-	4.00	667	632	bronze; spots; shallow pits
6.2 molal Cl^- + 0.01 M $S_2O_3^{2-}$	4.00	662	642	bronze; spots; small areas of shallow attack
9.1 molal Cl^- (as LiCl)	4.00	717	642	spots; no pits
14 molal Cl^- (as 40% $MgCl_2$)	—	21	−254	pits; etched; grains visible

APPENDIX D

STRESS CORROSION CRACKING EXPERIMENTS ON THE AUSTENITIC ALLOYS—DATA TABLES

Table D-1. Results of slow strain rate control tests ($\dot{\varepsilon}=1\times10^{-6}$ s^{-1}) for type 316L stainless steel and alloy 825 in glycerol

Specimen	T (°C)	Elong. (%)	Failure Time (h)
316L smooth	95	60.4	170.3
316L smooth	120	54.4	155.3
316L notched	95	2.10[a]	46.5
825 smooth	95	52.8	150.3
825 smooth	120	53.4	153.6
825 notched	95	2.21[a]	46.5

[a] = extension in mm

Table D-2. Results of slow strain rate tests ($\dot{\varepsilon}=1\times10^{-6}\ s^{-1}$) of type 316L stainless steel in dilute chloride solutions at 95 °C

Spec.	Cl^- (ppm)	SO_4^{2-} (ppm)	Gas	E_{corr} (mV_{SCE})	E_{app} (mV_{SCE})	Current (A)	Initial pH	Final pH	Elong. (%)	Failure Time (h)	Test Results
S	10,000	10,000	N_2	—	0	10^{-2}	4.0	—	20.2	59.5	Severe pitting
S	10,000	10,000	Air	0 to −200	O.C.	—	4.0	—	57.8	167.9	Ductile failure
S	1,000	1,000	N_2	—	0	10^{-5} to 10^{-6}	7.0	—	61.0	221.0	Ductile failure
S	1,000	20	CO_2	−510	50 to 0	3×10^{-4} to -6×10^{-6}	—	5.3	68.0	196.0	Ductile failure
S	1,000	20	CO_2	−520	100	1×10^{-4} to 8×10^{-4}	—	5.4	46.2	131.5	Ductile failure/ pitting
S	10,000	20	CO_2	−260	−100	-3×10^{-5} to 2×10^{-4}	—	5.3	55.0	152.0	Ductile failure
S	10,000	20	CO_2	−260	−50	10^{-4} to 10^{-3}	—	5.5	43.8	89.4	Ductile failure/ pitting
S	10,000	20	CO_2	−310	−50	2.0×10^{-4}	—	6.4	41.4	135.6	Ductile failure/ pitting
S[a]	10,000	20	CO_2	−320	−100	5×10^{-4} to 3×10^{-3}	—	5.4	57.8	162.9	Ductile failure/ pitting
S[a]	10,000	20	CO_2	−330	−130	5×10^{-6} to 1×10^{-5}	—	5.6	68.6	188.9	Ductile failure
N	1,000	20	CO_2	−250	100	5.0×10^{-3}	—	5.5	2.41[c]	58.9	Ductile failure
N[b]	1,000	20	CO_2	−260	0 to −280	5.2×10^{-6}	—	—	1.52[c]	57.5	Ductile failure
N[b]	1,000	20	CO_2	—	50	5.3×10^{-5}	—	—	1.78[c]	48.9	Ductile failure
N[b]	1,000	20	CO_2	−250	80	-5×10^{-6} to 10^{-3}	8.1	5.2	2.11[c]	45.5	Ductile failure
N[b]	10,000	20	CO_2	−250	−100	-1×10^{-5} to 5×10^{-4}	7.8	5.6	2.18[c]	47.3	Ductile failure

S – Smooth specimen N – Notched specimen O.C. – Open circuit a – with PTFE tape b – with O-ring c – extension in mm

Table D-3. Results of slow strain rate tests ($\dot{\varepsilon}$=2.2×10^{-7} s^{-1}) of type 316L stainless steel in deaerated 1 M NaCl solution at 95 °C using specimen with crevice-forming device

E_{corr} (mV_{SCE})	E_{app} (mV_{SCE})	Current (A)	Initial pH	Final pH	Elong. (%)	Failure Time (h)	Test Results
–265	–260 to –210	-10^{-6} to 2.8×10^{-5}	3.9	8.0	63.2[a]	176.5[a]	Ductile failure, small pits in crevice
–245	O.C. (–219 to –373)	—	3.9	8.0	60.4[a]	173.0[a]	Ductile failure, small pits in crevice
–256	–256 to –150	-10^{-6} to 2.0×10^{-4}	3.9	7.9	35.0	421.0	Ductile failure with pitting
–339	–250 to –150[b]	1×10^{-5} (Galvanostatic)	4.0	7.3	38*	470*	Ductile failure with pitting; some small cracks.
–259	—256 to –141[b]	$5–7\times10^{-5}$ (Galvanostatic)	4.0	7.9	34*	420*	Ductile failure with pitting; some small cracks.
–287	—275 to –214[b]	3×10^{-5} (Galvanostatic)	4.0	7.7	42.2	508.0	Crevice corrosion/pitting and ductile failure
-270	–300 to 0.059	3×10^{-6} (Galvanostatic)	4.0	8.2	42.2	516.0	Crevice corrosion/pitting and ductile failure; some small cracks

O.C. – open circuit a – $\dot{\varepsilon}$=1×10^{-6} s^{-1} b – potential variation during galvanostatic test * – approximate values

Table D-4. Results of slow strain rate tests of type 316L stainless steel in dilute chloride solutions with the addition of thiosulfate at 95 °C

Solution	Gas	E_{corr} (mV_{SCE})	E_{app} (mV_{SCE})	Current (A)	Initial pH	Final pH	Elong. (%)	Failure Time (h)	Test Results
1,000 ppm Cl^- + 10^{-3} M $Na_2S_2O_3$	CO_2	−232	−175 to 78	10^{-6} to 10^{-5}	8.3	6.5	60.4[a]	176[a]	Ductile failure
1,000 ppm Cl^- + 10^{-3} M $Na_2S_2O_3$	CO_2	−186	O.C. (−285 to −155)	—	8.3	6.5	64.2[a]	179[a]	Ductile failure
1,000 ppm Cl^- + 10^{-2} M $Na_2S_2O_3$	CO_2	−209	−183 to 20	10^{-6} to 9×10^{-5}	7.8	5.1	28.4[b]	364[b]	Localized corrosion; no SCC
1,000 ppm Cl^- + 10^{-2} M $Na_2S_2O_3$	CO_2	−237	O.C. (−238 to −296)	—	7.8	—	No failure	477[b]	Test interrupted; no SCC
1,000 ppm Cl^- + 10^{-3} M $Na_2S_2O_3$	CO_2	−200	−200	10^{-6}	7.7	5.2	2.51[d]	950[c]	Ductile failure
1,000 ppm Cl^- + 10^{-2} M $Na_2S_2O_3$[f]	CO_2	−179	O.C. (−180 to −120)	—	4.0	6.2	69.4[b]	787[b]	Ductile failure[f]

O.C. – Open circuit

a – $\dot{\varepsilon}=1.0\times10^{-6}$ s^{-1}

b – $\dot{\varepsilon}=2.2\times10^{-7}$ s^{-1}

c – Notched specimen at extension rate = 7.1×10^{-7} mm/s (2.8×10^{-8} in./s)

d – extension in mm

e – Constant deflection test at 105 percent yield for 476 hr and at 130 percent yield for 456 hr

f – Solution-annealed specimen

Table D-5. Results of constant extension tests of type 316L stainless steel in various solutions at 95 °C

Solution	Gas	E_{corr} (mV_{SCE})	E_{app} (mV_{SCE})	Current (A)	Initial/ Final pH	Elong. (%)	Test Time (h)	Test Results
1,000 ppm Cl^- +0.01 M $S_2O_3^{2-}$	N_2/ O_2	−155	O.C. (−155 to −67)	—	4.0/ 4.5	12	932	Localized corrosion; no SCC
1,000 ppm Cl^- +0.01 M $S_2O_3^{2-}$	N_2/ O_2	−142	−100 to −173	1.0×10^{-6} to 1.0×10^{-3}	4.0/ 7.5	12	932	Localized corrosion; no SCC
1 molar Cl^- [a]	N_2	−468	141 to −371	8.5×10^{-7} to 2.5×10^{-6} (Galvanostatic)	3.9/ 7.9	7.8	845	Crevice corrosion; no SCC
1 molar Cl^- [a] +0.01 M $S_2O_3^{2-}$	N_2	−353	−340 to −420	1.0×10^{-6} to 3.0×10^{-6} (Galvanostatic)	4.0/ 8.2	7.6	845	Crevice corrosion; some small cracks
O.C. – Open circuit [a] – PTFE/PFA crevice								

Table D-6. Results of slow strain rate tests ($\dot{\varepsilon}=1\times10^{-6}$ s^{-1}) of type 316L stainless steel in concentrated chloride solutions

Solution	T (°C)	E_{corr} (mV_{SCE})	E_{app} (mV_{SCE})	Current (A)	Initial/ Final pH	Elong. (%)	Failure Time (h)	Test Results
14.0 molal Cl^- (40% $MgCl_2$)	120	–311	O.C. (–343 to –306)	—	—	7.4	22.9	IGSCC and TGSCC
14.0 molal Cl^- (40% $MgCl_2$)	120	–280	–260 to –275	10^{-5} to 4×10^{-3}	—	4.6	12.4	IGSCC and TGSCC
9.1 molal Cl^- (30% $MgCl_2$)	110	–331	O.C. (–331 to –367)	—	4.9/ 5.9	49.4	138.6	IGSCC and ductile
9.1 molal Cl^- (30% $MgCl_2$)	110	–326	–316 to –360	10^{-5} to 3×10^{-3}	4.9/ 5.9	15.2	44.7	IGSCC and TGSCC
13.9 molal Cl^- (LiCl)	120	–356	O.C. (–345 to –402)	—	1.6/ 1.4	15.6	44.2	TGSCC and IGSCC
13.9 molal Cl^- (LiCl)	120	–353	–322	10^{-6} to 1.0×10^{-3}	1.6/ 2.0	2.6	7.2	TGSCC, some IGSCC
13.9 molal Cl^- (LiCl)	115	–333	O.C. (–312 to –400)	—	3.9/ 6.1	17.0	45.6	SCC, several secondary cracks
13.9 molal Cl^- (LiCl)	100	–328	O.C (–318 to –466)	—	4.0/ 6.4	27.8	78.0	TGSCC, some IGSCC
13.9 molal Cl^- (LiCl)	95	–340	O.C. (–319 to 376)	—	4.1/ 6.4	25.8	73.3	SCC, several secondary cracks
9.1 molal Cl^- (LiCl)	110	–353	O.C. (–353 to –370)	—	2.1/ 6.1	29.4	79.2	TGSCC, IGSCC some ductile
9.1 molal Cl^- (LiCl)	110	–343	–320 to –340	-1×10^{-5} to 10^{-3}	2.1/ 5.9	13.2	38.3	TGSCC and IGSCC
9.1 molal Cl^- (LiCl)	100	–339	O.C. (–298 to –391)	—	4.0/ 4.6	31.0	87.0	SCC

O.C. – open circuit

Table D-6. Results of slow strain rate tests ($\dot{\varepsilon}$=1×10^{-6} s^{-1}) of type 316L stainless steel in concentrated chloride solutions (cont'd)

Solution	T (°C)	E_{corr} (mV_{SCE})	E_{app} (mV_{SCE})	Current (A)	Initial/ Final pH	Elong. (%)	Failure Time (h)	Test Results
9.1 molal Cl^- (LiCl)	95	−342	O.C. (−319 to −367)	—	4.0/ 4.4	40.6	117.0	SCC
9.1 molal Cl^- (LiCl)	95	−347	−333 to −350	-5×10^{-7} to $>1.0\times10^{-3}$	3.9/ 5.3	33.4	92	SCC
9.1 molal Cl^- (LiCl)	95	−337	−307 to −399	-2×10^{-6} to 1.4×10^{-6}	3.9/ 5.3	63.6	180	Ductile failure; no sign of SCC
9.1 molal Cl^- (LiCl)	95	−339	−359 to −362	-2×10^{-6} to 4×10^{-5}	3.9/ 5.9	59.6	171	Ductile failure; small cracks in necked region
9.1 molal Cl^- (LiCl)	95	−348	−378 to −380	-2×10^{-6} to 1×10^{-6}	3.9/ 6.1	62.2	178	Ductile failure; some small pits
7.2 molal Cl^- (LiCl)	100	−342	O.C. (−319 to −356)	—	4.0/ 6.2	47.4	135.0	SCC
6.2 molal Cl^- (NaCl)	95	−361	O.C. (−350 to −390)	—	2.6/ —	64.0	177.7	Ductile failure
6.2 molal Cl^- (NaCl)	95	−363	−345 to −380	-1×10^{-5} to 2.0×10^{-3}	2.6/ 7.0	28.8	80.2	Ductile failure/pitting
6.2 molal Cl^- (NaCl)	95	−359	−360 to −380	10^{-7} to 10^{-4}	2.7/ 6.7	35.6^a	267.2^a	Ductile failure/pitting
6.2 molal Cl^- (NaCl)	95	−356	−340 to −380	5×10^{-3}	2.7/ 8.2	13.2^a	104.3^a	Severe pitting
6.2 molal Cl^- (LiCl)	95	−340	−320 to −348	5×10^{-3}	2.4/ 7.9	10.8^a	90.3^a	Severe pitting
6.2 molal Cl^- (LiCl)	95	−347	−294 to −680	-2×10^{-4} to 5×10^{-3}	2.5/ 5.6	56.0^a	435.1^a	Ductile failure/pitting

O.C. – open circuit   a – $\dot{\varepsilon}$=3.6×10^{-7} s^{-1}

Table D-6. Results of slow strain rate tests ($\dot{\varepsilon}=1\times10^{-6}$ s^{-1}) of type 316L stainless steel in concentrated chloride solutions (cont'd)

Solution	T (°C)	E_{corr} (mV_{SCE})	E_{app} (mV_{SCE})	Current (A)	Initial/ Final pH	Elong. (%)	Failure Time (h)	Test Results
6.2 molal Cl– (LiCl)	95	−362	−391 to −355	10^{-6} to 10^{-5}	3.2/ 5.8	30.6[b]	397[b]	Ductile failure/pitting
6.2 molal Cl^- (LiCl)	95	−342	−660 to −330	10^{-6} to 10^{-5}	3.7/ 3.9	36.4[b]	469[b]	Ductile failure/pitting
6.2 molal Cl^- (NaCl)	95	−352	O.C. (−350 to −340)[c]	10^{-6} to 3×10^{-4}	3.2/ 6.8	55.0[b]	650[b]	Ductile failure/pitting
6.2 molal Cl^- (NaCl)	95	−332	−330[c]	10^{-6} to 10^{-3}	3.2/ 7.3	63.4[b]	795[b]	Ductile failure/pitting
6.2 molal Cl^- (NaCl)	95	−347	−280 to −389[c,d]	2×10^{-5} (Galvanostatic)	4.4/ —	42.4[b]	554.4[b]	Ductile failure/pitting
6.2 molal Cl^- (NaCl)	95	−341	−237 to −374[c,d]	4×10^{-5} (Galvanostatic)	4.4/ 7.4	31.8[b]	404.5[b]	Ductile failure/pitting

O.C. – open circuit b – $\dot{\varepsilon}=2.2\times10^{-7}$ s^{-1} c – PFA/PTFE crevice d – potential variation during galvanostatic test

Table D-7. Results of slow strain rate tests ($\dot{\varepsilon}=2.2\times10^{-7}$ s^{-1}) of type 316L stainless steel and alloy 825 in concentrated chloride solutions with the addition of thiosulfate at 95 °C

Alloy	Solution	E_{corr} (mV_{SCE})	E_{app} (mV_{SCE})	Current (A)	Initial/ Final pH	Elong. (%)	Failure Time (h)	Test Results
Mill-annealed Type 316L SS	5.8 molal NaCl + 0.01 M $Na_2S_2O_3$	−393	O.C. (−386 to −450)	—	—/ —	12.2	155	IGSCC, TGSCC
Mill-annealed Type 316L SS	5.8 molal NaCl + 0.01 M $Na_2S_2O_3$	−391	−420 to −391	10^{-6} to 2×10^{-4}	—/ —	18.0	241	IGSCC, TGSCC
Mill-annealed Type 316L SS	6.2 molal NaCl + 0.01 M $Na_2S_2O_3$	−384	−137 to −400	-5×10^{-3} to 2.3×10^{-4}	4.0/ 5.3	9.2	126.6	IGSCC, TGSCC
Solution-annealed Type 316L SS	6.2 molal NaCl + 0.01 M $Na_2S_2O_3$	−381	O.C. (−358 to −438)	—	4.0/ 4.9	11.4	145	IGSCC, TGSCC
Alloy 825	5.8 molal NaCl + 0.01 M $Na_2S_2O_3$	−336	O.C. (−296 to −381)	—	3.4/ 3.8	47.6	613	Pitting/ductile failure (Pits at vapor/ solution interface)
Alloy 825	5.8 molal NaCl + 0.01 M $Na_2S_2O_3$	−339	−325 to −344	-3×10^{-6} to 3×10^{-4}	3.4/ 3.8	34.6	431	Pitting/ductile failure (Pits at vapor/ solution interface)
Alloy 825	5.8 molal NaCl + 0.01 M $Na_2S_2O_3$	−330	O.C. and −0.322	-1×10^{-5} to 10^{-4}	3.4/ —	2.62[a]	1,104[a]	No SCC

O.C. – open circuit a – Notched specimen; extension rate of 7.1×10^{-7} mm/s; elongation in mm; test interrupted without failure

* – PFA/PTFE crevice

Table D-8. Summary of U-bend test results for type 316L stainless steel in dilute chloride solutions at 95 °C

Solution	Purging Gas	E_{corr} (mV_{SCE})	E_{app} (mV_{SCE})	Current (A)	Initial pH	Final pH	Test Time (h)	Results
1,000 ppm Cl^- as NaCl	79% N_2 21% O_2	–130	O.C. (–130 to –230)	—	4.0	—	528	No SCC, shallow pits above V/S interface
1,000 ppm Cl^- as NaCl	79% N_2 21% O_2	–180	–140 to –100	10^{-4} to 10^{-6}	4.0	—	528	SCC on leg above V/S interface
1,000 ppm Cl^- as NaCl	79% N_2 21% O_2	–110 –180[a] –240[b]	O.C.	—	4.3 4.1[a] 4.5[b]	— 5.8[a] 8.3[b]	504 672[a] 672[b]	No SCC No SCC, shallow pits on leg above V/S interface[a] SCC on leg above V/S interface[b]
1,000 ppm Cl^- as NaCl	79% N_2 21% O_2	–70 –190[a] –170[b]	–55 to 5 –100[a] –100[b]	10^{-7} to 10^{-6} 10^{-6} to 10^{-5} 10^{-6} to 10^{-4}	4.3 4.1[a] 4.5[b]	— 5.8[a] 8.3[b]	504 672[a] 672[b]	No SCC, shallow pits on leg No SCC, pits on leg in vapor phase[a] SCC on leg above V/S interface[b]
1,000 ppm Cl^- as NaCl + 0.01 M $Na_2S_2O_3$	—	–130	O.C.	—	—	—	288	SCC on leg above V/S interface and pits at V/S interface
1,000 ppm Cl^- as NaCl + 0.01 M $Na_2S_2O_3$	—	–130	–20 to –110	10^{-5} to 10^{-6}	—	—	288	SCC on leg above V/S interface
1,000 ppm Cl^- as NaCl + 0.01 M $Na_2S_2O_3$	79% N_2 21% O_2	–270	O.C. (–270 to –200)	—	4.0	—	528	No SCC, pits above V/S interface
1,000 ppm Cl^- as NaCl + 0.01 M $Na_2S_2O_3$	79% N_2 21% O_2	–270	–220	10^{-6}	4.0	—	528	SCC at top of leg above bolt and V/S interface
1,000 ppm Cl^- as NaCl + 0.01 M $Na_2S_2O_3$	79% N_2 21% O_2	–240 –240[a]	O.C.	—	4.9 4.6[a]	— 8.3[a]	504 672[a]	No SCC, shallow pits on leg SCC on leg under bolt washer above V/S interface[a]

a – Second test period b – Third test period V/S – vapor/solution

Table D-8. Summary of U-bend test results for type 316L stainless steel in dilute chloride solutions at 95 °C (cont'd)

Solution	Purging Gas	E_{corr} (mV_{SCE})	E_{app} (mV_{SCE})	Current (A)	Initial pH	Final pH	Test Time (h)	Results
1,000 ppm Cl$^-$ as NaCl + 0.01 M $Na_2S_2O_3$ [a]	none	−128 −129	O.C. O.C.	— —	4.0 4.0	4.9 5.0	672 672 [c]	Pitting; no SCC Pitting; extensive localized corrosion
1,000 ppm Cl$^-$ as NaCl + 0.01 M $Na_2S_2O_3$ [a]	none	−147 −107	−60 to −160 −98 to −187	-10^{-5} to 10^{-4} -10^{-5} to 10^{-4}	4.0 4.0	4.9 5.0	672 672 [c]	Pitting; no SCC Pitting; extensive localized corrosion
1,000 ppm Cl$^-$ as NaCl + 0.01 M $Na_2S_2O_3$ [a,b]	none	−104	O.C.	—	4.0	5.1	672	SCC and severe pitting on apex above V/S interface
1,000 ppm Cl$^-$ as NaCl + 0.01 M $Na_2S_2O_3$ [a,b]	none	−122	−108 to −159	-10^{-4} to 10^{-4}	4.0	5.1	672	SCC and severe pitting on apex above V/S interface
1,000 ppm Cl$^-$ as NaCl [b]	none	−46 −30	O.C. (−46 to −115) O.C. (−30 to −235)	— —	4.0 4.0	5.5 7.2	672 672 [c]	Pitting/Broad crack at apex Pitting/Broad crack at apex
1,000 ppm Cl$^-$ as NaCl [b]	none	−44 +15	−28 to −118 12 to −79	-10^{-4} to 10^{-4} -10^{-5} to 10^{-4}	4.0 4.0	5.5 7.2	672 672 [c]	Pitting at apex above V/S interface Pitting at apex above V/S interface
1 molar Cl$^-$ as NaCl [b]	none	−236 −189	−229 to −325 −174 to −319	-10^{-4} to 10^{-3} -10^{-4} to 10^{-3}	4.0 4.0	6.8 7.5	672 672 [c]	Pitting; no SCC SCC at apex/pitting
1 molar Cl$^-$ as NaCl [b]	none	−241 −189	O.C. (−195 to −312) O.C. (−189 to −326)	— —	4.0 4.0	6.8 7.5	672 672 [c]	Pitting; no SCC SCC at apex/pitting

O.C. – open circuit   V/S – vapor/solution   a – mill-finished surface   b – inverted specimen   c – second test period

Table D-9. Summary of U-bend test results for type 316L stainless steel in concentrated chloride solutions at 95 °C

Solution	Purging Gas	E_{corr} (mV_{SCE})	$E_{applied}$ (mV_{SCE})	Current (A)	Initial pH	Test time (h)	Results
5.8 molal Cl^- as LiCl	79% N_2 21% O_2	–340	O.C.	—	4.0	528	SCC on bend and leg
5.8 molal Cl^- as LiCl	79% N_2 21% O_2	–340	–290	10^{-4}	4.0	528	SCC on bend and leg, pits on bend
9.03 molal Cl^- as LiCl	—	–350	O.C.	—	4.0	288	SCC on bend and leg
9.03 molal Cl^- as LiCl	—	–350	–320	10^{-5} to 10^{-3}	4.0	288	SCC on bend and leg
9.1 molal Cl^- as LiCl	none	–337	-405	-10^{-3}	4.0	672	No SCC below V/S interface. some small cracks above solution level
9.1 molal Cl^- as LiCl	none	–336	O.C. (–336 to –347)	—	4.0	672	Severe SCC above and below V/S interface
5.94 molal Cl^- as NaCl	79% N_2 21% O_2	–340	O.C.	—	4.0	528	SCC around pit on bend
5.94 molal Cl^- as NaCl	79% N_2 21% O_2	–350	–350 to –300	10^{-4}	4.0	528	SCC on bend and leg, pits on bend
6.2 molal Cl^- as NaCl	—	–390	O.C.	—	4.0	288	Pit on bend
6.2 molal Cl^- as NaCl	—	–390	–480 to –340	10^{-5} to 10^{-3}	4.0	288	SCC on leg
6.2 molal Cl^- as NaCl + 0.01 M $Na_2S_2O_3$	—	–350	O.C.	—	4.0	288	SCC on bend and leg
6.2 molal Cl^- as NaCl + 0.01 M $Na_2S_2O_3$	—	–350	–340	10^{-5} to 10^{-4}	4.0	288	SCC on bend and leg, some shallow pits

O.C. – open circuit V/S – Vapor/Solution

Table D-10. Summary of double U-bend test results for type 316L stainless steel in chloride solutions at 95 °C

Solution	Purging Gas	E_{corr} (mV_{SCE})	E_{app} (mV_{SCE})	Current (A)	Initial pH	Final pH	Test Time (h)	Results
1,000 ppm Cl^- as NaCl + 0.01 M $Na_2S_2O_3$	none	−163 −198	−150 to −227 −142 to −187	-10^{-5} to 10^{-4} -10^{-5} to 10^{-4}	4.0 4.0	5.1 6.0	672 [b] 672	Pitting. No SCC SCC on inner U-bend near apex below V/S interface
1,000 ppm Cl^- as NaCl + 0.01 M $Na_2S_2O_3$	none	−228 −188	O.C. O.C.	— —	4.0 4.0	5.1 6.0	672 672 [b]	Pitting. No SCC SCC on inner U-bend near apex below V/S interface
1,000 ppm Cl^- as NaCl + 0.01 M $Na_2S_2O_3$ [a]	none	−121	−2 to −205	-10^{-5} to 10^{-3}	4.0	6.5	672	SCC on inner U-bend near apex above V/S interface
1,000 ppm Cl^- as NaCl + 0.01 M $Na_2S_2O_3$ [a]	none	−134	O.C.	—	4.0	6.5	672	SCC on inner U-bend near apex above V/S interface
1,000 ppm Cl^- as NaCl [a]	none	−43	−29 to −120	-10^{-5} to 10^{-4}	4.0	5.9	672	Localized corrosion of both inner and outer U-bends. No SCC
1,000 ppm Cl^- as NaCl [a]	none	−98	O.C. (−84 to −128)	—	4.0	5.9	672	Localized corrosion of both inner and outer U-bends. No SCC
1 molar Cl^- as NaCl [a]	none	−245 −189	−150 to −300 −161 to −244	-10^{-5} to 10^{-4} -10^{-5} to 10^{-3}	4.0 4.0	6.8 7.0	672 672 [b]	Pitting at apex above V/S interface SCC inner U-bend below V/S
1 molar Cl^- as NaCl [a]	none	−216 −176	O.C. (−216 to −304) O.C. (−146 to −240)	— —	4.0 4.0	6.8 7.0	672 672 [b]	Pitting at apex above V/S interface SCC inner U-bend below V/S

O.C. – Open Circuit V/S – Vapor/Solution a – inverted specimen b – Second test period

Table D-11. Summary of U-bend test results for type 316L stainless steel (Heat P80746) in dilute chloride solutions at 95 °C

Solution	Purging Gas	E_{corr} (mV_{SCE})	E_{app} (mV_{SCE})	Current (A)	Initial pH	Final pH	Test Time (h)	Results
1,000 ppm Cl^- as NaCl + 0.01 M $Na_2S_2O_3$	none	–62 –39	O.C. O.C.	—	4.0 4.0	3.8 3.9	672 672 [b]	Pitting. No sign of SCC SCC above V/S interface
1,000 ppm Cl^- as NaCl + 0.01 M $Na_2S_2O_3$	none	–66 –39	–53 to –186 25 to –219	-10^{-5} to 10^{-4} -10^{-4} to 10^{-4}	4.0 4.0	3.8 3.9	672 672 [b]	Pitting. No sign of SCC SCC above V/S interface
1,000 ppm Cl^- as NaCl + 0.01 M $Na_2S_2O_3$ [a]	none	–102	O.C.	—	4.0	5.2	672	SCC and pitting on Apex above V/S interface
1,000 ppm Cl^- as NaCl + 0.01 M $Na_2S_2O_3$ [a]	none	–136	–100 to –178	-10^{-4} to 10^{-4}	4.0	5.2	672	SCC and pitting on Apex above V/S interface
1,000 ppm Cl^- as NaCl [a]	none	–53 +18	–37 to –122	-10^{-5} to 10^{-4}	4.0 4.0	5.5 7.5	672 672 [b]	Pitting at apex above V/S interface Pitting at apex above V/S interface
1,000 ppm Cl^- as NaCl [a]	none	–43	O.C. (–43 to –242)	—	4.0	5.5	672	SCC at apex above V/S interface
1,000 ppm Cl^- as NaCl [a]	none	–34	O.C. (–123 to –282)	—	4.0	7.5	672	SCC at apex above V/S interface
1 molar Cl^- as NaCl [a]	none	–256 –258	–247 to –317 –2 to –320	-10^{-5} to 10^{-4} -10^{-3} to $>10^{-3}$	4.0 4.0	7.1 7.3	672 672 [b]	No SCC SCC and pitting above and below V/S interface
1 molar Cl^- as NaCl [a]	none	–248 –220	O.C. (–248 to –290) O.C. (–220 to –342)	— —	4.0 4.0	7.1 7.3	672 672 [b]	No SCC Pitting at apex above V/S interface

O.C. – Open Circuit V/S – Vapor/Solution a – inverted specimen b – Second test period

Table D-12. Results of slow strain rate tests ($\dot{\varepsilon}=1\times10^{-6}$ s^{-1}) of alloy 825 in concentrated chloride solutions

Solution	T (°C)	E_{corr} (mV_{SCE})	E_{app} (mV_{SCE})	Current (A)	Initial/ Final pH	Elong. (%)	Failure Time (h)	Test Results
9.1 molal Cl^- (LiCl)	110	−297	−272 to −303	-2×10^{-6} to 7×10^{-5}	2.0/ 2.4	60.6	170.0	Pitting/ductile failure; pits at V/S interface
9.1 molal Cl– (LiCl)	110	−254	O.C. (−226 to −323)	—	2.0/ 1.8	62.6	179.0	Pitting/ductile failure; pits at V/S interface
9.1 molal Cl^- (LiCl)	110	−290	O.C. (−295 to −243)	—	2.0/ 3.0	1.96 [a]	757.0 [a]	No SCC; some small pits, corrosion in notched area
9.1 molal Cl^- [b] (LiCl)	115	−284	O.C. (−271 to −302)	—	3.8/ 6.2	51.4	167	Ductile/pitting failure
14 molal Cl^- (40% $MgCl_2$)	120	−262	−257 to −316	-2×10^{-6} to 3×10^{-4}	—/ —	36.4	102.5	TGSCC, many secondary cracks
14 molal Cl^- (40% $MgCl_2$)	120	−272	O.C. (−258 to −334)	—	—/ —	43.6	124.9	TGSCC, many secondary cracks

O.C. – open circuit V/S: vapor/solution

a – Notched specimen; extension rate of 7.2×10^{-7} mm/s (2.8×10^{-8} in./s); extension in mm; test interrupted without failure

b – Solution annealed and sensitized specimen (700 °C/15 hr)

Table D-13. Results of slow strain rate tests for alloy 825 (with a PTFE/PFA crevice) in concentrated chloride solutions

Solution	T (°C)	Gas	E_{corr} (mV_{SCE})	E_{app} (mV_{SCE})	Current (A)	Initial/ Final pH	Elong. (%)	Failure Time (h)	Test Results
6.2 molal Cl^-	100	N_2	−238	−165 to −300	-5×10^{-6} to $>4.0\times10^{-4}$	4.0/ 7.7	44.4	533.3^a	Crevice corrosion/ductile failure; no SCC
6.2 molal Cl^- + 0.01 M $S_2O_3^{2-}$	100	N_2	−332	−317 to −362	-3×10^{-5} to 1.4×10^{-4}	4.0/ 7.5	33.2	380.6^a	Crevice corrosion/ductile failure/SCC; many secondary cracks
9.1 molal LiCl	110	N_2	−260	−247 to −300	-1×10^{-5} to 1×10^{-3}	4.0/ 3.9	41.6	116.3^b	Ductile/SCC failure; many secondary cracks
9.1 molal LiCl	110	N_2	−290	O.C. (−250 to −400)	—	4.0/ 3.6	53.6	152.6^b	Ductile/SCC failure; some secondary cracks
40% $MgCl_2$ (14 molal Cl^-)	120	N_2	−275	O.C. (−260 to −322)	—	—	40.6	115.0^b	Ductile/SCC failure; many secondary cracks
40% $MgCl_2$ (14 molal Cl^-)	95	N_2	−280	O.C. (−255 to −314)	—	—	49.0	139.3^b	Ductile/SCC failure; some secondary cracks

O.C. – open circuit a – $\dot{\varepsilon}=1.0\times10^{-6}\ s^{-1}$ b – $\dot{\varepsilon}=2.2\times10^{-7}\ s^{-1}$

Table D-14. Summary of U-bend test results for alloy 825 in concentrated chloride solutions at 95 °C

Solution	E_{corr} (mV_{SCE})	E_{app} (mV_{SCE})	Current (A)	Initial pH	Final pH	Test Time (h)	Results
6.2 molal Cl$^-$ as NaCl	−170 to −270	O.C.	—	4.2 ±0.5	6.3±0.3	4,536	No SCC
6.2 molal Cl$^-$ as NaCl	−160	−160	-10^{-7} to 10^{-4}	3.8	—	504	No SCC; large pit on specimen leg
5.8 molal Cl$^-$ as LiCl	−260	O.C.	—	4.5±0.6	6.3±0.2	4,536	No SCC
5.8 molal Cl$^-$ as LiCl	−220	−220	10^{-6} to 10^{-3}	3.4	—	504	No SCC; large pit near apex of specimen
6.2 molal Cl$^-$ as NaCl	−270 to −180	−260 to −170	10^{-6} to 10^{-5}	4.2±1.3	5.8	1,344	No SCC; localized corrosion
5.8 molal Cl$^-$ as LiCl	−260 to −230	−250 to −220	10^{-6} to 10^{-4}	4.7±0.7	6.3±0.2	4,032	No SCC
9.0 molal Cl$^-$ as LiCl	−300 to −260	−290 to −260	-6×10^{-5} to 2×10^{-4}	4.3±0.1	—	3,360	No SCC; pits above and below V/S interface
9.0 molal Cl$^-$ as LiCl	−300 to −260	O.C.	—	4.3±0.1	—	3,360	No SCC; pits above and below V/S interface
6.2 molal Cl$^-$ as NaCl	−300 to −280	−260 to −330	-10^{-5} to 4×10^{-4}	4.1±0.6	6.5±0.2	2,688	No SCC
5.8 moles Cl$^-$ as LiCl	−310 to −260	O.C.	—	4.9±0.4	6.0±0.2	2,688	No SCC
5.8 moles Cl$^-$ as LiCl	−310 to −250	−300 to −320	-10^{-5} to 2×10^{-4}	4.9±0.4	6.0±0.2	2,688	No SCC

O.C. – open circuit V/S – vapor/solution

Table D-14. Summary of U-bend test results for alloy 825 in concentrated chloride solutions at 95 °C (cont'd)

Solution	E_{corr} (mV_{SCE})	E_{app} (mV_{SCE})	Current (A)	Test Time (h)	Results
14 molal Cl^- as $MgCl_2$	−266 to −278	−252 to −310	-10^{-4} to 10^{-4}	2,016	Pitting and SCC above and below V/S interface
14 molal Cl^- as $MgCl_2$	−260 to −269	O.C.	—	2,016	Pitting and SCC above and below V/S interface
14 molal Cl^- as $MgCl_2$ [a]	−265 to −291	O.C.	—	2,016	Pitting and SCC above and below V/S interface
14 molal Cl^- as $MgCl_2$ [a]	−259 to −273	−249 to −330	-10^{-4} to 10^{-4}	2,016	Pitting and SCC above and below V/S interface
14 molal Cl^- as $MgCl_2$ [b]	−276 to −285	−256 to −340	-10^{-4} to 10^{-4}	2,016	Crevice corrosion and SCC of inner U-bend above and below V/S interface
14 molal Cl^- as $MgCl_2$ [b]	−271 to −285	O.C.	—	2,016	Crevice corrosion and SCC of inner U-bend above and below V/S interface

O.C. – open circuit V/S – vapor/solution [a] – mill-finished surface [b] – Double U-bend

APPENDIX E

MICROSTRUCTURES OF ALLOY 825

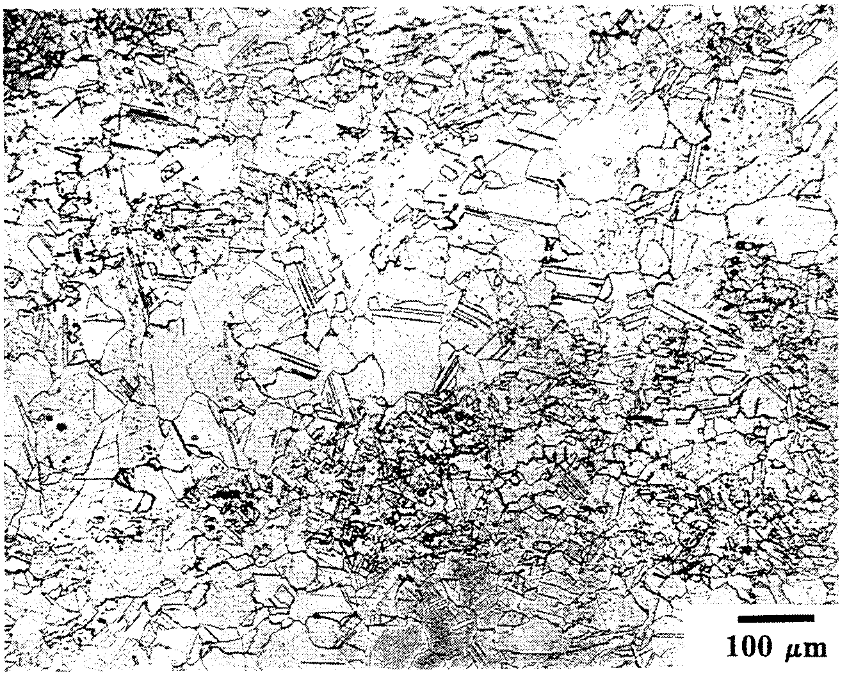

Figure E-1. Microstructure of mill-annealed alloy 825 (transverse cross-section) at low magnification

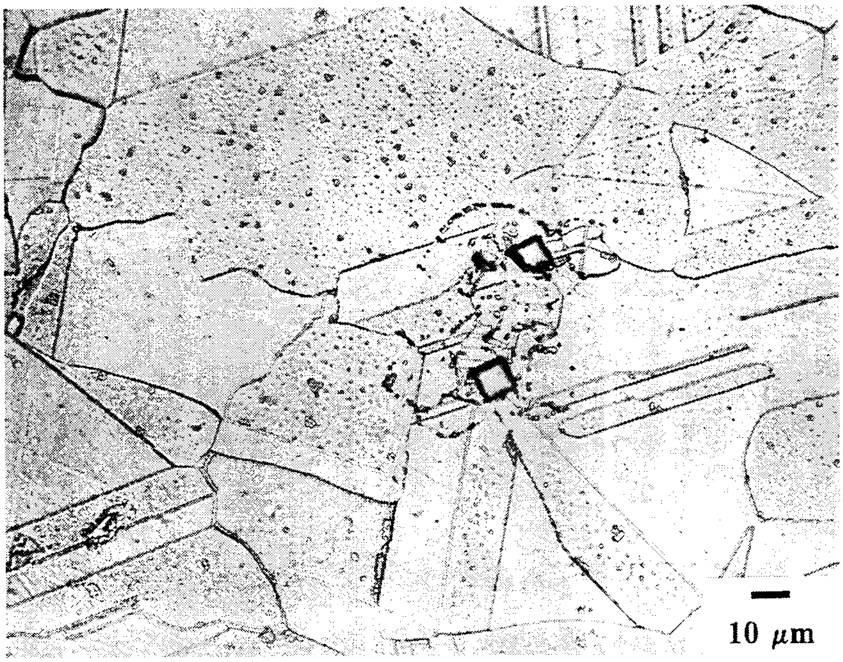

Figure E-2. Microstructure of mill-annealed alloy 825 (transverse cross-section) at high magnification

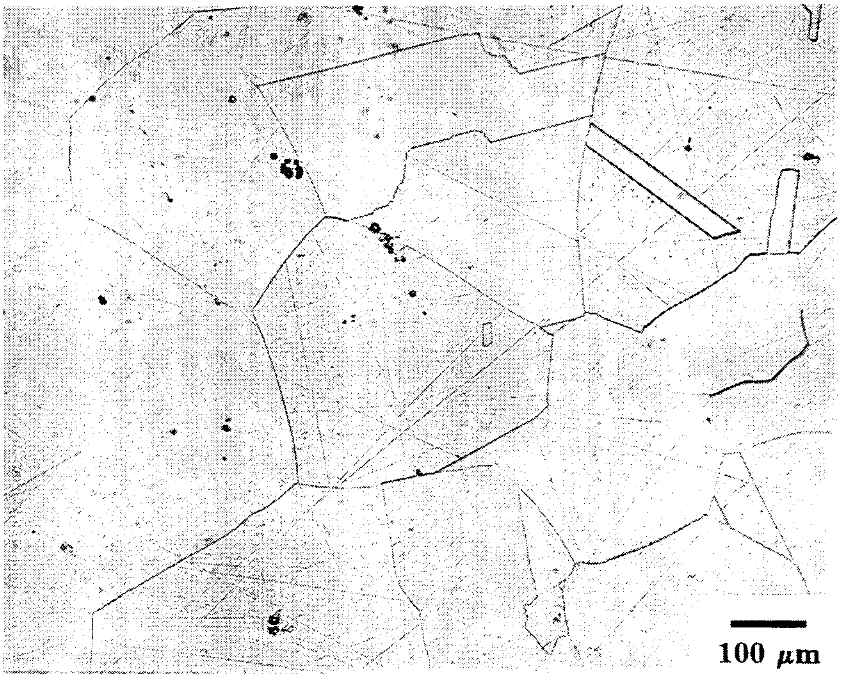

Figure E-3. Microstructure of solution-annealed alloy 825 (transverse cross-section) at low magnification

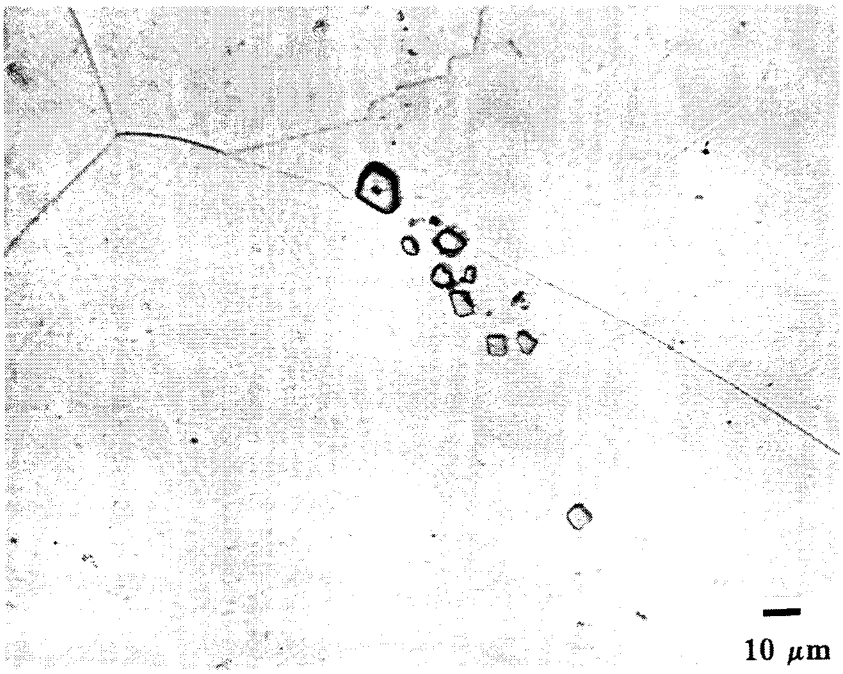

Figure E-4. Microstructure of solution-annealed alloy 825 (transverse cross-section) at high magnification

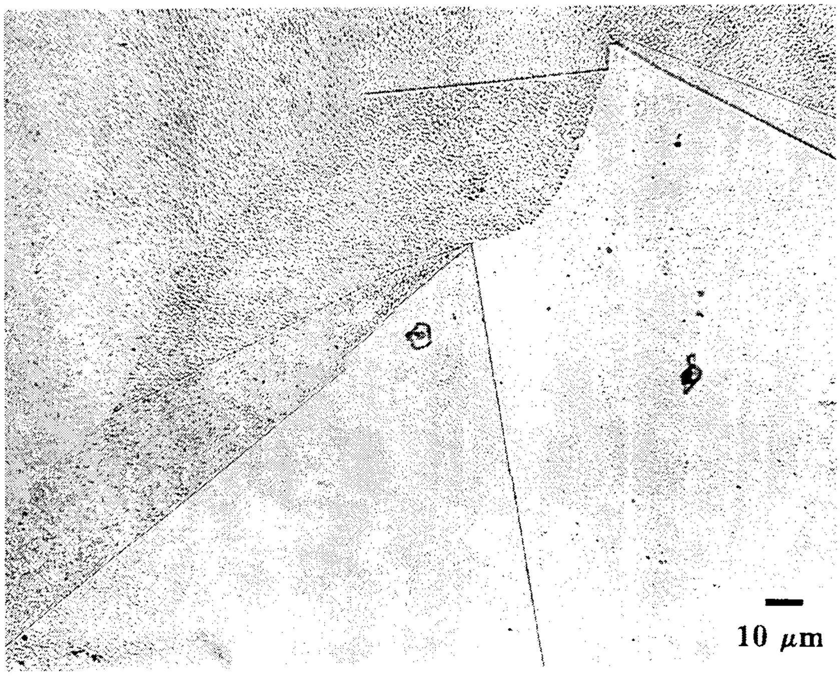

Figure E-5. Micrograph of solution-annealed alloy 825 heat-treated at 700 °C for 0.1 hr

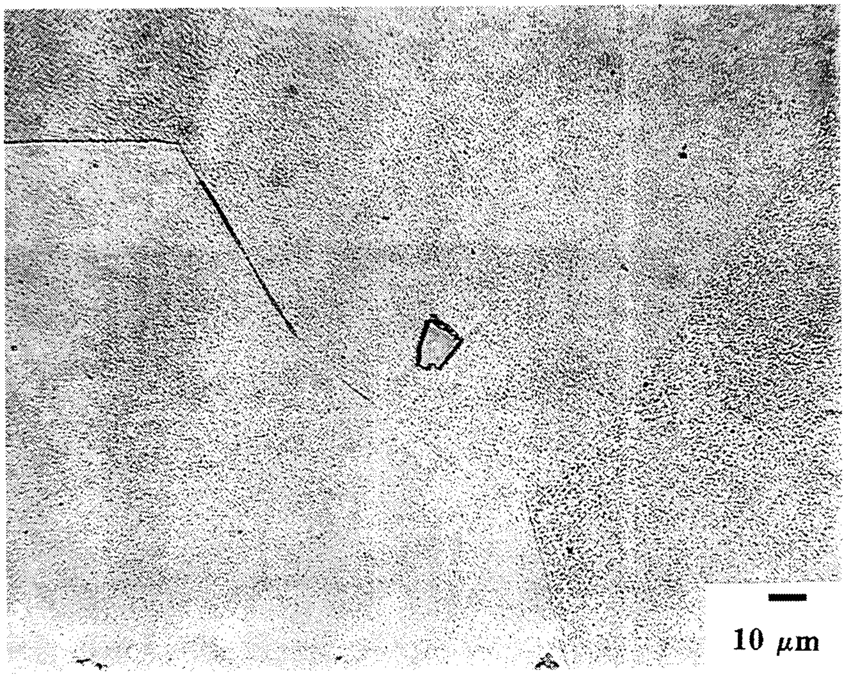

Figure E-6. Micrograph of solution-annealed alloy 825 heat-treated at 700 °C for 1.0 hr

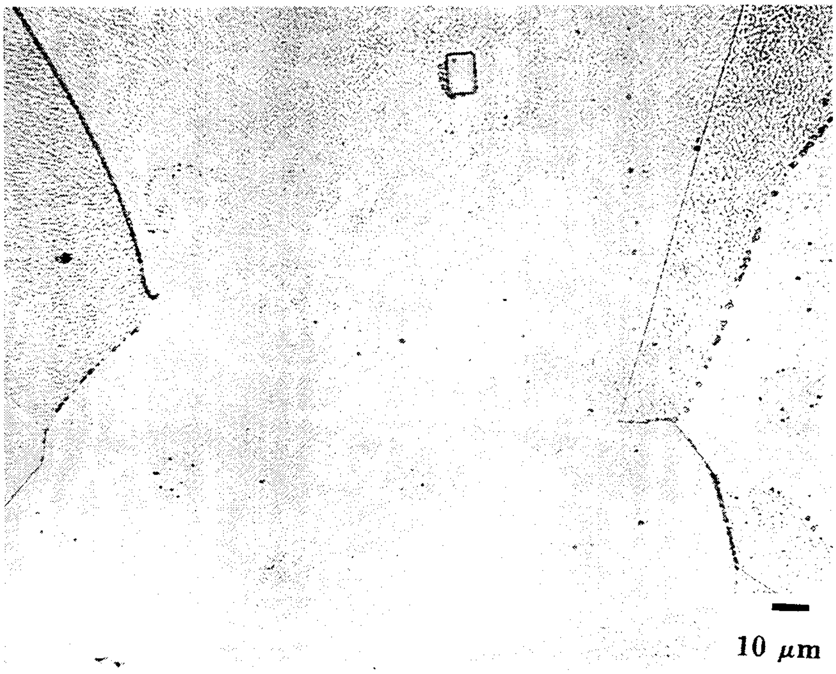

Figure E-7. Micrograph of solution-annealed alloy 825 heat-treated at 700 °C for 15 hr

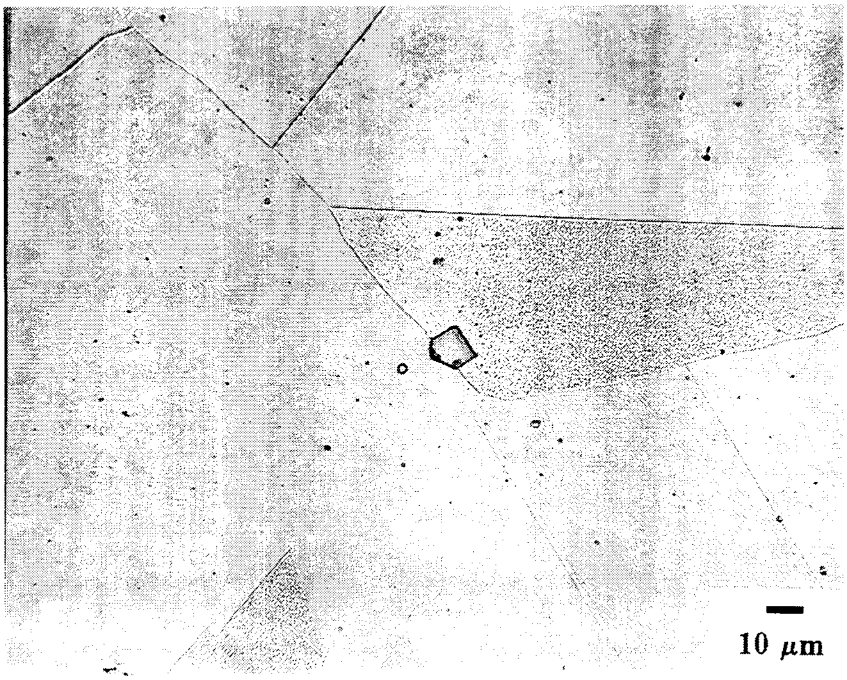

Figure E-8. Micrograph of solution-annealed alloy 825 heat-treated at 600 °C for 15 hr

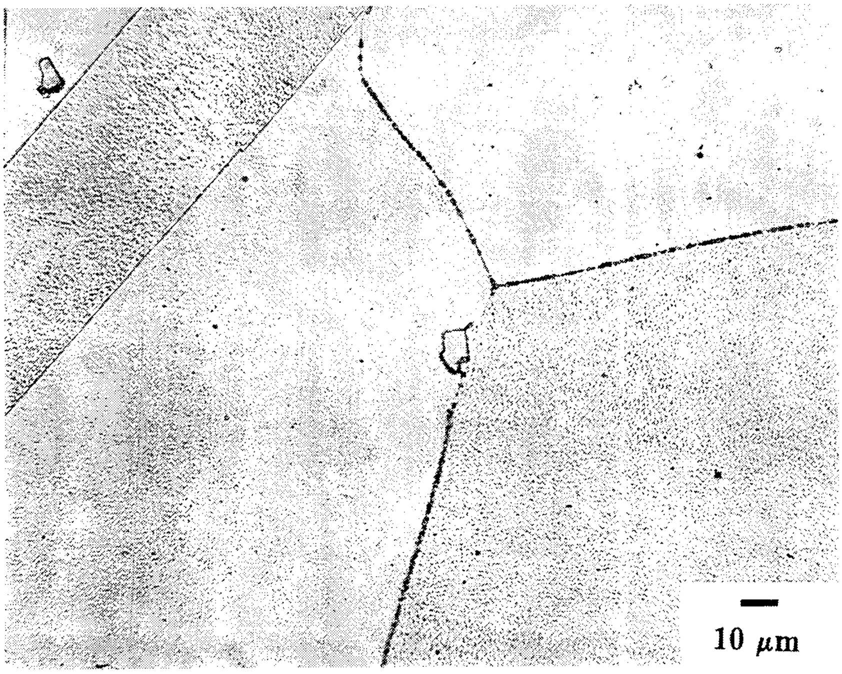

Figure E-9. Micrograph of solution-annealed alloy 825 heat-treated at 750 °C for 15 hr

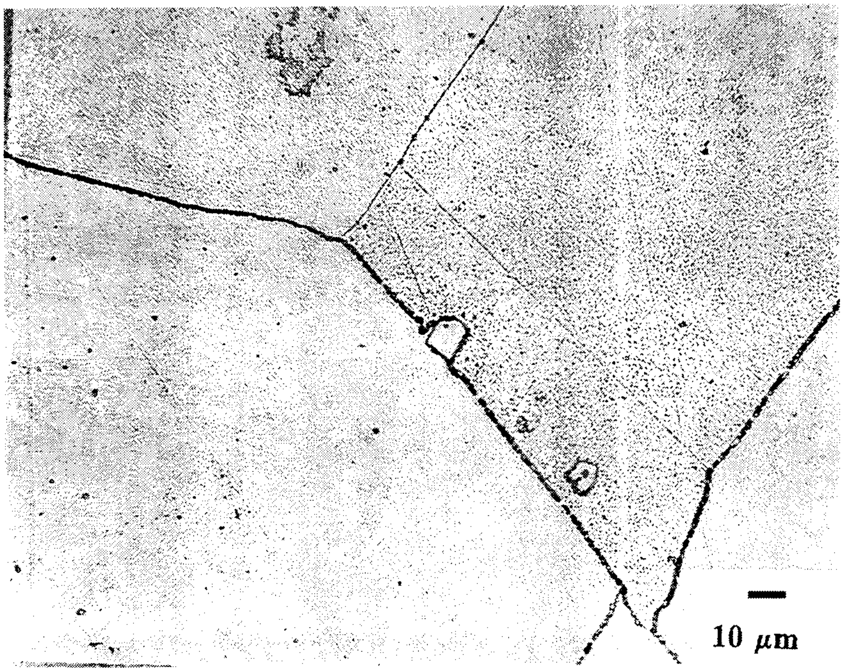

Figure E-10. Micrograph of solution-annealed alloy 825 heat-treated at 800 °C for 15 hr

APPENDIX F

INTERGRANULAR CORROSION TESTS OF ALLOY 825—DATA TABLES

Table F-1. Average corrosion rates of mill-annealed specimens of alloy 825 (Heat HH4371FG) in boiling 65 percent HNO_3 acid (240 hours exposure) after various heat treatments

			Corrosion Rate			
			(mm/year)		(mg/dm^2·d)	
Specimen	Temp (°C)	Time (hr)	Method 1	Method 2	Method 1	Method 2
MA			0.107	0.109	23.9	24.4
MA*A1*T1	600	0.1	0.125	0.128	28.0	28.5
MA*A1*T2	600	1.0	0.138	0.142	30.8	31.7
MA*A1*T3	600	15.0	0.229	0.235	51.2	52.4
MA*A2*T1	638	0.1	0.101	0.102	22.6	22.6
MA*A2*T2	638	1.0	0.160	0.160	35.7	35.8
MA*A2*T3	638	15.0	1.029	1.029	229.5	229.5
MA*A3*T1	700	0.1	0.123	0.123	27.4	27.4
MA*A3*T2	700	1.0	0.177	0.177	39.5	39.5
MA*A3*T3	700	15.0	1.262	1.262	281.3	281.4
MA*A4*T1	750	0.1	0.128	0.128	28.5	28.5
MA*A4*T2	750	1.0	0.103	0.105	23.1	23.3
MA*A4*T3	750	15.0	1.125	1.153	250.8	257.1
MA*A5*T1	800	0.1	0.115	0.118	25.7	26.3
MA*A5*T2	800	1.0	0.132	0.136	29.3	30.3
MA*A5*T3	800	15.0	0.211	0.218	47.0	48.5
MA*A6*T1	900	0.1	0.110	0.110	24.5	24.5

Table F-2. Average corrosion rates of solution-annealed specimens of alloy 825 (Heat HH4371FG) in boiling 65 percent HNO_3 acid (240 hours exposure) after various heat treatments

			Corrosion Rate			
			(mm/year)		$(mg/dm^2 \cdot d)$	
Specimen	**Temp (°C)**	**Time (hr)**	**Method 1**	**Method 2**	**Method 1**	**Method 2**
SA			0.116	0.118	25.9	26.1
SA*A1*T1	600	0.1	0.199	0.207	44.4	46.2
SA*A1*T2	600	1.0	0.107	0.107	23.9	23.9
SA*A1*T3	600	15.0	0.226	0.228	50.5	50.8
SA*A2*T1	638	0.1	0.120	0.120	26.7	26.8
SA*A2*T2	638	1.0	0.158	0.159	35.3	32.3
SA*A2*T3	638	15.0	1.397	1.397	311.5	311.4
SA*A3*T1	700	0.1	0.113	0.114	25.3	25.3
SA*A3*T2	700	1.0	0.341	0.341	76.0	76.1
SA*A3*T3	700	15.0	15.459	15.459	3447.6	3447.7
SA*A4*T1	750	0.1	0.127	0.128	28.4	28.5
SA*A4*T2	750	1.0	3.775	3.999	841.8	892.0
SA*A4*T3	750	15.0	4.937	5.059	1100.9	1123.1
SA*A5*T1	800	0.1	0.288	0.299	64.2	66.7
SA*A5*T2	800	1.0	0.533	0.533	118.9	119.0
SA*A5*T3	800	15.0	1.315	1.380	293.4	307.7
SA*A6*T1	900	0.1	0.173	0.173	38.5	38.5

Table F-3. Average corrosion rates of solution-annealed and solution-annealed + cold-worked specimens of alloy 825 (Heat HH7004FK) in boiling 65 percent HNO_3 acid and in boiling ferric sulfate-sulfuric acid after various heat treatments

Specimen	Temp. (°C)	Time (hr)	Corrosion Rate (mm/yr)			
			Nitric Acid		Ferric Sulfate	
			No Cold Work	25% Cold Work	No Cold Work	25% Cold Work
SA′			0.100	0.094	0.220	0.220
SA′*A0*T3	550	15	0.109	0.107	—	—
SA′*A1*T3	600	15	0.096	0.093	—	—
SA′*A1*T4	600	100	0.381	—	0.450	—
SA′*A1*T5	600	1,000	1.653	—	0.433	—
SA′*A2*T3	640	15	0.380	0.085	—	—
SA′*A2*T4	640	100	0.679	—	0.350	—
SA′*A2*T5	640	1,000	38.688	—	4.575	—
SA′*A3*T3	700	15	12.486	11.212	0.19	—
SA′*A3*T4	700	100	28.33	—	1.36	—
SA′*A4*T3	750	15	5.967	3.665	0.35	0.27
SA′*A4*T4	750	100	19.49	—	0.57	—
SA′*A5*T3	800	15	—	—	0.18	—